Influence of Grain Boundary Chemistry on the properties of CIGS photovoltaic cells

Mohit Raghuwanshi

Normandie Université

THESE

Pour obtenir le grade de Docteur

opéré par l'Université de Rouen

Spécialité : Physique des Matériaux

Influence de la chimie des joints de grains sur les propriétés des cellules photovoltaïques $Cu(In,Ga)Se_2$

Présentée et soutenue publiquement par

Mohit RAGHUWANSHI

Thèse soutenue publiquement le 20 Octobre 2015 devant le jury composé de		
M. Pere ROCA I CABARROCAS	Directeur de recherches – LPICM, Paris	Rapporteur
M. Olivier BRIOT	Directeur de recherches – Lab. C. Coulomb, Montpellier	Rapporteur
M. John KESSLER	Professeur – IMN Nantes	Président
M. Nicolas BARREAU	Maître de conference – IMN Nantes	Examinateur
M. Philippe PAREIGE	Professeur – GPM Rouen	Directeur de thèse
M. Sébastien DUGUAY	Maître de conférence– GPM Rouen	Encadrant
M. Emmanuel CADEL	Ingénieur de recherche – GPM Rouen	Invité

Thèse dirigée par Pr. Philippe PAREIGE

Groupe de Physique des Matériaux

UMR 6634 CNRS, Université de Rouen, INSA Rouen

To My Parents

Acknowledgements

Research work presented in this thesis was carried out in the laboratory of Groupe de Physique des Matériaux (GPM), Université et INSA de Rouen along with fruitful collaboration of Institut de Matériaux de Nantes. Firstly, I would like to thank the director of GPM lab Prof. Philippe Pareige and the director of Ecole Doctorale Prof. Didier Blavette for allowing me to pursue my research in best atmosphere.

I immensely thank my thesis director Prof. Philippe Pareige for encouraging me in every meeting and allowing me to express and implement my ideas with liberty. His training and remarks were invaluable which will definitely help me in the future. I am highly thankful to my thesis supervisor Dr. Sébastien Duguay for his supervision and regular interactions about my work. He never hesitated to help me in research or issues outside research. Guidance of both of them helped me throughout my thesis from first experiment to thesis writing. I am also very thankful to Dr. Emmanuel Cadel for his guidance in APT & FIB experiments. His experience in this field was very helpful to me. I thank Dr. Nicolas Barreau for preparation of various CIGSe samples and also for regular interactions, discussions and answering my questions. I exceptionally thank the funding of Région Haute Normandie for my PhD and their grants which allowed me to travel for conferences.

I sincerely thank my thesis reporters and examinators for critical reading of the manuscript. Their suggestions and corrections were very helpful and scientific discussions with them were invaluable.

I am thankful to Dr. L. Arzel for essential characterization of thin films, Dr. I. Braems for important discussions involved in this work and Dr. F. Couzinie-Devy for his helpful suggestions. I am also thankful to Dr. J. Le Perchec and Dr. A. Lanterne for their help in understanding Si solar cells.

Instruments don't work in the absence of their guardians. I am grateful to G. Da Costa, J. Houard, F. Cuvilly and I. Blum for their contributions in solving APT and FIB experimental issues, C. Castro for her help in TEM analysis and B. Foulon for her help in laboratory work. I highly appreciate all the administration and IT members of GPM who were always available for any assistance and helped me during the course of my PhD keeping me out of any worries. I am very thankful to all GPM members for maintaining a pleasant and friendly environment.

I would like to thank Dr. G.V. Pavan Kumar, whose training and advises during my masters proved to be helpful in my PhD. I am thankful to BCS clubs for keeping me energetic and

entertained throughout the years. I am very thankful to Antoine and Mme Saint-Martin for their kind help in apartment assistance.

Physical fitness is very important in a PhD, award for big thanks goes to Mykola and Harsh for their sportive vibrations and recreation. I am very thankful to Nooshin, Isabelle, Manon and Megha for their helpful assistances. I thank my officemates Claire, Alfiya, Romain and wishes them the very best for their PhD.

Award for marvelous thanks goes to Monika and Deodatta, for their support and entertainment was prodigious, these two amazing friends were there every day with me. Thanks for this extraordinary journey and making the PhD a memorable one.

Finally, I would like to thank all my family members who were always with me, even from 8000KM. I thank my parents for whom words are never enough, your support and affection was never less. Thank you for believing in me and supporting me to fulfil my desires. Thanks for being the most wonderful parents.

Table of Contents

List of Figures

Introduction

The most abundant energy resource on earth is "Solar Energy" which we receive every day for no cost. Despite of this fact, solar energy is not utilized to meet even 0.5% of world's total energy demands and 80% of the world's total energy is produced by non-renewable sources of energy. Figure below shows the statistics of world's total energy consumption by source, and it is evident that contribution of solar energy towards world's energy consumption is very low.

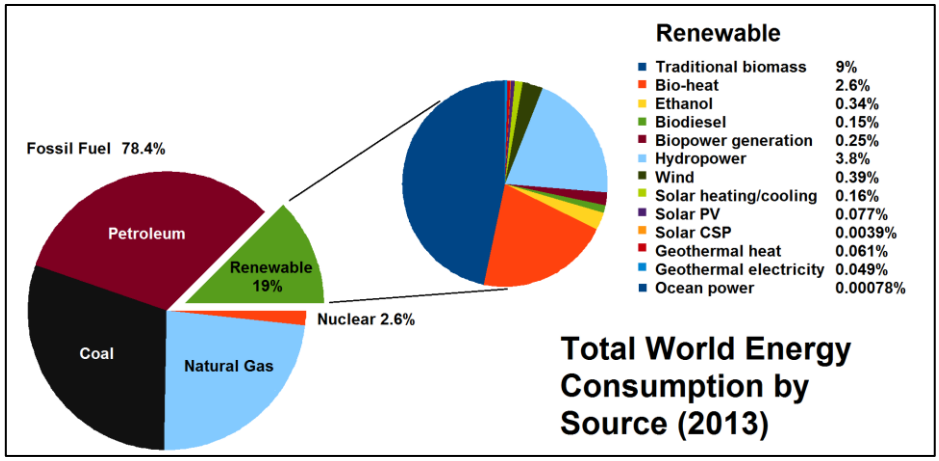

Figure: Statistics of world energy consumption by source. Image courtesy: REN21 Renewables 2014 Global Status Report

Apart from huge availability of the resource, solar energy is not currently utilized to a large extent. The question is why? Answer is: It is mainly because of expensive installations, almost inexistent storage capacities and not very high conversion efficiencies of solar cells. The development and capitalization of solar cells require research progress towards better understanding of various materials properties and efforts in increasing their efficiency.

Recently, thin film solar cells like $Cu(In,Ga)(S,Se)_2$, CdTe, CZTS have shown to be of high efficiency even with ≈ 2 µm absorber thickness due to their very high absorption coefficient. Thin film solar cells contribute today around 9% of total PV market and the remaining share is mainly dominated by silicon. Due to its stability and good efficiency, $CuInSe_2$ semiconductors have gained importance in past years as a promising and potential material for solar cells. Ga addition to this compound demonstrated enhanced efficiency, making $Cu(In,Ga)Se_2$ (CIGSe) the most efficient solar cell under thin film category with efficiency close to 22%. Efficiency of this device has continuously increased in past few years leading

to dominance of CIGSe in thin film PV. In 2013, CIGSe contributed to 2% of the total installed solar cell modules over the world.

In this work we focus on the understanding of these thin film solar cells properties, namely: Copper Indium Gallium Selenide (CIGSe) solar cells. This work is performed in collaboration with IMN (Institut de Matériaux de Nantes), where synthesis and primary characterization of polycrystalline CIGSe thin films were performed under the supervision of Dr. Nicolas Barreau.

It is known that polycrystalline CIGSe (7.5% Ga concentration) performs better than its monocrystalline counterpart due to beneficial effects of grain boundaries. To improve these cells further, we need to understand how grain boundaries (GBs) may affect these cells. Thus to understand the role of GBs which are few atomic layers thick, a technique able to resolve materials at the atomic scale is required. Hence Atom Probe Tomography (APT), a technique able to explore atomic distribution at sub nanometer resolution is utilized as the main tool in this research. APT is used here to investigate 3D atomic distribution of various elements in vicinity of GBs and to understand their important role in influencing device performance of CIGSe.

The maximum efficiency of CIGSe to date (21.7%) is observed for 8% overall Ga concentration. However, despite of their optimum band gap value ($E_g \approx 1.4$ eV) for solar energy conversion, wide band gap CIGSe cells (18% Ga) present lower efficiency (10%). This puzzle lead to debate for past two decades and various theories were proposed to explain poor efficiency of Ga rich (wide band gap) CIGSe. Recently some theories proposed that changes in GB properties could be the reason for poor performance of Ga rich CIGSe cells. In this work, APT is used to detect atomic level changes in vicinity of GBs (termed as GB chemistry) of CIGSe to understand their role in device performance.

GB chemistry of CIGSe for various Ga/In concentration were investigated to understand properties of GBs. Experimental evidences were found in this work showing that GB chemistry is significantly modified as a function of Ga concentration which is the main reason for poor performance of Ga rich cells.

The first chapter gives a brief explanation of physical principles of solar cells and essential solar cell parameters used in this work. An extensive survey of different experiments and theories which are developed in past years is discussed to explain beneficial effects of GBs in CIGSe. Various theories developed in past few years explaining poor performance of Ga rich CIGSe are also reviewed.

The second chapter illustrates physical principles of various instruments namely: APT, EBSD, EDX, SEM/FIB, and XRD which are used extensively in this work.

The third chapter illustrates device performance of CIGSe, phase identification using XRD and explores grain distribution of CIGSe using EBSD at micrometer scale. Experimental optimizations for APT performed in this work are explained.

The fourth chapter explores GB chemistry of CIGSe at various Ga contents using APT which explains degraded performance of wide band gap CIGSe cells. An experimental evidence of changes in GB chemistry for different Ga contents is provided. Various theories based on our results are developed and discussed.

The fifth chapter explores some possibilities of improving Ga rich CIGSe based on our results. Performance of Ga rich CIGSe is hence improved by addition of some chemicals before thin film deposition. In the end a general conclusion and perspectives for future work are given.

1. Chapter One: Solar cells based on $Cu(In,Ga)Se_2$ thin films

Solar cell works on the principle of converting light energy to electrical energy, in other words photon energy is converted to directional motion of electrons. Photovoltaic effect was first observed by A.E. Becquerel in 1839 and more than 100 years later the first photovoltaic (PV) cell was developed at Bell laboratories in 1954 [1]. Since then research in photovoltaics picked a greater pace and interests realizing need for cleaner and cheaper source of energy. Initial research and development in solar cells were mainly performed on Silicon but different materials have been realized since then as listed in Figure 1.1 demonstrating steady improvement in performance of solar cells over years. Figure 1.1 shows evolution of different PV technologies with time. Considering thin film PV technologies (green color), remarkable improvement is evident for $Cu(In,Ga)Se_2$ (CIGSe) solar cells in past two decades and today they are most efficient solar cells in thin film. Good stability and performance of CIGSe makes the material highly attractive and one of the most promising semiconductor for photovoltaic industry.

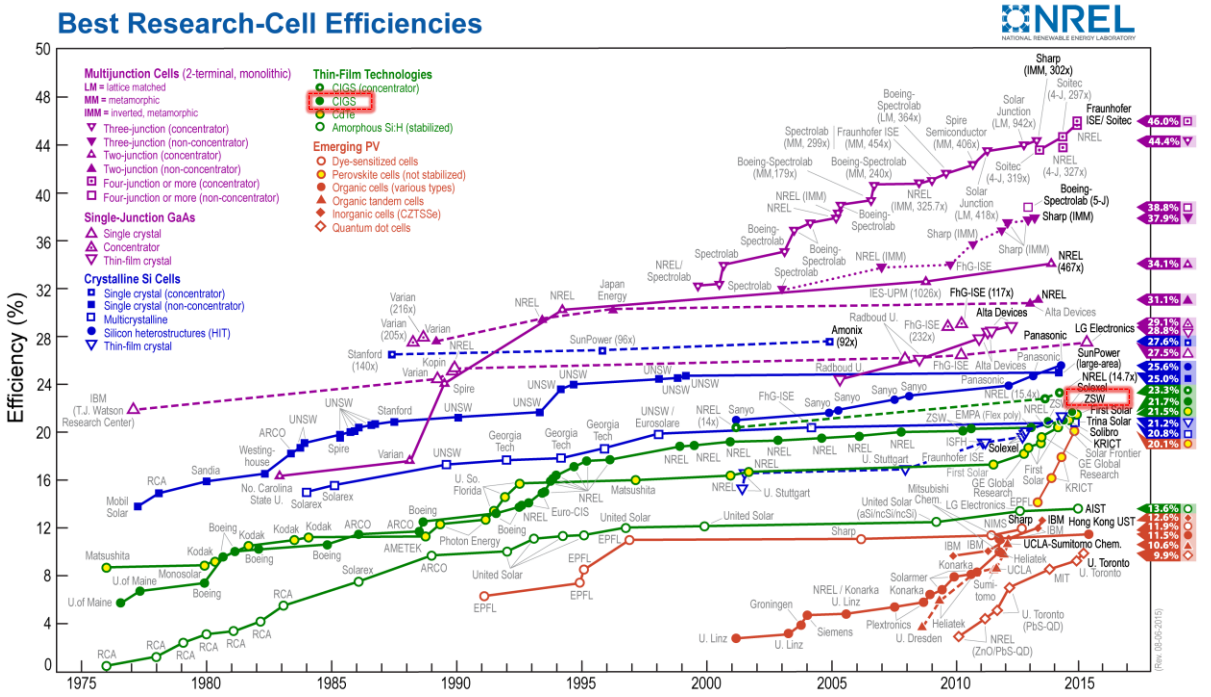

Figure 1.1: Best research cell efficiency over years. Source: National Renewable Energy Laboratory (NREL)

Key role of an efficient solar cell is to effectively generate and transport charge carriers formed during light illumination to produce current. Basic principles of solar cells are

discussed in this chapter considering Si solar cell model and present the case of CIGSe. Material properties of CIGSe thin films, crystal structure, phase diagram and other properties are discussed to understand the effects and importance of Ga content in the system. This chapter then gives an overview of research works performed on CIGSe thin films during past years to understand the material's properties and their approaches towards improvement.

1.1 Solar cells: Physics and Principles

To convert light energy to electricity, one needs materials which can absorb light and convert photon energy to unidirectional motion of electrons. Semiconductors have optimum band gap and are best suited as absorber layers for solar cells. Reasons for preference of semiconductors over other materials are presented in this chapter.

Three key processes are involved in functioning of a typical solar cell:

1) Generation of electron hole pair after light absorption
2) Separation of these carriers by pn junction
3) Collection of carriers through external circuit

1.1.1 Generation: Interaction of light and semiconductor

Interaction of light and semiconductor mainly depends on material properties of semiconductor and energy of photons, different instances are discussed below.

a) Absorption

There are three possibilities after the incidence of photon on the surface of a material: reflection, absorption, transmission. For a photovoltaic device to operate, the photon is required to be absorbed to generate power. Absorbed photon may excite electron from valence band to conduction band depending on the energy of photon (E_{ph}) and band gap energy (E_g) of the semiconductor. Semiconductors requiring assistance of phonon to be absorbed between conduction band minima (CBM) and valence band maxima (VBM) are called indirect band gap semiconductors such as Si. And the ones which can make a direct transition between VBM and CBM are called direct band gap semiconductors such as CIGSe, GaAs etc. Considering the case of direct band gap semiconductors, irradiation of photons on material's surface results in any of the three consequences:

1) $E_{ph} < E_g$ → Photon does not interact with semiconductor and passes through (except for less probable multi photon absorption).

2) $E_{ph}=E_g$ → Photon is efficiently absorbed and excites an electron from valence band to conduction band leaving behind a hole.
3) $E_{ph}>E_g$ → Photons is strongly absorbed, in most cases remaining energy is wasted in thermal energy. In some cases, remaining energy may excite another electron from valence band to conduction band by Auger process.

In addition some parameters specific to semiconductor materials plays a major role in performance of a solar cell and are:

a) Absorption Coefficient: Quantifies the absorbing capability of semiconductor at a particular wavelength. Highly absorbing materials (such as CIGS) have high absorption coefficient and can efficiently absorb light even in few micrometers thickness.
b) Absorption depth: As absorption coefficient is specific to wavelength, light with different wavelengths penetrate materials at different depths. Absorption depth is given by the inverse of absorption coefficient and measures distance from the surface where light intensity drops by a factor of 1/e. Figure 1.2b shows absorption coefficient of $CuInSe_2$ (CIS) and other materials used for solar cells over wide spectral range demonstrating strong absorption properties of CIS which is beneficial for solar cells.

Although CIS has high absorption quality, its lower band gap (≈1.0 eV) limits its device performance. Hence alloying with higher band gap material $CuGaSe_2$ (≈1.67 eV) is expected to improve its performance [2,3] by forming quaternary alloy CIGS. One of the best advantages of using $Cu(In,Ga)Se_2$ (CIGSe) solar cells is tunability of its bandgap by varying Ga/In compositions in $CuIn_{1-x}Ga_xSe_2$. Varying Ga to In ratio (named here as x=[Ga]/[In]+[Ga]), the band gap of CIGSe can be tuned co-linearly from 1.02 eV (x=0) to 1.67 eV (x=1) [4].

High efficient Si cells comprise of 100 μm of thickness have similar efficiency than few micrometers of CIGSe. Cost effectiveness with better efficiency makes CIGSe one of the most promising materials for solar cell preparation.

Solar energy received on earth surface is in the form of electromagnetic waves released due to fusion reaction between hydrogen atoms forming helium. A part of solar energy is absorbed by sun and earth's atmosphere and rest received on land is denoted in form of AM (Air Mass) spectrum. AM1.5G is the solar spectrum received on surface of earth (usually

used in latitudes near Europe, 1.5 correspond to 1.5 times more air atmosphere compared to direct sunlight on earth (which is AM0G) as shown in Figure 1.2a and is an important parameter to capitalize solar cells.

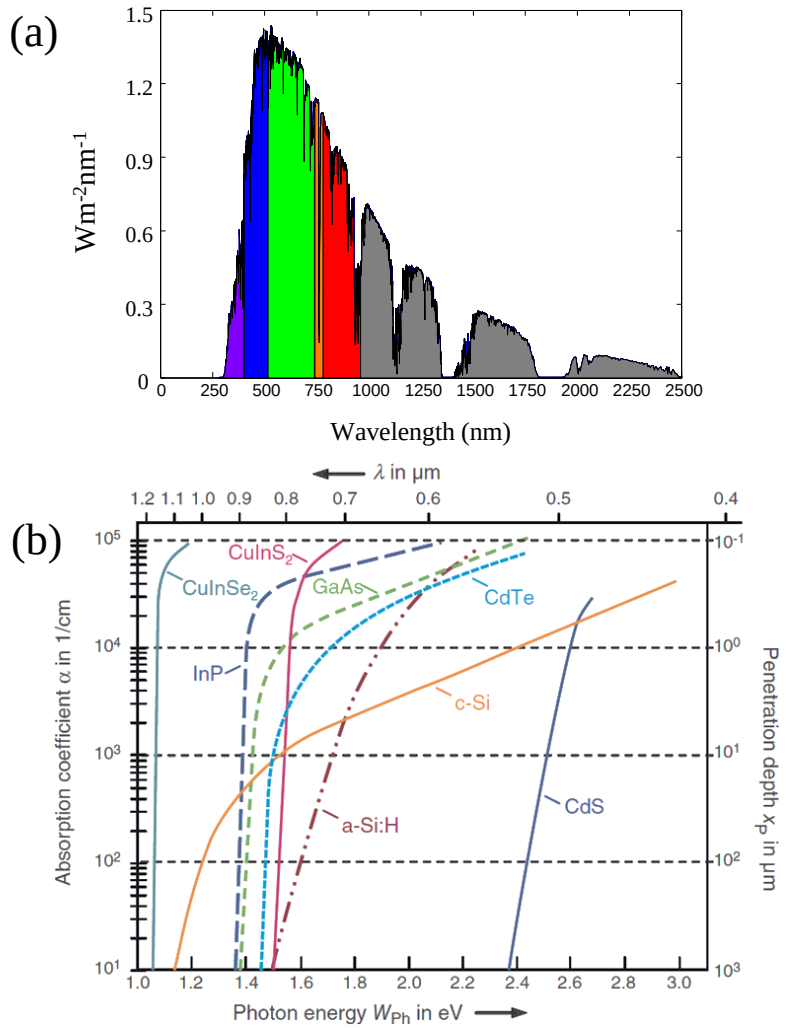

Figure 1.2 (a) Solar irradiance as a function of wavelength. (b) Absorption coefficient of CuInSe2 and other materials as a function of photon energy and wavelength.

b) Recombination

All electron hole pairs generated due to light absorption may not be all used in generating electricity even in presence of intrinsic electric field. Electrons in the conduction band are in metastable state and can jump back to valence band before being collected. This jump back allows lowering their energy and stabilizing. Electron stabilizing to valence band is equivalent to pairing up with a hole, this process is called recombination. Recombination is detrimental to solar cell performance and is one of the major factors limiting the efficiency. There are typically three types of recombination:

a) Radiative recombination: Electron from conduction band releases energy in form of a photon and comes back to valence band.
b) Auger recombination: Energy emitted due to electron hole recombination is absorbed by an electron in the conduction band raising its energy level to unstable state and eventually thermalizing back to conduction level.
c) Shockley-Read-Hall recombination (SRHR): Defects in semiconductors give rise to defect states. Instead of directly relaxing to valence band from conduction band, electron can pass in between through defect levels completing the process in two steps. Pure semiconductors without any defects do not exhibit this type of recombination.

c) Diffusion length

Average distance from point of charge carrier generation to their point of recombination is called diffusion length of the carrier. Thus larger diffusion length increases lifetime of carriers and hence increase their chance of collection at the terminals. Efficient transfer of minority carriers is more important for a solar cell as they are very less in concentration as compared to majority carriers and hence their collection determines performance. Electrons are the minority carriers in p-type CIGSe hence diffusion length of electrons in CIGSe would be an important parameter to be considered. Thus diffusion length of minority carrier is considered as more important parameter. Diffusion length for monocrystalline silicon is around 100 – 300 μm [5], and 0.3 – 2 μm for polycrystalline CIGSe [6].

1.1.2 Separation: pn junction

pn junction forms the basis and heart behind operation of laser diodes, LEDs, transistors and also solar cells. For simplicity, a model of silicon (Si) is used here to explain doping in semiconductors. In a pure Si wafer, Si atoms are covalently bonded together such that each atom fulfils its octet to complete 8 electrons in their outermost shell as shown in Figure 1.3a. A boron (B) atom has 3 electrons (one e^- less than Si) in the outermost shell. If one Si atom is replaced by one B atom, a hole (no physical quantity, term used for absence of an electron) is formed as shown in Figure 1.3b. This intentional way of substituting elements is called substitutional doping. B doped in Si decreases overall electron concentration making the system positively charged and hence is called p-type doping.

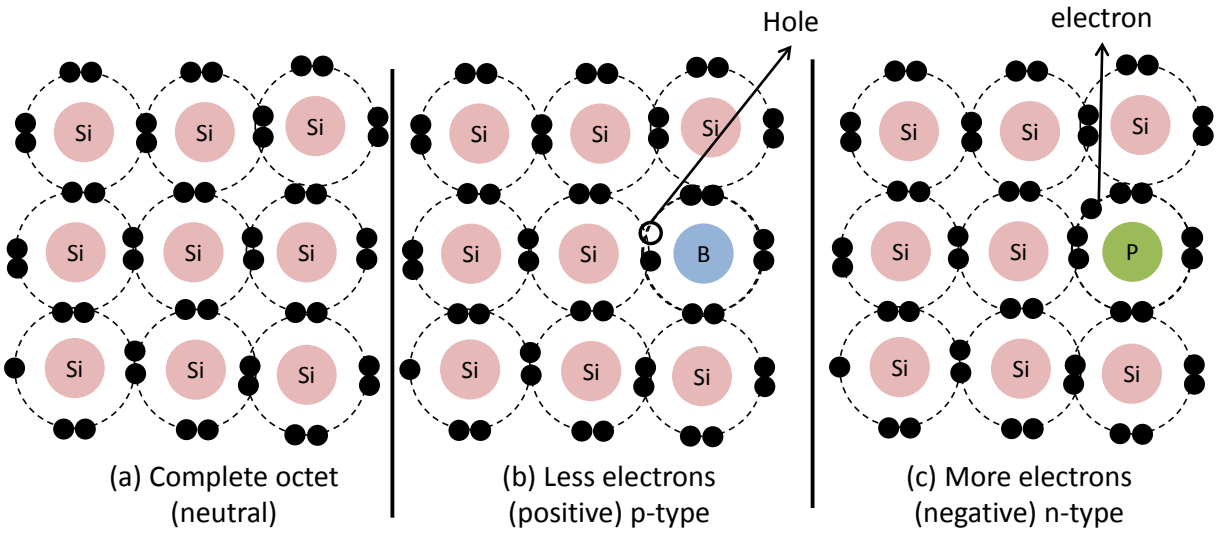

Figure 1.3 Electronic structure of silicon for (a) undoped (b) p-type doped (c) n-type doped

Similarly, Si can be doped with another atom with an additional electron in the outermost shell such as P, As, Sb (5 electrons in outermost shell). This type of doping leads to overall negative charge because of an extra free electron per Phosphorus atom and is called n-type semiconductor as shown in Figure 1.3c. Hence n-type (or p-type) doping increases the concentration of electrons (or holes) or in general, concentration of carriers is increased due to doping thereby increasing conductivity of the semiconductor. Hence majority carriers in p and n-type semiconductors are holes and electrons respectively; adjoining these two parts (p and n) forms pn junction with properties very different even if the bulk materials are identical. Similar explanation for doping is not possible in compound semiconductors like CIGSe. n-type or p-type doping of CIGSe semiconductors are believed to result from the intrinsic defects [6]. Twelve intrinsic point defects are reported in CISe semiconductors, among them six antisite defects: In_{Cu},In_{Se}, Cu_{In}, Cu_{Se}, Se_{Cu} and Se_{In}. Three interstitials Se_i, Cu_i and In_i and three vacancies V_{Se}, V_{Cu}, V_{In}. CIGSe considered here is a p-type semiconductor containing free hole density typically around 10^{16} to 10^{17} cm^{-3} resulting from intrinsic defects. Ga addition in CISe further increases the number of defects as it will be discussed in section 1.3.4.

A pn junction is formed by joining p-type semiconductor to n-type semiconductor as shown in Figure 1.4a. Free electrons from n-type diffuse towards p-type and holes from p-type diffuse towards n-type, leading to the formation of depletion region at equilibrium. Due to this phenomenon, p-type side (in depletion region) becomes overall negatively charged and n-type side becomes overall positively charged, thus forming an intrinsic electric field

between the junctions in direction from n side to p side as shown in Figure 1.4a. At equilibrium, there is no net flux of charge carriers across the junction and the presence of the intrinsic electric field separates electron hole pairs preventing them to recombine. Light illumination generates electron hole pairs which are separated due to this electric field and can be collected at the terminals producing electric current; this is the basic principle of a solar cell.

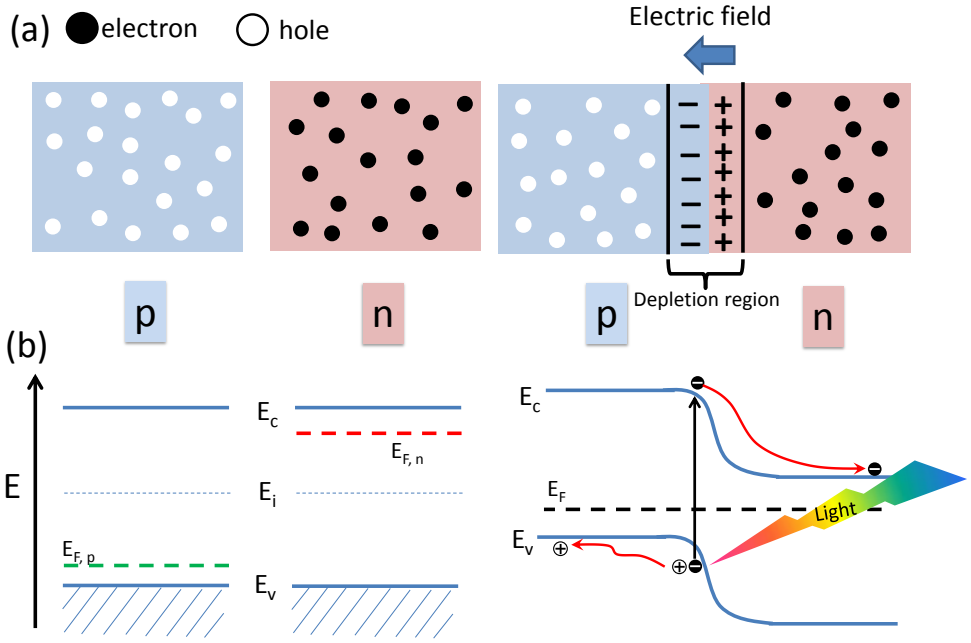

Figure 1.4: (a) Distribution of holes and electrons in p and n-type semiconductor, schematic image before and after forming pn junction. (b) Schematic energy level diagram for p and n-type semiconductor & for pn junction at thermal equilibrium

Fermi energy in an intrinsic semiconductor (E_i) is defined as the highest energy of electrons in the valence band at 0 K and is in the middle of the conduction and valence band for an intrinsic semiconductor in ideal conditions (absence of any defect). A semiconductor doped with p-type dopant results in reduction of electron concentration, hence the Fermi energy is lower than E_i and is closer to the valence band energy ($E_{F,p}$), similarly for n-type doping, Fermi energy increases and shifts towards conduction band ($E_{F,n}$) as shown in Figure 1.4b. After forming the pn junction, Fermi levels on the two sides match under thermal equilibrium (E_F). Photons with energy greater than band gap get absorbed and generate electron hole pair. Electron is excited to conduction band which is then relaxed and moves towards n-type region. Similarly, hole is carried towards p-type. Spontaneous recombination of electron hole pairs is now prevented due to built-in potential. Hence connecting the two ends by a conducting wire, electricity is produced due to motion of electrons. Electron and hole would

eventually recombine when the circuit is completed but motion of these carriers along the circuit creates output electric current.

1.1.3 Collection: Solar Cell structure

A typical solar cell device consists of minimum four regions each contributing importantly in the production of output power. Four regions as shown in Figure 1.5 are front contact, emitter, base and back contact. Absorption of photons followed by generation of carriers takes place in emitter and base regions. Due to intrinsic electric field, generated electrons and holes are separated to n and p regions respectively and are then transported to the external circuit and collected via front and back contacts respectively. More details about carrier collection at different load voltages are described in next section.

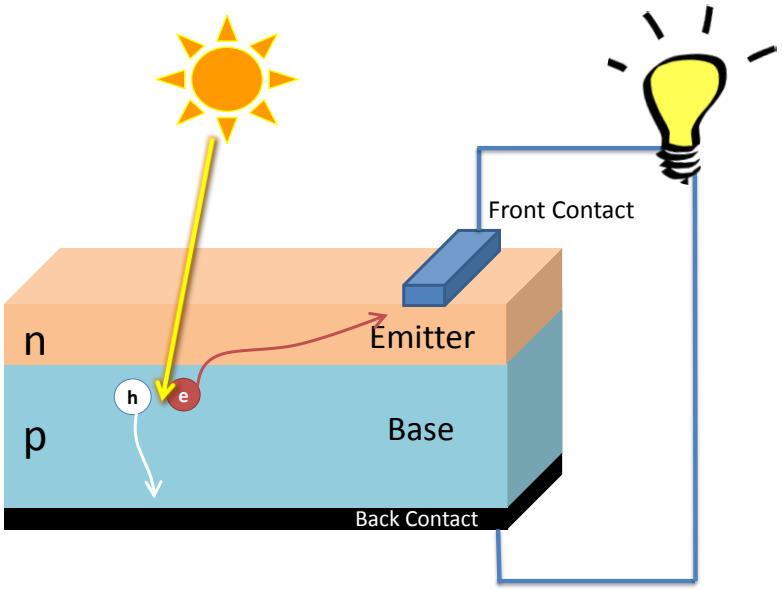

Figure 1.5: Schematic diagram of a typical solar cell consisting mainly of four different regions as shown: emitter, base, front and back contacts.

Latest solar cell modules include anti-reflective coating to minimize reflection losses from surface of the solar cell; Si solar cell modules introduce surface texturization [7] for efficient absorption. Above solar cell design completes the basic pre-requisite for a solar cell to work. Advanced modules make use of more than one pn junction to absorb maximum solar spectrum, they are called multi-junction solar cells or tandem solar cells that will not be described here but explained in ref. [8].

CIGSe solar cell structure

Schematic representation of a typical CIGSe solar cell is shown in Figure 1.6a and respective energy levels of valence band, conduction band and Fermi energy at zero bias are presented schematically in Figure 1.6b. The preparation and elaboration of different layers involved here are described in chapter 2. Here CIGSe is the main absorber layer with p-type semiconducting nature. In Figure 1.6b an example is shown with CIGSe band gap value =1.2 eV for x=0.32. Majority of collected carriers are generated in space charge region (SCR) as it closer to *pn* junction. And carrier collection due to quasi neutral region (QNR) is minor as it is far from intrinsic electric field region where recombination is dominant. n-type region consist of buffer layer CdS accompanied by n^+ (heavily doped n-type) layer of ZnO.

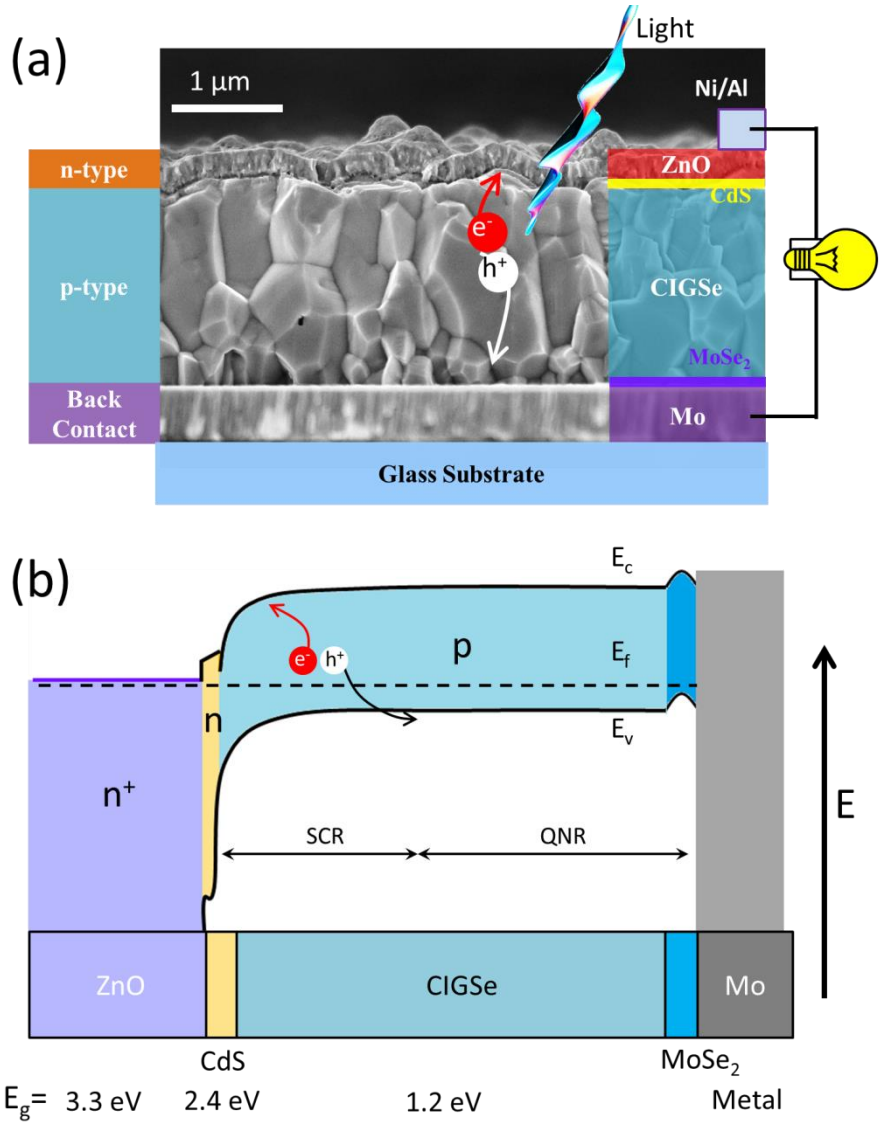

Figure 1.6 (a) Cross section SEM image (this work) of completed CIGSe solar cell (x=0.32) showing different layers involved. Schematic energy band diagram of a completed CIGSe solar cell at zero bias. SCR is space charge region and QNR is quasi neutral region.

CdS buffer layer is deposited on CIGSe to form effective pn junction and to prevent oxidation of CIGSe during ZnO deposition. Band gap of CdS is 2.4 eV and absorbs solar spectrum for wavelengths near UV. Transparent conducting oxide (TCO) on top of thin film solar cells is important for charge collection; here we use ZnO as TCO for CIGSe solar cells. ZnO layer acts as front surface and window layer with band gap 3.3 eV and allows majority of solar spectrum to pass through. pn junction is formed between p-type CIGSe and n-type CdS. At thermal equilibrium, p-type and n-type regions are aligned as shown in Figure 1.6. Due to difference in band gaps of the respective semiconductors band diagram in Figure 1.6 is not continuous as observed in different conductive nature of same semiconductor shown in Figure 1.4. Molybdenum (Mo) is deposited on glass substrate before CIGSe deposition and serves as metallic back contact of the material. $MoSe_2$ is formed between CIGSe and Mo [9,10] acting as quasi-ohmic contact and raising valence and conduction energy levels [11]. The remaining electron/hole dynamics is similar to as described previously.

1.2 Electrical parameters of solar cells: Influence of band gap

Energy of incoming photon must be equal to or greater than band gap energy of semiconductor in order to generate charge carriers; hence semiconductor selectively absorbs a part of solar spectrum. Electrical parameters play critical role in solar cell performance and vary systematically as a function of band gap. Thus it is important to study variation of solar cell parameters with changing band gap and this is described in this section.

1.2.1 I-V Curve and efficiency

I-V curve or current-voltage curve of a solar cell represents the value of output current measured at different load voltages. Current voltage measurements determine output power and efficiency and the most important parameters to characterize solar cell. For comparing cell modules and different cells, one compares their current densities (J) versus voltage curves which is commonly expressed as:

In Dark:

$$J(V) = J_0.\left[\exp\left(\frac{qV}{nkT}\right) - 1\right] \quad \textbf{(1.1)}$$

Under Light:

$$J(V) = J_0.\left[\exp\left(\frac{qV}{nkT}\right) - 1\right] - J_{photon} \quad \textbf{(1.2)}$$

The output power can be simply written as JxV

Where, J_{photon} = Light generated current

J_0 = Dark saturation current

n = ideality factor

T = temperature (K)

q = charge of electron

Plotting equations (1.1) & (1.2) one can obtain J-V curve under dark and under light and product of JV gives output power as shown in Figure 1.7.

According to equation (1.2) for solar cells under light illumination, an additional current J_{photon} is produced due to charge carrier generation at pn junction and forms the basis for output power generation in solar cells. As can be noticed from Figure 1.7, at zero voltage bias across the solar cell there is still some current flowing through circuit which is the current due to light illumination. Current running through the circuit even at zero external voltage is called **short circuit current (I_{sc})**, in other words this is the current flowing when the device is short circuited. Current drops to zero at higher values of positive forward bias and change its direction when increased further. Maximum voltage which can be exploited from a solar cell is the **open circuit voltage (V_{oc})**.

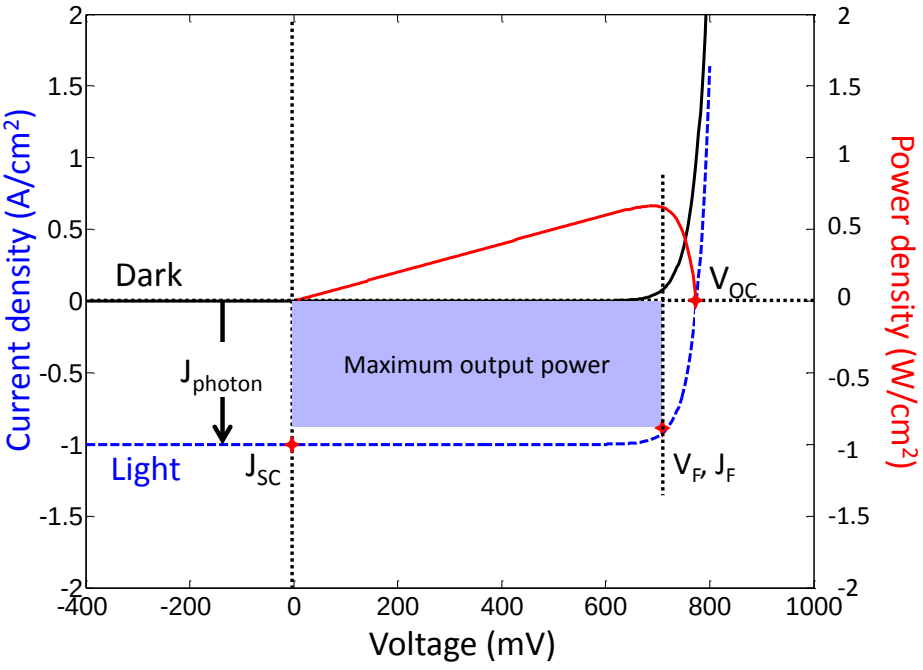

Figure 1.7: Current density – voltage (J-V) curves of a solar cell under dark (black) and under light illumination (blue-dash). Power density is shown in red and is maximum at (V_F,J_F).

V_{oc} is observed at zero circuit current and can also be explained as: output voltage obtained from solar cell when the circuit is open (not connected) and is due to generation of carriers under light.

V_{oc} and I_{sc} correspond to maximum voltage and maximum current which can be obtained from the solar cell which occur at zero current and zero voltage respectively. Power obtained from a solar cell is given by the product of current and voltage and is zero at these extreme values. However, a term **"fill factor" (FF)** is used to determine maximum power output from a solar cell which occur at (V_F, J_F) corresponding to maximum area obtainable from coordinate axes. FF is given by the ratio of areas swept by J_F,V_F to J_{sc},V_{oc}.

$$FF = \frac{J_F V_F}{J_{SC} V_{OC}} \tag{1.3}$$

Efficiency (η) of a solar cell determines how effectively the solar cell can convert light energy to electrical energy; it is the ratio of output power obtained from the solar cell to light energy incident on solar cell. It is the most general parameter to compare performances of different solar cells. Efficiency of a photovoltaic device can be measured from I-V curve of the cell. Efficiency is the most general term used to quantify solar cell performance and is given by:

$$\eta = \frac{J_F V_F}{P_{in}} \tag{1.4}$$

Where, P_{in} is power (of photons) incident on solar cell.

According to theory, if other parameters are kept equal, then the direct band gap value at which one should obtain the most efficient solar cell is around 1.4 – 1.5 eV [12]. Theoretical calculations in refs [13–15] demonstrates variation of efficiency, Jsc and Voc as a function of band gap of the material keeping other parameters constant of a typical solar cell under AM 1.5G spectrum conditions.

Open circuit voltage depends strongly on bandgap and can be written as:

$$V_{oc} = \frac{E_g}{q} - \frac{kT}{q} \ln\left(\frac{J_{sc}}{J_0}\right) \tag{1.5}$$

Figure 1.8 shows variation of η, J_{sc} and V_{oc} with band gap using theoretical calculations. It is observable from the figure that maximum theoretical efficiency must correspond to band gap of 1.4 eV (according to Green's model) if other parameters are kept constant.

Band gap of CIGSe can be tuned with Ga/In ratio and if there is no major changes at microstructural and atomic level one must obtain most efficient CIGSe corresponding to band

gap 1.4 eV. However, this is not usually observed in the case of CIGSe solar cells and most efficient cells are observed for band gaps around 1.1eV to 1.2 eV (Ga poor cells) [16–21].

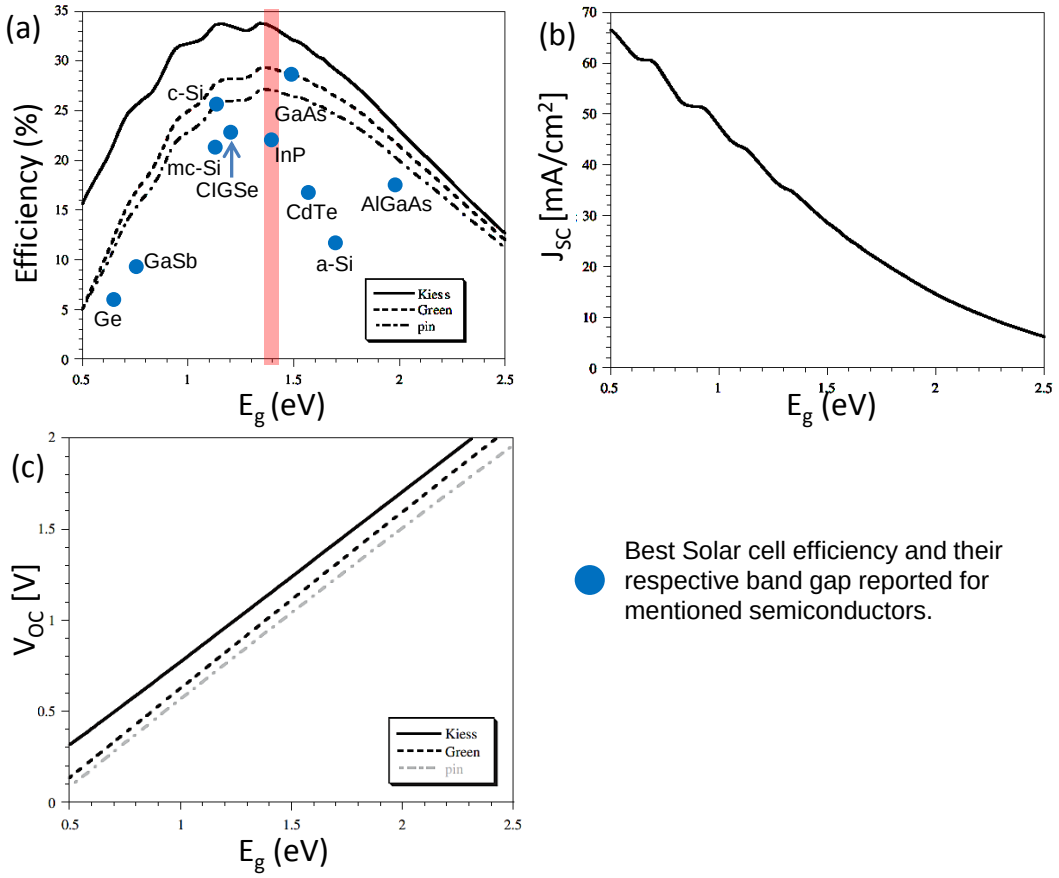

Figure 1.8: Efficiency, J_{sc} and V_{oc} as a function of band gap from [13–15]. Red region correspond to band gap energy of 1.4 eV, indicating maximum theoretical efficiency.

Figure 1.9 shows measured efficiency of CIGSe cells with different band gaps (different Ga ratio) observed by different laboratories. These results demonstrate the superiority of Ga poor cells. Comparing Figure 1.8 a) and Figure 1.9, highlighted region shows band gap corresponding to maximum theoretical efficiency. J_{sc} of CIGSe with different x is usually observed to be consistent with theoretical expectations [22].

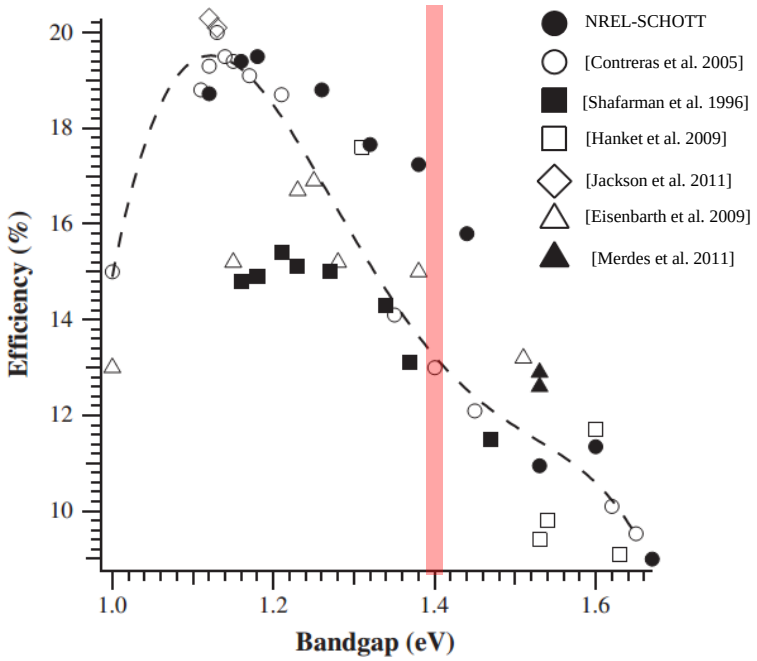

Figure 1.9: CIGSe efficiency for different Ga content, Image source: Contreras et.al (2012) [22]. Red region represent band gap of 1.4 eV corresponding to maximum theoretical efficiency.

Hence according to equation (1.3), V_{OC} and/or FF must be the limiting factor degrading photovoltaic performance of Ga rich CIGSe. Experiments by above authors demonstrate the same as shown in Figure 1.10. Figure shows saturation of V_{OC} after 1.3 eV bandgap. It is interesting to note that V_{oc} and efficiency deviate from expectations after this band gap value.

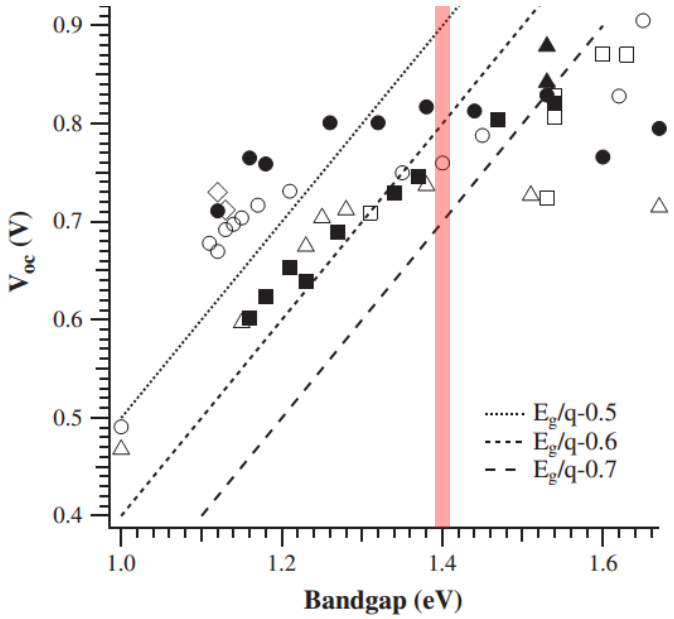

Figure 1.10: Open circuit voltage measured for different x in CIGSe, Image source [22]. Symbols follow according to Figure 1.9.

Different theories exist behind this observed deviation from theoretical expectations and are discussed in later sections of this chapter.

I-V curves represent collective output power obtained from a solar cell under solar spectrum conditions containing all incident wavelengths. In order to check the solar cell behavior at specific monochromatic wavelengths we measure its quantum efficiency.

1.2.2 Quantum Efficiency

Quantum efficiency (QE) measures how efficiently light at a particular wavelength can generate carriers. QE is calculated for all wavelengths covering solar spectrum and shows the behavior of carrier generation at these wavelengths. QE can be sub classified in two types: External quantum efficiency (EQE) and Internal quantum efficiency (IQE).

EQE takes into account all possibilities of photon interaction including reflection, absorption and transmission, hence given by:

$$EQE = \frac{no.\ of\ carriers\ collected\ by\ the\ solar\ cell}{no.\ of\ photons\ of\ a\ given\ energy\ incident\ on\ solar\ cell} \quad \textbf{(1.6)}$$

EQE can be obtained at all wavelengths of solar spectrum and is shown for CIGSe in Figure 1.11.

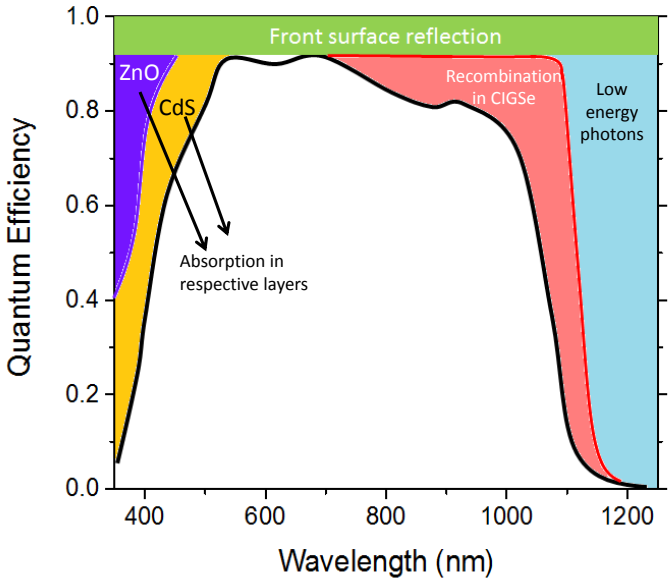

Figure 1.11: EQE of a typical CIGSe solar cell x=0.3 (this work). Different (colored) regions representing energy loss.

In the ideal case i.e. all incident photons generate charge carriers and all carriers are successfully collected by the solar cell, QE must be equal to 1 for photon energy greater than band gap of the semiconductor. However due to absorption in different regions, QE observed is never equal to 1 as shown in Figure 1.11 for CIGSe.

Above figure is divided in different regions corresponding to losses observed in experimental EQE from ideal case and is described here:

1) Reflection: Loss due to charge collection grids at the top surface and due to reflection from front surface which can be minimized by using anti reflection coatings.
2) Unwanted absorption: Most of the incident energy is lost in first parts due to absorption in ZnO layer corresponding to high band gap material and absorbing high energy photons. Also, absorption in CdS buffer layer (band gap = 2.3 eV) drops QE for photon energy greater than 2.3 eV.
3) The red region in Figure 1.11 corresponds to weak absorption of low energy photons. This region also suffers recombination at rear surface in quasi neutral region where recombining possibility is greater. EQE curve shows a tail in red region because photon energy lower than band gap (1.2 eV) are not absorbed, if the band gap is increased further the tail shifts further left and more photons are left unabsorbed. Similarly for lower band gap, tail shifts towards right resulting in more photon absorption.
4) (Blue region) Photons with energy lower than the band gap of the material are not absorbed.

Results discussed in later chapters deals with EQE, however one can calculate IQE using the following relation:

$$IQE = \frac{no.\ of\ carriers\ collected\ by\ the\ solar\ cell}{no.\ of\ photons\ of\ a\ given\ energy\ absorbed\ by\ solar\ cell} \qquad \textbf{(1.7)}$$

IQE does not take into account the reflected photons and is defined as ratio of number of carriers collected by solar cell to number of photons of a given energy absorbed by the cell.

IQE is calculated from EQE by measuring and subtracting transmission and reflection losses from EQE.

To understand CIGSe better one must know the material properties of CIGSe and their behavior under different compositions and preparation conditions.

1.3 Material properties of CIGSe thin films

CIGSe is a I-III-VI_2 semiconductor and is the main absorber layer used in CIGSe solar cells. Many different phases of this alloy exist depending on growth conditions. Major parameters affecting phases and properties of the alloy are: temperature during growth, flux of elements during growth, substrate used etc. CIGSe is usually most stable as p-type but can also be made n-type [6] by tuning the above factors. It is difficult to dope CIGSe as n-type for wider bad gap compounds [23], as we study CIGSe in this work for both narrow and wide band gap compounds it is convenient to form and discuss CIGSe with similar conductive nature. Hence here we discuss only on p-type CIGSe films prepared by the most common 3-stage and CuPRO processes, processes which will be detailed in the next chapter.

1.3.1 Crystal structure

CIGSe has a chalcopyrite crystal structure and its single unit cell can be considered as a composite of two sphalerite (zinc blende) unit cells. A typical unit cell of CIGSe is shown in Figure 1.12.

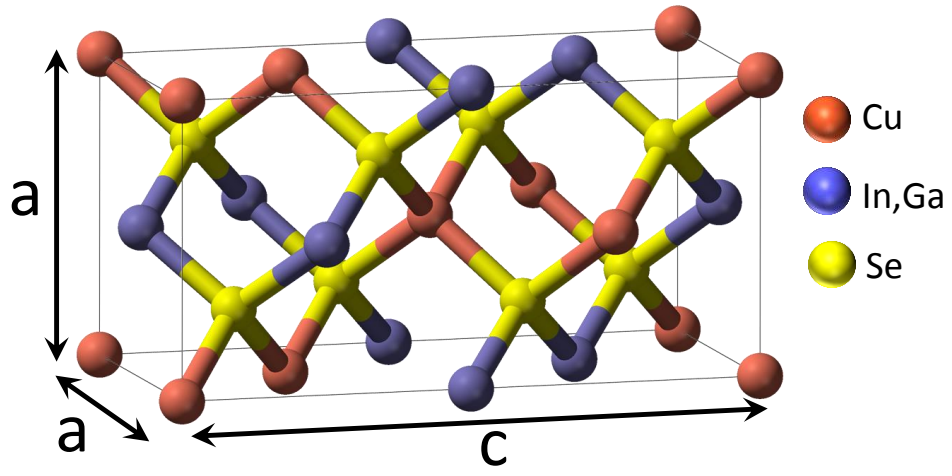

Figure 1.12: Schematic representation of a Cu(In,Ga)Se_2 unit cell. Lattice parameters are represented by a and c.

Bonding between Cu and Se atoms here results from *p-d* hybridization of their respective orbitals [24]. The unit cell can be considered tetragonal which is made up of two cubic unit cells but with some tetragonal distortion i.e. $c \neq 2a$ in most cases. However, the difference between c and 2a is very small and is referred here as δ (i.e $c - 2a = \delta$). Electronic charge distribution, as depicted in ref [25], indicates ionic character of Ga–Se, In–Se bond and covalent character of Cu-Se bond. Difference in characteristics of the two bonds leads to

different bond lengths and hence results in tetragonal distortion. As illustrated in Figure 1.13, the unit cell parameters (c,a) of $CuIn_{1-x}Ga_xSe_2$ vary linearly with Ga ratio (x). Thus lattice constants for any Ga ratio can be calculated from respective positions in the plot. Difference between c/2 and a as a function of x illustrates the tetragonal distortion (δ) in CIGSe. For $CuInSe_2$, δ > 0, Ga addition decreases δ and at x=0.25 there is no tetragonal distortion (i.e. δ=0). Distortion then increases with Ga content till $CuGaSe_2$ where it is maximum. Decrease in δ here is mainly due to lower radius of Ga as compared to In. A systematic variation of the tetragonal distortion is shown in Figure 1.13, where x=0.25 represent no tetragonal distortion and CGSe exhibit maximum tetragonal distortion.

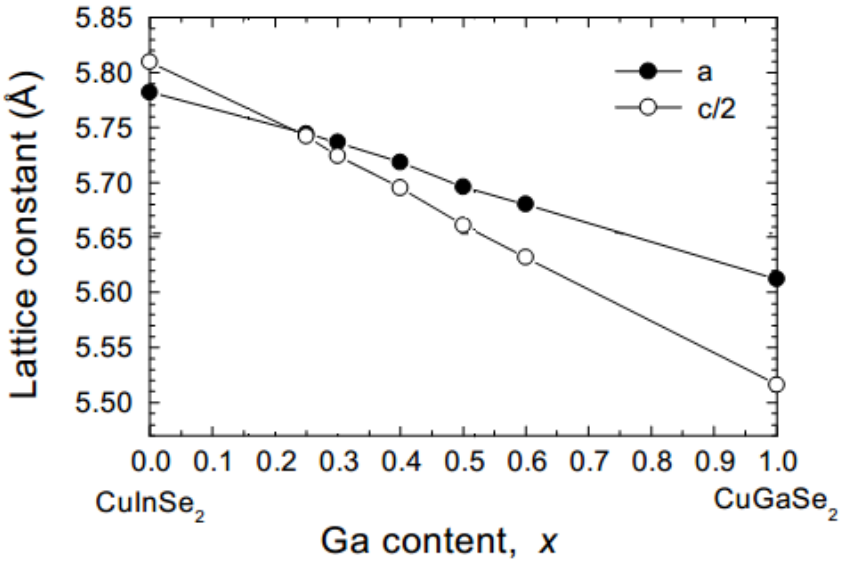

Figure 1.13: Lattice constants a and half of c for $CuIn_{1-x}Ga_xSe_2$. X is the Ga ratio. Source: Suri et.al [26]

1.3.2 Phase Diagram

CIGSe involves interplay of mainly four elements and also impurities involving Na, or K [27,28], making the system a complex subject to study. Thin film growth of CIGSe depends strongly on flux of different elements, temperature of the substrate and type of substrate. Changes in one or more of these values may lead to significant variation in properties of the thin films. Growth process of thin films involves depositions at high temperatures (≈600^{o}C) with variations in both temperatures and elemental fluxes making the system under non thermal equilibrium. However thermal equilibrium phase diagrams may help us understand the growth process of the thin films.

Pseudoternary phase diagram for quaternary compound CIGSe at room temperature was first described in ref. [29] and is shown in Figure 1.14. Single chalcopyrite phase "α" is known to produce high efficient CIGSe cells [30] and particular synthesis conditions are employed here to form this phase in CIGSe thin films. Figure 1.14 demonstrates wider domain of single α phase towards Ga rich side i.e. single α phase region widens with increasing Ga content. This means it is flexible (or easier) to form single phase Ga rich CIGSe than single phase Ga poor CIGSe. In other words less control over the molecular proportions is required to form single phase CGSe compared to formation of single phase CISe, regardless of preparation techniques [31].

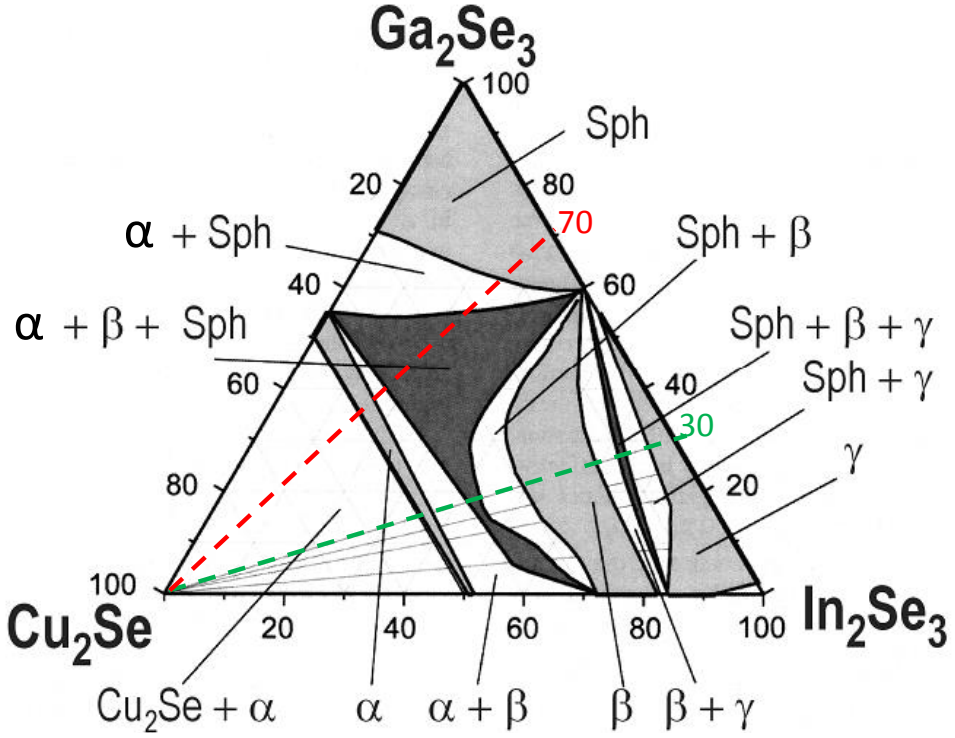

Figure 1.14: Pseudoternary phase diagram for CIGSe at room temperature (Source: [29]). α → Cu(In,Ga)Se_2, β→ Cu(In,Ga)$_3Se_5$, γ→ Cu(In,Ga)$_5Se_8$, Sph→ Sphalerite structure of Ga_2Se_3. Lines emerging from Cu_2Se vertex represent constant [In]/[Ga] ratio along the respective line. Green and red lines represent Ga poor and Ga rich CIGSe respectively.

Lines with constant [In]/[Ga] ratio can be drawn starting from Cu_2Se vertex. Green line shown is for Ga poor CIGSe and red line correspond to Ga rich CIGSe. It can be noted from the figure that region corresponding to mixture of 3 phases α+β+Sph is more extended in Ga rich CIGSe compared to Ga poor demonstrating more possibility of multi-phase existence in Ga rich CIGSe. Formation of several phases in thin films are found to degrade performance of thin films [6], hence CIGSe films are developed to contain single phase throughout the layer.

1.3.3 Superiority of polycrystalline CIGSe

Monocrystalline materials are solids consisting of a single crystal with well-defined crystal structure and orientation throughout the material. A polycrystalline material is a solid made up of many different sized crystallites oriented in random direction. These crystallites are called grains and the boundary between two different crystallites is called a grain boundary (GB). It is generally believed and observed that monocrystalline semiconductors exhibit better photovoltaic properties than their polycrystalline counterpart simply to avoid high probability of recombination at grain boundary.

Contrary to conventional materials used for photovoltaics, efficiency and photovoltaic properties of CIGSe are proved to be much better in their polycrystalline form [17]. Highest single crystal efficiency reported for $CuInSe_2$ is ~ 11% [33], whereas polycrystalline $CuInSe_2$ demonstrated ~ 15% [34]. This unexpected improvement of polycrystalline CIGSe is very interesting and is still under debate [35–42]. Many theories accounting for this improved performance are summarized in this section.

a) Effect of Alkali impurities at Grain Boundaries:

Hedstrom et.al [43] in early 90's realized that alkali impurities such as Sodium (Na) when added during thin film preparation improves mainly the V_{oc} and efficiency of the device with minor or no effect on short circuit current. Today most commonly CIGSe thin films are grown on soda lime glass substrate with glass acting as the source of Na. Whether added from external sources or from within the glass substrate, Na has shown to be a promising impurity when incorporated in optimal amounts [43,44] during preparation. However improvement due to Na is also still a matter of debate and various theories proposing different mechanisms can be summarized as follows:

1) Sodium at grain boundaries: Various models described in refs. [45–47] propose segregation of Na at the GBs. Calculations by Persson and Zunger [37] show that the creation of charge neutral defect Na^0_{Cu} at grain surface (or GB) may act like hole barrier leading to improved photovoltaic properties. Combining SEM and SIMS analysis, segregation of Na at the GBs was suspected [44]. However planar segregation of Na atoms along GB was first illustrated using Atom Probe Tomography (APT) by Cadel et.al [48] confirming presence of Na at the GB experimentally.

2) Built-in potential due to Na at GB: scanning Kelvin Probe force measurements (SKPM) on CIGSe was performed by Yan et.al [41] on sodium free and sodium rich glass substrate demonstrating electrically benign character of GB for Na free CIGSe. They showed that the segregation of Na at GB formed charged defects resulting in a built-in potential at GB which is mainly due to presence of Na. The latter would repel holes and attracts electrons hence reducing recombination and enhancing carrier collection.
3) Increased acceptor density: Due to reduction in donor density by an increase in point defect mobility, Na introduction is shown to increase p-type conductivity (or increase hole concentration) in p-type CIGSe [49][46].
4) Texture modification: Na incorporation also plays vital role in modifying microstructural properties of CIGSe. <112> texture is strongly enhanced for the films grown on soda lime glass substrate [43] as compared to soda free substrate. However strong texture may not necessarily enhance photovoltaic properties of CIGSe but it is generally observed that both of these properties occur simultaneously. In fact, grain size is found to increase for thin films with Na [50,51] although the exact mechanism is still not yet known.

b) Other effects at Grain Boundaries:

Apart from beneficial effects of Sodium, some researchers also proposed that even GBs itself makes polycrystalline CIGSe better than monocrystalline counterpart due to following reasons:

1) Cu depletion at grain boundary: Calculations by Persson and Zunger [37] show that Cu vacancy at the GB is the main reason for hole repulsion at GB. Valence band maximum (VBM) is lowered at GB due to Cu vacant sites, hence resulting in hole repulsion and better photovoltaic performance. Hetzer et.al [52] demonstrate significant removal of Cu atoms at GB (≈50% Cu compared to grain) which results in change in valence band levels between grain interior and GB, thus again resulting in hole repulsive GB and better carrier collection. APT results by Couzinie-Devy et.al [53,54] have already shown significant depletion of Cu at GB accompanied by In enrichment for Ga poor cells.

2) Type inversion at GB: Probst et.al [55,56] demonstrated that n-type ordered defect compounds (ODC) like $CuIn_3Se_5$ forms on surface of grain of p-type CIGSe. As GBs exhibit properties similar to grain surface, n-type $CuIn_3Se_5$ phase may form at GB and resulting in type inversion at GB. N-type GBs thus channels electrons towards n side (CdS) reducing recombination probability by effective transport of minority carriers. Also Scanning capacitance measurements by Sadewasser et.al [57] show existence of dark contrast at GBs indicating type inversion at GB.

Presence of grain boundaries have shown to play an advantageous role towards CIGSe cell performance. In addition, device performance of CIGSe is also specific to its Ga content in and small changes in Ga ratio (x) reflect in its properties. Ga addition to CIS is shown to have positive impact on its device properties only up to certain level above which degradation is apparent. Following section discusses importance and influence of Ga content in CIGSe.

1.3.4 Influence of Ga content in Cu(In,Ga)Se_2 solar cells and theories behind limited performance of Ga rich CIGSe

During 80's and early 90's it was realized that $CuInSe_2$ is one of the most promising materials for thin film solar cells [3]. With extraordinary properties such as: low cost, high absorption, high efficiency (>14%), $CuInSe_2$ was believed to be most appropriate semiconductor for solar cells [3]. Band gap of $CuInSe_2$ is 1.0 eV, quite far from ideal value for maximum solar energy conversion value of 1.4-1.5eV [12]. Being a suitable material for photovoltaics it was recommended to alloy this material with Ga [2,58] in order to increase its band gap and adapt itself to incoming solar radiation. Ga additions were performed mainly by alloying (mixing) $CuInSe_2$ with $CuGaSe_2$ [43,59] and later by using precursor compounds like $(In_x,Ga_{1-x})_2Se_3$ [60]. According to band gap modulation, Ga ratio corresponding to the most favorable band gap (1.4 eV) is around x = 0.7. However new world record CIGSe solar cells with ~21.7% efficiency contains overall ~8% Ga concentration (or x=0.32) [61]. However cells above this Ga concentration (x≈0.32) results in reduced photovoltaic properties [22,30] which is debated over last two decades. Major chemical and physical effects due to Ga addition in CISe are summarized as follows:

1) Increase in band gap:

Main idea behind Ga addition is to increase band gap for maximum energy conversion. Stoichiometric form of CIGSe is usually written as a function of Ga ratio (x): $CuIn_{1-x}Ga_xSe_2$. Band gap, $E_g(x)$ increases co-linearly as a function of Ga ratio (x) [4]:

$$E_g(x) = (1-x)E_g(CIS) + xE_g(CGS) - bx(1-x) \quad \textbf{(1.8)}$$

Where E_g(CIS) = 1.0 eV, E_g(CGS) = 1.67 eV, b is the optical bowing coefficient with value b = 0.15 to 0.24 [62]. Record cells produced during past few years consist of Ga ratio x≈0.32 (E_g≈1.2 eV) [18,28,63]. Ga addition thus resulted in increase in band gap which in turn resulted in enhanced efficiency and increased V_{oc} consistent with equation (1.5) and Figure 1.8 up to x ≈ 0.35-0.40.

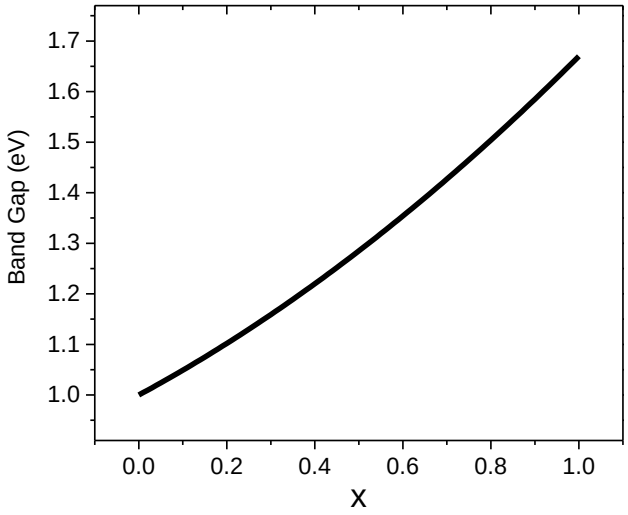

Figure 1.15: Band gap of $Cu(In_{1-x}Ga_x)Se_2$ as a function of 'x' as plotted from equation (1.8).

2) Stability in chalcopyrite phase

As shown in Figure 1.14, the pseudo ternary phase diagram shows widening of α phase towards Ga rich compounds. This means it is relatively easier and flexible to synthesize pure chalcopyrite phase for Ga rich CIGSe as compared to Ga rich compounds [64] [31].

3) Increase in hole concentration:

Ga addition leads to a net increase in acceptor density and decrease in acceptor level depth as shown in refs. [65][55]. However no significant influence of Ga addition was observed in hole mobility [65] and it remains unaffected.

4) Microstructural changes

Cross sectional analysis of CIGSe with different Ga content was performed using Electron back scattered diffraction (EBSD) analysis demonstrating major changes in microstructure by Abou-Ras et.al [66][67] as shown in Figure 1.16. Ga addition was found to increase grain size till x =0.23 and then decreased till $CuGaSe_2$, CGS being the sample with smallest grain size [66] and least efficiency.

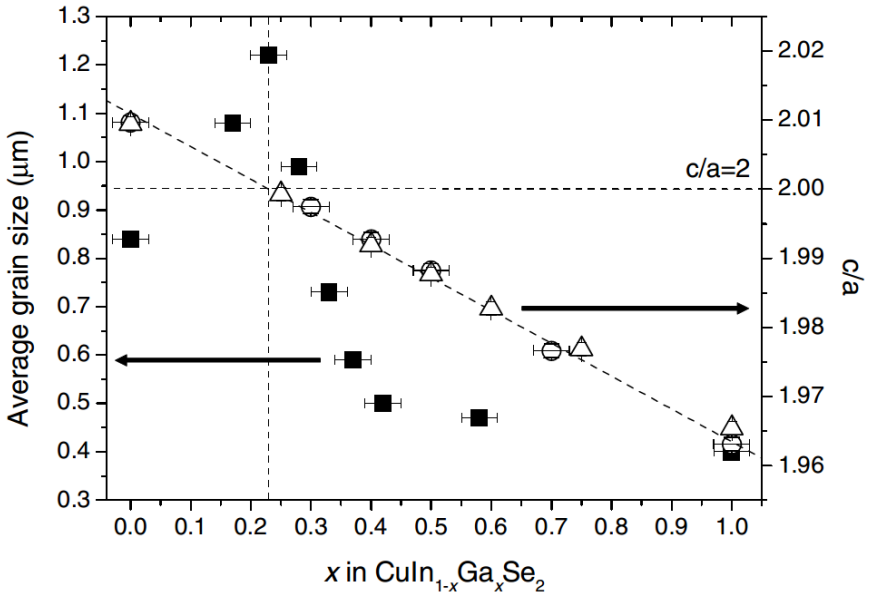

Figure 1.16: Average grain size (in µm) of CIGSe and ratio of lattice constants c/a from ref. [26] (white circle) and [Schorr unpublished works] (white triangle) as a function of Ga ratio x. Image courtesy: Abou-Ras et.al [66].

However grain size could not be correlated directly to the photovoltaic properties, but very small grain sizes (< 0.5 µm) apparently result in degraded photovoltaic properties. However, grain sizes are known to increase with Cu rich growth [68] in polycrystalline CIGSe and hence a Cu rich step is generally used during 3-stage co-evaporation synthesis process [69].

5) Interface recombination

Formation of a stable n-type inverted surface is useful in reducing recombination at CdS-CIGSe heterojunction in CIGSe [30] and is found to be absent in Ga rich CIGSe, hence increasing recombination in the latter case. Qualitative band diagrams by Bosio et.al [32] as shown in Figure 1.17 show that pn junction moves from CdS-CIGSe heterojunction towards buried in CIGSe surface due to formation of an n-type ordered defect compound (ODC) $Cu(In,Ga)_3Se_5$.

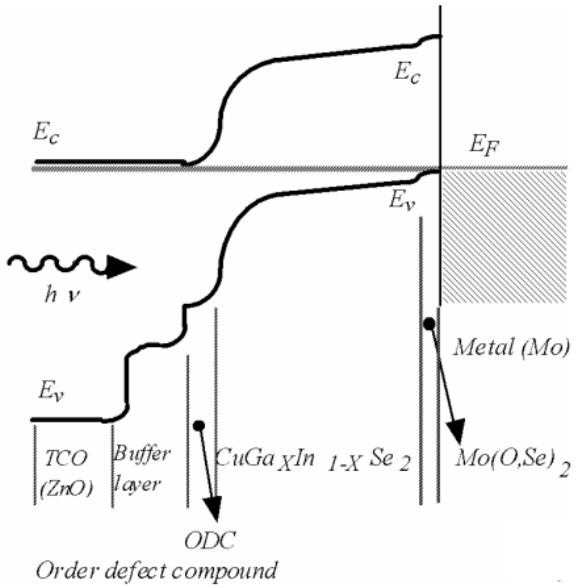

Figure 1.17 Energy band offset expected alignment for a typical CIGSe solar cell. Image courtesy: Bosio et.al. [32]

Contreras et.al [22] demonstrated improved performance of Ga rich CIGSe and showed that Ga addition leads to detrimental effects in interfaces and increases interfacial recombination hence degrading cell performance. EBIC study on Ga rich CIGSe shows that major loss in carrier collection is due to presence of some grains with poor collection efficiency. These grains are termed as "dead grains" which is observed by Contreras et.al [22]. Open circuit voltage is observed independent of absorber band gap when considering interfacial recombination between buffer and absorber layer [70][71]. Gloeckler et.al [71] recommend replacement of conventional window layers and/or CIGSe surface modification for further improvement of wide band gap CIGSe. However Nadenau et.al [72] finds efficiency of Ga rich CIGS cells can also be increased with CdS buffer layer deposited at higher temperatures (80^{o}C). Diffusion of CdS is enhanced at high temperature and leads to reduced tunneling rate.

6) Bulk Recombination

Electrical analysis by Rau et.al [73] showed that the recombination in space charge region (SCR) may explain degraded photovoltaic properties of Ga rich compounds and recombination increases with Ga content. The dominant recombination phenomenon in the space charge region is thus due to tunneling-enhanced recombination [74]. Hanna et.al [75] showed that the minimum bulk defect concentration (1.2×10^{15} cm^{-3}) is obtained for

x=0.3 and that defects increase till CGS (5.6×10^{15} cm^{-3}). This demonstrates that the presence of increased bulk defects may be a reason for limited performance of Ga rich CIGSe. Bulk volume defects increase as a function of Ga and minimum defects for x near most efficient cells x=0.28. Hence minimizing SCR, an increase in efficiency is observed by Nadenau et.al [72] and explained by a reduction in doping level and tunneling rate due to modified SCR. Hence for further improvement of Ga rich CIGSe one must understand influence of Ga on defect concentration of CIGSe [75]. It is observed that bulk defects can also be suppressed by alloying CIGSe with Sulphur (S) to form $Cu(In,Ga)(Se,S)_2$ resulting in consistently improvement of the device performance [73].

7) Local potential at GB

Jiang et.al [76] demonstrated presence of a local built-in potential at GB using KPFM (Kelvin probe force microscope), which shows that GBs in CIGSe are positively charged leading to better electron collection. Experiments on different Ga ratio CIGSe samples showed variations in local potential at GB with Ga content [77] as shown in Figure 1.18.

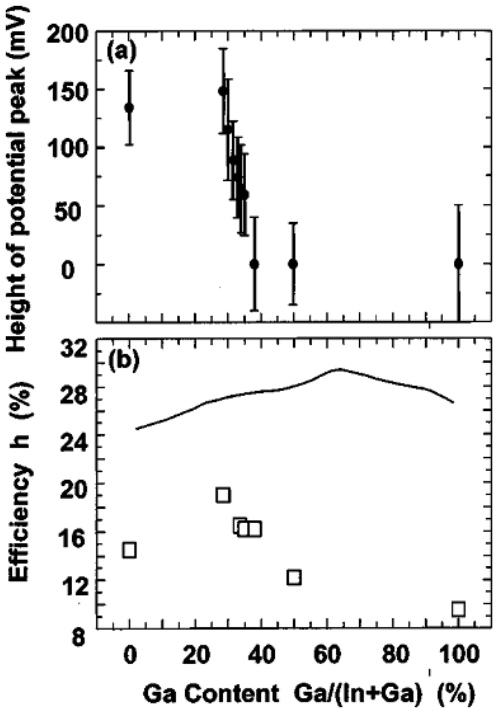

Figure 1.18: (a) Local potential peak height at GB and (b) efficiency of CIGSe as a function of Ga content. Image courtesy: Jiang et.al [77]

Few hundreds of millivolts of potential were observed at GB for Ga poor cells however a sharp decrease in potential at GB is observed between x=0.28 to 0.38 and further increasing Ga ratio results in negligible potential at GB [77].

These findings indicate lowering in potential at GB may increase minority carrier recombination for Ga rich samples. However experimental findings by Baier et.al [78] demonstrate presence of both positive and negative potentials at GB and no effect of Ga addition were evidenced on properties of GBs.

8) Band Offsets

Valence band energy calculations performed by Wei et.al [62] and Turcu et.al [79] demonstrated that valence band energy levels of CIS and CGS are very close and there is hardly any influence of Ga addition on valence band energy levels.

9) Other effects

Phillips et.al [80] and Shafarman et.al [81] propose that degraded performance of Ga rich compounds are possibly due to a significant reduction in minority carrier diffusion length which is electron in this case.

Many theoretical and experimental researches have been done in this field but no clear explanation has yet been demonstrated in order to explain limited performance of Ga rich CIGSe. Extensive research has been performed on CIGSe thin films and interfaces using electron microscopy. A comprehensive review has been made by Abou-Ras et.al [82] describing several electron microscopy techniques used in past years towards better understanding of CIGSe material properties and interfaces including use of following techniques: SEM, TEM, EBSD, cathodoluminescence, EDX (Energy Dispersive X-ray) spectroscopy, EBIC (Electron Beam Induced Current). In addition TEM-EELS (Electron Energy Loss Spectroscopy) has also been performed demonstrating composition changes at GB [83]. EELS give generally quantitative results for interfaces or layers with few nm width, however very low signal to background noise ratio makes EELS less reliable and less quantitative while measuring elemental changes at GB [84], in addition TEM specimen must be very thin and carefully prepared without any contamination due to external sources involved during TEM specimen preparation. However, despite of this large amount of work

no clear experimental evidence has been found yet explaining declined performance of CIGSe.

Conclusions

Key principle of functioning of a solar cell is efficient generation and collection of charge carriers. Polycrystalline CIGSe solar cells are observed to be more efficient than their monocrystalline counterpart and it is mainly due to segregation of Na atoms at the GB introduced during thin film preparation. Also many theories are discussed in this chapter demonstrating various phenomenons due to presence of Na and beneficial role of GBs in the material. Influence of Ga addition is also discussed in the chapter and raised the most obvious question of limited performance of Ga rich CIGSe. Plenty of research work has been done till date to explain poor performance of Ga rich CIGSe but still today it is the matter of debate which may open the door for much improved performance of this material.

Technical limitations to explore this material are expressed, encouraging us to opt for techniques with higher resolution. Hence here we will make use of Atom Probe Tomography (APT), a technique able to explore 3D atomic composition with high resolution [85]. Previous works on CIGSe using APT demonstrated better quantitative chemical composition profile at GB [48,53,86] and at interfaces [88,89]. Therefore we use APT in here to focus on GB chemistry for different Ga contents in CIGSe materials. The next chapter focuses on preparation of CIGSe cells studied in this work and details of the characterization techniques.

References

1. April 25, 1954: Bell Labs Demonstrates the First Practical Silicon Solar Cell. Available at: http://www.aps.org/publications/apsnews/200904/physicshistory.cfm

2. Hörig W, Möller W, Neumann H, Reccius E, Kühn G. Optical properties of Culn1−xGaxSe2 mixed crystals. *phys stat sol (b)* 1979; **92**: K1–K4. DOI: 10.1002/pssb.2220920142

3. Rockett A, Birkmire RW. CuInSe2 for photovoltaic applications. *Journal of Applied Physics* 1991; **70**: R81–R97. DOI: doi:10.1063/1.349175

4. Tinoco T, Rincón C, Quintero M, Pérez GS. Phase Diagram and Optical Energy Gaps for CuInyGa1−ySe2 Alloys. *physica status solidi (a)* 1991; **124**: 427–434. DOI: 10.1002/pssa.2211240206

5. Stutenbäumer U. Minority carrier lifetime in monocrystalline, polycrystalline and amorphous silicon solar cells using photo-induced open-circuit voltage decay (ocvd) technique. *SINET: Ethiopian Journal of Science* 2004; **22**: 15–30. DOI: 10.4314/sinet.v22i1.18131

6. Kodigala SR. *Cu(In$_1$_xGax)Se$_2$ based thin film solar cells*. Amsterdam: Elsevier/Academic Press 2010;

7. Campbell P, Green MA. Light trapping properties of pyramidally textured surfaces. *Journal of Applied Physics* 1987; **62**: 243–249. DOI: 10.1063/1.339189

8. Green MA. Third generation photovoltaics: solar cells for 2020 and beyond. Physica E: Low-dimensional Systems and Nanostructures 2002; 14: 65–70. DOI: 10.1016/S1386-9477(02)00361-2

9. Kohara N, Nishiwaki S, Hashimoto Y, Negami T, Wada T. Electrical properties of the Cu(In,Ga)Se2/ MoSe2/Mo structure. *Solar Energy Materials and Solar Cells* 2001; **67**: 209–215. DOI: 10.1016/S0927-0248(00)00283-X

10. Bär M, Weinhardt L, Heske C, Nishiwaki S, Shafarman WN. Chemical structures of the Cu(In,Ga)Se2/Mo and Cu(In,Ga)(S,Se)2/Mo interfaces. *Phys Rev B* 2008; **78**: 075404. DOI: 10.1103/PhysRevB.78.075404

11. Bär M, Nishiwaki S, Weinhardt L, Pookpanratana S, Shafarman WN, Heske C. Electronic level alignment at the deeply buried absorber/Mo interface in chalcopyrite-based thin film solar cells. *Applied Physics Letters* 2008; **93**: 042110. DOI: 10.1063/1.2955532

12. Shockley W, Queisser HJ. Detailed Balance Limit of Efficiency of p-n Junction Solar Cells. *Journal of Applied Physics* 1961; **32**: 510–519. DOI: 10.1063/1.1736034

13. Meillaud F, Shah A, Droz C, Vallat-Sauvain E, Miazza C. Efficiency limits for single-junction and tandem solar cells. *Solar Energy Materials and Solar Cells* 2006; **90**: 2952–2959. DOI: 10.1016/j.solmat.2006.06.002

14. Green MA. *Solar cells: operating principles, technology, and system applications*. Englewood Cliffs, NJ: Prentice-Hall 1982;

15. Kiess H, Rehwald W. On the ultimate efficiency of solar cells. *Solar Energy Materials and Solar Cells* 1995; **38**: 45–55. DOI: 10.1016/0927-0248(94)00214-2

16. Contreras MA, Ramanathan K, AbuShama J, Hasoon F, Young DL, Egaas B, Noufi R. SHORT COMMUNICATION: ACCELERATED PUBLICATION: Diode characteristics in state-of-the-art ZnO/CdS/Cu(In1−xGax)Se2 solar cells. *Prog Photovolt: Res Appl* 2005; **13**: 209–216. DOI: 10.1002/pip.626

17. Shafarman WN, Klenk R, McCandless BE. Characterization of Cu(InGa)Se2 solar cells with high Ga content. in , *Conference Record of the Twenty Fifth IEEE Photovoltaic Specialists Conference, 1996*, 763–768. DOI: 10.1109/PVSC.1996.564240

18. Jackson P, Hariskos D, Lotter E, Paetel S, Wuerz R, Menner R, Wischmann W, Powalla M. New world record efficiency for Cu(In,Ga)Se2 thin-film solar cells beyond 20%. *Progress in Photovoltaics: Research and Applications* 2011; **19**: 894–897. DOI: 10.1002/pip.1078

19. Merdes S, Mainz R, Klaer J, Meeder A, Rodriguez-Alvarez H, Schock HW, Lux-Steiner MC, Klenk R. 12.6% efficient CdS/Cu(In,Ga)S2-based solar cell with an open circuit voltage of 879 mV prepared by a rapid thermal process. *Solar Energy Materials and Solar Cells* 2011; **95**: 864–869. DOI: 10.1016/j.solmat.2010.11.003

20. Hanket GM, Boyle JH, Shafarman WN. Characterization and device performance of (AgCu)(InGa)Se2 absorber layers. in *2009 34th IEEE Photovoltaic Specialists Conference (PVSC)*, 001240–001245. DOI: 10.1109/PVSC.2009.5411241

21. Eisenbarth T, Unold T, Caballero R, Kaufmann CA, Abou-Ras D, Schock H-W. Origin of defects in CuIn1 − xGaxSe2 solar cells with varied Ga content. *Thin Solid Films* 2009; **517**: 2244–2247. DOI: 10.1016/j.tsf.2008.10.142

22. Contreras MA, Mansfield LM, Egaas B, Li J, Romero M, Noufi R, Rudiger-Voigt E, Mannstadt W. Wide bandgap Cu(In,Ga)Se2 solar cells with improved energy conversion efficiency. *Prog Photovolt: Res Appl* 2012; **20**: 843–850. DOI: 10.1002/pip.2244

23. Zunger A. Practical doping principles. *Applied Physics Letters* 2003; **83**: 57–59. DOI: 10.1063/1.1584074

24. Shay JL, Tell B, Kasper HM, Schiavone LM. p-d Hybridization of the Valence Bands of I-III-VI_2 Compounds. *Phys Rev B* 1972; **5**: 5003–5005. DOI: 10.1103/PhysRevB.5.5003

25. Jaffe JE, Zunger A. Electronic structure of the ternary chalcopyrite semiconductors CuAlS2, CuGaS2, CuInS2, CuAlSe2, CuGaSe2, CuInSe2. *Phys Rev B* 1983; **28**: 5822–5847. DOI: 10.1103/PhysRevB.28.5822

26. Suri DK, Nagpal KC, Chadha GK. X-ray study of CuGaxIn1−xSe2 solid solutions. *Journal of Applied Crystallography* 1989; **22**: 578–583. DOI: 10.1107/S0021889889008289

27. Wuerz R, Eicke A, Kessler F, Paetel S, Efimenko S, Schlegel C. CIGS thin-film solar cells and modules on enamelled steel substrates. *Solar Energy Materials and Solar Cells* 2012; **100**: 132–137. DOI: 10.1016/j.solmat.2012.01.004

28. Chirilă A, Reinhard P, Pianezzi F, Bloesch P, Uhl AR, Fella C, Kranz L, Keller D, Gretener C, Hagendorfer H, et al. Potassium-induced surface modification of Cu(In,Ga)Se2 thin films for high-efficiency solar cells. *Nat Mater* 2013; **12**: 1107–1111. DOI: 10.1038/nmat3789

29. Cornelia Beilharz. *Charakterisierung von aus der Schmelze gezüchteten Kristallen in den Systemen Kupfer-Indium-Selen und Kupfer-Indium-Gallium-Selen für photovoltaische Anwendungen*. 1999;

30. Herberholz R, Nadenau V, Rühle U, Köble C, Schock HW, Dimmler B. Prospects of wide-gap chalcopyrites for thin film photovoltaic modules. *Solar Energy Materials and Solar Cells* 1997; **49**: 227–237. DOI: 10.1016/S0927-0248(97)00199-2

31. Stanbery BJ. Copper Indium Selenides and Related Materials for Photovoltaic Devices. *Critical Reviews in Solid State and Materials Sciences* 2002; **27**: 73–117. DOI: 10.1080/20014091104215

32. Bosio A, Romeo N, Podestà A, Mazza.m.u.to S, Canevari V. Why CuInGaSe2 and CdTe polycrystalline thin film solar cells are more efficient than the corresponding single crystal? *Crystal Research and Technology* 2005; **40**: 1048–1053. DOI: 10.1002/crat.200410484

33. Du H, Champness CH, Shih I. Results on monocrystalline CuInSe2 solar cells. *Thin Solid Films* 2005; **480–481**: 37–41. DOI: 10.1016/j.tsf.2004.11.057

34. Stolt L, Hedström J, Kessler J, Ruckh M, Velthaus K-O, Schock H-W. ZnO/CdS/CuInSe2 thin-film solar cells with improved performance. *Applied Physics Letters* 1993; **62**: 597–599. DOI: 10.1063/1.108867

35. Hanna G, Glatzel T, Sadewasser S, Ott N, Strunk HP, Rau U, Werner JH. Texture and electronic activity of grain boundaries in Cu(In,Ga)Se2 thin films. *Appl Phys A* 2006; **82**: 1–7. DOI: 10.1007/s00339-005-3411-1

36. Lei C, Li CM, Rockett A, Robertson IM. Grain boundary compositions in Cu(InGa)Se2. *Journal of Applied Physics* 2007; **101**: 024909–024909–7. DOI: doi:10.1063/1.2426962

37. Persson C, Zunger A. Anomalous Grain Boundary Physics in Polycrystalline CuInSe_{2}: The Existence of a Hole Barrier. *Phys Rev Lett* 2003; **91**: 266401. DOI: 10.1103/PhysRevLett.91.266401

38. Rau U, Taretto K, Siebentritt S. Grain boundaries in Cu(In, Ga)(Se, S)2 thin-film solar cells. *Appl Phys A* 2009; **96**: 221–234. DOI: 10.1007/s00339-008-4978-0

39. Rockett A. The effect of Na in polycrystalline and epitaxial single-crystal CuIn1−xGaxSe2. *Thin Solid Films* 2005; **480–481**: 2–7. DOI: 10.1016/j.tsf.2004.11.038

40. Taretto K, Rau U, Werner JH. Numerical simulation of grain boundary effects in Cu(In,Ga)Se2 thin-film solar cells. *Thin Solid Films* 2005; **480–481**: 8–12. DOI: 10.1016/j.tsf.2004.11.043

41. Yan Y, Jiang C-S, Noufi R, Wei S-H, Moutinho HR, Al-Jassim MM. Electrically Benign Behavior of Grain Boundaries in Polycrystalline CuInSe_{2} Films. *Phys Rev Lett* 2007; **99**: 235504. DOI: 10.1103/PhysRevLett.99.235504

42. Siebentritt S, Sadewasser S, Wimmer M, Leendertz C, Eisenbarth T, Lux-Steiner MC. Evidence for a Neutral Grain-Boundary Barrier in Chalcopyrites. *Phys Rev Lett* 2006; **97**: 146601. DOI: 10.1103/PhysRevLett.97.146601

43. Hedstrom J, Ohlsen H, Bodegard M, Kylner A, Stolt L, Hariskos D, Ruckh M, Schock H. ZnO/CdS/Cu(In,Ga)Se2 thin film solar cells with improved performance. in , *Conference Record of the Twenty Third IEEE Photovoltaic Specialists Conference, 1993*, 364–371. DOI: 10.1109/PVSC.1993.347154

44. M. Bodegard, L. stolt, J. Hedstrom. in *Proceedings of the 12th European Photovoltaic Solar Energy Conference, , pp. 1743*

45. Niles DW, Al-Jassim M, Ramanathan K. Direct observation of Na and O impurities at grain surfaces of CuInSe2 thin films. *Journal of Vacuum Science & Technology A* 1999; **17**: 291–296. DOI: 10.1116/1.581583

46. Niles DW, Ramanathan K, Hasoon F, Noufi R, Tielsch BJ, Fulghum JE. Na impurity chemistry in photovoltaic CIGS thin films: Investigation with x-ray photoelectron spectroscopy. *Journal of Vacuum Science & Technology A* 1997; **15**: 3044–3049. DOI: 10.1116/1.580902

47. Rockett A. The Electronic effects of point defects in Cu(InxGa1−x)Se2. *Thin Solid Films* 2000; **361–362**: 330–337. DOI: 10.1016/S0040-6090(99)00766-X

48. Cadel E, Barreau N, Kessler J, Pareige P. Atom probe study of sodium distribution in polycrystalline Cu(In,Ga)Se2 thin film. *Acta Materialia* 2010; **58**: 2634–2637. DOI: 10.1016/j.actamat.2009.12.049

49. Schroeder DJ, Rockett AA. Electronic effects of sodium in epitaxial CuIn1−xGaxSe2. *Journal of Applied Physics* 1997; **82**: 4982–4985. DOI: doi:10.1063/1.366365

50. Probst V, Karg F, Rimmasch J, Riedl W, Stetter W, Harms H, Eibl O. Advanced Stacked Elemental Layer Process for Cu(InGa)Se2 Thin Film Photovoltaic Devices. in *Symposium J – Thin Films for Photovoltaic and Related Device* MRS Online Proceedings Library. DOI: 10.1557/PROC-426-165

51. Probst V, Rimmasch J, Riedl W, Stetter W, Holz J, Harms H, Karg F, Schock H-W. The impact of controlled sodium incorporation on rapid thermal processed Cu(InGa)Se2-thin films and devices. in *IEEE Photovoltaic Specialists Conference - 1994, 1994 IEEE First World Conference on Photovoltaic Energy Conversion, 1994., Conference Record of the Twenty Fourth*, 144–147 vol.1. DOI: 10.1109/WCPEC.1994.519828

52. Hetzer MJ, Strzhemechny YM, Gao M, Contreras MA, Zunger A, Brillson LJ. Direct observation of copper depletion and potential changes at copper indium gallium diselenide grain boundaries. *Applied Physics Letters* 2005; **86**: 162105. DOI: 10.1063/1.1906331

53. Couzinie-Devy F, Cadel E, Barreau N, Pareige P, Kessler J. Atom probe contribution to the caracterisation of CIGSe grain boundaries. in 2011 37th IEEE Photovoltaic Specialists Conference (PVSC), 001966 –001971. DOI: 10.1109/PVSC.2011.6186339

54. Couzinie-Devy F, Cadel E, Barreau N, Arzel L, Pareige P. Atom probe study of Cu-poor to Cu-rich transition during Cu(In,Ga)Se2 growth. *Applied Physics Letters* 2011; **99**: 232108–232108–3. DOI: doi:10.1063/1.3665948

55. Matson RJ, Contreras MA, Tuttle JR, Swartzlander AB, Parilla PA, Noufi R. Effects of the Concentration of Ga on Junction Formation in Thin-film ZnO/CdS/CuInXGal-XSe2 /Mo Photovoltaic Devices. in *Symposium J – Thin Films for Photovoltaic and Related Device* MRS Online Proceedings Library. DOI: 10.1557/PROC-426-183

56. Schmid D, Ruckh M, Grunwald F, Schock HW. Chalcopyrite/defect chalcopyrite heterojunctions on the basis of CuInSe2. *Journal of Applied Physics* 1993; **73**: 2902–2909. DOI: 10.1063/1.353020

57. Sadewasser S, Abou-Ras D, Azulay D, Baier R, Balberg I, Cahen D, Cohen S, Gartsman K, Ganesan K, Kavalakkatt J, et al. Nanometer-scale electronic and microstructural properties of grain boundaries in Cu(In,Ga)Se2. *Thin Solid Films* 2011; **519**: 7341–7346. DOI: 10.1016/j.tsf.2010.12.227

58. Schumann B, Neumann H, Tempel A, Kühn G, Nowak E. Structural and electrical properties of CuIn0.7Ga0.3Se2 epitaxial layers on GaAs substrates. *Krist Techn* 1980; **15**: 71–76. DOI: 10.1002/crat.19800150111

59. Devaney WE, Chen WS, Stewart JM, Mickelsen RA. Structure and properties of high efficiency ZnO/CdZnS/CuInGaSe2 solar cells. *IEEE Transactions on Electron Devices* 1990; **37**: 428–433. DOI: 10.1109/16.46378

60. Gabor AM, Tuttle JR, Albin DS, Contreras MA, Noufi R, Hermann AM. High-efficiency CuInxGa1−xSe2 solar cells made from (Inx,Ga1−x)2Se3 precursor films. *Applied Physics Letters* 1994; **65**: 198–200. DOI: doi:10.1063/1.112670

61. Jackson P, Hariskos D, Wuerz R, Kiowski O, Bauer A, Friedlmeier TM, Powalla M. Properties of Cu(In,Ga)Se2 solar cells with new record efficiencies up to 21.7%. *phys stat sol (RRL)* 2015; **9**: 28–31. DOI: 10.1002/pssr.201409520

62. Wei S-H, Zunger A. Band offsets and optical bowings of chalcopyrites and Zn-based II-VI alloys. *Journal of Applied Physics* 1995; **78**: 3846–3856. DOI: doi:10.1063/1.359901

63. Herrmann D, Kratzert P, Weeke S, Zimmer M, Djordjevic-Reiss J, Hunger R, Lindberg P, Wallin E, Lundberg O, Stolt L. CIGS module manufacturing with high deposition rates and efficiencies. in *Photovoltaic Specialist Conference (PVSC), 2014 IEEE 40th*, 2775–2777. DOI: 10.1109/PVSC.2014.6925505

64. Wei S-H, Zhang SB, Zunger A. Effects of Ga addition to CuInSe2 on its electronic, structural, and defect properties. *Applied Physics Letters* 1998; **72**: 3199–3201. DOI: doi:10.1063/1.121548

65. Schroeder DJ, Hernandez JL, Berry GD, Rockett AA. Hole transport and doping states in epitaxial CuIn1−xGaxSe2. *Journal of Applied Physics* 1998; **83**: 1519–1526. DOI: 10.1063/1.366860

66. Abou-Ras D, Caballero R, Kaufmann CA, Nichterwitz M, Sakurai K, Schorr S, Unold T, Schock HW. Impact of the Ga concentration on the microstructure of CuIn1–xGaxSe2. *phys stat sol (RRL)* 2008; **2**: 135–137. DOI: 10.1002/pssr.200802059

67. Abou-Ras D, Schorr S, Schock HW. Grain-size distributions and grain boundaries of chalcopyrite-type thin films. *Journal of Applied Crystallography* 2007; **40**: 841–848. DOI: 10.1107/S0021889807032220

68. Tuttle JR, Albin DS, Noufi R. Thoughts on the microstructure of polycrystalline thin film CuInSe2 and its impact on material and device performance. *Solar Cells* 1991; **30**: 21–38. DOI: 10.1016/0379-6787(91)90034-M

69. Gabor AM, Tuttle JR, Bode MH, Franz A, Tennant AL, Contreras MA, Noufi R, Jensen DG, Hermann AM. Band-gap engineering in Cu(In,Ga) Se2 thin films grown from (In,Ga)2Se3 precursors. *Solar Energy Materials and Solar Cells* 1996; **41–42**: 247–260. DOI: 10.1016/0927-0248(95)00122-0

70. Turcu M, Rau U. Fermi level pinning at CdS/Cu(In,Ga)(Se,S)2 interfaces: effect of chalcopyrite alloy composition. *Journal of Physics and Chemistry of Solids* 2003; **64**: 1591–1595. DOI: 10.1016/S0022-3697(03)00137-9

71. Gloeckler M, Sites JR. Efficiency limitations for wide-band-gap chalcopyrite solar cells. *Thin Solid Films* 2005; **480–481**: 241–245. DOI: 10.1016/j.tsf.2004.11.018

72. Nadenau V, Rau U, Jasenek A, Schock HW. Electronic properties of CuGaSe2-based heterojunction solar cells. Part I. Transport analysis. *Journal of Applied Physics* 2000; **87**: 584–593. DOI: doi:10.1063/1.371903

73. Rau U, Schmidt M, Jasenek A, Hanna G, Schock HW. Electrical characterization of Cu(In,Ga)Se2 thin-film solar cells and the role of defects for the device performance. *Solar Energy Materials and Solar Cells* 2001; **67**: 137–143. DOI: 10.1016/S0927-0248(00)00273-7

74. Rau U. Tunneling-enhanced recombination in Cu(In, Ga)Se2 heterojunction solar cells. *Applied Physics Letters* 1999; **74**: 111–113. DOI: 10.1063/1.122967

75. Hanna G, Jasenek A, Rau U, Schock HW. Influence of the Ga-content on the bulk defect densities of Cu(In,Ga)Se2. *Thin Solid Films* 2001; **387**: 71–73. DOI: 10.1016/S0040-6090(00)01710-7

76. Jiang C-S, Noufi R, AbuShama JA, Ramanathan K, Moutinho HR, Pankow J, Al-Jassim MM. Local built-in potential on grain boundary of Cu(In,Ga)Se2 thin films. *Applied Physics Letters* 2004; **84**: 3477–3479. DOI: doi:10.1063/1.1737796

77. Jiang C-S, Noufi R, Ramanathan K, AbuShama JA, Moutinho HR, Al-Jassim MM. Does the local built-in potential on grain boundaries of Cu(In,Ga)Se2 thin films benefit photovoltaic performance of the device? *Applied Physics Letters* 2004; **85**: 2625–2627. DOI: 10.1063/1.1793346

78. Baier R. Electronic grain boundary properties in polycrystalline Cu(In,Ga)Se2 semiconductors for thin film solar cells. 2012; Available at: http://www.diss.fu-berlin.de/diss/receive/FUDISS_thesis_000000038126 [Accessed July 7, 2015]

79. Turcu M, Kötschau IM, Rau U. Composition dependence of defect energies and band alignments in the Cu(In1−xGax)(Se1−ySy)2 alloy system. *Journal of Applied Physics* 2002; **91**: 1391–1399. DOI: 10.1063/1.1432126

80. Phillips JE, Shafarman WN. Analysis of Cu(In, Ga)Se2 solar cells: Why performance decreases with increasing Ga content. in *AIP Conference Proceedings* (AIP Publishing), 120–125. DOI: 10.1063/1.57959

81. Shafarman WN, Klenk R, McCandless BE. Device and material characterization of Cu(InGa)Se2 solar cells with increasing band gap. *Journal of Applied Physics* 1996; **79**: 7324–7328. DOI: 10.1063/1.361431

82. Abou-Ras D, Dietrich J, Kavalakkatt J, Nichterwitz M, Schmidt SS, Koch CT, Caballero R, Klaer J, Rissom T. Analysis of Cu(In,Ga)(S,Se)2 thin-film solar cells by means of electron microscopy. *Solar Energy Materials and Solar Cells* 2011; **95**: 1452–1462. DOI: 10.1016/j.solmat.2010.11.008

83. Abou-Ras D, Schmidt SS, Caballero R, Unold T, Schock H-W, Koch CT, Schaffer B, Schaffer M, Choi P-P, Cojocaru-Mirédin O. Confined and Chemically Flexible Grain Boundaries in Polycrystalline Compound Semiconductors. *Advanced Energy Materials* 2012; **2**: 992–998. DOI: 10.1002/aenm.201100764

84. Leapman R. "EELS Quantitative Analysis," in *Transmission Electron Energy Loss Spectrometry in Materials Science and The EELS Atlas*, ed. C. C. Ahn (Wiley-VCH Verlag GmbH & Co. KGaA), 49–96. Available at: http://onlinelibrary.wiley.com/doi/10.1002/3527605495.ch3/summary [Accessed February 16, 2015]

85. Gault B. *Atom probe microscopy*. New York: Springer 2012; Available at: http://dx.doi.org/10.1007/978-1-4614-3436-8 [Accessed August 20, 2013]

86. Choi P-P, Cojocaru-Mirédin O, Wuerz R, Raabe D. Comparative atom probe study of Cu(In,Ga)Se2 thin-film solar cells deposited on soda-lime glass and mild steel substrates. *Journal of Applied Physics* 2011; **110**: 124513–124513–7. DOI: doi:10.1063/1.3665723

88. Choi P-P, Cojocaru-Mirédin O, Wuerz R. Compositional gradients and impurity distributions in CuInSe2 thin-film solar cells studied by atom probe tomography. *Surface and Interface Analysis* 2012; **44**: 1386–1388. DOI: 10.1002/sia.4948

89. Cojocaru-Mirédin O, Choi P, Wuerz R, Raabe D. Atomic-scale characterization of the CdS/CuInSe2 interface in thin-film solar cells. *Applied Physics Letters* 2011; **98**: 103504–103504–3. DOI: doi:10.1063/1.3560308

2 Chapter Two: Synthesis of $Cu(In,Ga)Se_2$ Solar Cells and Methods of Characterization

This chapter details CIGSe solar cell preparation, characterization techniques and instrumentation used in the present work. Starting from deposition of molybdenum back contact, synthesis of CIGSe absorber layer using different processes and different compositions and completion of CIGSe solar cells are discussed. Deposition of buffer and window layers used in current study are also discussed.

Physical principles of characterization techniques such as XRD, SEM, and EDX which are used in this study for primary characterization of the thin films are described in this chapter. Principles of APT, theory of field evaporation and sample preparation techniques involved in APT are thoroughly discussed in this chapter.

2.1 Synthesis of CIGSe thin film solar cells

Over the years mainly three different CIGSe synthesis processes are used namely:

1. Co-evaporation: Deposition of thin films directly from evaporation of different elemental sources [1]. This technique provides better control of stoichiometry and hence provides high efficiency cells.
2. Sequential process: Sputtered deposition of Cu, In and Ga followed by selenization [2]
3. Ink based spray/spin coating: Oxides of Cu, In, Ga is heated and selenized under N_2, H_2Se gas to form CIGSe thin film [3].

Many other processes like electrodeposition, chemical spray deposition etc. have also been used in past. Today, the co-evaporation synthesizing process is mostly used for CIGSe thin film preparation, and is used in this work to study CIGSe solar cells.

2.1.1 Molybdenum as back contact

CIGSe here is grown on Molybdenum (Mo) coated on top of a standard soda lime glass substrate. Soda lime glass substrate used here is the only source of Na during thin film preparation, importance of Na in CIGSe is already discussed in chapter 1. Non-reactiveness and stability against CIGSe makes Mo one of the most preferred metals to serve as back contact of the material and is well known to control diffusion of elements from glass

substrate [4]. Also formation of $MoSe_2$ is generally found to form between Mo and CIGSe [5] and serves as ohmic (resistive) contact between the two due to higher band gap (1.4 eV) than CIGSe and is beneficial for its photovoltaic performance [6]. Mo is coated using DC sputtering method using DC-magnetron Mo target (99.99% pure) of 8 inch in diameter. Environment argon gas pressure was maintained at 0.27 Pa with DC power 3 W/cm^2. Mo is deposited up to 500 nm in thickness as shown in Figure 2.4. These standard conditions of Mo deposition on glass substrate were used for all the samples synthesized in this research.

2.1.2 Co-evaporation techniques for deposition of CIGSe absorber layer

Currently co-evaporation process is the mostly used to grow thin film CIGSe. Current world record of CIGSe cells are processed using this method [7]. In co-evaporation process, different elements involved (Cu, In, Ga, Se) are thermally evaporated from their pure element sources and intermixed on top of Mo coated glass substrate at high temperature (~600^{o}C). All elements are mixed and react on top of substrate at high temperature where growth of the layer takes place. Variation of elemental flux during co-evaporation process is very critical to control thin film growth and to establish desired chalcopyrite phase. Different established processes have been used to obtain desired composition gradient of CIGSe composition using co-evaporation method and are described in this section.

Schematic experimental set up is shown in Figure 2.1 along with image of instrument (from inside) used in this work.

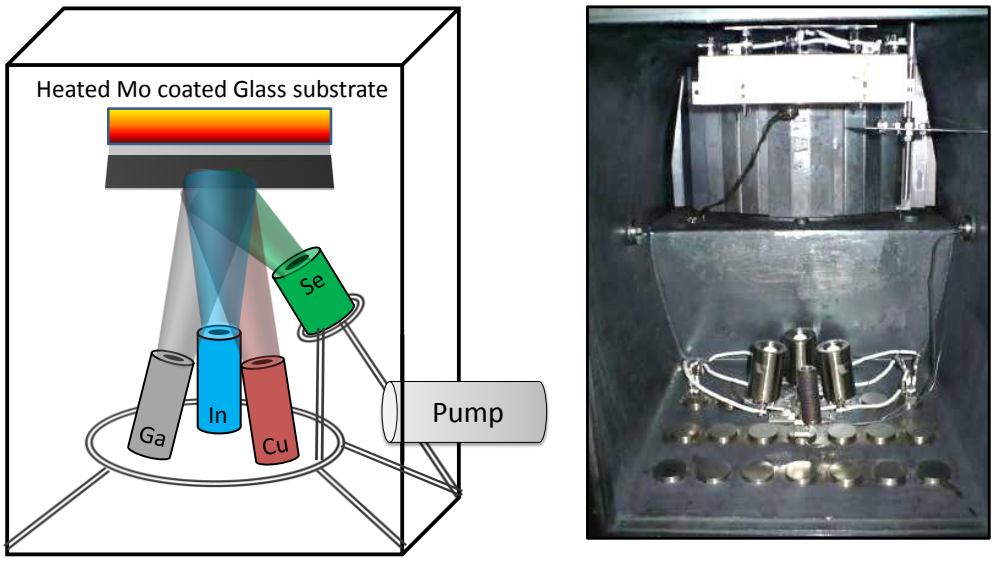

Figure 2.1: (Left) Schematic experimental setup of Co-evaporation technique for CIGSe deposition. (Right) Co-evaporation instrument at IMN (Institut de Matériaux de Nantes), Nantes (all syntheses were performed in this machine) Image courtesy: Dr. N. Barreau.

Co-evaporation technique in itself is very flexible. Tuning evaporation flux of different elements results in modified properties of the films and are very critical for device performance, evaporation flux of different elements can be tuned by varying their respective source temperature. Thickness of thin films can be increased by increasing overall time of thin film deposition maintaining similar fluxes. Phase, composition profile, Ga gradient etc. change accordingly with the flux variation; hence plethora of different processes are possible to form CIGSe. Most of the APT research work performed here is based on cells synthesized using CuPRO (Cu poor-rich-off) process due to two main reasons: 1) to ensure homogeneity of the CIGS film (wherever is fabricated the Atom Probe Tomography sample in the film, the composition will be the same) and 2) to form small size grains of CIGSe in order to increase the probability of observing GB in APT analysis. However most efficient cells are prepared using 3-stage process, these two processes used in this work are described below.

a) Three Stage Process

Three stage (or 3-stage) process developed by Gabor et.al [8] is known to produce high efficient CIGSe cells [7,9,10] and the most efficient CIGSe solar cell today is synthesized using this process [7]. As the name suggests, 3 stage process involves three stages which are shown in Figure 2.2 for bithermal process. Flux of Selenium (Se) is kept constant throughout the process, whereas fluxes of other elements varied during the process. This is shown in terms of Cu/(In+Ga) ratio (y) in Figure 2.2b. [Ga]/ [In] flux ratio is generally kept constant throughout the process.

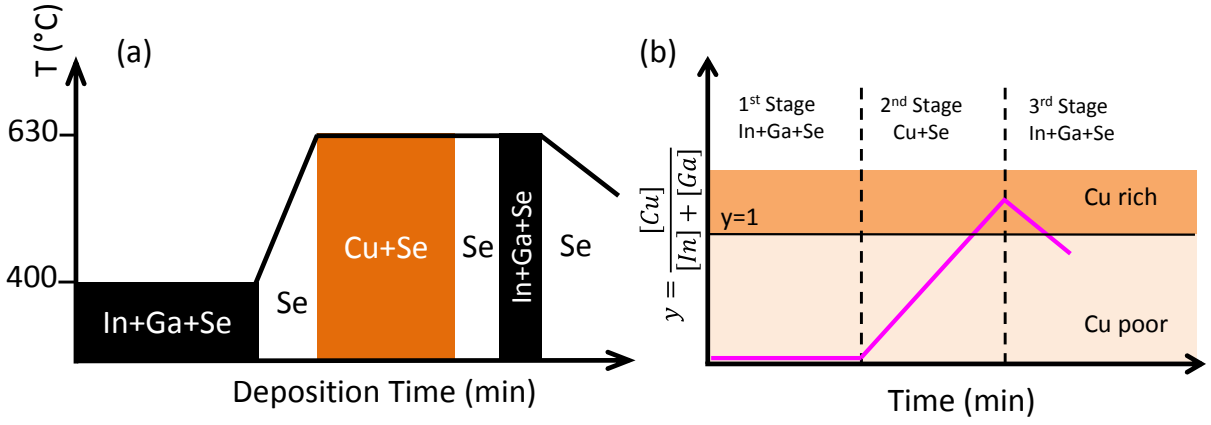

Figure 2.2: (a) Elemental flow of 3-stage process with time. (b) Time evolution of Cu content inside grain, (Vertical axis) y is the Cu ratio, above and below y=1 line represents Cu rich and Cu poor respectively.

3-stage process may or may not involve temperature variation of substrate during the process, each case producing different thin film characteristics. 3-stage process gives rise to Ga grading along the depth which is particularly known to have beneficial effect on CIGSe cells. However ratio of Ga/In being constant throughout the process, Ga gradient is formed without any forced alterations in stoichiometry and is mostly believed to be due to the self-assembly of the system itself.

In those structures, Ga content increases towards the back contact and near pn junction. This is illustrated in Fig 2.3a which represents Ga grading and a minimum of Ga content is found at around 100 nm from pn junction as illustrated in the concentration profile measured using APT (this work) in Figure 2.3a. This type of grading is called double grading.

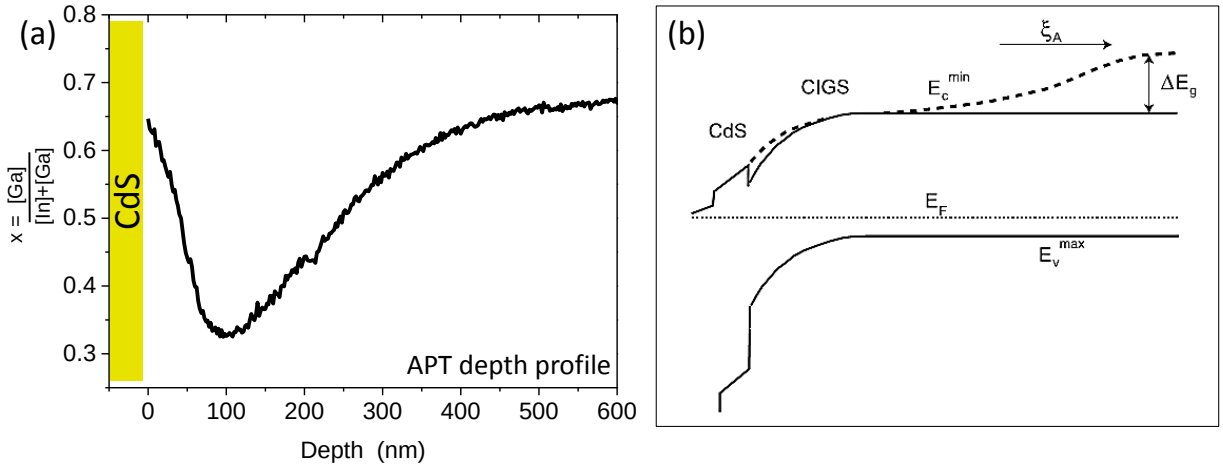

Figure 2.3: (a) APT depth profile of Ga ratio (x) versus depth up to 600 nm from hetero junction for CIGSe prepared using bithermal 3-stage (this work). (b) Energy band diagram comparison for graded (dash) and ungraded (straight) band gap CIGSe (source: [11]). An additional electric field ξ_A is created in QNR assisting in better charge separation in the region leading to reduced recombination in QNR.

As the band gap of CIGSe depends on the x ratio ([Ga]/[In]+[Ga]) (see equation (1.8)), band gap is also graded respectively with Ga content [12]. Band gap grading helps in better collection of the charge carriers due to potential gradient formed in the Fermi energy band diagram as shown in Figure 2.3b. An additional electric field ξ_A is created in QNR assisting in better charge separation in the region, hence leading to reduced recombination in QNR. QNR is the recombination dominant region and a better separation in this region significantly improves the device performance. Improvement in quantum efficiency in high wavelength region is observed by Lundberg et.al [11] due to Ga grading in the cell.

b) CuPRO process

Isothermal Copper Poor Rich Off (CuPRO) process developed by Kessler et.al [13] demonstrated unique process to synthesize CIGSe layer with no compositional gradient across or with depth in the film. As a major part of researches performed here deals with Atom Probe Tomography (APT) allowing analyses of a maximum volume of ~ 50×50×500 nm^3, it is crucial to ensure the homogeneity of the grain composition in order to have a better reproducibility of the results. A comparison of grain size is shown in cross section SEM image in Figure 2.4 for similar overall Ga content.

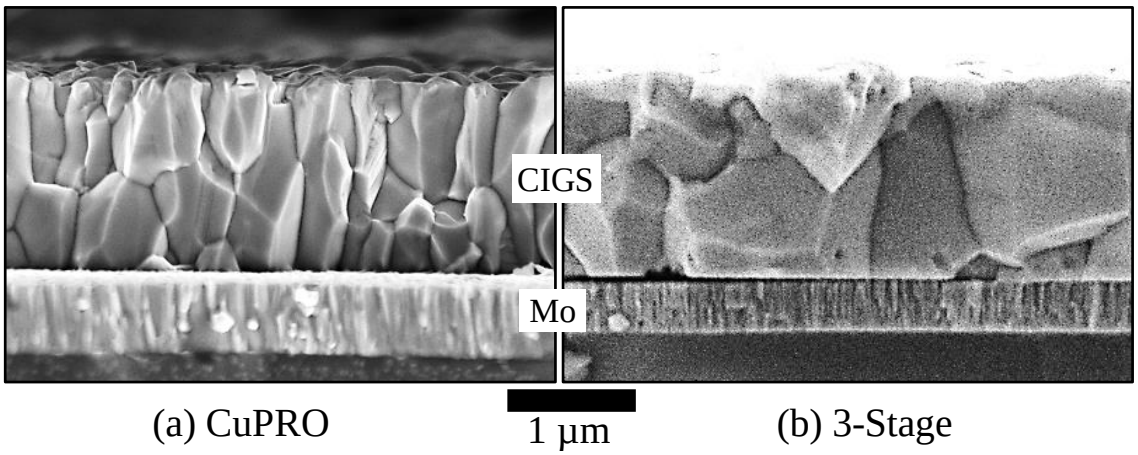

Figure 2.4: (This work) Cross-section SEM image of CIGSe thin film on Mo coated glass substrate synthesized using (a) CuPRO process and (b) 3-stage process

The process consist of constant temperature and constant flux of Se, In and Ga throughout the process. The only parameter that varies during the process is the flux of Cu. As the name suggests Cu flux is initially kept low then high then off (zero flux). Time evolution of CuPRO process is shown in Figure 2.5.

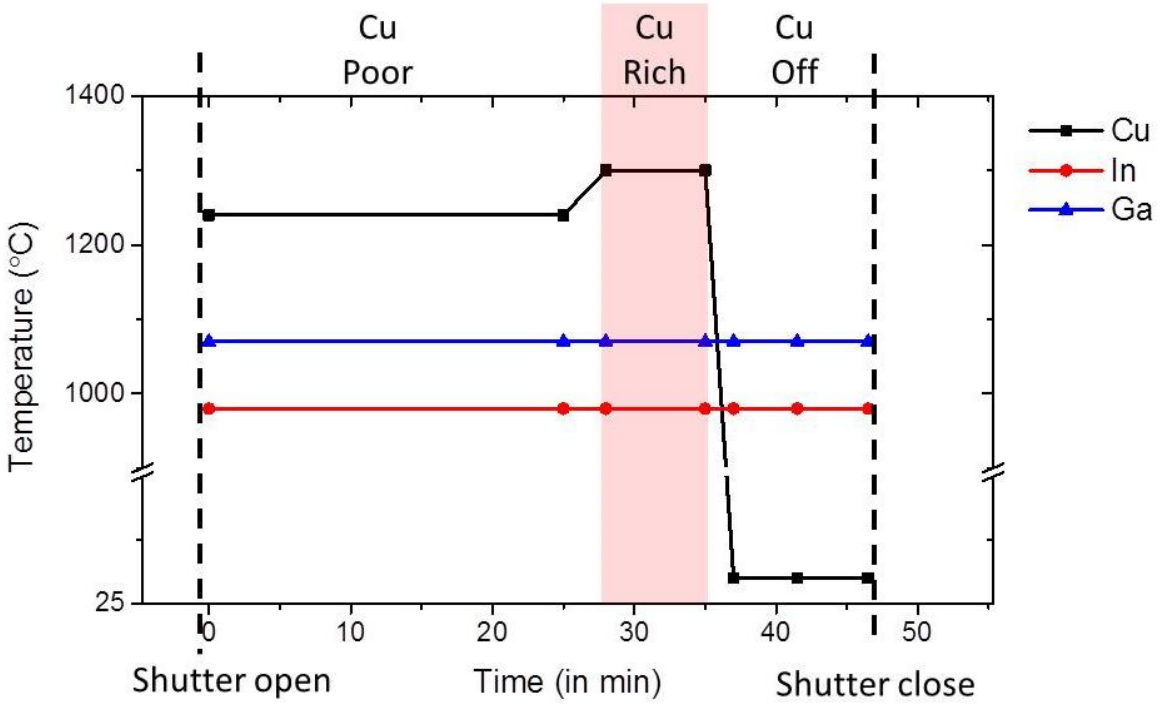

Figure 2.5: Process flow with time for CuPRO process. Left axis represents temperature of respective element sources.

Temperature of Se source is kept at 300°C and substrate temperature is maintained at 600°C throughout the process. As evaporation flux of elemental sources is proportional to their source temperature, flux of elements can be controlled by controlling respective source temperature. Flux of In, Ga is kept constant by keeping their respective sources at constant temperatures. Ga content can be changed for different cells by changing temperatures of Ga and In. Temperature of the Ga source vary from chamber temperature (meaning pure In sample) to 1130°C (meaning pure Ga sample). Similarly the temperature of In source is varied from chamber temperature (pure Ga sample) to 1020°C (pure In sample). Temperature of Cu source varied from 1240°C to 1300°C to 30°C (heating off) for all samples to maintain appropriate Cu flux. Total of 8 CIGSe cells were processed with this technique with different Ga concentrations by varying Ga/In elemental flux during co-evaporation including $CuGaSe_2$ and $CuInSe_2$.

However cells grown using this method do not present high efficient devices but results in homogenous grain composition and narrower grains.

Both of the processes form absorber layer of 2 μm to 3 μm, and 3-stage process produces more high efficient cells. In both of the above processes, end point detection (EPD) method by Kessler et.al [14] is used to recognize Cu poor – Cu rich – Cu poor transition. Emissivity

of the compound depends on its respective composition and at the point of transition (Cu poor to rich or vice versa), there is overall change in emissivity which can be determined by tracking the output power of substrate heater keeping the substrate at constant temperature. It can be noticed that both of the above processes starts and ends with Cu poor process with a Cu rich stage in between. The main reasons are:

1) Cu poor (or no Cu) step in the beginning: To avoid formation of $Cu_{2-x}Se$ at the back contact and to assist formation of $MoSe_2$.
2) Cu rich step: Cu rich CIGSe is known to have large sized grains. Indeed, very small grains are not desired for thin film solar cells due to active recombination at GBs, we use a Cu rich step to increase grain size via recrystallization [15].
3) Cu poor (or off) step in end: To avoid the formation of a Cu rich CIGSe surface which might degrade the film surface because of air oxidation that may form copper oxides on surface.

There are numerous possibilities to vary elemental fluxes during thin film preparation to form CIGSe but only certain strategies as discussed above provide high efficient cells. Both of the above described processes are essential in order to obtain desired composition profile.

2.1.3 Deposition of CdS, ZnO layers and completion of cell

The thin film deposition is followed by deposition of a buffer layer and a front surface and collection grids. Each plays an essential role for a better collection of charge carriers.

a) CdS buffer layer deposition

The formation of n-type semiconductor starts with deposition of Cadmium Sulphide (CdS). Various processes exist for CdS deposition. Here we use a chemical bath deposition which is also used in record efficient cells [7]. Chemical bath contained solutions of Cadmium acetate (0.0026M), thiourea $SC(NH_2)_2$ (0.095M) and ammonia (1M) mixed together to form CdS which was then deposited at 60°C for 7 minutes. Experimental set up is demonstrated in Figure 2.6.

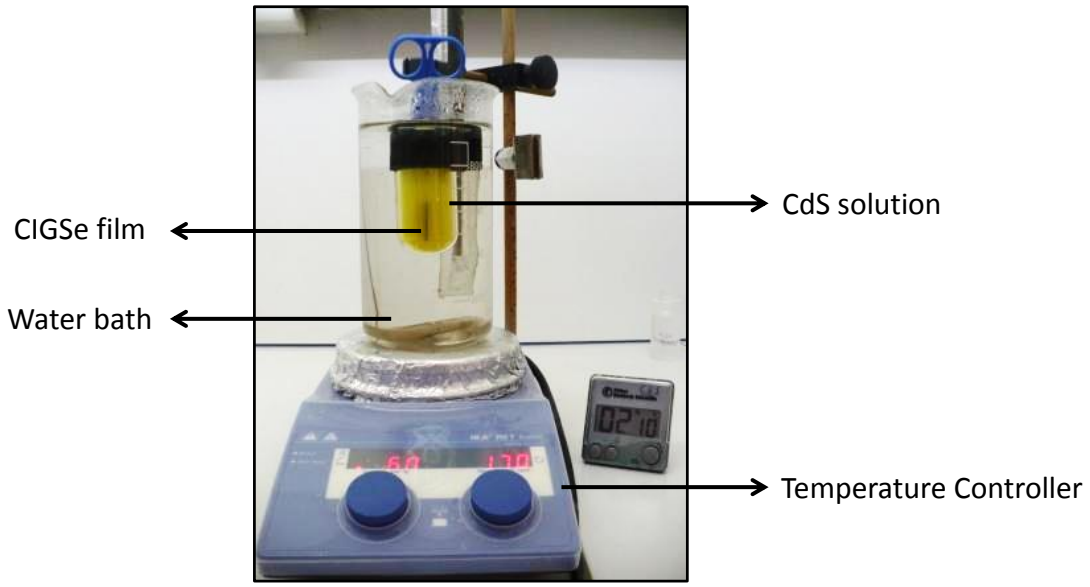

Figure 2.6: Chemical bath deposition of CdS on CIGSe. Image Courtesy: Dr. N. Barreau

CdS deposition forms the pn heterojunction with CIGSe and also acts as the buffer layer. Better lattice match [16,17] and higher band gap (2.4eV, figure 1.6) is the main reason for using CdS as n type semiconductor. Also Cd diffusion in first few nanometers of top surface of CIGSe is evidenced by [16,18,19] and is known to have beneficial effect on photovoltaic performance of the cells. Reaction forming CdS from precursors can be described as:

$$Cd(NH_3)_4^{2+} + SC(NH_2)_2 + 2OH^- \rightarrow CdS + CN_2H_2 + 4NH_3 + 2H_2O \quad \textbf{(2.1)}$$

There are also some issues with CdS layer. Indeed, since it absorbs some part of solar spectrum (wavelengths up to 516 nm), respective part of solar spectrum is not utilized and does not contribute towards output power. Also CdS is a highly toxic material and dangerous for health, hence search for a better alternative buffer layer is always required for CIGSe cells. In_2S_3 is an alternative but does not provide high efficient cells. A review of materials used as buffer layers for CIGSe is available in [20].

b) ZnO window layer deposition

ZnO is deposited on top of CdS layer and serves as a transparent front contact surface due to its transparency and high band gap (~3.3 – 3.8 eV). Sequencing of ZnO-CdS-CIGSe also favors band gap alignment for better photovoltaic performance (figure 1.6). ZnO is deposited

using RF sputtering by using ZnO as target material. Ar^+ ions collides on target material under vacuum and deposits ZnO on top. 200nm to 500nm of ZnO is deposited on top and act as front surface. ZnO is the best material as window layer but is not very conductive to pass the current effectively.

c) Formation of Ni/Al contact grids

Efficient transport of minority carriers (electrons here) is very important for generation of output power and can be best achieved with metallic contacts. Current collection to external circuit is supported by deposition of Ni/Al metallic grids on front surface. Metal grid is opaque and absorbs almost all the wavelengths, hence it is suggested to use minimum surface area of grid with maximum carrier collection. Cells of area 0.5 cm^2 were used in this work to obtain J-V and EQE measurements. As Ni forms good contact with ZnO, it is deposited first on top layer containing ZnO in finger shaped grids and followed by deposition of Al which is better in forming electrical contacts. Both Ni and Al are deposited using electron beam evaporation applying grid mask.

To obtain characteristics of developed thin films some primary characterization techniques were employed and are described in next sections.

2.2 X-Ray diffraction: Principles and limitations

X-ray diffraction (XRD) works on the principle of scattering of x-rays from lattice planes of the material and is used to identify phases of crystalline and polycrystalline materials. Our main study is focused on chalcopyrite phase of polycrystalline CIGSe, and identification of desired phases could be confirmed using XRD. A schematic diagram of principle of XRD is shown in Figure 2.7. Beam of x-ray is scanned at different incoming angles and detector measures the scattered radiation. X-ray beam source used here is Cu-kα radiation whose wavelength (λ) is known and is equals to 0.1540 nm. At specific incident angles, maximum scattered intensity is observed due to constructive interference between scattered waves from different planes occurring at integral values of n.

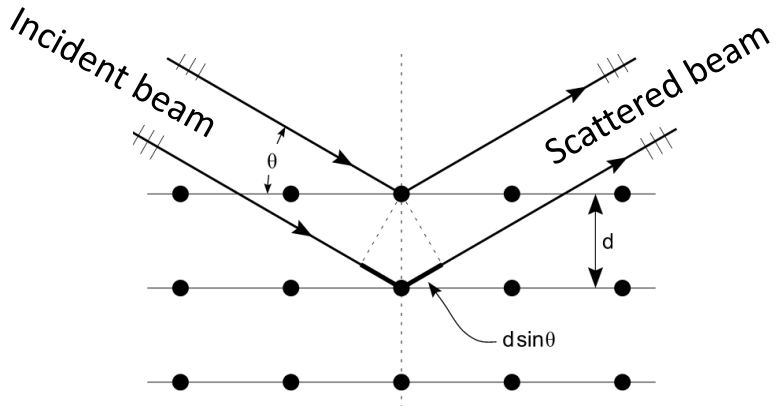

Figure 2.7: Schematic diagram explaining physical principles of XRD.

Using this phenomenon lattice spacing can be determined from Figure 2.7 and is known as Bragg's law:

$$2dsin(\theta) = n\lambda \tag{2.2}$$

Where, λ is the wavelength of incoming radiation, d is the spacing between diffracting planes, θ is the angle of incoming beam. As wavelength of incoming radiation is known, thus using equation (2.2) and angles at which maximum intensity is observed, lattice spacing "d" can be determined. XRD is used in the present work to characterize the chalcopyrite phase and lattice properties of CIGSe absorber layer for various Ga concentration. As study here mainly deals with chalcopyrite phase of different Ga content in CIGSe, it is crucial to confirm presence of same phase for all samples to be studied. Figure 2.8 shows a typical XRD pattern of a CIGSe sample deposited using CuPRO co-evaporation process on a Mo coated glass substrate. Main diffraction peaks of CIGSe detected are (112), (204/220), (116/312) and of Mo (110). This XRD pattern is shown for $CuIn_{0.83}Ga_{0.17}$ sample and results of other samples are discussed in next chapter.

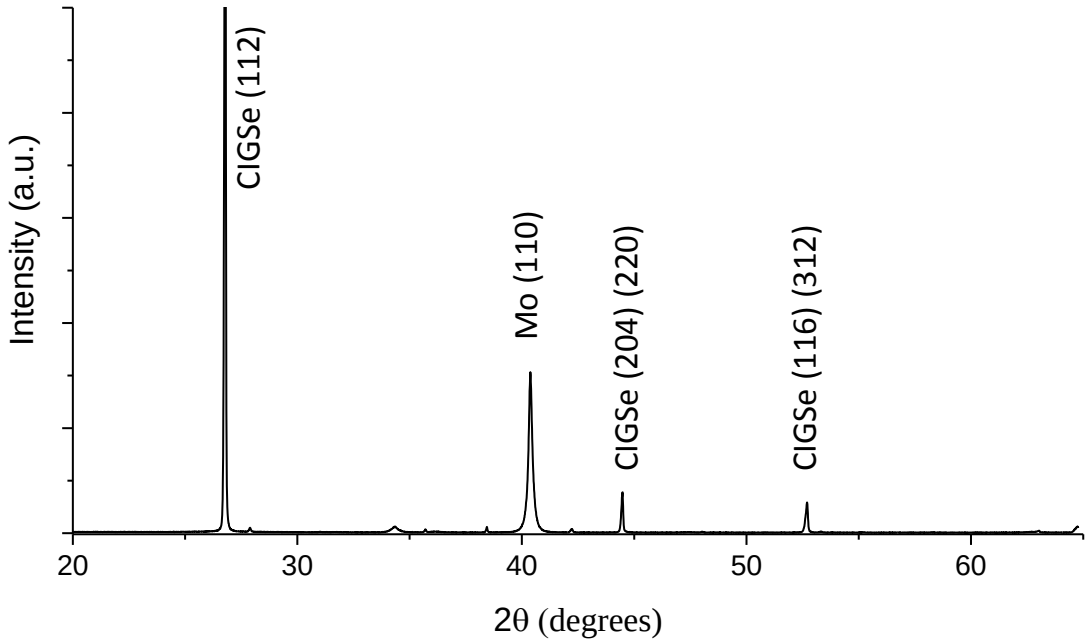

Figure 2.8: XRD pattern of a CIGSe sample (x=0.17) deposited using co-evaporation process on a Mo coated glass substrate.

To get further characteristics of the film, like surface texture, cross section of the thin films, GB distribution and density of CIGSe thin films, electron microscopy techniques were used and are detailed in the next section.

2.3 Electron Microscope and components

2.3.1 Scanning Electron Microscope:

Electron microscope is used because optical microscope cannot resolve materials with size below diffraction limit. Indeed, considering a 550 nm green light wavelength (lower wavelengths are not visible in optical microscope), the lowest resolvable size is around 200 nm. Due to shorter wavelengths of electrons ($\lambda=h/mv$) one can use electrons to obtain images with a sub-nanometer resolution. Scanning electron microscope (SEM) is a type of electron microscope which scans the surface of sample with a beam of electrons focused using electro-magnetic focusing lens as shown in Figure 2.9a.

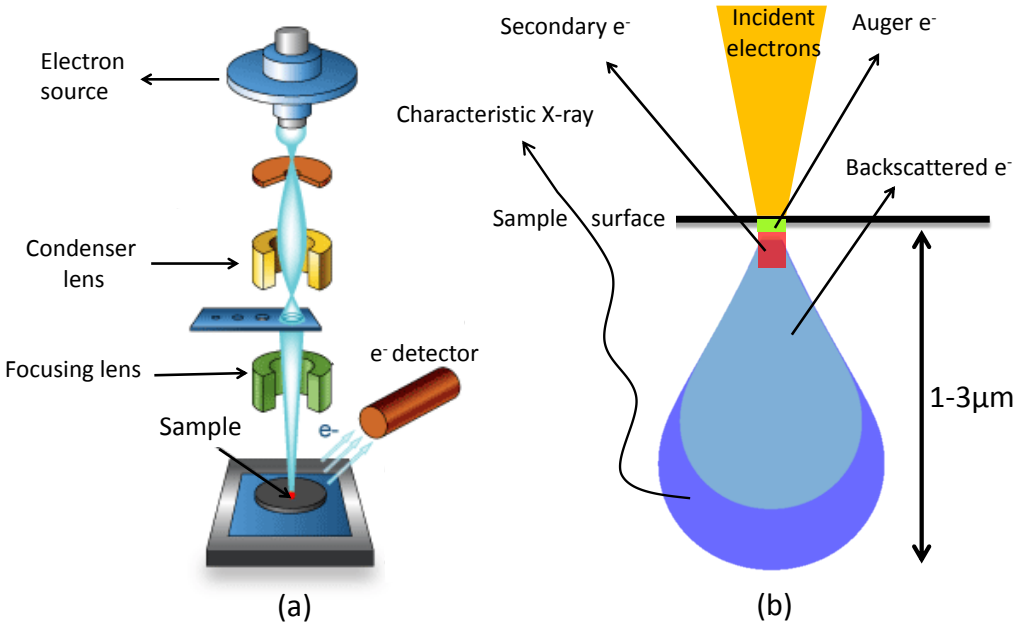

Figure 2.9: (a) Schematic diagram of working of SEM (b) different rays and electrons produced after interaction of electrons and material's surface.

Figure 2.9b illustrates various phenomenon taking place upon interaction of electrons with a material. Formation of characteristic x-rays and ejection of secondary, Auger and backscattered electrons are because of interaction of electrons and material. First few nanometers of the sample surface produce Auger electrons; further few nanometers produce secondary electrons and are detected by electron detectors where image is processed and is the main detector of SEM. Backscattered electrons produce images using back scattered electron detector and may reveal grain size. Characteristic X-rays are produced from 1 to 3 µm depth of the sample.

2.3.2 Energy Dispersive X-ray spectroscopy (EDX)

Characteristic X-ray is produced due to interaction of high energy incident electrons with atoms of the sample. As each element has different and unique atomic structure and orbitals, X-rays produced by each element will correspond to specific electron transitions. Typical electronic transitions in an atom are illustrated in Figure 2.10a. High energy incoming electrons kick-out electrons from the atom of the sample and are followed by subsequent transitions of electrons from higher energy shells to lower energy shells. Due to quantized energy of these shells (K, L, M..) only specific energy orbits are available. Hence for a typical atom Kα, Kβ, Lα .. energy transitions are specific. Thus composition of different

elements can be measured using EDX spectrum by quantifying relative intensities of each elements present using any of the transition line.

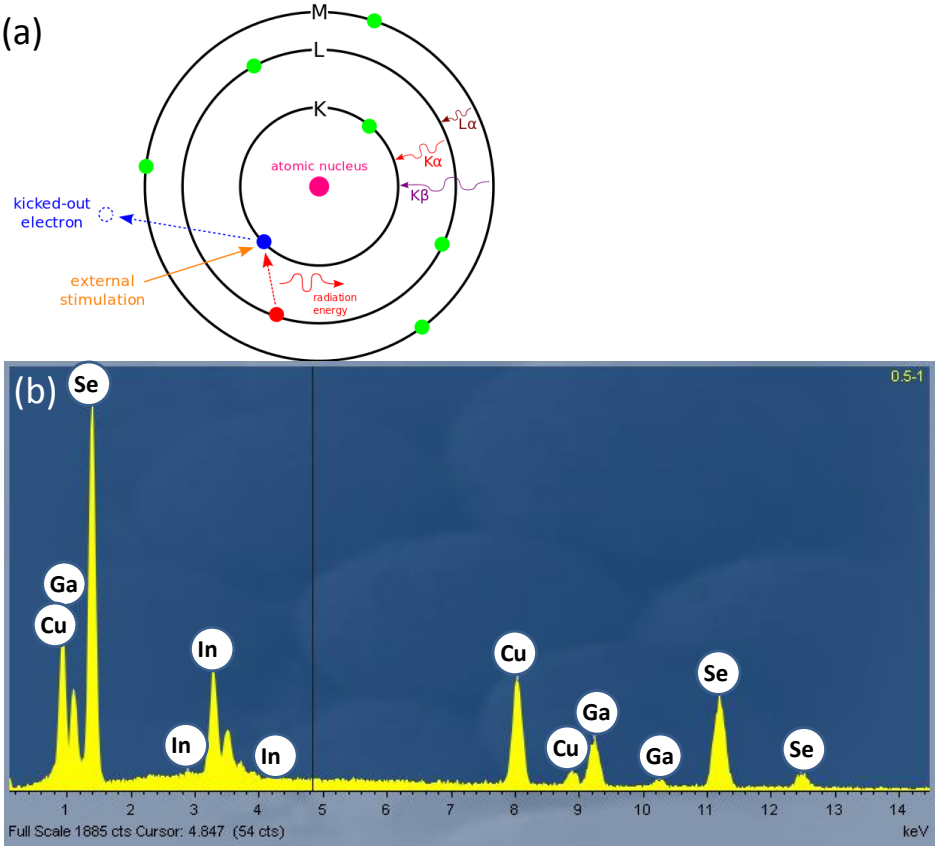

Figure 2.10: (a) Schematic atomic structure and possible transitions in a particular atom (b) a typical EDX spectrum of CIGSe, peaks originating due to different elements are illustrated.

As different elements produce their specific characteristic peaks in x-ray spectrum, quantification and compositions of different elements present in the sample can be calculated using EDX. Here specific K lines are used to determine stoichiometry of CIGSe cell. Figure 2.10b shows a typical EDX spectrum of CIGSe sample obtained in this work using INCA software installed in SEM/FIB - ZEISS-1530 XB. The final composition is calculated in atomic percent using the software and uncertainties also calculated by the software due to overlaps in peaks. Accurate compositions of respective elements are obtained using EDX within error limits calculated using the software which is given in Table 2-1. Eight different CIGSe samples were processed using CuPRO process with different Ga concentration. Compositions of respective elements of different samples as measured in this work by EDX are presented in Table 2-1.

Table 2-1: Compositions (in atomic %) of respective elements in CIGSe and Ga ratio x for different samples prepared.

Sample#	Cu (%)	In (%)	Ga (%)	Se (%)	x(Ga/In+Ga) (±0.10)
1	24.8±0.9	26.5±1.3	0.0	48.3±1.4	0.00
2	24.6±0.9	22.2±1.3	3.9±0.8	48.5±1.4	0.17
3	24.8±0.8	17.5±1.0	9.9±0.8	47.8±1.4	0.39
4	23.2±0.9	15.7±1.3	9.7±0.8	51.4±1.4	0.47
5	23.4±0.9	14.6±1.3	11.1±0.8	51.0±1.4	0.56
6	23.6±0.9	12.4±1.3	13.0±0.8	51.1±1.4	0.67
7	24.5±0.9	4.5±1.0	20.7±1.0	50.3±1.4	0.84
8	24.3±0.8	0.0	26.9±1.0	48.4±1.3	1.00

2.3.3 Focused Ion Beam (FIB)

FIB is generally equipped with SEM and is primarily used to sputter (or mill) the specimen, and to deposit materials at sub micrometer level. Here we use Zeiss FIB Nvision 40 equipped with a Kleindieck micromanipulator to make specific APT samples. FIB system makes use of Ga^+ ions to physically ablate the material as shown in Figure 2.11. There are many reasons behind using Ga as the ion source such as:

1) Low melting point (29.8°C): appropriate to work at room temperature
2) Low volatility: promising longer source life
3) Low surface free energy: better viscosity
4) Excellent mechanical and electrical properties

and many more useful properties of Ga as described in the reference Giannuzzi et.al. [21]. Figure 2.11a shows direction of Ga ions relative to electrons. At cross-beam position iso-position image can be obtained from both electrons and Ga ions and is located about 5 mm from pole piece for our instrument. Various currents and acceleration voltages are available to ablate the material accordingly. One example of selective sputtering using FIB to create CIGSe chunk is shown in Figure 2.11c. Higher currents ablate the specimen strongly and also form unwanted damages. These unwanted damages in the sample are apparent due to Ga contamination at high ion energy (30 kV, 6.5 nA).

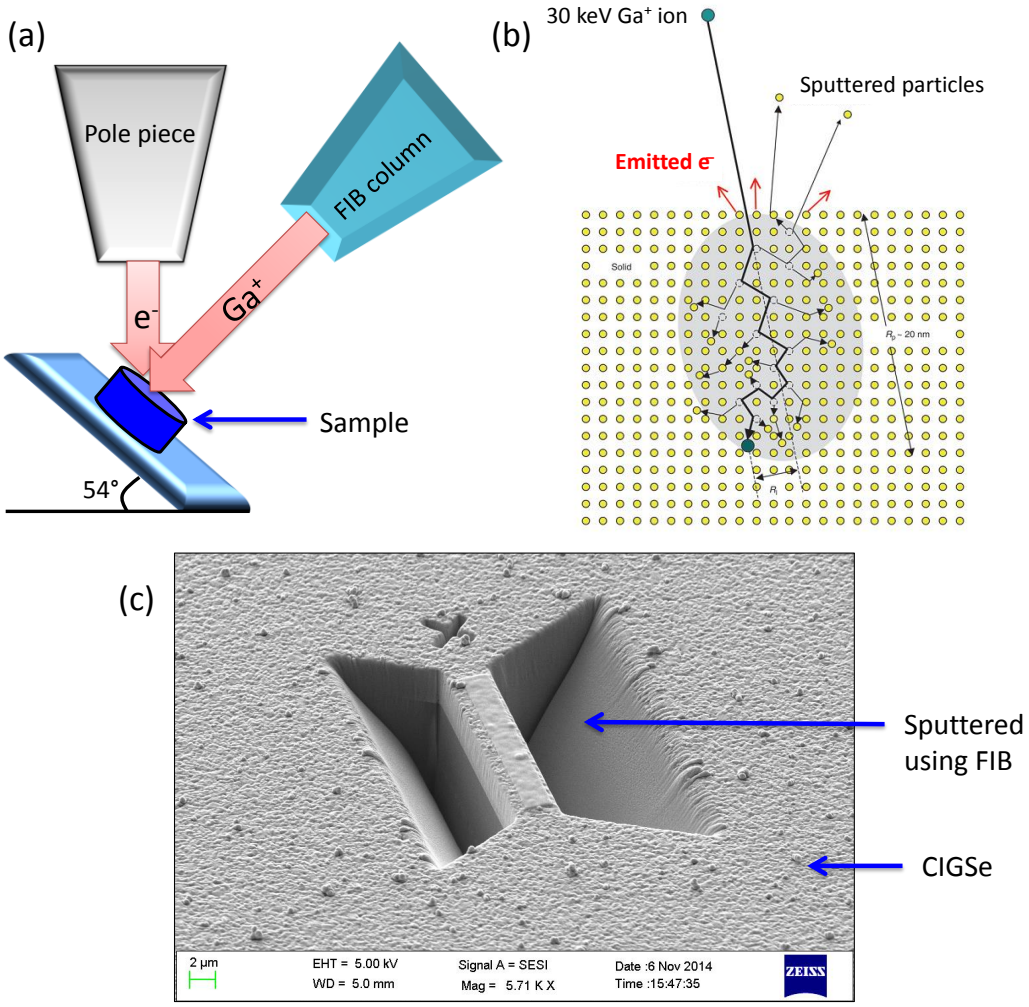

Figure 2.11: Schematic diagram depicting (a) relative position of Ga ion source and electron source in SEM/FIB. (b) Various mechanisms upon interaction of high energy Ga ions with material. (c) CIGSe lamella prepared after sputtering surrounding region with Ga ions in FIB.

Sample preparation techniques using FIB are discussed in later parts of this chapter. The instrument is also equipped with EBSD which is detailed in the next section.

2.4 Electron Back Scattered Diffraction (EBSD)

EBSD is a microstructural characterization technique used to study phase distribution, crystal orientation, defects of a crystalline or polycrystalline material. EBSD is a highly useful technique to characterize polycrystalline materials like CIGSe and can provide useful information like: crystallographic orientation of grains, misorientation between grains, grain size statistics, misorientation angle distribution, texture quality of different planes at micrometer levels. EBSD is used in this work to obtain grain size distribution, misorientation

between grains and to count number of GBs for CIGSe samples with different Ga concentration.

2.4.1 EBSD technique: Experiments and Principles

EBSD technique works on the principle of detection of Kikuchi lines and hence EBSP (Electron Back Scattered diffraction Pattern). An EBSP is created due to the interaction of high energy electrons (~20 kV) with specimen and is specific to respective crystal structure, crystal orientation, lattice parameters and composition. Kikuchi bands (pair of Kikuchi lines) are formed due to scattering of incoherent electrons from a sufficiently thick crystal material. As shown in Figure 2.12a, electrons from source are projected on a tilted specimen, due to presence of diffracting planes electrons are scattered and channeled systematically in forward direction depending on crystal structure of the specimen. Kikuchi patterns are detected on phosphorus screen on detector and are specific for every crystal structure. Pair of Kikuchi bands is also called EBSP. Image of an EBSP of CIGSe created with interaction of 20kV (accelerating voltage) electrons is shown in Figure 2.12a, revealing the Kikuchi lines. The latter are particular and fixed for a crystal system and hence can be used for indexing (Figure 2.12b) and hence determining crystallographic system and orientation.

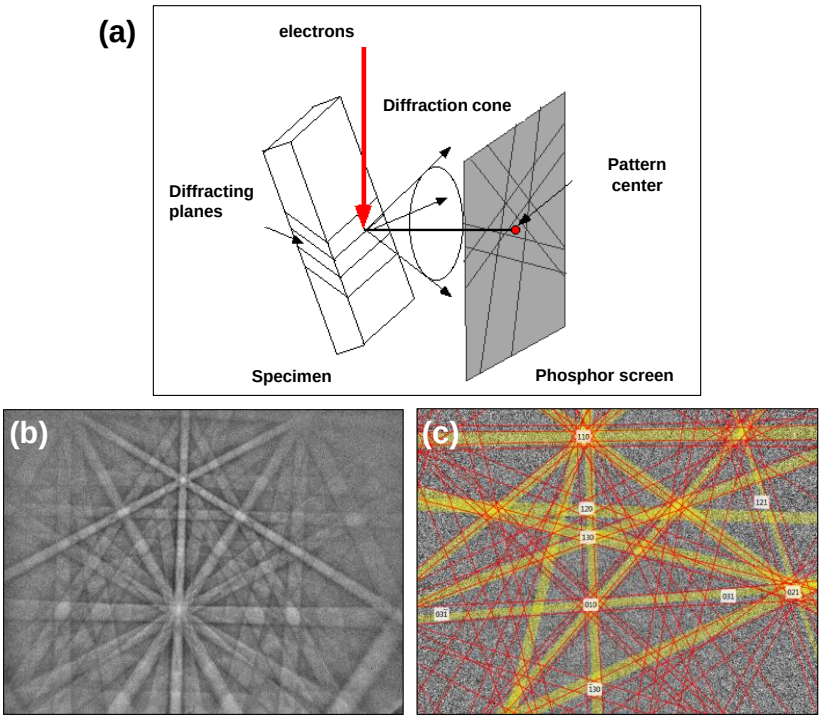

Figure 2.12: (a) Schematic representation of formation of Kikuchi patterns when electrons are projected on diffracting planes (b) Kikuchi bands detected for CIGSe (c) indexing performed by the software

The experimental setup of EBSD instrument is shown in Figure 2.13. Experiment is generally performed in a SEM chamber equipped with EBSD detector. A view of the inside of the SEM chamber is shown in Figure 2.13b. Specimen is tilted at 70° with horizontal and is subjected to high energy electrons (20keV) from top as illustrated in Figure 2.13b.

Oxford instrument's AZtecHKL software is used to detect and index EBSP patterns produced by the sample an indexed EBSP is shown in Figure 2.12b. Electron beam is scanned over the surface of the specimen and subsequent EBSD pattern respective to points specified are imaged in the software. A particular grain gives the similar Kikuchi pattern and is changed when beam traverse from one grain to another grain. However at grain boundaries, Kikuchi pattern of two corresponding grains overlap and give a zero solution. Hence GBs are detected by lines containing zero solutions.

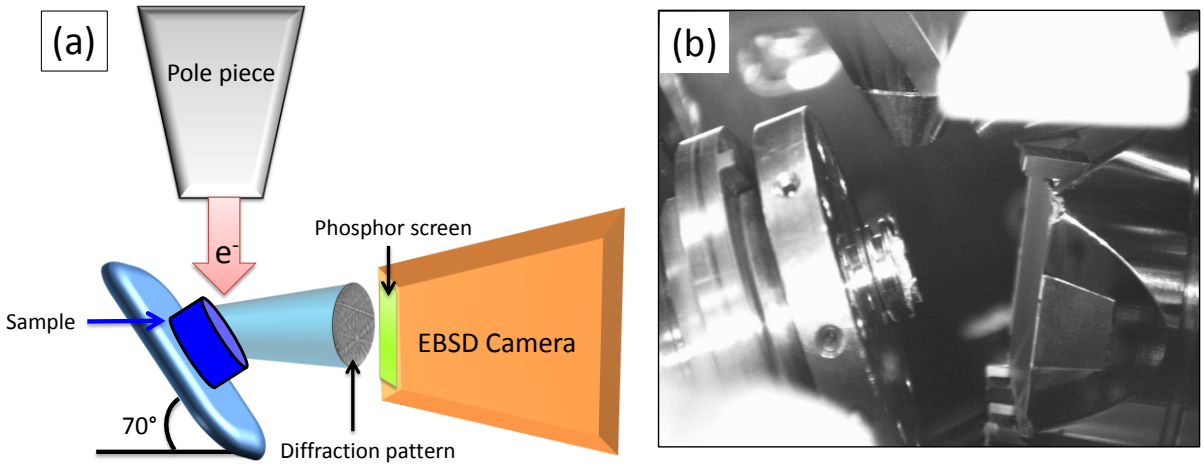

Figure 2.13 (a) Schematic experimental setup for EBSD experiment (b) actual view inside the SEM chamber.

EBSD is a very useful technique to obtain many statistics of a polycrystalline material; however it is unable to determine atomic distribution at grains or GBs. To obtain atomic distribution and atomic scale quantitative information we make use of atom probe tomography.

2.5 Atom Probe Tomography

Atom Probe Tomography (APT) is an instrument enabling analysis of materials at atomic scale. Using this technique, 3D visualization of atomic distribution, segregation and clustering of atoms, characterization of grain boundaries etc. at atomic level is now achievable. APT requires specimen in a sharp needle shape with an apex radius lower than 50

nm. The result of an analysis is the reconstruction in 3D of a volume up to 50nm×50nm×200nm with atomic position and chemical identification.

In 1935, E. Müller started to work on field electron emission microscope. In 1955 Field Ion Microscope (FIM) was developed demonstrating instrument's capability to resolve single atoms. FIM uses imaging gas (H/He/Ne ..) to image surface atoms on the apex of the sample (with a tip shape). Individual atoms are seen in FIM but their chemical identity could not be known using this technique. It was later realized that by applying high enough voltage and creating electric field force at the surface may evaporate these surface atoms and project them onto detector. This phenomenon is due to evaporation of surface atoms due to applied DC voltage and can be activated by applying simultaneously voltage pulses or laser pulses. This technique of stimulated desorption of surface atoms is called field desorption microscopy (FDM). Inclusion of triggered field desorption enabled FDM combined with time of flight mass spectrometry, demonstrating its capability to identify elements present by measuring time of flight [22]. Cerezo et.al. [23] combined this technique with XY detection system, historically known as position sensitive atom probe to detect projection of evaportated atoms in XY dimensions. Later, third dimension calculations enabled reconstruction of data in three dimensions (XYZ) depicting 3D distribution of atoms at nanometer scale.

APT was first used for metallic materials utilizing electrical pulses to trigger field evaporation. Femtosecond laser pulses were then used to analyse poor conducting materials like semiconductors and insulators using this technique [24].

Herein, we use laser-assisted wide-angle tomographic atom probe (LAWATAP) [25] to perform analysis of CIGSe semiconductors. This section gives a brief introduction of the underlying principle, theories of field evaporation, sample preparation techniques, post analysis and functioning of laser assisted APT.

2.5.1 Pulsed laser atom probe: Principles

Atom Probe is an instrument which combines Field Desorption Microscope and time-of-flight mass spectrometry with a position sensitive detector which provides a three dimensional reconstructed volume and identities of atoms present in the sample. A needle shaped fine tip of end radius <50nm is placed in an ultrahigh vacuum chamber ($\approx 10^{-10}$ mBar) at 20K – 80K temperature. High positive voltage (V_0 = 1 kV – 15 kV) is applied to the tip raising electric field up to 10^{11} V/m.

Voltage pulses or laser pulses (in this work) are now applied to the tip resulting in ejection of atoms in form of singly or multiply charged ions. Time of flight (Tof) is measured using the time difference between detection of ions at the microchannel plate and application of laser pulse. XY projection of atoms is detected on position sensitive detector as shown in Figure 2.14. Position sensitive detection system used here is based on advanced delay line detection (ADLD) system developed by Da Costa et.al [26] to minimize multi hit detections.

Atom by atom, layer by layers, the sample is evaporated and its constitutive elements detected on the detection system. GBs in CIGSe are decorated by planar segregation of Na atoms as depicted schematically in Figure 2.14. So atoms before, after and at GB are evaporated and detected respectively by detection system.

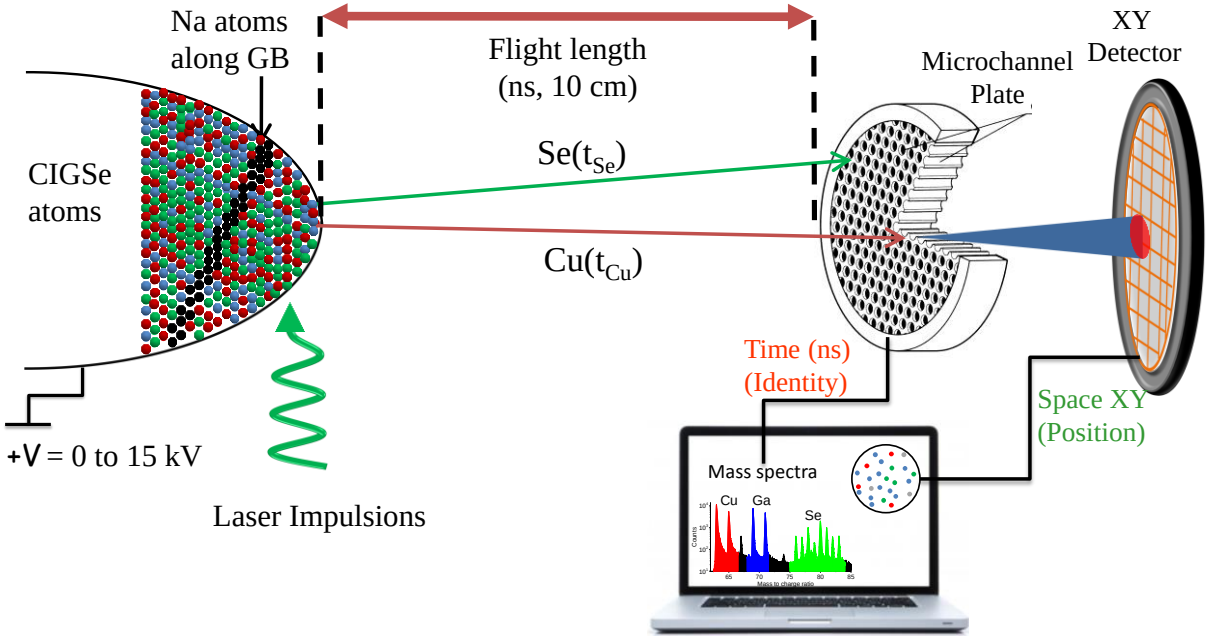

Figure 2.14: Schematic diagram of a laseer assisted atom probe instrument (image not to scale)

At the end of analysis, data of each detected atom is saved, containing information of its evaporation voltage, Time of flight, XY spatial detection, number of detected ion. These informations are then used to reconstruct data in three dimensions using GPM3Dsoft software using protocols discussed in later sections. By selecting atomic peaks of Na (23 a.m.u.), GB can be identified by planar segregation of Na atoms in 3D volume.

From sample preparation to APT analysis, various parameters are critical in order to obtain best quantitative results. All experiments performed here are carried out in laser assisted wide angle tomographic atom probe (LAWATAP).

2.5.2 Theory of field evaporation

Field evaporation is the underlying physical process operating in an atom probe. When atoms leave the surface in a single or multiple charge state under very intense electric field (around 10-60 V/nm), the process is called field evaporation. Field at the surface of the tip apex depends on the applied voltage and shape and radius at tip apex. The Electric field (F) at the tip surface is given by:

$$F = \frac{V_0}{k_f R} \tag{2.3}$$

Where V_0 is the voltage applied to the tip, R is the tip radius, k_f is the field factor which accounts for tip shape (not perfectly hemispherical) and electrostatic environment around the tip [27] and varies linearly with the shank angle of the tip [28]. k_f ranges from 2 to 8 [29]. Thus for very sharp tips (i.e. low R value) even few kV of voltage can produce a very high electric field. As CIGSe is a semiconductor, laser pulses are used to trigger field evaporation which is termed as laser assisted field evaporation.

Laser assisted field evaporation

Figure 2.15 shows different pulsing modes, i.e. one may increase field by tension pulses and the other one may increase temperature via laser pulses for successful field evaporation.

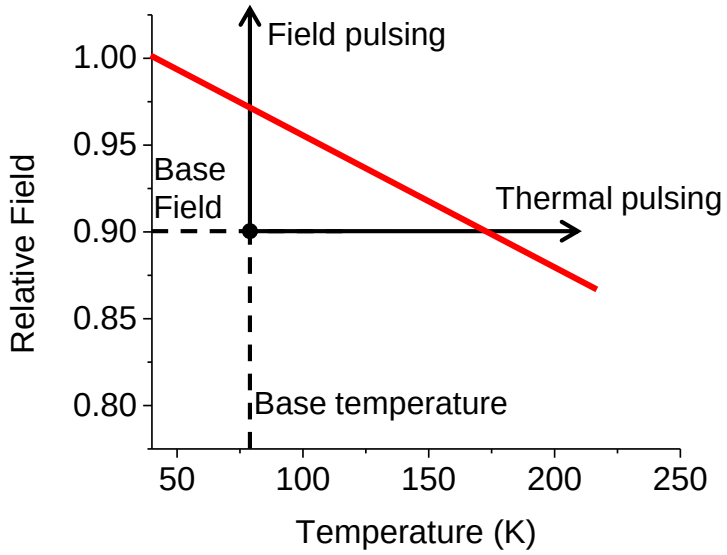

Figure 2.15: Two different modes of pulsing (field and thermal) to trigger field evaporation.

As the research here is focused on semiconductors, we discuss field evaporation mechanism triggered by laser pulses only. Laser pulses were first realized in 1970s to field evaporate specimens [31,32] and also semiconductors [33]. Potential energy diagram of ions are

modified under external electric field F making them more stable than atomic states in electric field. Field evaporation theories discussed in above section account activation energy "Q_n" required for field evaporation in case of metal and is given by [34] :

$$Q_n = \Lambda + \sum_n I_n - n\varphi_e - f(F) \quad \textbf{(2.4)}$$

Where Q = Desorption energy, Λ = sublimation energy, In= nth ionization energy, ϕ=work function, function *f(F)* is model specific. In metals, Fermi energy is very close to conduction electrons. Atoms at high electric field are subjected to laser pulses, laser energy is absorbed directly by electrons and subsequent relaxations to lattice atoms as thermal vibrations lead to successful ejection of surface atoms. Hence it is mostly believed that laser pulses act as pure thermal pulse to desorb atoms from surface of tip for metals [35, 36]. However in case of semiconductors Fermi energy level lies between valence band and conduction band, hence laser energy does not convert directly to thermal energy. Because of forbidden energy bands present in semiconductors, laser assisted field evaporation mechanism is more complicated when compared to metals [34]. Studies show that field evaporation of semiconductors depends strongly on band gap of material and properties of laser used. Previous studies were mostly based on Silicon due to its pure form, availability and large applications in photovoltaics and microelectronics industries. Different regimes of laser assisted field evaporation in silicon are summarized below [34].

1) Photoionization regime

Atoms residing on surface can absorb a photon to excite electrons from valence band to conduction band leading to eventual ionization. Hence surface atoms may evaporate by photoionization with evaporation rate proportional to ionization rate and hence laser intensity. Rate of evaporation was found linearly related to laser intensity for laser energy near to semiconductor's band gap [37]. However for energies above band gap a non-linear behavior was observed by Kellogg and Tsong [35] which may be due to multi excitation process.

2) Fast and slow evaporation regimes

Thermally assisted field evaporation is shown to dominate over photoionization for high laser intensities [34]. For high laser intensities and high photon energy Si shows very fast evaporation and a slow evaporation due to delayed induction from rest of the tip. As shown in

Figure 2.16a changing wavelength does not affect the fast evaporation peak but duration of slow evaporation [38].

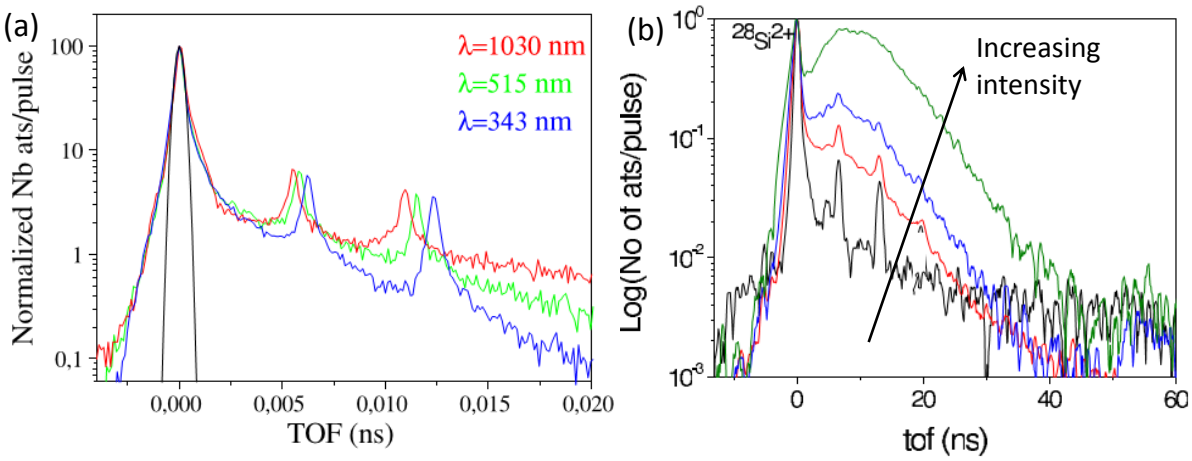

Figure 2.16: (a) Mass spectrum of Si^{2+} for different laser wavelengths source: [34] (b) Mass spectrum of Si^{2+} for IR laser at different laser intensities, Image courtesy: Ref. [38].

Delayed (slow) evaporation is also observed at lower photon energies (than material's direct band gap) and high laser intensities as shown in Figure 2.16b. This is mainly due to heating of tip far from tip apex and subsequent thermal induction towards apex after several nanoseconds. In a pulsed laser atom probe, thermal activation is the triggering process of field evaporation. High electric field and laser impulsions on the tip apex cause thermal agitation at the tip surface making them to vibrate and eventually leave the surface.

Component of this vibration normal to the surface has a frequency ν, ($\nu_0 \approx 10^{12}$ to 10^{13} Hz and is temperature dependent [39] playing a significant role in field evaporation. Evaporation rate (K_n) is given as:

$$K_n = \nu \cdot e^{\frac{-Q_n}{k_B T}} \tag{2.5}$$

Where k_B is the Boltzmann constant, Q_n is the activation energy and T is temperature of the specimen.

At present, direct calculation of evaporation rate from the specimen is not possible however we can measure detection rate in number of atoms per pulses. Detection rate $\phi_{detection}$ is given by:

$$\phi_{detection} = \eta . N_{at} . e^{\frac{-Q(F)}{k_B T}} \tag{2.6}$$

Where, η is detection efficiency (0.63 for LAWATAP), Q(F) is the field dependent height barrier, N_{at} is the number of imaged surface atoms. From equation (2.5) and (2.6) we can

deduce that temperature and field dependent height barrier are key parameters deciding field evaporation. Higher temperature and low field barrier leads to increased evaporation. Thus parameters like temperature of the specimen, laser power must be optimized while performing atom probe experiment to obtain reliable results. Otherwise it may result in: Preferential retention or preferential evaporation as explained in Figure 2.17 for two different elements (A and B) with different evaporation fields (F_A and F_B) present in a sample. Black dots at point 1 and point 2 represent setting of field and temperature at which evaporation has to be controlled by controlling laser pulse. As laser pulse induce thermal impulsions it causes rise in temperature hence the arrows are shown horizontal. Traversing through right of the F-T diagram leads to field evaporation of the respective specie. At point 1 none of the specie evaporates, after applying laser pulse it can be noticed that evaporation rate of B would be considerably higher than that of A leading to preferential retention of A. At point 2, field is high enough to evaporate specie B without laser impulsions which causes evaporation of specie B between laser pulses and hence is not controlled. This leads to underestimation of amount of specie B, this scenario is preferential evaporation of specie B.

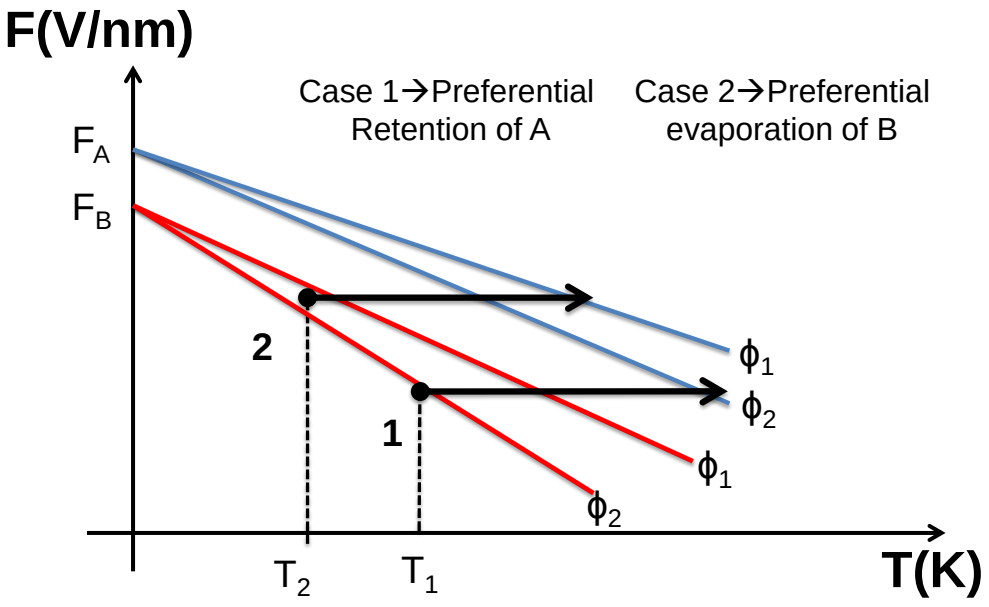

Figure 2.17: Electric field versus temperature (F-T) diagram for a compound having two elements A and B. ϕ_1 and ϕ_2 are evaporation rates of A and B. F_A and F_B represent evaporation field of A and B species. Two different scenarios are shown: 1: preferential retention of A and 2: preferential evaporation of B.

Length of the arrow in Figure 2.17 is determined by laser power. To uniformly evaporate all species present in the sample, laser power and specimen temperature must be optimized.

Laser power and temperature are optimized for CIGSe to obtain uniform evaporation of all the specie present in CIGSe, which is described in next chapter.

a) Identification of atoms: Mass-charge ratio

One of the major features that distinguish APT from FIM is the calculation of mass to charge ratio using time-of-flight (t) mass spectrometry. Time-of-flight here is the time travelled by an ion from surface (at the application of laser pulse) of the tip to the micro-channel plates. The mass to charge ratio (m/n) can be calculated using energy conservation and assuming constant velocity throughout the course of travel. Potential energy of ion at the tip is converted to kinetic energy:

$$mv^2/_2 = ne(V_{dc}) \quad \textbf{(2.7)}$$

$$\frac{m}{n} = 2e(V_{dc}) \times \left(\frac{t}{L}\right)^2 \quad \textbf{(2.8)}$$

Where m and n are the mass and ion charge state of the ion respectively, e is charge of single electron, L is the length of flight, V_{dc} is applied voltage and v is velocity which is ratio of length of flight to time of flight.

The above equation applies to atom probes utilizing laser pulse to field evaporate atoms. In case of electrical pulse atom probe, total $V=V_{dc}+V_{pulse}$ where V_{pulse} is voltage due to electrical pulses. Here we use only equation (2.8) as we deal with laser pulses only to analyze semiconductors. Figure 2.18 represents a typical mass spectrum of CIGSe obtained after a successful APT analysis. As flight length is specific to atom probe and already known (in this case 10 cm) mass spectrum obtained only depends on time of flight of ions. As each of the elements (Cu, In, Ga, Se) have specific mass, time of flight of each element is different and specific following equation (2.8). As Cu has two isotopes with mass 63 a.m.u. and 65 a.m.u., peaks corresponding to 63 and 65 are visible in mass spectrum. In Figure 2.18 certain peaks are detected corresponding to multiply charged ions, that is n=2 following equation (2.8). Hence doubly charged Cu ions are detected at 31.5 and 32.5 respectively. Also certain elements may evaporate together from tip apex and appears in the mass spectrum as molecular ions. For example $CuSe^+$ ions are detected at positions corresponding to sum of the masses of the two elements.

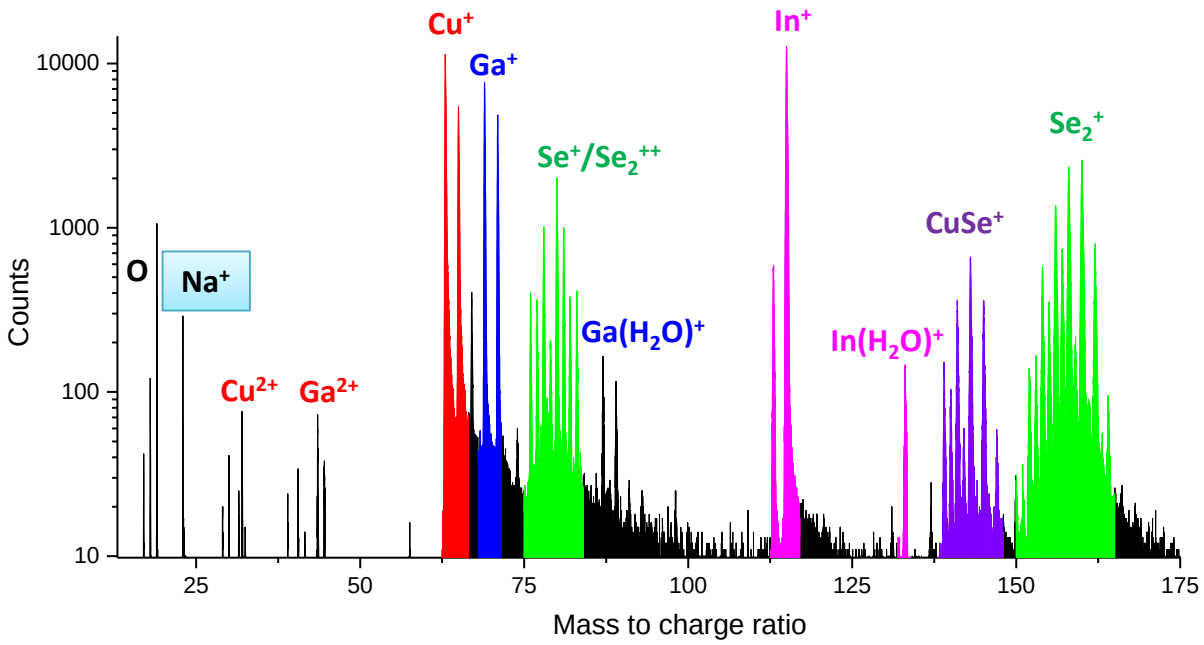

Figure 2.18: A typical mass spectrum of CIGSe (x=0.36). Left axis represents number of detected counts and bottom axis represents mass to charge ratio corresponding to detected ions. Chemical identity of ions detected corresponding to respective peaks is shown.

b) Magnification in APT and Trajectory of ions

To distinguish individual atoms it is necessary to magnify the surface of the specimen around million times, thus inventing an optical microscope of such capacity was impossible. Atoms are evaporated and XY position hits are recorded on detector. These hits on detector are their hit positions on detector and of course not the positions on the specimen itself. Hence determination of atomic distribution in the sample requires a projection formula using which we can back calculate the position of atoms from the XY distribution data obtained from the detector. A schematic diagram of ion trajectories during/after evaporation is shown in Figure 2.19.

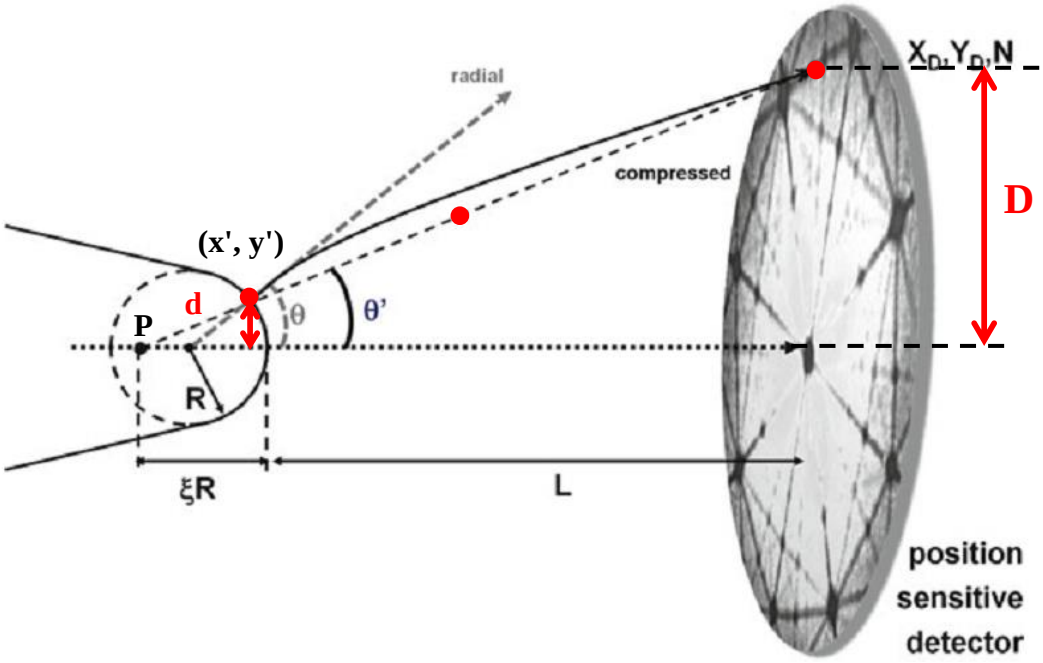

Figure 2.19: Schematic view of ion trajectory in an atom probe experiment. Image courtesy: Gault et.al. [40]

As illustrated in the figure, the calculation of ion trajectories involves knowledge of the tip radius, distance between the tip and detector, curvature of tip. Red dot shown in the figure is the atom evaporated from the specimen tip surface at position (x',y') and detected on detector at position (x,y). Θ' is the observed angle between the tip axis and the line joining (X_D, Y_D) and (x',y'), Θ is the angle between the tip axis and the line joining center of tip circle and (x',y'). As can be seen from the figure, if we extrapolate the line joining (X_D, Y_D) and (x',y') to the tip axis, it intersects at point P which is the projection point and is same for all other trajectories.

Using the point projection model, the compression factor and magnification can be calculated and are equal to [40]:

$$\xi \approx \frac{\theta}{\theta'} \tag{2.9}$$

$$M_{proj} = \frac{D}{d} \approx \frac{L}{\xi R} = \frac{L}{(m+1)R} \tag{2.10}$$

Using this magnification formula, back calculation and distribution of atoms on the tip surface is possible.

c) Depth coordinates calculation:

As APT tip is evaporated atom by atom, layer by layer, the surface of tip is continuously moved farther from detector. Third dimension of reconstruction use this evaporation sequence and assigns a depth $z^{(i)}$ for the i^{th} detected ion which follows below relation:

$$z^{(i+1)} = z^{(i)} + dz \tag{2.8}$$

Where dz is incremental shift and can be calculated using total analyzed volume which equals sum of individual volume (Ω_i) of all ions.

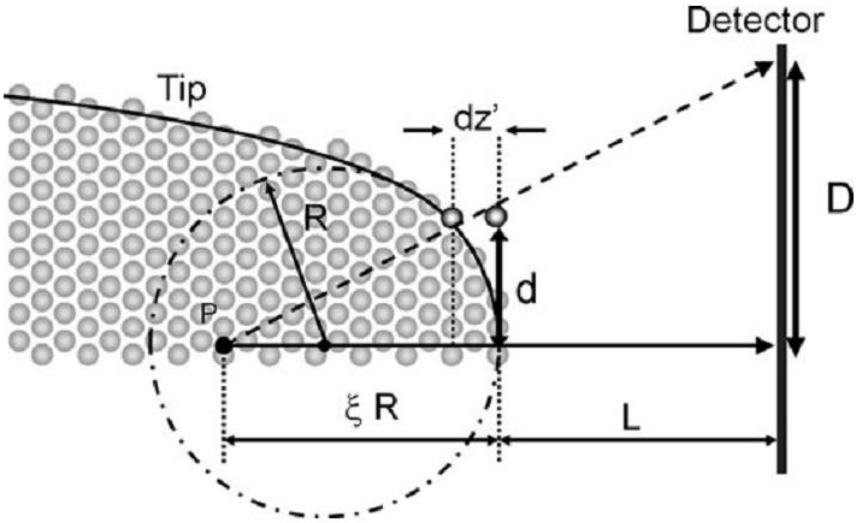

Figure 2.20: Depth coordinate model according to Bas et.al. protocol. Image courtesy Gault et.al [40].

dz can hence be calculated as:

$$dz = \frac{\Omega}{\eta w_v(z)} \tag{2.9}$$

Where η is the detection efficiency and $W_v(z)$ is a function relating the increase in analyzed volume with depth and various methods are available calculating this function. Different approaches can be used to reconstruct volume in three dimensions which include: 1) Using SEM image of tip before analysis, 2) Using radius and shank angle of tip, 3) using E_{Beta} value of material i.e. voltage required to maintain fixed flux at specific radius, 4) using Local magnification by known ratio $(M_{proj} +1)/E_\beta$. A summary of the latter can be found in ref. 29–33. Thanks to GPM 3Dsoft reconstruction software which makes this tedious process quite easy and displays atomic distribution on the surface and also reconstructs it in third dimension depicting full information about the specimen.

Functioning of APT requires preparation of specimen in form of a very sharp tip which is of outmost importance since it defines the properties of the microscope. Hence specific procedures have been developed concerning sample preparation.

2.5.3 Sample preparation techniques for atom probe: FIB lift out

Electrochemical polishing is generally used for metallic specimens to chemically etch and sharpen tips. For semiconductors this method usually fails and we use FIB to prepare location specific atom probe tips.

a) Standard lift out procedure

Standard lift out technique is described in Miller et.al [46] using dual beam FIB. Using this technique tips are prepared perpendicular to the substrate as illustrated in Figure 2.21. This technique is best to analyze layers or interfaces parallel to substrate, for example CdS-CIGSe interfaces in this case. As grains of CIGSe are columnar in nature as shown in Figure 2.21, this technique is not the best to analyze GBs in this case. Preparing tips perpendicular to substrate reduce chance of observing GBs. Instead tips prepared in transverse direction i.e. parallel to substrate increase possibility to detect GBs because of columnar nature.

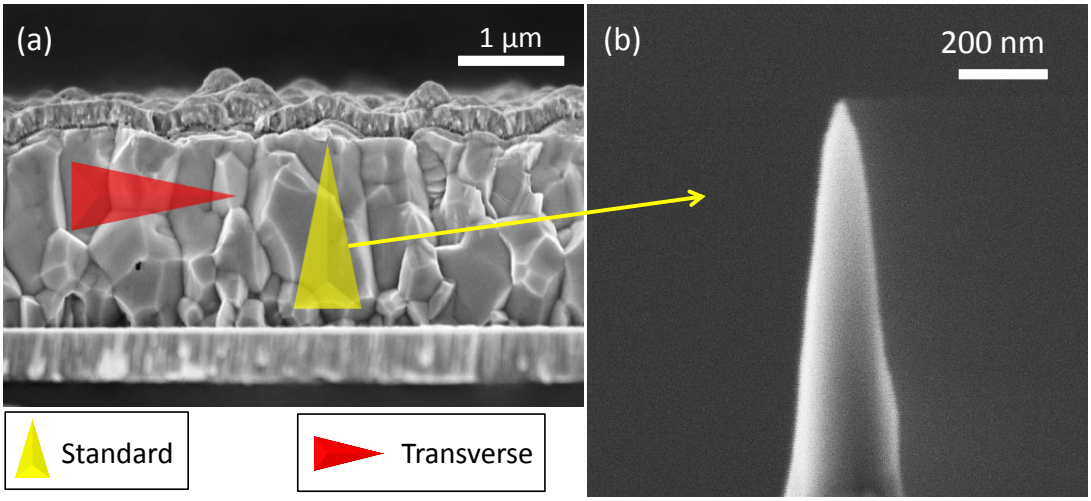

Figure 2.21: (a) SEM cross section of CIGSe and approximate location of an APT tip for standard lift out method and for transverse method (b) An APT tip prepared by Std. lift-out

b) Transverse lift out procedure

Chance to detect GBs in atom probe is more in this case using transverse lift-out technique. GBs observed here are usually normal to analysis direction in APT due to columnar nature of

grains. Also GBs normal to analysis direction is shown to give better results as studied by Blavette et.al [47]. Tips prepared using this method are prepared parallel to substrate and requires special preparation techniques described here. Figure 2.22 shows series of images captured during transverse lift out procedure and is explained using figure as follows:

a) (SEM view) A thin Platinum (Pt) layer is deposited (15 µm × 2 µm) with Pt-carbon composite gas using GIS (gas injection system) on top of CIGSe at 30keV,150pA and milled sideways using high Ga currents (6.5nA 30keV), resulting in formation of CIGSe lamella. Bottom of the lamella is milled subsequently (Mo/glass substrate in this case) to detach from substrate. Right side of the lamella is milled as shown.

b) (FIB view) micromanipulator is welded with Pt-carbon composite gas using GIS towards right side of lamella. Left side is now milled. CIGSe lamella is now only attached with micromanipulator and lifted upwards (downwards according to figure shown). In next step CIGSe material is removed from chamber and is replaced by chemically polished and sharpened Tungsten (W) tip in a horizontal SEM-tip holder.

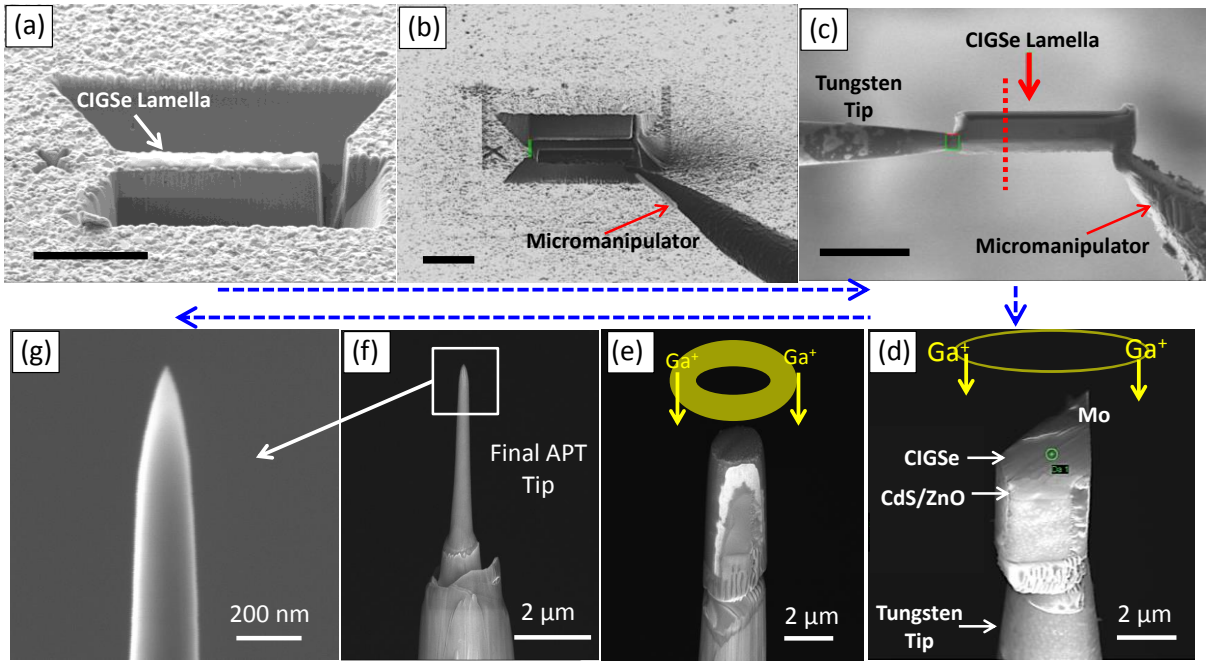

Figure 2.22: (a-g) SEM/FIB images captured during transverse lift-out. Scale bars in black are 10 µm in width.

c) (FIB view) Apex of W tip is cleaned at some angles by milling at high Ga currents (6.5nA 30keV) up to 2µm width. W tips is then welded using Pt-C on left side and 3-5

μm of lamella is cut as shown in fig c resulting in formation of a chunk. Rest of the lamella may be used in repeating this process and making further chunks.

d) (SEM view) Prepared chunk is positioned parallel to FIB gun. Different layers are identified in SEM due to difference in contrast as shown in fig d. Annular milling is then performed using feature mill option in FIB. Green circle in center of chunk represent approximate and desired region of interest of tip location. Chunk is milled annularly keeping green circle as center as shown. Initial steps involve higher probe current milling (30 keV, 700 pA).
e) After first few steps of annular milling tip shapes in cone-cylindrical shape as shown in fig e. Probe current is now decreased in order to reduce Ga contamination from sideways. Choice of probe current during this step: 30keV, 10 pA to 150 pA.
f) Steps of annular milling are stopped when apex radius is < 50 nm. As higher currents may have introduced Ga contamination final step involve cleaning of tip at low probe current and voltage (2keV 30 pA).
g) Cleaning of tip also makes tip in conical shape as shown in figure. Tip is then transferred to APT chamber and is now ready to be analyzed in atom probe. Final SEM image of tip is saved and is very useful to reconstruct data in 3D during post analysis.

Higher Ga currents used during tip preparation may also produce defects on tip, a typical case in CIGSe is formation of Cu agglomerates [48] due to reaction with Ga. Figure 2.23 represents a case in this study illustrating formation of Cu agglomerates at higher Ga currents (30 kV, 700 pA) which is cleaned at low Ga currents (2kV, 30 pA) to minimize FIB contamination.

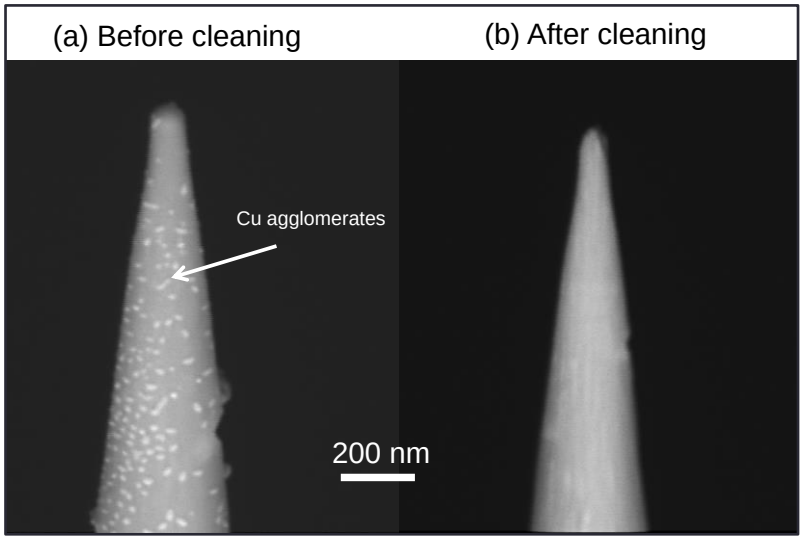

Figure 2.23: APT tip (a) before low Ga cleaning and (b) after low Ga cleaning (2kV, 30pA)

While preparing tip for atom probe, most of the FIB contamination is apparently on the side surface of the tip, whereas analyzed volume in APT comes only from middle region of the tip thus avoiding a large part of contaminated region. However Ga contamination may still exist which is essential to be identified. As CIGSe contains Ga and also Ga ions are used in FIB during tip preparation, the presence of Ga in CIGSe makes it impossible to determine Ga contamination from FIB. Hence tip preparation process is first optimized for a **NON** Ga sample ($CuInSe_2$).

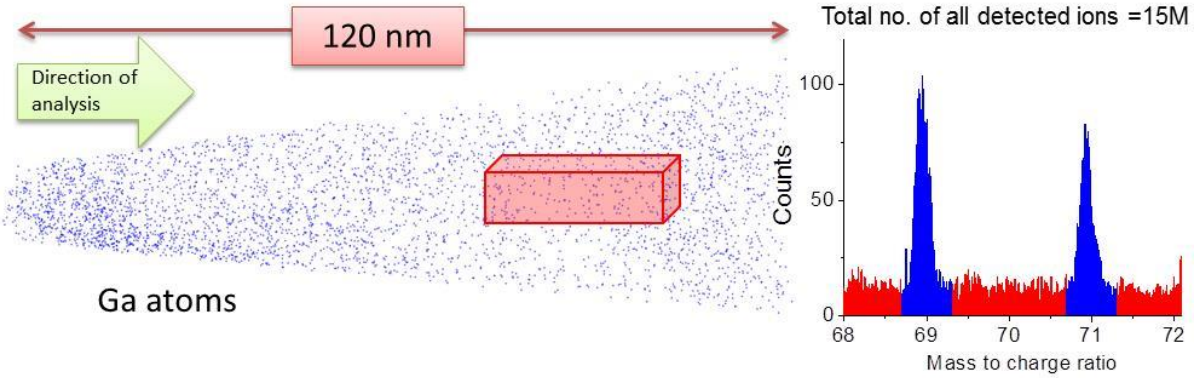

Figure 2.24: Reconstructed tip of CISe sample (left), and its mass spectra (right) showing mass range from 68 a.m.u. to 72 a.m.u. Ga atoms are shown blue in color and atomic counts in red region in mass spectrum correspond to background noise.

Ga atoms distribution in a reconstructed tip is shown in Figure 2.24. Ga contamination is very less as compared to analyzed volume and is mainly concentrated on top and side surface of the tip which is not accounted during quantitative analysis in all measurements. For example,

selected red region does not contain any Ga atoms and atoms visible are just due to noise background.

Conclusions

This chapter detailed growth processes of CIGSe thin films and other required layers, which are important in obtaining desired composition, structure and other properties of thin films. Principles and working of different techniques used in this work are discussed. As research performed here mainly deals with APT, principle of this technique was described in more details here. Starting from basic principles and history of APT, some aspects of APT were given in this chapter including theories of field evaporation, 3D reconstruction and appropriate specimen preparing techniques. Optimization of parameters, data treatment and use of this technique for CIGSe is described in upcoming chapters.

References

1. R. A. Mickelsen and W. S. Chen, "Development of a 9. 4% efficient thin-film CuInSe//2/CdS solar cell," in Proceedings of the 15th IEEE Photovoltaic Specialists Conference, pp. 800–804, 1981.

2. Liang H, Liu W, Lee S, Van Duren J, Franklin T, Patten M, Nijhawan S. High efficiency CIGSe solar cells by combinatorially sputtered Cu(In,Ga) followed by selenization. in *2012 38th IEEE Photovoltaic Specialists Conference (PVSC)*, 003102–003107. DOI: 10.1109/PVSC.2012.6318237

3. Kapur VK, Bansal A, Le P, Asensio OI. Non-vacuum processing of CuIn1−xGaxSe2 solar cells on rigid and flexible substrates using nanoparticle precursor inks. *Thin Solid Films* 2003; **431–432**: 53–57. DOI: 10.1016/S0040-6090(03)00253-0

4. Ma X, Liu D, Yang L, Zuo S, Zhou M. Molybdenum (Mo) back contacts for CIGS solar cells. in, 906814–906814–11. DOI: 10.1117/12.2053498

5. Wada T, Kohara N, Negami T, Nishitani M. Chemical and Structural Characterization of Cu(In,Ga)Se2/Mo Interface in Cu(In,Ga)Se2 Solar Cells. *Jpn J Appl Phys* 1996; **35**: L1253. DOI: 10.1143/JJAP.35.L1253

6. Kohara N, Nishiwaki S, Hashimoto Y, Negami T, Wada T. Electrical properties of the Cu(In,Ga)Se2/ MoSe2/Mo structure. *Solar Energy Materials and Solar Cells* 2001; **67**: 209–215. DOI: 10.1016/S0927-0248(00)00283-X

7. Jackson P, Hariskos D, Wuerz R, Kiowski O, Bauer A, Friedlmeier TM, Powalla M. Properties of Cu(In,Ga)Se2 solar cells with new record efficiencies up to 21.7%. *phys stat sol (RRL)* 2015; **9**: 28–31. DOI: 10.1002/pssr.201409520

8. Gabor AM, Tuttle JR, Albin DS, Contreras MA, Noufi R, Hermann AM. High-efficiency CuInxGa1−xSe2 solar cells made from (Inx,Ga1−x)2Se3 precursor films. *Applied Physics Letters* 1994; **65**: 198–200. DOI: doi:10.1063/1.112670

9. Chirilă A, Reinhard P, Pianezzi F, Bloesch P, Uhl AR, Fella C, Kranz L, Keller D, Gretener C, Hagendorfer H, et al. Potassium-induced surface modification of Cu(In,Ga)Se2 thin films for high-efficiency solar cells. *Nat Mater* 2013; **12**: 1107–1111. DOI: 10.1038/nmat3789

10. Herrmann D, Kratzert P, Weeke S, Zimmer M, Djordjevic-Reiss J, Hunger R, Lindberg P, Wallin E, Lundberg O, Stolt L. CIGS module manufacturing with high deposition rates and efficiencies. in *Photovoltaic Specialist Conference (PVSC), 2014 IEEE 40th*, 2775–2777. DOI: 10.1109/PVSC.2014.6925505

11. Lundberg O, Edoff M, Stolt L. The effect of Ga-grading in CIGS thin film solar cells. *Thin Solid Films* 2005; **480–481**: 520–525. DOI: 10.1016/j.tsf.2004.11.080

12. Wei S-H, Zunger A. Band offsets and optical bowings of chalcopyrites and Zn-based II-VI alloys. *Journal of Applied Physics* 1995; **78**: 3846–3856. DOI: doi:10.1063/1.359901

13. Kessler J, Chityuttakan C, Lu J, Schöldström J, Stolt L. Cu(In,Ga)Se2 thin films grown with a Cu-poor/rich/poor sequence: growth model and structural considerations. *Progress in Photovoltaics: Research and Applications* 2003; **11**: 319–331. DOI: 10.1002/pip.495

14. Kessler J, Scholdstrom J, Stolt L. Rapid Cu(In,Ga)Se2 growth using "end point detection". in *Conference Record of the Twenty-Eighth IEEE Photovoltaic Specialists Conference, 2000*, 509–512. DOI: 10.1109/PVSC.2000.915883

15. Barreau N, Painchaud T, Couzinié-Devy F, Arzel L, Kessler J. Recrystallization of CIGSe layers grown by three-step processes: A model based on grain boundary migration. *Acta Materialia* 2010; **58**: 5572–5577. DOI: 10.1016/j.actamat.2010.06.025

16. Nakada T, Kunioka A. Direct evidence of Cd diffusion into Cu(In, Ga)Se2 thin films during chemical-bath deposition process of CdS films. *Applied Physics Letters* 1999; **74**: 2444–2446. DOI: 10.1063/1.123875

17. Nakada T. Nano-structural investigations on Cd-doping into Cu(In,Ga)Se2 thin films by chemical bath deposition process. *Thin Solid Films* 2000; **361–362**: 346–352. DOI: 10.1016/S0040-6090(99)00767-1

18. Hiepko K, Bastek J, Schlesiger R, Schmitz G, Wuerz R, Stolwijk NA. Diffusion and incorporation of Cd in solar-grade Cu(In,Ga)Se2 layers. *Applied Physics Letters* 2011; **99**: 234101. DOI: 10.1063/1.3665036

19. Cojocaru-Mirédin O, Choi P, Wuerz R, Raabe D. Atomic-scale characterization of the CdS/CuInSe2 interface in thin-film solar cells. *Applied Physics Letters* 2011; **98**: 103504–103504–3. DOI: doi:10.1063/1.3560308

20. Hariskos D, Spiering S, Powalla M. Buffer layers in Cu(In,Ga)Se2 solar cells and modules. *Thin Solid Films* 2005; **480–481**: 99–109. DOI: 10.1016/j.tsf.2004.11.118

21. Giannuzzi LA, Stevie FA. *Introduction to focused ion beams: instrumentation, theory, techniques, and practice*. New York: Springer 2005;

22. Kelly TF, Miller MK. Atom probe tomography. *Review of Scientific Instruments* 2007; **78**: 031101–031101–20. DOI: doi:10.1063/1.2709758

23. Cerezo A, Godfrey TJ, Smith GDW. Application of a position-sensitive detector to atom probe microanalysis. *Review of Scientific Instruments* 1988; **59**: 862–866. DOI: 10.1063/1.1139794

24. Oberdorfer C, Stender P, Reinke C, Schmitz G. Laser-Assisted Atom Probe Tomography of Oxide Materials. *Microscopy and Microanalysis* 2007; **13**: 342–346. DOI: 10.1017/S1431927607070274

25. Deconihout B, Vurpillot F, Gault B, Da Costa G, Bouet M, Bostel A, Blavette D, Hideur A, Martel G, Brunel M. Toward a laser assisted wide-angle tomographic atom-probe. *Surf Interface Anal* 2007; **39**: 278–282. DOI: 10.1002/sia.2491

26. Da Costa G, Vurpillot F, Bostel A, Bouet M, Deconihout B. Design of a delay-line position-sensitive detector with improved performance. *Review of Scientific Instruments* 2004; **76**: 013304–013304–8. DOI: doi:10.1063/1.1829975

27. Gomer R, Swanson LW. Theory of Field Desorption. *The Journal of Chemical Physics* 1963; **38**: 1613–1629. DOI: doi:10.1063/1.1776932

28. Larson, D.J., Russell, K.F., Miller, M.K. Effect of specimen aspect ratio on the reconstruction of atom probe tomography data. *Microscopy and Microanalysis* 1995;930–1.

29. Mulvey T. Atom Probe Field Ion Microscopy M K Miller, A Cerezo, M G Hetherington and G D W Smith. *Measurement science & technology* 1997; **8**: 689.

30. Müller EW. Field Desorption. *Phys Rev* 1956; **102**: 618–624. DOI: 10.1103/PhysRev.102.618

31. Tsong TT, Block JH, Nagasaka M, Viswanathan B. Photon stimulated field ionization. *The Journal of Chemical Physics* 1976; **65**: 2469–2470. DOI: doi:10.1063/1.433338

32. Nishigaki S, Drachsel W, Block JH. Photon-induced field ionization mass spectrometry of ethylene on silver. *Surface Science* 1979; **87**: 389–409. DOI: 10.1016/0039-6028(79)90537-5

33. Viswanathan B, Drachsel W, Block JH, Tsong TT. Photon enhanced field ionization on semiconductor surfaces. *The Journal of Chemical Physics* 1979; **70**: 2582–2583. DOI: 10.1063/1.437726

34. Vella A. On the interaction of an ultra-fast laser with a nanometric tip by laser assisted atom probe tomography: A review. *Ultramicroscopy* 2013; **132**: 5–18. DOI: 10.1016/j.ultramic.2013.05.016

35. Kellogg GL, Tsong TT. Pulsed-laser atom-probe field-ion microscopy. *Journal of Applied Physics* 1980; **51**: 1184–1193. DOI: doi:10.1063/1.327686

36. Lee MJG, Reifenberger R, Robins ES, Lindenmayr HG. Thermally enhanced field emission from a laser-illuminated tungsten tip: temperature rise of tip. *Journal of Applied Physics* 1980; **51**: 4996–5006. DOI: 10.1063/1.328379

37. Mazumder B, Vella A, Gilbert M, Deconihout B, Schmitz G. Reneutralization time of surface silicon ions on a field emitter. *New Journal of Physics* 2010; **12**: 113029. DOI: 10.1088/1367-2630/12/11/113029

38. Mazumder B, Vella A, Vurpillot F, Martel G, Deconihout B. Surface carrier recombination of a silicon tip under high electric field. *Applied Physics Letters* 2010; **97**: 073104–073104–3. DOI: doi:10.1063/1.3473816

39. Kellogg GL. Measurement of activation energies for field evaporation of tungsten ions as a function of electric field. *Phys Rev B* 1984; **29**: 4304–4312. DOI: 10.1103/PhysRevB.29.4304

40. Gault B. *Atom probe microscopy*. New York: Springer 2012; Available at: http://dx.doi.org/10.1007/978-1-4614-3436-8 [Accessed August 20, 2013]

41. Gault B, Haley D, De Geuser F, Moody MP, Marquis EA, Larson DJ, Geiser BP. Advances in the reconstruction of atom probe tomography data. *Ultramicroscopy* 2011; **111**: 448–457. DOI: 10.1016/j.ultramic.2010.11.016

42. Gault B, Moody M, Marquis EA, De Geuser F, Geiser BP, Larson DJ, Kelly TF, Ringer SP, Smith GDW. Tomographic Reconstruction in Atom Probe Microscopy: Past, Present... Future? *Microscopy and Microanalysis* 2009; **15**: 10. DOI: 10.1017/S1431927609092988

43. Vurpillot F, Gault B, Geiser BP, Larson DJ. Reconstructing atom probe data: A review. *Ultramicroscopy* 2013; DOI: 10.1016/j.ultramic.2013.03.010

44. Blavette D, Sarrau JM, Bostel A, Gallot J. Direction et distance d'analyse à la sonde atomique. *Revue de Physique Appliquée* 1982; **17**: 435–440. DOI: 10.1051/rphysap:01982001707043500

45. Bas P, Bostel A, Deconihout B, Blavette D. A general protocol for the reconstruction of 3D atom probe data. *Applied Surface Science* 1995; **87–88**: 298–304. DOI: 10.1016/0169-4332(94)00561-3

46. Miller MK, Russell KF, Thompson GB. Strategies for fabricating atom probe specimens with a dual beam FIB. *Ultramicroscopy* 2005; **102**: 287–298. DOI: 10.1016/j.ultramic.2004.10.011

47. Blavette D, Duval P, Letellier L, Guttmann M. Atomic-scale APFIM and TEM investigation of grain boundary microchemistry in Astroloy nickel base superalloys. *Acta Materialia* 1996; **44**: 4995–5005. DOI: 10.1016/S1359-6454(96)00087-0

48. Abou-Ras D, Marsen B, Rissom T, Frost F, Schulz H, Bauer F, Efimova V, Hoffmann V, Eicke A. Enhancements in specimen preparation of Cu(In,Ga)(S,Se)2 thin films. *Micron* 2012; **43**: 470–474. DOI: 10.1016/j.micron.2011.11.004

3 Chapter Three: Characterization of $Cu(In,Ga)Se_2$ solar cells: Influence of Ga concentration

Both experimental and theoretical explanations of changes in device performance due to Ga addition in $CuInSe_2$ have been discussed in chapter 1. This chapter details our experimental research on the modifications in CIGSe microstructure and its performance with varying Ga concentration for cells prepared with CuPRO process. Electrical and microstructural characterization techniques discussed in the previous chapter are employed here to investigate modifications in CIGSe. Indeed, before moving on to atomic scale studies, it is important to know whether the desired CIGSe properties and composition, phase and structure are formed. In this chapter, we examine accurately the desired compositions, phase and grain structure of CIGSe.

3.1 Device performance as a function of Ga content

Due to modifications in the band gap value and other properties of CIGSe as a function of Ga content, variations in the device performance are expected. Variations in current voltage (J-V) and External Quantum Efficiency (EQE) measurements as a function of Ga content are presented here.

3.1.1 Current-Voltage measurements

Eight CIGSe cells with different Ga ratios (x=0.00, 0.17, 0.39, 0.47, 0.56, 0.67, 0.84, 1.00) are prepared by controlling Ga/In flux during co-evaporation. Compositions of CIGSe films were determined using EDX spectrum. Electrical measurements, J-V and EQE, were performed at IMN, University of Nantes under the supervision of Dr. Nicolas Barreau. J-V measurements were experimentally measured on cells at room temperature (25°C), with a cell surface area of 0.5 cm^2 and under the AM 1.5G solar spectrum. J-V measurements for cells with different x values (Ga ratio, from zero up to one) are presented in Figure 3.1. These curves clearly follow the J(V) equation under light illumination.

$$J(V) = J_0.\left[\exp\left(\frac{qV}{nkT}\right) - 1\right] - J_{photon} \quad \textbf{(3.1)}$$

J-V curves under light illumination vary significantly with light absorption properties of semiconductor. As discussed earlier, band gap strongly affects light absorption in semiconductor and is one of the important parameter to transform J-V curve via parameter

J_{photon}. As illustrated in Figure 3.1, significant variation in J-V curves with different x values (Ga content) is observed which is mainly due to band gap modulation. Intercepts on Y-axis (J) are currents observed at zero biased voltage which is J_{sc} (short circuit current) and vary as a function of x as shown in figure. Intercepts on X-axis are voltage observed at zero current and is called open circuit current (V_{oc}). From Figure 3.1 it can be noticed that up to x=0.47, V_{oc} is increasing and saturates for x above 0.47. All the values of J_{sc}, V_{oc}, FF (fill factor) and efficiency for different x values are summarized in Table 3-1.

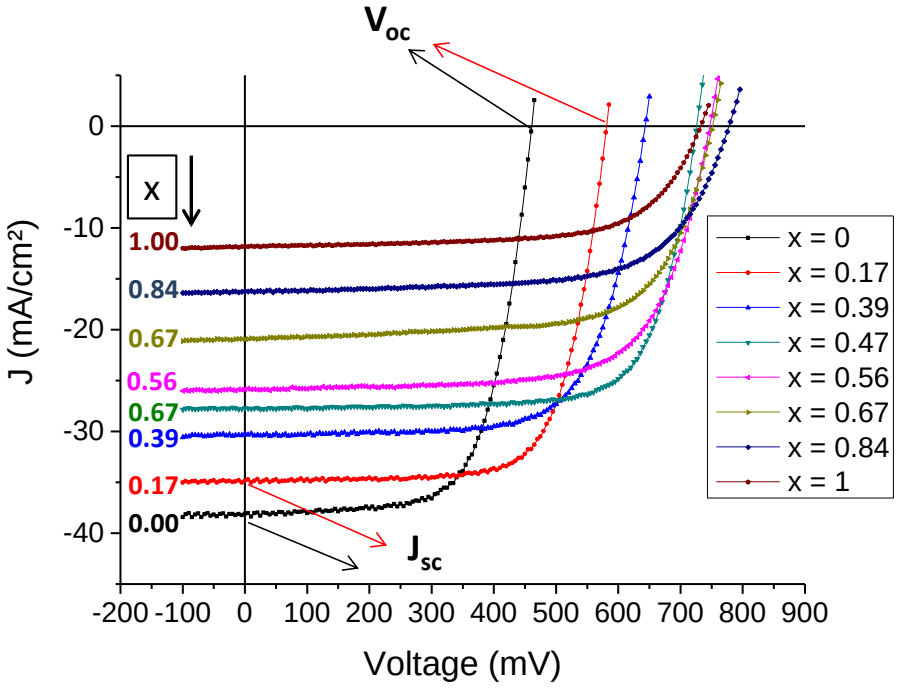

Figure 3.1: J-V curve for $Cu(In_{1-x}Ga_x)Se_2$ cells with different Ga ratios

Table 3-1: Representative photovoltaic parameters of prepared CIGSe cells with various Ga ratio 'x'.

x	E_g (eV)	V_{oc} [mV]	J_{sc} [mA/cm^2]	FF	Efficiency [%]
0.0	1.04	462	38.1	0.68	11.9
0.17	1.11	581	34.9	0.72	14.6
0.39	1.22	665	31.0	0.72	14.9
0.47	1.28	720	27.8	0.73	14.5
0.56	1.34	748	25.9	0.69	13.4
0.67	1.40	750	21.0	0.70	11.0
0.84	1.54	780	16.2	0.67	8.5
1	1.67	734	11.8	0.67	5.8

Under ideal conditions of band gap modulation (i.e. varying only band gap with no change in materials properties), J_{sc} varies with E_g [1] according to following relation as discussed in Singh et.al [2]:

$$J_{sc} = q \int_{h\nu=E_g}^{\infty} \frac{dN_{ph}}{dh\nu} d(h\nu) \quad \textbf{(3.2)}$$

Where N_{ph} is the photon flux and depends on illuminated spectral conditions, ν is the frequency of light. Following equation (2.1), an increase in band gap would lead to a decrease in J_{sc} as increasing band gap reduces amount of absorbed photons resulting a linear decrease in J_{sc} with band gap.

Figure 3.2 represents measured J_{sc} values as a function of x in $CuIn_{1-x}Ga_xSe_2$ compared with theoretical expectations [1]; A non-linear monotonic decrease in J_{sc} from x=0 to x=1 is observed which is consistent with equation (3.2). As experimental J_{sc} is consistent with theoretical expectations, we investigate next on variation in efficiency and V_{oc} with Ga content.

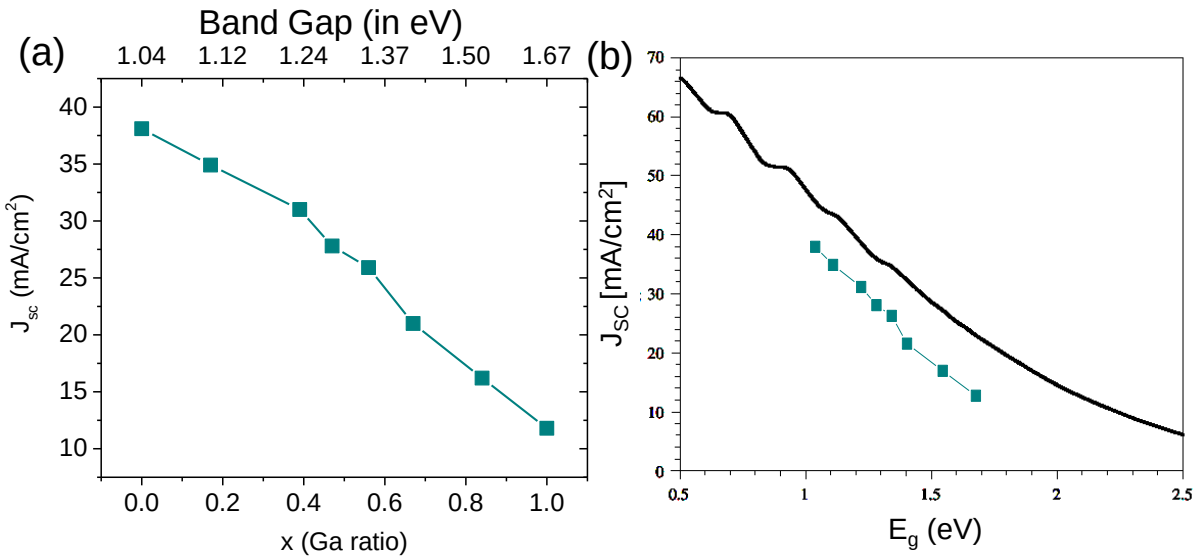

Figure 3.2: Variation of short circuit current (Jsc) as a function of Ga ratio 'x' in $CuIn_{1-x}Ga_xSe_2$ as (a) measured in this work and (b) compared with theoretical calculations in ref. [1]. Top axis represents band gap values of respective CIGSe composition.

The efficiency (η) can be extracted from J-V curve using equation (3.3) for various Ga concentrations, where J_FV_F represent current and voltage coordinate in JV curve corresponding to fill factor and P_{in} is input power equal to 100 mW/cm^2.

$$\eta = \frac{J_F V_F}{P_{in}} \quad \textbf{(3.3)}$$

Variation of η as a function of band gap (Ga content) is plotted in Figure 3.3(a) obtained in this work for CIGSe samples and compared with theoretical expectations in Figure 3.3(b) from refs [1,3,4]. All three theoretical models presented in Figure 3.3(b) predict maximum efficiency for band gap (E_g) = 1.4 eV. However, experimentally observed efficiency of the device increases with band gap till E_g = 1.2 eV (x=0.4) and then a drop in efficiency is observed till E_g = 1.67 eV (x=1.0). Some changes at atomic or microstructural level are expected behind this deviation in observed efficiency. Study in this research is dedicated to explain possible reasons behind this deviation.

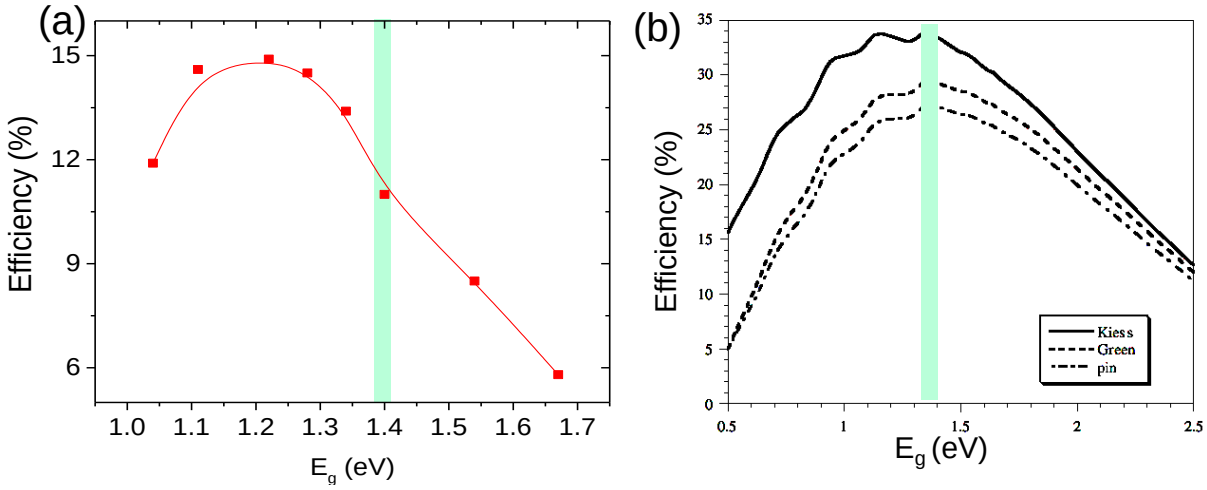

Figure 3.3: (a) Efficiency obtained in this work as a function of band gap for CIGSe samples (b) theoretical calculations performed for calculation of efficiency as a function of band gap in refs. [1,3,4]. Highlighted region (green) indicate maximum efficiency theoretically predicted in all the models.

Figure 3.4 represent efficiency of CIGSe for various band gaps (Ga ratio) obtained in this work (on CuPRO process synthesized samples) compared with observations made by other groups (3-stage processed samples) summarized in Contreras et.al [5]. Results obtained in this work are consistent with observations obtained by other groups and similar variations in efficiency are observed as a function of band gap. In all the cases, efficiency of the device increases with band gap till $E_g \approx$ 1.2-1.3 eV and then a drop in the efficiency is observed for wider band gaps. It can also be noted that efficiency observed in this work is relatively less when compared to other groups and is mainly due to CuPRO process employed in this work. CuPRO process produces CIGSe thin films with no Ga gradient and hence produces less efficient cells due to absence in electric field in QNR as described in chapter 2. Indeed, it is remarkable to note that the variation in efficiency as a function of band gap is not dependent on the synthesis process.

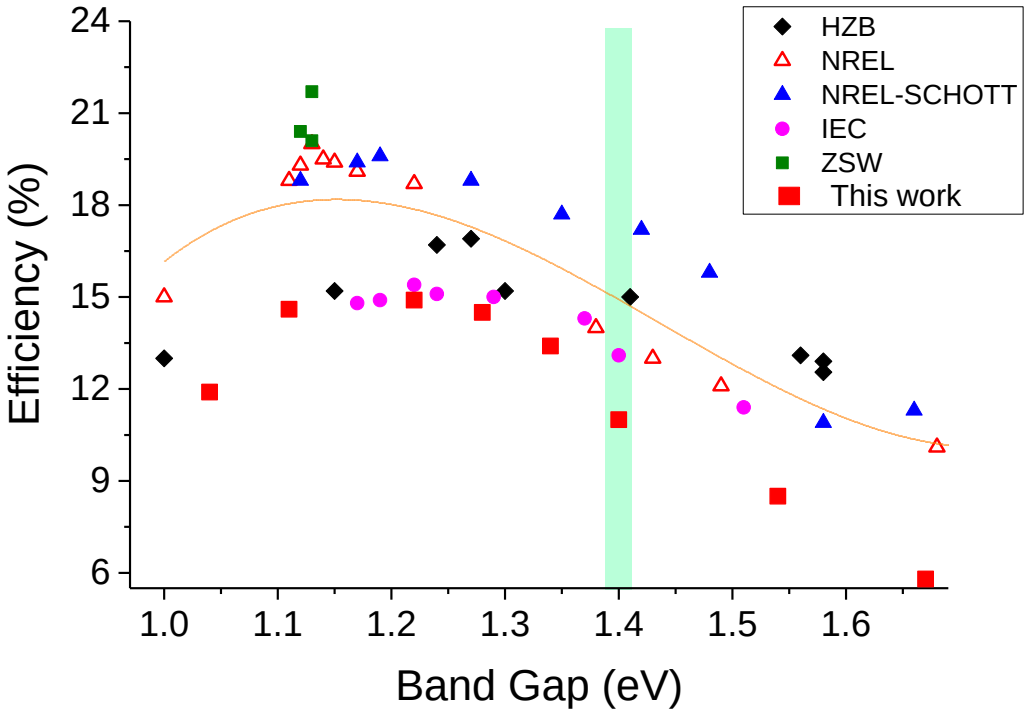

Figure 3.4: Efficiency (η) versus band gap for CuPRO processed CIGSe samples studied in this work (red squares), and compared with results obtained by other groups (on 3-stage process samples). Highlighted regions (green) correspond to expected theoretical efficiency. Results from other groups are adapted from following refs. NREL-SCHOTT, [Contreras et al. 2005], IEC [Shafarman et al. 1996], [Hanket et al. 2009], ZSW [Jackson et al. 2011] [Jackson et al. 2015], HZB [Eisenbarth et al. 2009], HZB [Merdes et al. 2011]. Refs: [5–11]

As the variation of J_{sc} with x is consistent with theoretical expectations, reasons for the decrease in efficiency are expected to be due to limitations in V_{OC}. V_{OC} varies with E_g as:

$$V_{oc} = \frac{E_g}{q} - \frac{nkT}{q}\ln\left(\frac{J_{sc}}{J_0}\right) \qquad \textbf{(3.4)}$$

Figure 3.5 represents the observed variation in V_{OC} as a function of the Ga content (x) and is compared to the theoretical expectations developed for band gap increment according to equation (3.4). Here, assumptions for theoretical curve are: ideal *pn* junction with ideality factor n=1, 25°C temperature (kT= 25meV), n=1. Variation in V_{OC} for low x values follows expectations (blue dot) and increases with x till x=0.4. However after this threshold value, V_{OC} deviates from the theoretical curve and saturates for high 'x' values. For x=0.67, deviation in V_{oc} from theory is 136 mV and the deviation increases till 400 mV for x=1.0.

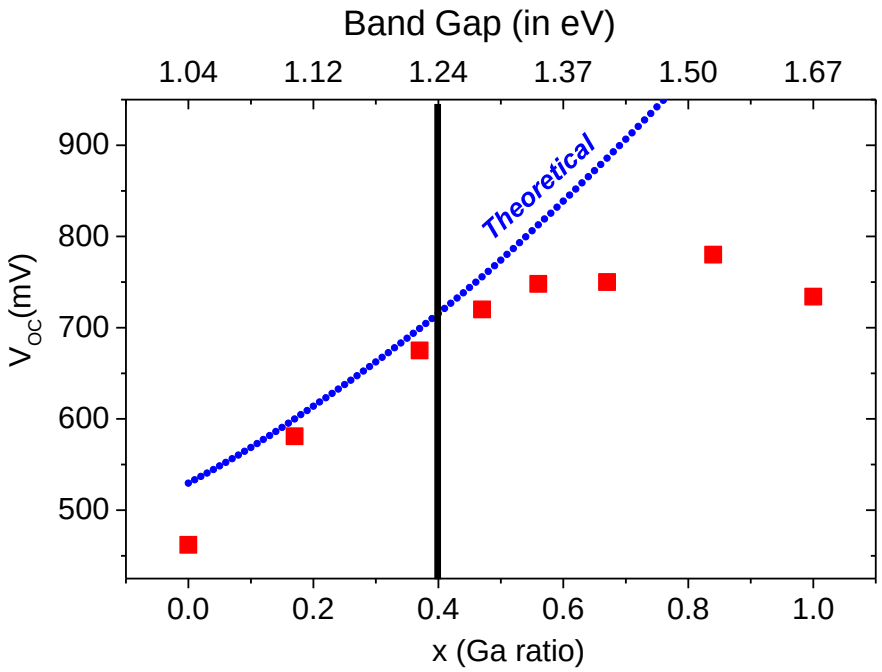

Figure 3.5: Theoretical Voc (blue) and Observed Voc (red) versus Ga ratio 'x' in $CuIn_{1-x}Ga_xSe_2$. Line at x=0.4 represent emergence of deviation of observed Voc from theoretical calculations.

It is satisfying to note that variation in V_{OC} observed here as a function of x is consistent with findings observed by other groups as represented in Figure 3.6. Figure 3.6 represents variation of V_{oc} as a function of band gap measured in references [5–11] on 3-stage processed CIGSe samples. CuPRO process has been used in present work and shows consistency with results obtained by other groups. An apparent behavior of Voc with band gap is shown in the figure which shows deviation in Voc after band gap ≈1.28 eV. It can be observed that regardless of the deposition processes used, Voc deviates after this band gap. These deviations from theoretical predictions must be due to changes in microstructure, grains, grain boundaries, interfaces or other factors.

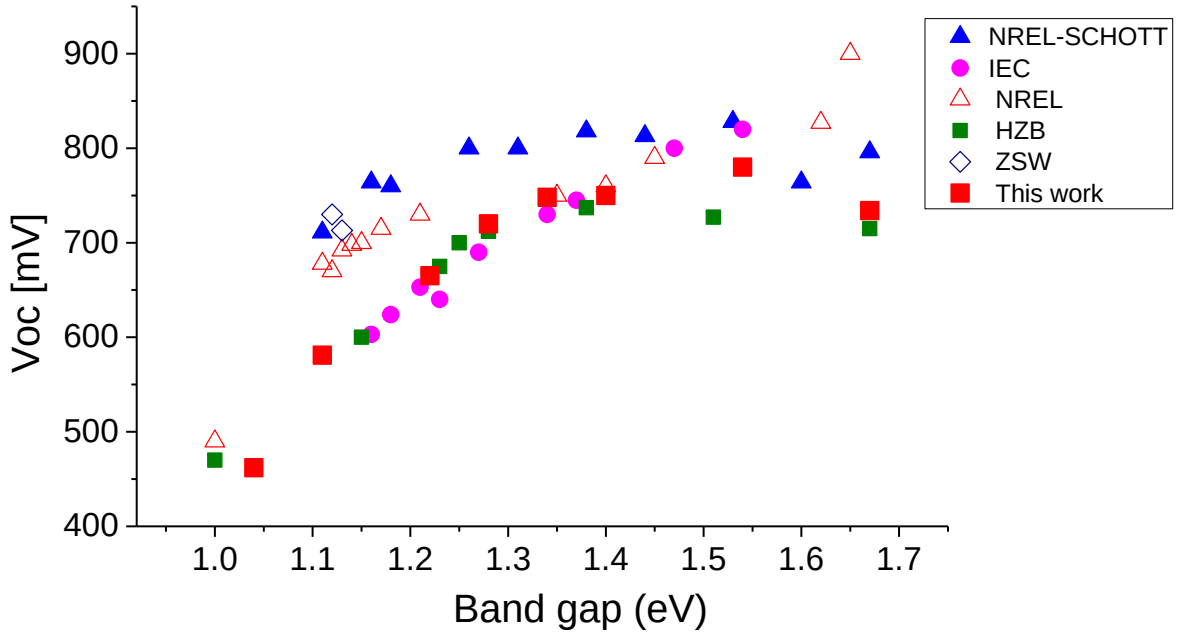

Figure 3.6: Voc as a function of band gap measured in this work (red square) from CuPRO processed samples is compared with results obtained by other groups on 3-stage process. Apparent pattern of Voc is a guide for eye. Data adapted from Contreras et.al [5]. Results from other groups are adapted from following refs. NREL-SCHOTT, [Contreras et al. 2005], IEC [Shafarman et al. 1996], [Hanket et al. 2009], ZSW [Jackson et al. 2011] [Jackson et al. 2015], HZB [Eisenbarth et al. 2009], HZB [Merdes et al. 2011]. Refs: [5–11]

These results presented here are performed on AM 1.5G incoming radiation consisting of majority of all wavelengths received on earth's atmosphere. However understanding the cell performance at specific wavelengths could be beneficial in order to improve cells by measuring their quantum efficiency. This will be discussed in the next section.

3.1.2 External Quantum Efficiency

As Ga addition in $CuInSe_2$ induces significant changes in band gap, major changes in QE are expected. EQE is measured for CIGSe cells with different x and is presented in Figure 3.7. As solar cells do not absorb incoming radiations with energy below optical band gap of its respective semiconductor, EQE of CIGSe with different 'x' would be significantly different due to variation in their band gap. Poor EQE in ultra-violet region is due to absorption followed by strong recombination in ZnO front layer. In the visible region at wavelengths around 512 nm, a small hump is observed which correspond to CdS band gap (2.42 eV) and indicates maximum absorption in CdS layer in this regime. Due to the increase in band gap from x=0 (1.04 eV) to x=1 (1.67 eV), tail of the EQE curve is blue shifted with increasing x as expected. In visible wavelength region from 500 nm to 700 nm, Ga poor cells have high

EQE (close to 0.90), representing better conversion efficiency of Ga poor cells within their respective domains of band gap. In ideal case of band gap modulation (i.e. change in band gap with no change in other parameters of the material), the region within domain of absorber band gaps must provide high QE even for Ga rich cells.

As can be noticed from Figure 3.7, a systematic decline in EQE is observed as a function of x for high Ga samples, i.e. a significant decrease in QE is observed for cells with x above 0.5, which means increased recombination of electrons and holes in CIGSe for Ga rich cells.

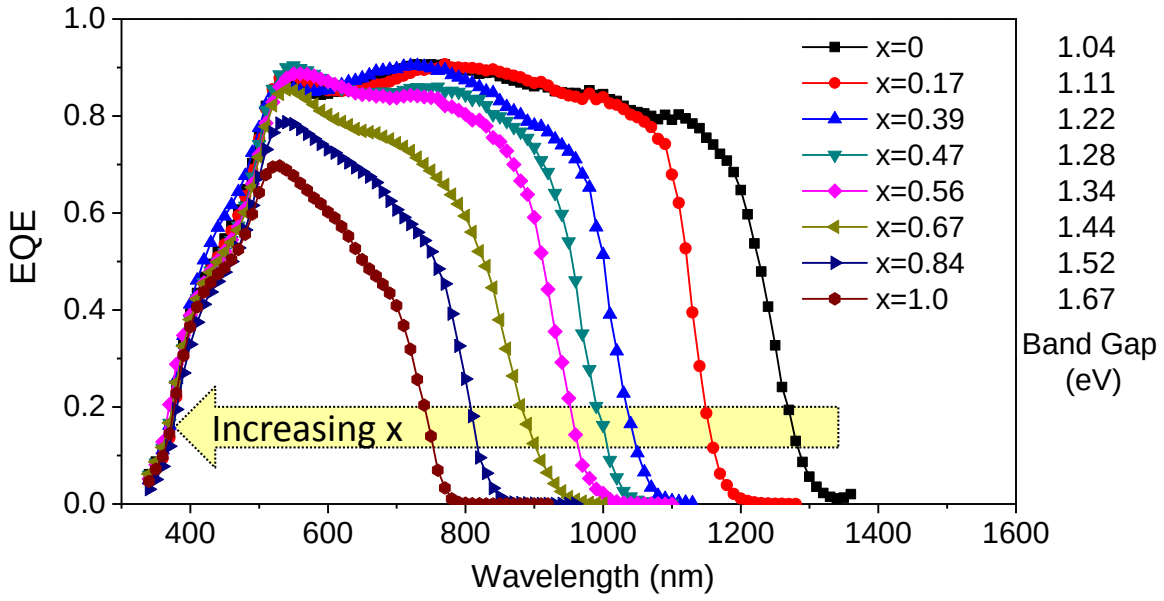

Figure 3.7: External Quantum efficiency for Cu($In_{1-x}Ga_xSe_2$) cells with different x (Ga ratio), small arrows on each curve indicate their respective band gap values which are listed on right.

For example, considering EQE curve for x=1.0 having band gap E_g=1.67ev (λ=742nm), EQE is less than 0.7 between wavelengths 520 nm (above CdS) and 742 nm. However Ga poor cells exhibited high EQE (≈0.9) demonstrating lower 'photon to carrier conversion' for Ga rich CIGSe cells. It can be noticed that decline in EQE in wavelength region 520 nm to 742 nm is observed for x higher than 0.5 which explains degradation in J-V curve for Ga rich cells.

Hence it is important to investigate changes in the material at atomic and microstructural level to identify factors limiting the efficiency and performance of the cells, finding which one can enhance and improve cells. Deviation in device performance may arise from formation of undesired phase in thin films. Hence we use XRD to confirm formation of same phase for cells prepared with various Ga contents.

3.2 X-Ray diffraction studies for different x in $CuIn_{1-x}Ga_xSe_2$

XRD measurements are used to identify the formation of desired phases, as the presence of an undesired phase may change properties of CIGSe. XRD measurements were performed on all CIGSe cells using X-rays produced by Cu Kα radiation (wavelength=0.15406 nm) at atmospheric pressure and room temperature. Samples were scanned from θ to 2θ angles (Bragg mode) and patterns from 2θ = 25° to 55° are shown for five CIGSe samples to demonstrate evident trend in XRD spectrum in Figure 3.8a. for Ga ratios x=0, 0.17, 0.39, 0.84, 1.0 processed using CuPRO method. Major peaks corresponding to different atomic planes are shown in the figure and peaks corresponding to lattice planes identified are [112], [211], [204]-[220], [116]-[312].

Peaks at 40.4 degrees are observed for all cells which correspond to Mo back contact and is obviously same for all cells as similar conditions were used to deposit Mo on glass substrate to serve as back contact. A systematic shift of [112] peak and [204] [220] doublet peak towards higher angles is observed for higher 'x' samples. This mainly arises due to change in relative Ga content. Indeed peaks are shifted towards higher angles due to the decrease in lattice constants with Ga content following Bragg's law (equation 2.1). As atomic radius of Ga is smaller than In, Ga rich cells have lower values of lattice constant, hence lattice spacing is reduced in Ga rich samples leading to diffraction peak shift towards higher angles.

Figure 3.8b represents a typical XRD pattern obtained by Kodigala et.al [12] for CIGSe samples with x=0.0 and x=0.25 prepared using 3-stage co-evaporation process. XRD diffraction diagram observed here are compared with results from Kodigala et.al [12] . In this work they show that samples are formed of a single chalcopyrite phase. It can be noticed from XRD patterns of different samples that a single chalcopyrite CIGSe phase exists for all samples with their respective overall composition.

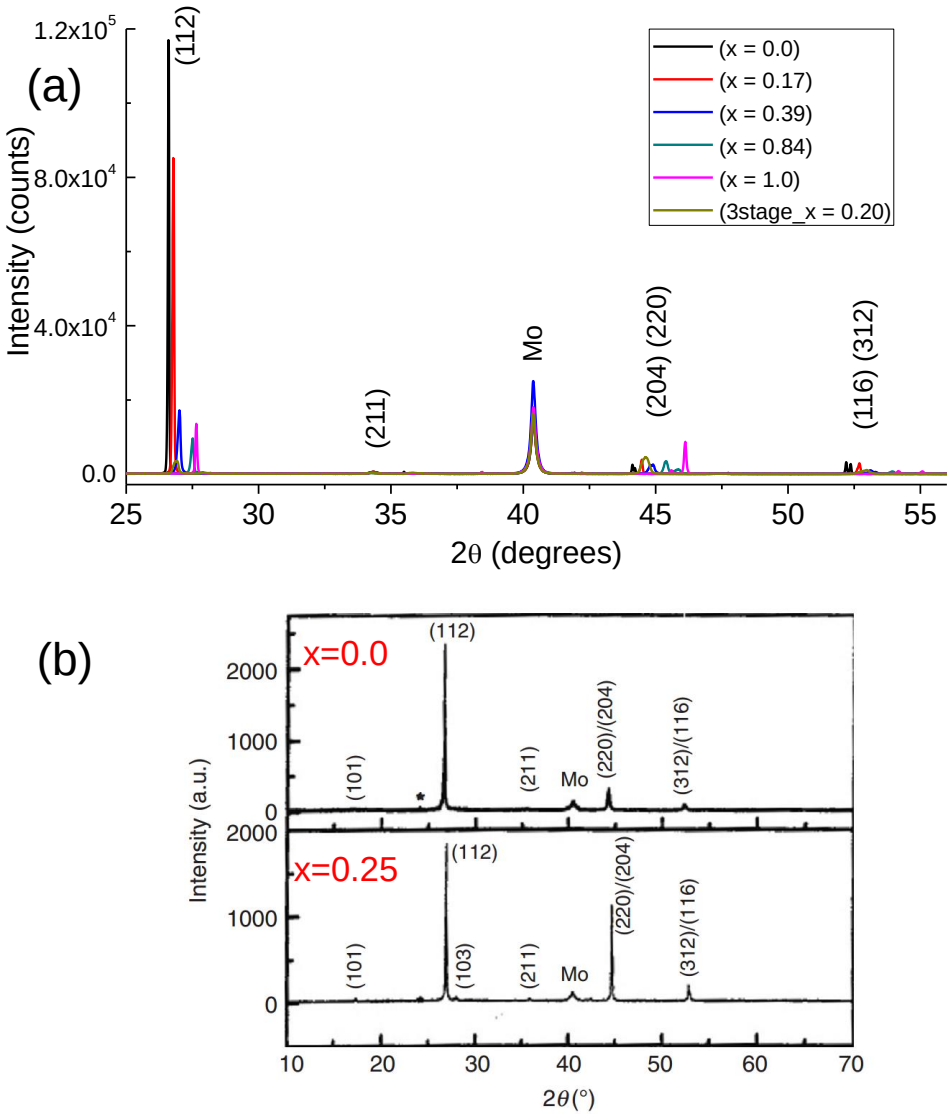

Figure 3.8: (a) XRD spectra obtained in this work for CuPRO process synthesized samples. (b) XRD spectra of CIGSe for x=0.0 and x=0.25 (Image courtesy: Kodigala et.al [12])

Figure 3.9a represents the ratio of [112] / [220][204] peak intensities observed for different 'x' values in CIGSe. As can be noted from Figure 3.8 and Figure 3.9a, CIGSe cells demonstrate strong [112] texture (selective crystallographic orientation) for cells under x=0.3 (Ga poor). Figure 3.9b represents FWHM (Full Width at Half maximum) of [112] peak for different Ga contents. FWHM for CIS and CGS samples (i.e. at x=0 and x=1) is minimum and is equal to instrumental width of XRD (width below this is not measureable in the instrument). Broadening of peak is more pronounced for middle values of x as compared to extreme points (x=0 or 1). This is attributed to higher quality of $CuInSe_2$ and $CuGaSe_2$ phase and chemical inhomogeneity in quaternary compounds [13].

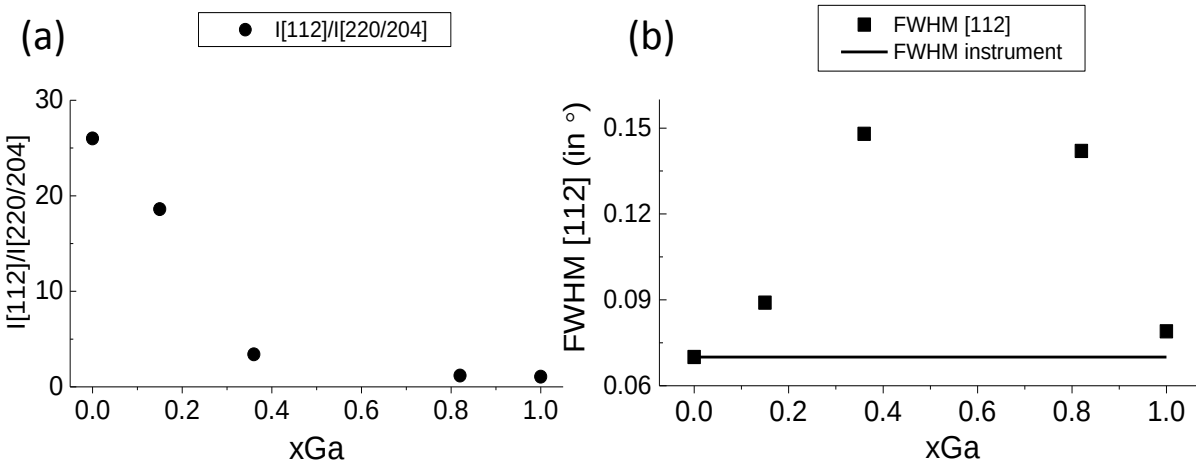

Figure 3.9: Comparison of (a) Integrated Intensity ratio of 112 peak and doublet 220/204 peaks and (b) FWHM (in degrees) of 112 peak for different Ga content x.

Although CuPRO process is used in this work, XRD spectrum shows the formation of the desired chalcopyrite phase of CIGSe. Indeed, our results match considerably well with results obtained in previous years as described in Figure 3.8a [12]. From results discussed above, XRD patterns hence confirm the formation of a solid solution composed of a single chalcopyrite phase throughout the layer. XRD provided information about crystal lattice and phase; to have an actual insight of a material at micrometer level SEM analyses were performed.

3.3 SEM cross-section analysis

SEM cross section analysis is performed here to identify the grain size distribution with depth. Before analyzing at atomic scale it is important to know approximate expectancy of analyzing GB in atom probe. APT's detection limit is within 1µm in analysis direction, which is actually very rare and in a successful analysis of CIGSe tip one usually obtains a typical atomic volume of 40×40×200 nm^3 (on the average in the present study) for around 17 million detected ions. Hence smaller grains are preferred, usually less than 1µm to increase chance and to analyze more GBs. In worst case not even one GB is detected even with 50 million detected atoms. Hence for higher grain sizes it is thus recommended to perform correlative EBSD-APT or correlative TEM-APT on side of the APT sample (tip) to know the location of the GB. Knowing the position of GB on tip, one can sputter the tip at low energy of Ga^+ ions in FIB to localize GB within few nanometers from tip apex. EBSD/TEM analysis involve projection of high energy electrons (>20 kV) for some time on tip surface which usually

contaminates the surface of the tip and may even make the tip brittle for APT analysis. Correlative EBSD-APT experiments were performed on some tips which resulted in tip rupture after few minutes of experiment which might happen due to tip embrittlement while performing EBSD on 100 nanometer thick tip at high voltages. Hence, correlative EBSD-APT experiments were not performed in this work. This is an apparent observation and no detailed study of this behavior has yet been performed. As Na atoms accumulate on GBs, GB identification in this work was based on detection of planar segregation of Na atoms.

CIGSe solar cells were mechanically cleaved at representative regions using diamond pen glass cutter. Grains of the thin films are thus expected to cleave without dissection (breaking of a grain in two). Cross sections of thin films can now be scanned using secondary electron detectors in SEM by placing substrate parallel to the electron gun. Figure 3.10 shows the microstructure of grains in CIGSe for different Ga concentrations grown using CuPRO process.

The following conclusions can be drawn from Figure 3.10:

1) CIGSe grains are narrow and columnar in nature regardless of Ga concentration. This means grains are longer in depth as compared to width and hence size of grains with depth are referred to grain length. This is due to the CuPRO process used in this work in order to improve the chance of localizing GB in APT tip.
2) Grain length observed is maximum for x=0.17 (1.5 μm), however it is also found in ref. [14] that maximum grain length for CIGSe correspond to x=0.23 for 3-stage process. It may be the same for the CuPRO process and the maximum may be between x = 0.17 and x = 0.39. No samples were prepared between these two values of x so we do not know the exact Ga ratio corresponding to maximum grain length.
3) Grain length decreased with Ga content after x=0.17 (1.5 μm) and minimum grain size (0.3 μm) is observed for $CuGaSe_2$.
4) Homogenous grain size distribution along the depth of the film for these samples is observed. This is apparently due to the absence of Ga grading.

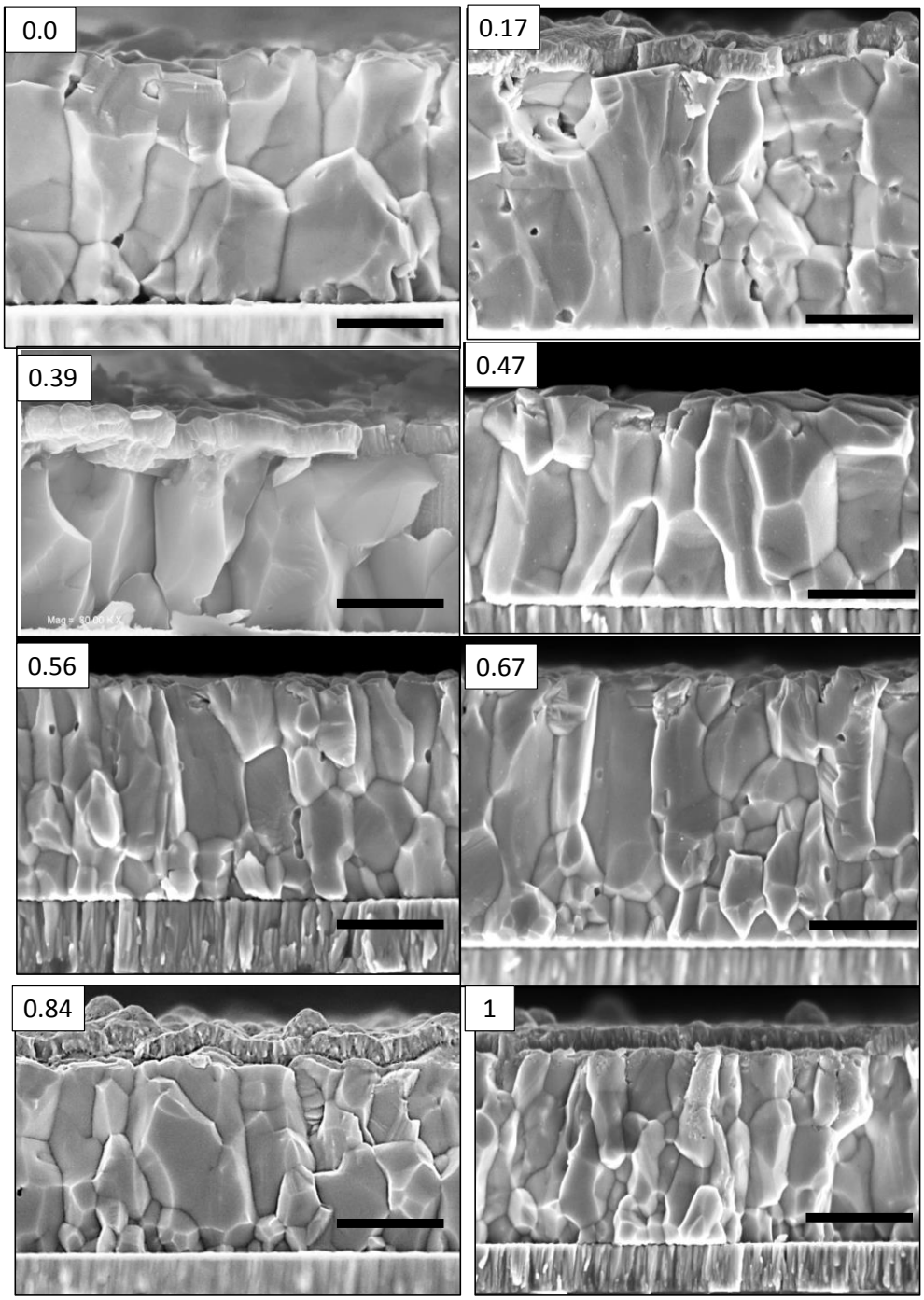

Figure 3.10: SEM cross section images of CIGSe with different Ga ratios x as noted on top left corner of each cells. Scale bars (black) are 1µm in width.

Cross section SEM provided a good idea of grain distribution as a function of depth but could not give sufficient quantitative statistics of grain distribution laterally to substrate. To analyze distribution of grains on surface and to obtain more statistical information on grain size and misorientation between grains we perform (Electron Back Scatter Diffraction) EBSD analysis.

3.4 Microstructural characterization of grains in CIGSe using EBSD

Transmission Electron Microscopy (TEM) analysis can be used to identify grain orientation and to calculate misorientation between two grains. Statistically TEM is not good in this aspect and is limited to analyze only a small part of the thin film. Additionally specimen preparation for TEM is time consuming. SEM analyses as shown in the previous section, show the grain shape and size distribution along the cross section of the sample. However it could not provide orientation of grains and misorientation profile between different grains. EBSD is one of the best techniques to characterize polycrystalline materials providing distribution of grain size, GB misorientation profiles etc. with relatively sufficient statistics.

3.4.1 In-situ sample preparation techniques for EBSD

As EBSD technique works on detection of Kikuchi patterns formed by forward scattered electrons. The surface of the sample needs to be very smooth at nanometer level. However surface of CIGSe is very rough as shown in Figure 3.11a. Thus some in-situ techniques are employed to smoothen the surface. Smoothening of CIGSe surface was carried out in NVision40 SEM/FIB chamber using a technique developed for this work and Figure 3.11 shows series of different SEM images captured during sample preparation.

(a) Shows very rough surface of top layer of CIGSe solar cell (ZnO) which is highly inappropriate for EBSD measurements, also this layer needs to be removed to reveal pure CIGSe part

(b) A representative part of sample is chosen and using mechanical cutting we locate it near to the edge of the SEM stub. As illustrated in Figure 3.11b, 15-25 μm width of sample are milled using high currents (30keV 11 nA) in FIB by positioning sample normal to the FIB column. (c) Sample is positioned now parallel to FIB column and around 300-500 nm from top surface is milled using high currents (30keV 6.5nA) and then cleaned using low currents (30keV 0.15nA) to avoid formation of Cu droplets on the surface. Image shows very smooth surface appropriate for EBSD measurements, also it is evident that only 10-15 % of CIGSe top surface is removed. However some curtailing lines are visible in figure (c) which is produced due to FIB milling on surface. Presence of these curtailing lines may not give the best results but EBSD experiments show very little difference due to these thin lines. Thick

curtailing lines do not provide promising results due to irregular scattering of electrons from rough surface.

(d) Shows SEM/EBSD image after a successful EBSD analysis. This image is just to demonstrate the good capability of our applied technique.

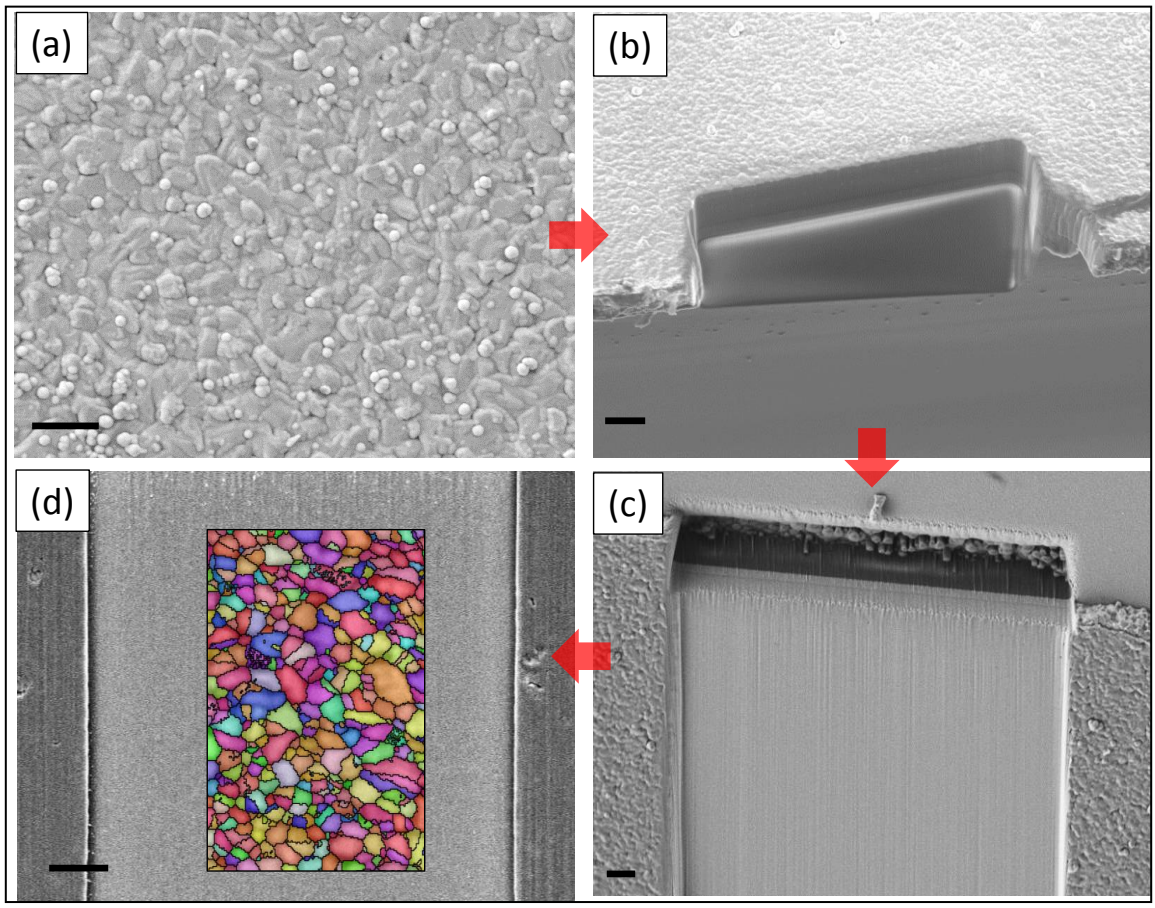

Figure 3.11: SEM images after different steps during sample preparation (a) surface SEM image of CIGSe, (b) edge cleaned using FIB, (c) around 200 nm surface cleaned using FIB for (d) successful EBSD experiment. Scale bars (black) shown are 2µm in length.

Space-charge region (SCR) of CIGSe solar cells is in the first 500 – 800 nm below the CdS-CIGSe heterojunction. Hence first half of grain statistics is more important and critical factor in deciding fate of device's performance. Therefore in this work we cleaned up to 300 nm from CdS-CIGSe junction in order to perform EBSD in SCR. Hence all the EBSD measurements in this work are performed in direction parallel to substrate.

3.4.2 Optimizations and corrections in EBSD

Oxford instrument's AZtecHKL software is used here to perform continuous detection and indexing of EBSPs for $CuInSe_2$ tetragonal system with lattice constants: a=5.78 c= 11.61.

Specimen was titled on a horizontal SEM holder at 70°. Secondary electron imaging mode was used for EBSD analysis at 20 kV (Extra High Tension) voltage. 2×2 binning mode is used during analysis with 43 milli-second exposure time, automatic background corrections and static background corrections were performed to better resolve EBSPs. As grain sizes (diameter) of CIGSe is particularly small (0.3μm to 3μm as seen in SEM), we choose small area and small point to point scanning distance for appropriate results. Scanning area chosen is from 100 μm^2 to 300 μm^2, point to point scanning distance is kept 50 nm as also suggested in ref. [15] for CIGSe.

Post processing

Data obtained after analysis is in OIP (Oxford software) format and is converted to CPR (channel project report) format which is compatible to CHANNEL 5 post processing software. Due to poor indexing and/or low quality of EBSPs, noise appears as a form of clustered unidentified pixels which couldn't be identified by the software. By 'extrapolating zero solutions' option, unidentified pixels (black) are filled with information of their neighboring pixels and thus performs noise correction as shown in Figure 3.12. A tetragonal CIGSe unit cell can be considered as composite of two sphalerite structures as discussed in section 1.3.1. Hence c/a ratio deviates from 2 which is attributed as pseudosymmetry [16]. Hence pseudosymmetry is an important issue to be considered while quantifying grains and grain boundaries statistics. This issue has been accounted by correcting the inappropriate indexing performed by the software. Pseudosymmetric issues in EBSD were found for various axes and were removed by disregarding them up to a maximum deviation of 5 degrees. An example is shown in Figure 3.12 where mis-indexed pixels in the grains are corrected by performing pseudosymmetric correction.

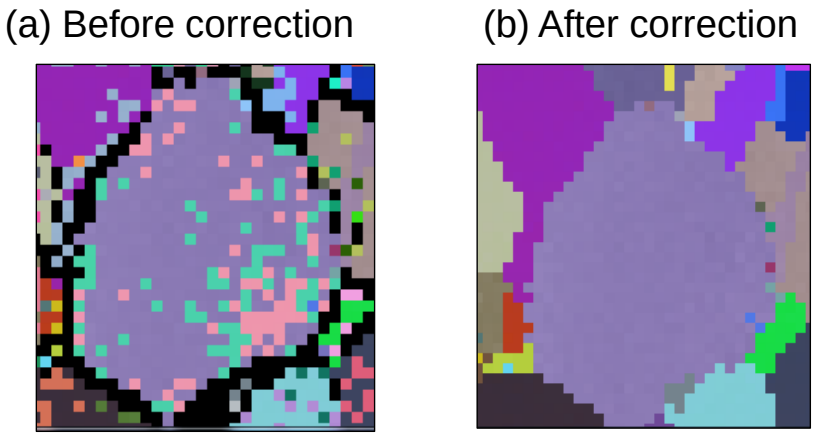

Figure 3.12: Image obtained after EBSD analysis of CIGSe sample, (a) Before pseudosymmetric and noise correction (b) after pseudosymmetric and noise correction.

Neglection of pseudosymmetric correction may consider collection of few misinterpreted points as different grains. Hence pseudosymmetric corrections are essential to obtain accurate grain size distribution.

3.4.3 Grain size distribution

Figure 3.13 shows the distribution of grains and their orientation relationship for different Ga ratio in CIGSe. Scanning area chosen for EBSD analysis was within 150 μm^2 to 300 μm^2 however only ≈150 μm^2 area is shown in Figure 3.13 in order to compare grain size distribution from different samples. In order to get a quantitative idea of grain size variation we analyze only five samples of CIGSe including extreme concentrations (x=0, 1) in order to observe changes in microstructure with Ga ratio. As depicted from Figure 3.13, grain shapes and size of CIGSe are homogenously distributed for all samples with their respective Ga ratios. However significant changes in size and orientation of grains are evident while comparing different Ga content samples.

(112) oriented grains are shown in magenta and (220) oriented grains are shown in blue color. It can be noticed that orientations of grains are not randomly distributed rather they show a more (112) texture for Ga poor samples. EBSD results are found consistent with XRD measurements as grain orientation along (112) is strongly enhanced for Ga poor cells and (220) orientation is enhanced in Ga rich cells as marked in EBSD maps by blue color.

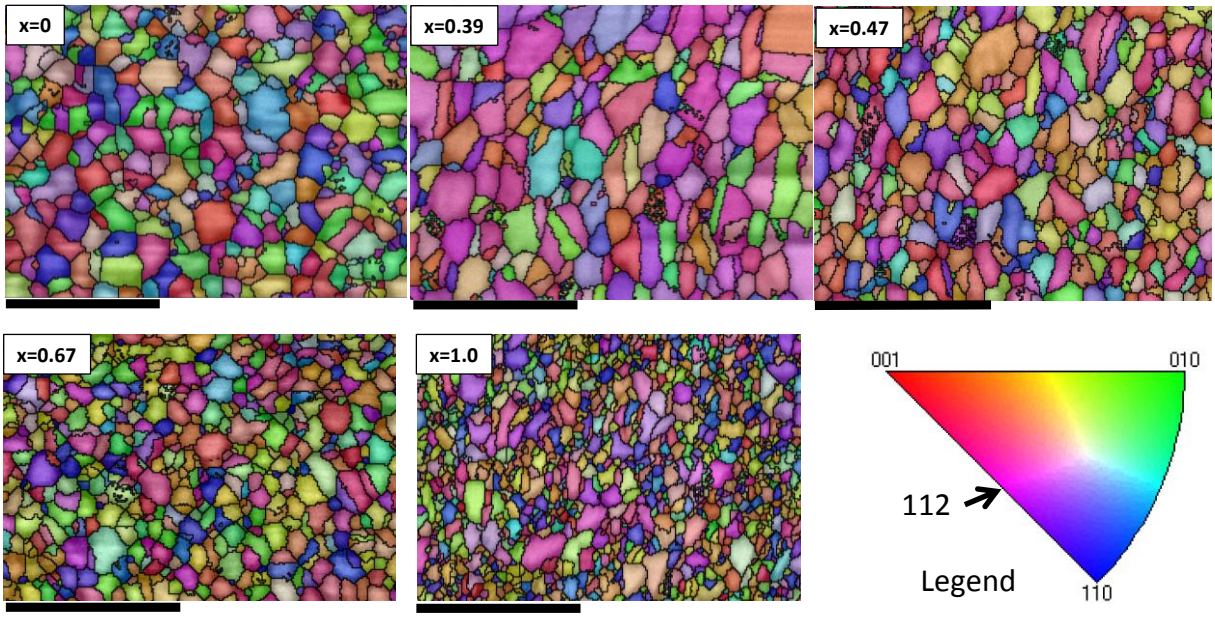

Figure 3.13: Orientation distribution maps (Inverse pole figure color maps) combined with back contrast image of CIGSe with different Ga contents grown using CuPRO process, scale bars (in black color) is 5μm in width. Color legend is shown for reference.

Grain distribution maps shown in Figure 3.13 are scanned over cleaned surface of CIGSe (50-200 nm from CdS) which correspond to space charge region of CIGSe solar cell. Hence distribution of grains in this region matters most for device performance. The size of grain here is determined by calculating the diameter of a disk whose area is equivalent to that of the grain. Grain size here is represented for width of the grain in direction parallel to substrate (not to be confused with grain length which is used previously for length of grain along cross section). While quantifying size distribution, it is important to obtain statistics with minimum possible errors. Experimental parameters for EBSD used in study are discussed in chapter 2 where we used 50 nm point to point distances. As discussed in Refs. [15,17], to obtain accurate results, one must consider the least accountable area of atleast ten measuring points. As point to point distance is 50 nm, area containing ten measuring points is around 0.025 μm^2 corresponding to diameter (or grain size) of about 0.16 μm. Hence to have accurate results only grains with size greater than 0.16 μm are considered in this study. Grain size distribution of CIGSe for different samples is shown in Figure 3.14 illustrating systematic distribution and variation in grain size of CIGSe as a function of Ga content. Maximum average grain size is observed for x=0.39 and minimum is observed for x=1 ($CuGaSe_2$). Our results are consistent with cross-sectional EBSD analysis performed by Abou-Ras et.al [14] who also observed minimum grain size for x=1 and maximum for x=0.23. However we observed

maximum average grain size for x=0.39 and following the distribution (Figure 3.14f) the actual maximum may be anywhere between x= 0 and x= 0.47.

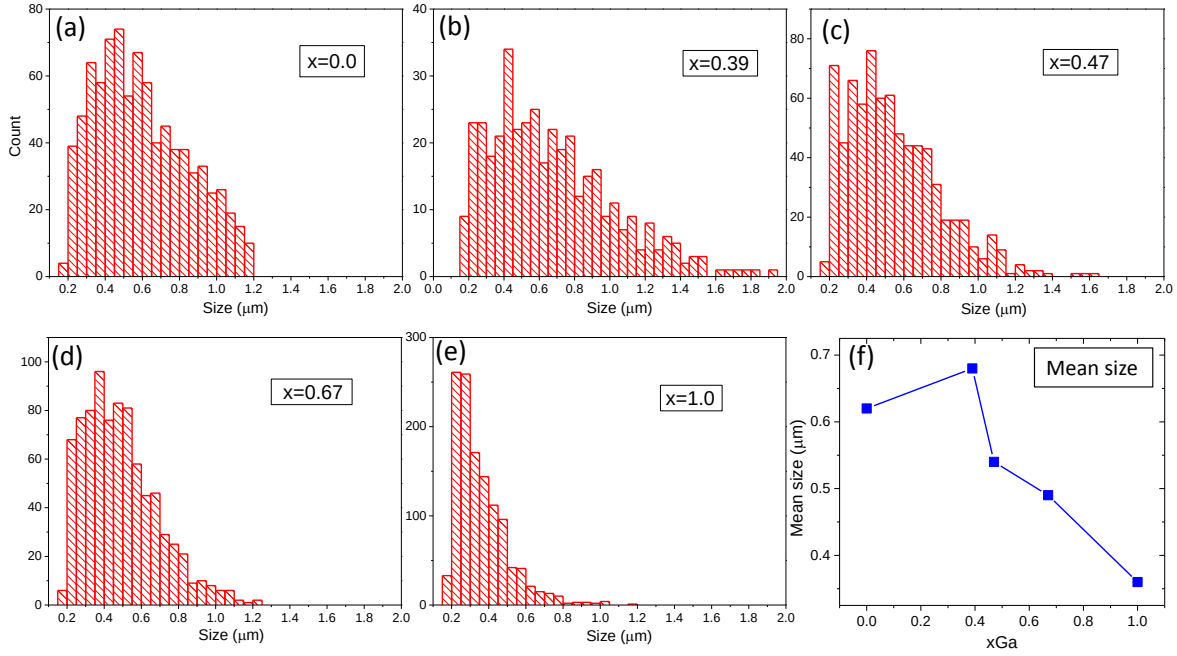

Figure 3.14: (a-e) Grain size distribution of CIGSe for different Ga concentration, (f) Mean grain size Vs Ga content x.

Apparently it seems that grain size follow close correlation with efficiency; however it has been demonstrated in Figure 3.15 from ref. [14] that the maximum grain size does not coincide with cell of maximum efficiency. Figure 3.15 shows that the maximum efficiency of CIGSe film is observed for 0.6 μm grain size and a sharp decrease in efficiency is apparent for grain sizes below 0.45 μm. As discussed earlier we expected maximum efficiency around x=0.7 and EBSD results show that grain size for x=0.67 is 0.5 μm which suggests decreased efficiency is not due to grain size.

Also recent studies by Jackson et.al. [18] presented very low or minimum effects of grain size on preparation of high efficiency Cu(In,Ga)Se_2 solar cells for Ga poor compounds. Hence less effect of grain size is expected on device performance, provided the grain size is not very small (< 0.45 μm).

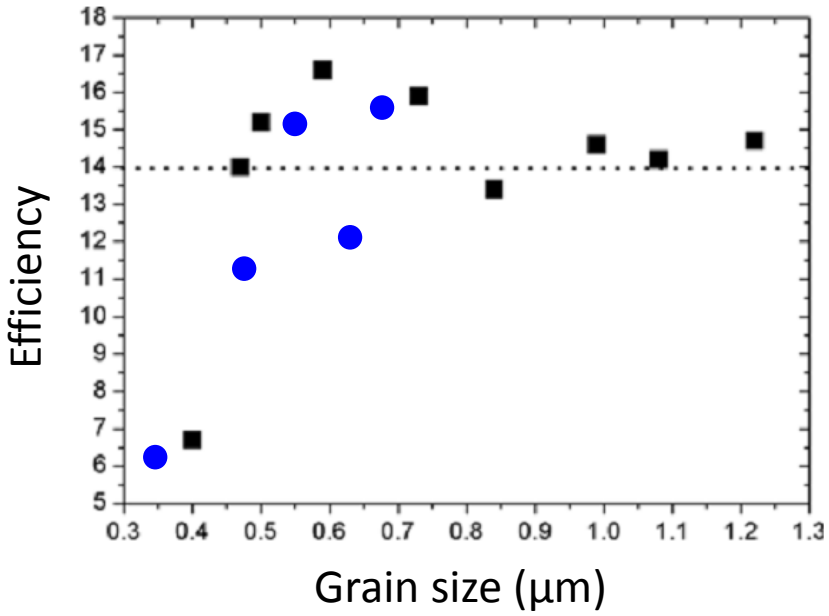

Figure 3.15: Solar cell efficiency for different grain size of $CuIn_{1-x}Ga_xSe_2$. Image reference: Abou-Ras et.al [14] compared with results in this work (blue dots).

As illustrated in Figure 3.14f, average grain size distribution follows a pattern similar to efficiency where maximum is approximately from x=0.2 to x=0.4. As already discussed in Chapter 1 about beneficial effects of GBs in CIGSe, such as existence of Cu-poor GBs acting as hole barrier, a decrease in grain size to some extent (up to 0.5 µm) must improve device quality accounting diffusion length of minority carriers in CIGSe (≈ 0.4 µm). Hence considering appropriate grain size and optimum band gap, one would expect highest efficiency for x=0.7 provided there is no element/phase change in the grains or at GBs with Ga content.

EBSD and XRD studies revealed there is no major change in phase of the grains. Hence reasons for this drop in efficiency is maybe due to one or more of the following reasons:

1. Elemental or phase changes at GBs from Ga poor to Ga rich cells.
2. Change in defect physics of CIGSe.
3. Change in interfacial chemistry of CdS-CIGSe heterojunction from Ga poor to Ga rich cells.
4. Change in interfacial chemistry of CIGSe-Mo from Ga poor to Ga rich cells which may decimate $MoSe_2$ formation.

Contreras et.al [5] observed changes in electrical properties of grains with Ga content and hence suggested that during transition from Ga poor to Ga rich CIGSe a change in GBs must be the origin of degraded performance of Ga rich CIGSe.

3.4.4 Misorientation between grains

Interface or boundary between two adjacent grains or crystallites is called a grain boundary. Grain boundaries are mostly referred to as defects in the material and are expected to degrade electrical properties of a semiconductor. Different grains in a polycrystalline material have their respective grain (crystal) orientation. The rotation required to rotate crystal axes of grain 1 to match that of grain 2 keeping reference frame fixed is called the misorientation between these two grains. A schematic interpretation of grains separated by grain boundaries is shown in Figure 3.16. In other words misorientation between two grains is the difference in their respective crystallographic orientation [19].

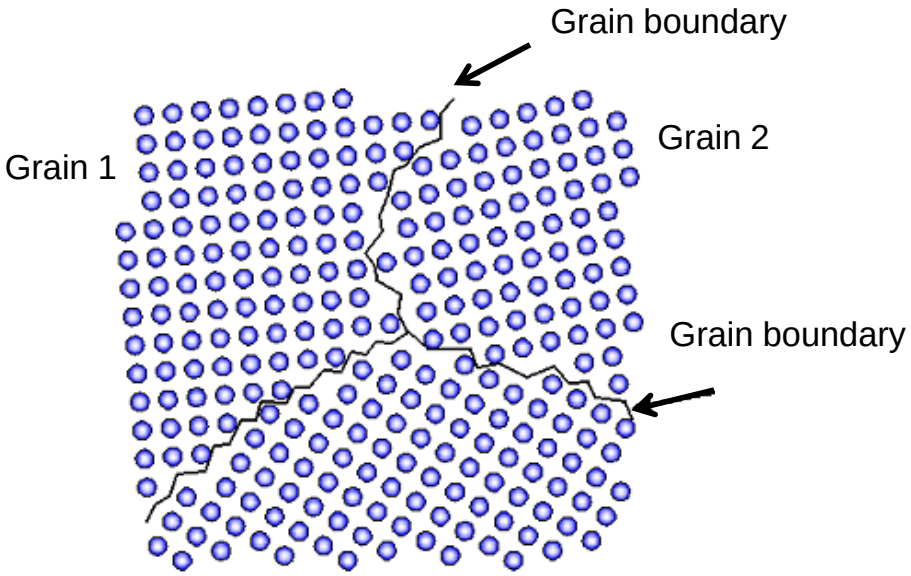

Figure 3.16: Schematic representation of a typical grain boundary. Image courtesy: [20]

There are various types of GBs separating two grains. GBs having misorientation angle lower than 15° are classified as low angle GBs and GBs with higher misorientation angles are called high angle GBs. Some 'special boundaries' are also present in polycrystalline materials whose interfacial energy is lower than high angle grain boundaries. Figure 3.17 represents a Tilt boundary, when axis of rotation is parallel between the two grains and twist boundaries when axis of rotation is perpendicular to the grain boundary plane.

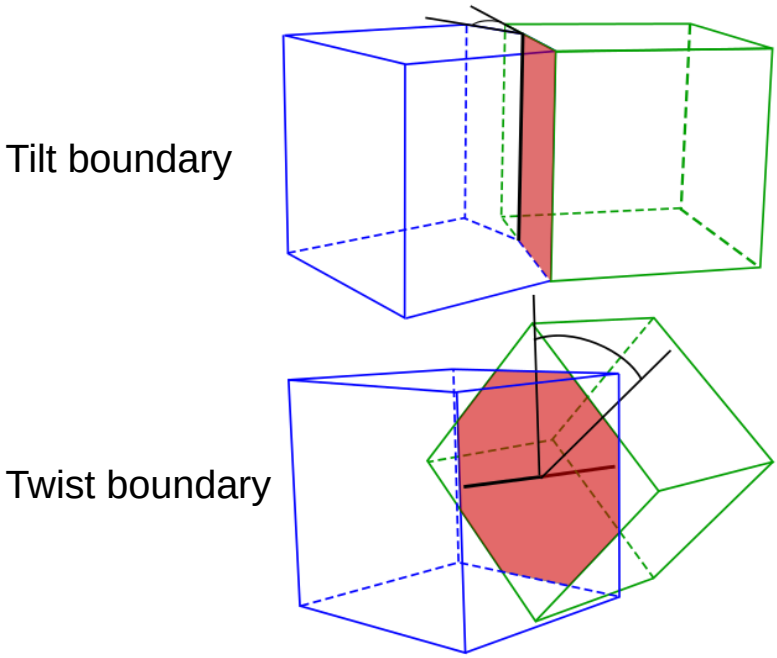

Figure 3.17: Schematic representation of a tilt boundary and twist boundary between two grains. Plane in red is the GB plane separating two grains in blue and green. Image courtesy: [21]

Misorientation between grains can be measured using electron diffraction pattern in TEM. However the process is time consuming and in order to have large statistics TEM is not a suitable technique. Thanks to modern hardware and software tools of EBSD which can provide sufficient statistics in relatively short time duration, it takes only few hours of analysis. CHANNEL5 post-processing software tool has been used in this study to obtain misorientation angle distribution and is illustrated in Figure 3.18 for different Ga ratios. It must be mentioned that these measurements were performed after performing Pseudosymmetric corrections as described previously. Figure 3.18 shows that misorientation angles between grains are not randomly distributed. Indeed misorientation at 60° and 71° are evident and significantly higher than other angles.

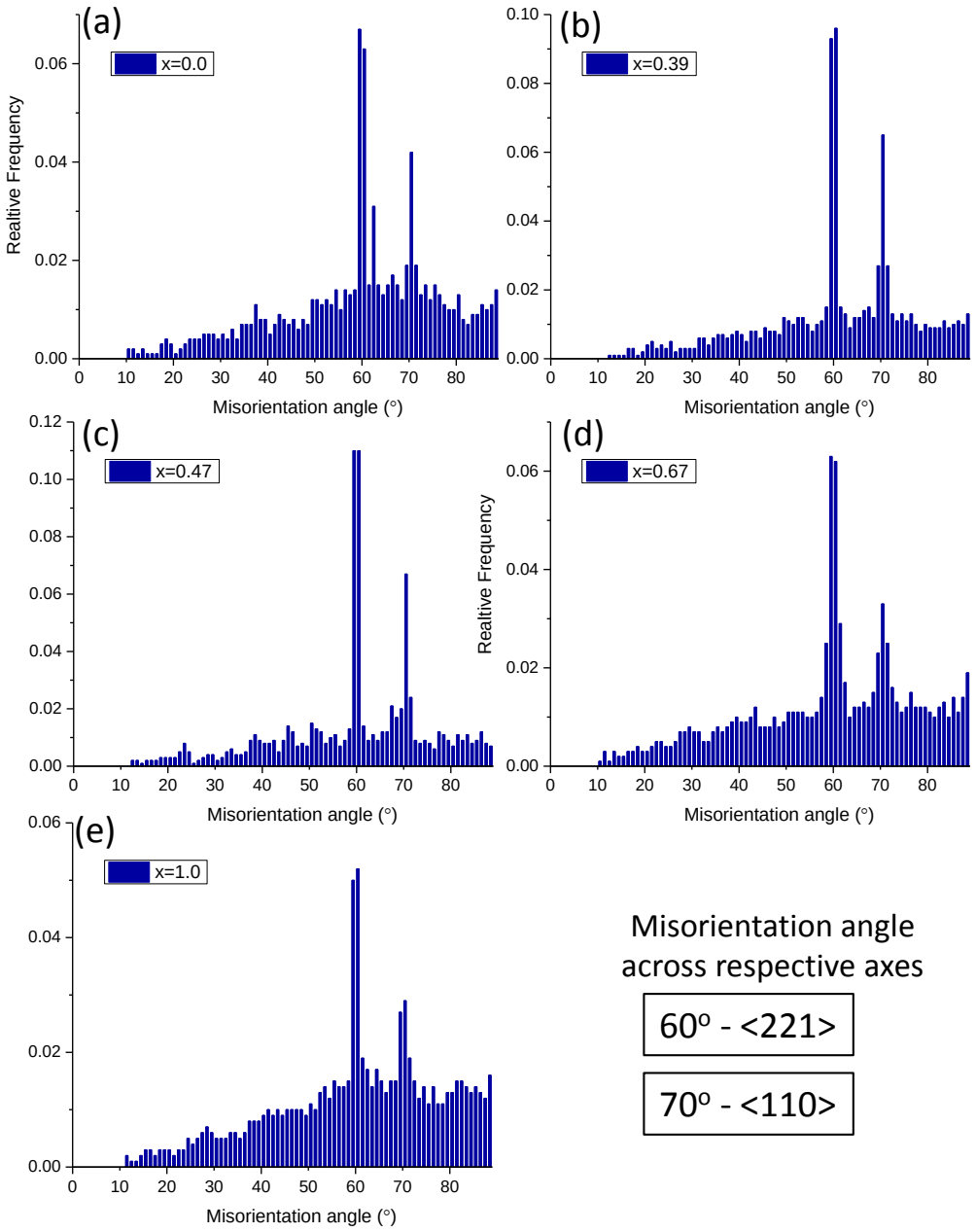

Figure 3.18: Misorientation angle distribution for respective CIGSe samples with different Ga ratio. Misorientation angles of 60° and 71° across <221> and <110> respective axes were found most prominent.

These two misorientations are particular to CIGSe chalcopyrite structure and have also been observed in previous studies [16] which attributes to 60° misorientation across <221> and 71° misorientation across <110> axis respectively as shown in Figure 3.19. 60° misorientation across <221> axis is shown in Figure 3.19 (a) and (b) with different perspectives in (a) viewing normal to (112) plane and (b) viewing parallel to (112) plane. Cu, In/Ga occupy cation sites and Se occupies anion sites in CIGSe, coincidence sites (larger

circles) are observable. 71° misorientation across <110> axis is shown in Figure 3.19 (c) and (d) with different perspectives in (a) viewing normal to (220) plane and (b) viewing parallel to (220) plane. Figure 3.19 shows that these grain boundaries are twin boundaries of (near) Σ3 type and identified as rotation of 60° and 71°, which is also well demonstrated in ref. [15].

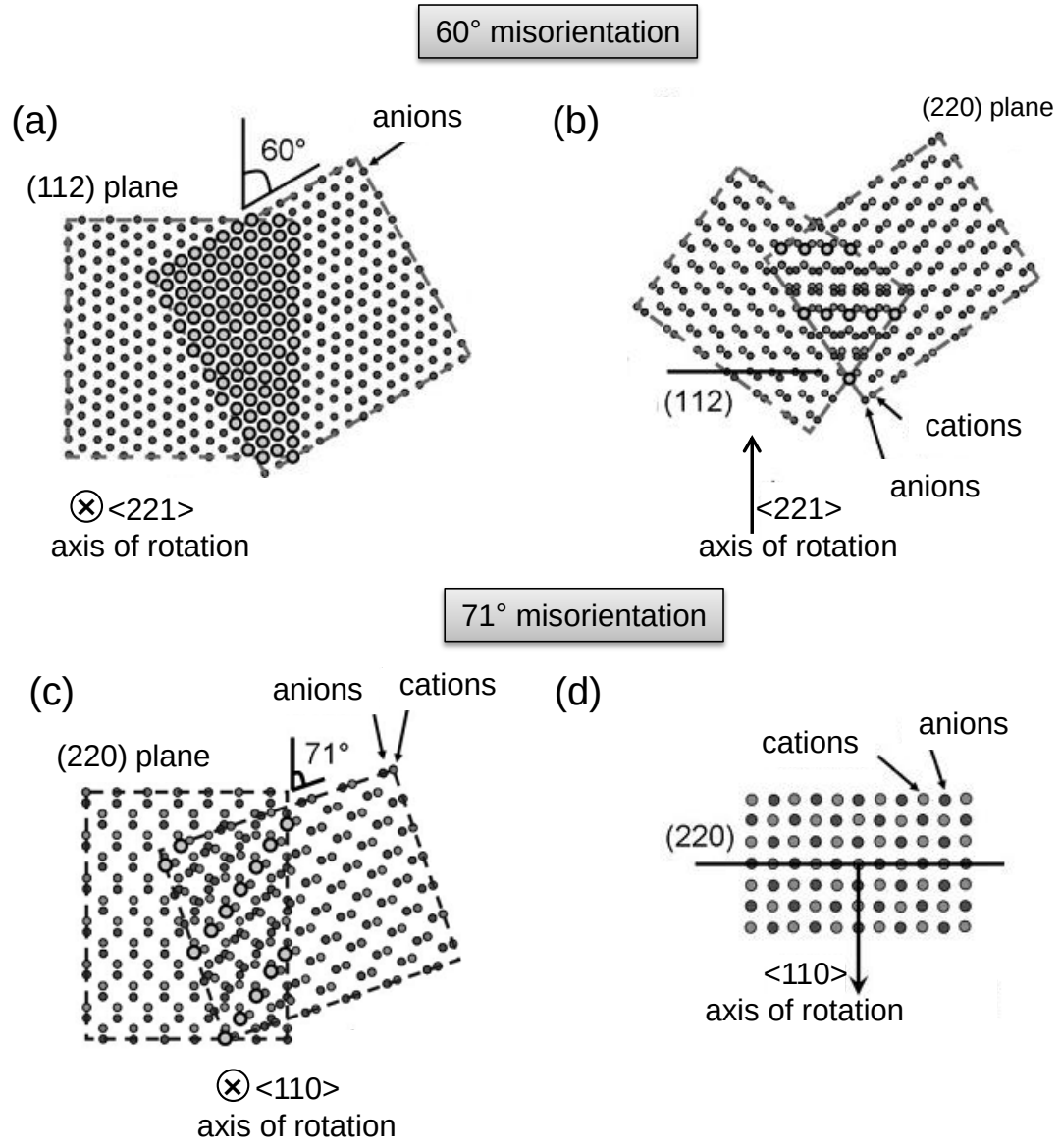

Figure 3.19: Schematic representation of 60° and 71° misorientation angle across GBs in CIGSe, Cu and In/Ga occupy the cation sites and anion sites are occupied by Se. (a) two superimposed grains of (112) plane are oriented in $[221]_{tet}$ direction with a misorientation angle of 60°, sites shown in larger circles are coincidence sites. (b) Same case as in (a) viewed from (220) plane, (112) plane is horizontal and axis of rotation <221> is vertical. (c) Two superimposed grains of (220) plane are oriented in $[110]_{tet}$ direction with a misorientation of 71°. (d) Same case as in (c) viewed in perpendicular direction with axis of rotation <110>. Image source: Abou-Ras et.al [15].

It is interesting to note that misorientation angle distribution is similar for all samples with different Ga content. This shows that CIGSe compound with various Ga/In concentration exhibit similar chalcopyrite microstructure with specific misorientations independent of its Ga content. This is important to check before APT studies because changes in misorientation angles might modify CIGSe microstructure properties.

3.4.5 Counting no. of GBs

EBSD analysis gives a lot of quantitative information in polycrystalline samples. As this study is based on characterization of GBs, it is useful to know approximate number of GBs in a selected area, in order to quantify amount of Na segregation in thin films. To calculate the total no. of GBs in a given area it is essential to know the number of grains neighboring a single given grain. Thanks to advanced software techniques in CHANNEL 5 post processing software, the neighboring grain distribution (NGD) can be obtained. NGD for five CIGSe samples with different Ga contents are shown in Figure 3.20 . It is interesting to note that irrespective of the Ga content, NGD is similar for all samples and hence mean number of neighboring grains around a single grain is same for all the samples. However there is a significant change in grain size and orientation despite this, number of their neighboring grains is same.

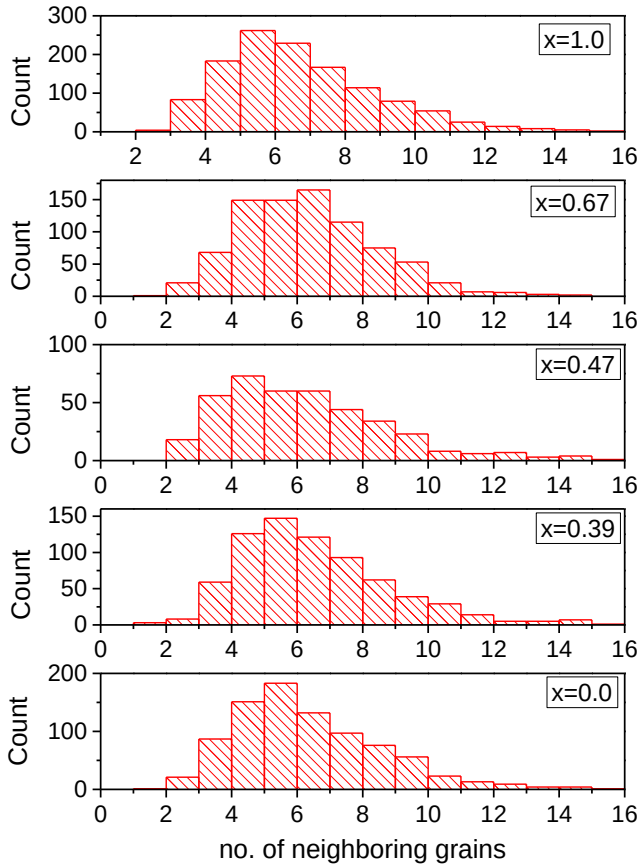

x	Mean no. of neighboring grains
0.0	5.9 ± 0.3
0.39	6 ± 0.3
0.47	5.8 ± 0.3
0.67	5.9 ± 0.3
1.0	6.3 ± 0.3

Figure 3.20: Neighboring grain distribution for respective CIGSe samples with shown Ga content. (top right) typical EBSD pattern (bottom right) statistics for respective samples.

Utilizing information obtained from Figure 3.20 and grain size information from Figure 3.14, total number of grain boundaries (N_{GB}) can be calculated in a fixed area (A) using the following relation.

$$N_{GB} = \frac{A}{\gamma} \times \frac{\Omega}{2} \tag{3.5}$$

Where, Ω is the mean number of neighboring grains and γ is the mean surface-size of a grain, both for respective Ga content. Factor of 2 comes due to repetitive counts of one GB. As Ω is the same for all samples, it is obvious that total number of GBs in a fixed area follows inverse relation of the mean surface size of grain (γ). Figure 3.21a represents mean surface size of grains in CIGSe as a function of x and Figure 3.21b shows N_{GB} versus x. As already discussed in chapter 1, GBs in CIGSe are Na enriched which is beneficial for device performance and increase in number of GB was expected to improve device performance further. An increase in number of GBs would mean an increase in amount of Na in thin films provided similar amount of Na segregation at GB. Amount of Na atoms segregating at GB could be measured using statistical APT calculations. This has been measured for CIGSe

samples with various x in next chapter which shows similar amount of Na segregation at GB regardless of its x value. Hence an increase in number of GBs indicates an overall increase in Na in thin films, which mainly comes from soda lime glass substrate used. It is interesting to note that amount of Na in thin films is not same for all samples regardless of their similar preparation conditions. Reasons behind this are unknown and are beyond the scope of present work.

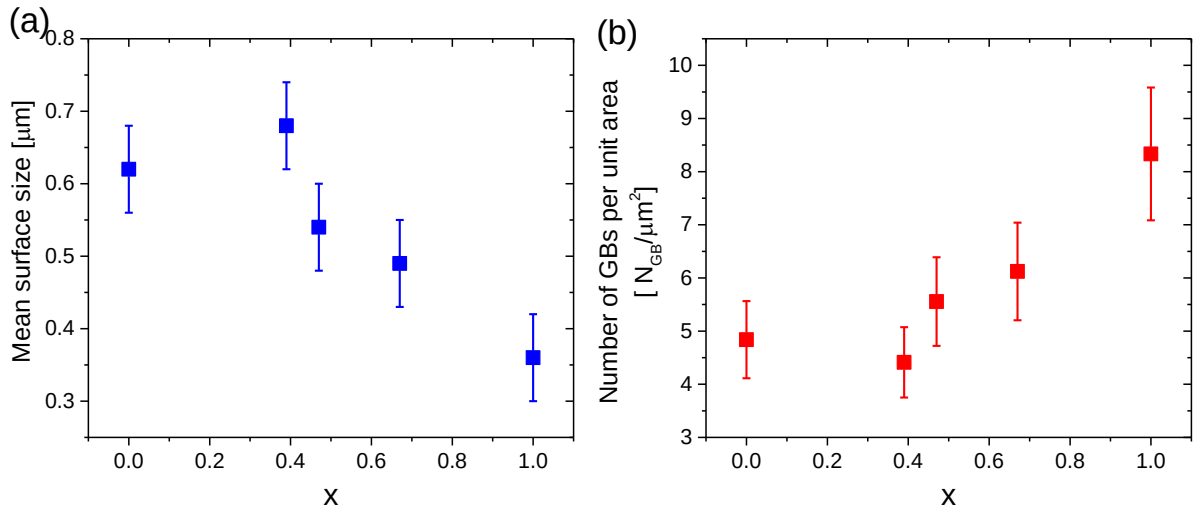

Figure 3.21: (a) Mean surface size of grains (in µm) and (b) number of GBs per unit area ($N_{GB}/\mu m^2$) as a function of x.

As GBs are one-two atomic planes thick, exploring and quantifying GBs properties is very difficult and requires high resolution instrumentation techniques. Herein we use Atom probe tomography (APT) to explore GBs in CIGSe for different Ga contents. But first in order to calibrate the instrument, we examine distribution of atoms in grains using APT in next section. Characterization of GBs is discussed in next chapter.

3.5 Atom Probe Tomography

To investigate grains and grain boundaries of CIGSe at atomic level we employ APT. Analysis in APT requires various experimental parameters and post processing optimizations to obtain accurate results, here we detail this technique for CIGSe.

3.5.1 Pulsed laser atom probe: Optimizations for CIGSe

a) Optimization of experiment parameters

Major tunable parameters involved during APT experiment are temperature of specimen, applied voltage, detection flux, laser type and laser power. These parameters are specific for each kind of materials and hence must be optimized in this work for CIGSe to ensure reliable and reproducible data. CIGSe compounds consists mainly of four elements Cu, In, Ga, Se, having different field evaporation properties. Hence temperature of the specimen and laser parameters must be optimized to ensure a homogeneous evaporation of all elements avoiding chances of preferential retention or preferential evaporation [22].

1) Laser Optimization:

Laser options in LAWATAP are wavelengths of 1030 nm, 515 nm and 343 nm corresponding to IR, Green and UV respectively. APT analyses were performed using the three laser modes and mass spectrums obtained are respectively presented in Figure 3.22 for x=0.36. ;

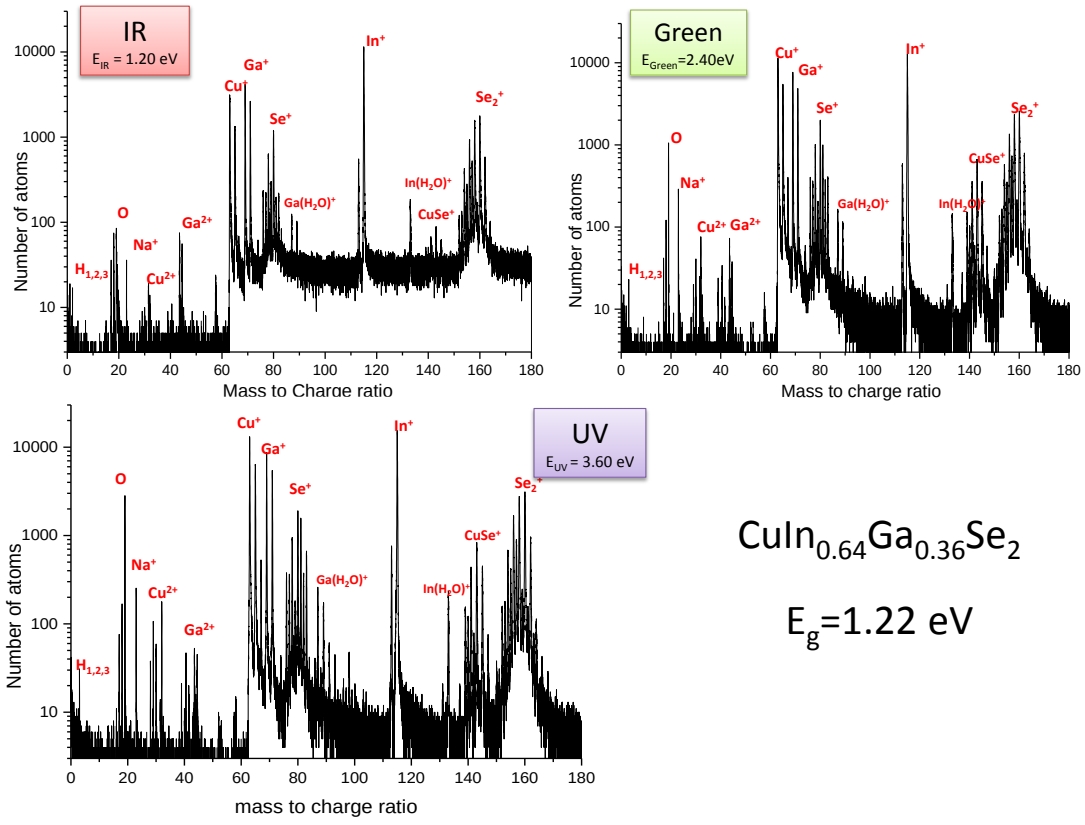

Figure 3.22: Mass spectrum obtained for CIGSe sample x=0.36 using IR, Green and UV laser.

Background noises mainly arise from evaporation of atoms between pulses and contamination in analysis chamber. IR laser demonstrates high background noise and very low signal to background ratio. For example considering signal to background ratio of In in IR laser is ≈300 and in UV and green laser, signal to background ratio is ≈ 1000. Green and UV present better signal to background ratio and is optimum for analyses. Band gap (E_g) of $CuIn_{0.64}Ga_{0.36}Se_2$ is 1.22 eV which is higher than IR energy (1.20 eV) and lower than that of green (2.40eV) and UV (3.60 eV) and may explain high background noise observed in IR. More studies on wavelength dependence of incident laser on field evaporation can be found in Ref. [23] which suggests laser with energy higher than optical band gap must be employed to obtain accurate results. Hence in this case Green or UV laser could be considered optimum for APT analysis.

2) Laser Power and temperature optimization

Field evaporation in atom probe depends on element's respective evaporation fields. Evaporation field of an element A represents electric field at which A starts evaporating. For example, elements in CIGSe in their purest form exhibit different evaporation fields, for Cu, In, Ga it is 30, 12, 15 V/nm respectively and Se is sensitive to desorption (evaporates in vacuum). Due to higher evaporation field of Cu than other elements, it is probable to observe preferential retention of Cu due to its high evaporation field and preferential evaporation of Se due to its desorption properties.

Because of preferential retention of Cu or preferential evaporation of Se, chemical compositions obtained from APT mass spectrum are biased and require alternate measurements to calibrate laser power and specimen temperature. EDX measurements were performed to extract accurate chemical compositions of different CIGSe cells prepared and were used to calibrate APT experiment parameters. EDX provides chemical composition using signals from specimen volume of 1 μm^3, however this could not be used to obtain atomic compositions with nanometer scale precision. As GBs are few nanometers thick, APT is used to measure compositions with nanometer scale resolution.

Composition measured in EDX is compared with composition measured in APT by varying specimen temperature and laser power and is illustrated in Figure 3.23. Figure 3.23 is a ternary composition diagram with three vertices as concentration of Se, Cu and In. Composition measured by EDX (red box) is used as calibration point which measures stoichiometric ratio of Cu:In:Se = 1:1:2 as in $CuInSe_2$, hence composition of elements are

Cu=25%, In=25% and Se=50%. Green boxes and blue boxes represent compositions measured using APT by varying laser power and specimen temperature respectively.

To optimize laser power, power of the laser is varied from 1.20 mW to 0.08mW during analysis keeping constant detection flux in APT (0.0010 ± 0.0002 atoms per pulse) and constant specimen temperature (70 K). Higher laser power (1.2 mW) results in higher Se concentration measured by APT (62 at %). Decreasing laser power results in decrease in Se concentration and optimum Se concentration (50 at. %) is observed for laser power = 0.1mW. Using specimen temperature 50 K and laser power 0.1 mW composition of $CuInSe_2$ obtained using APT matches with EDX. Increase in laser power indicates preferential evaporation of Se, hence laser power is lowered to obtain quantitative results.

Similarly, to optimize specimen (tip) temperature in APT, Temperature is varied during analysis (80 K to 50 K) keeping constant detection flux in APT (0.0010 ± 0.0002 atoms per pulse) and constant laser power (1.0mW). Specimen temperature is decreased from 80 K to 50 K resulting in change in composition as shown in Figure 3.23. Higher specimen temperature (80 K) reflects in decreased Cu concentration (18 at. %) and decreasing till 50 K, composition of Cu reaches 25% and matched with EDX value. Higher tip temperature reflects in decreased Cu concentration due to preferential retention of Cu and is shown in Figure 3.24.

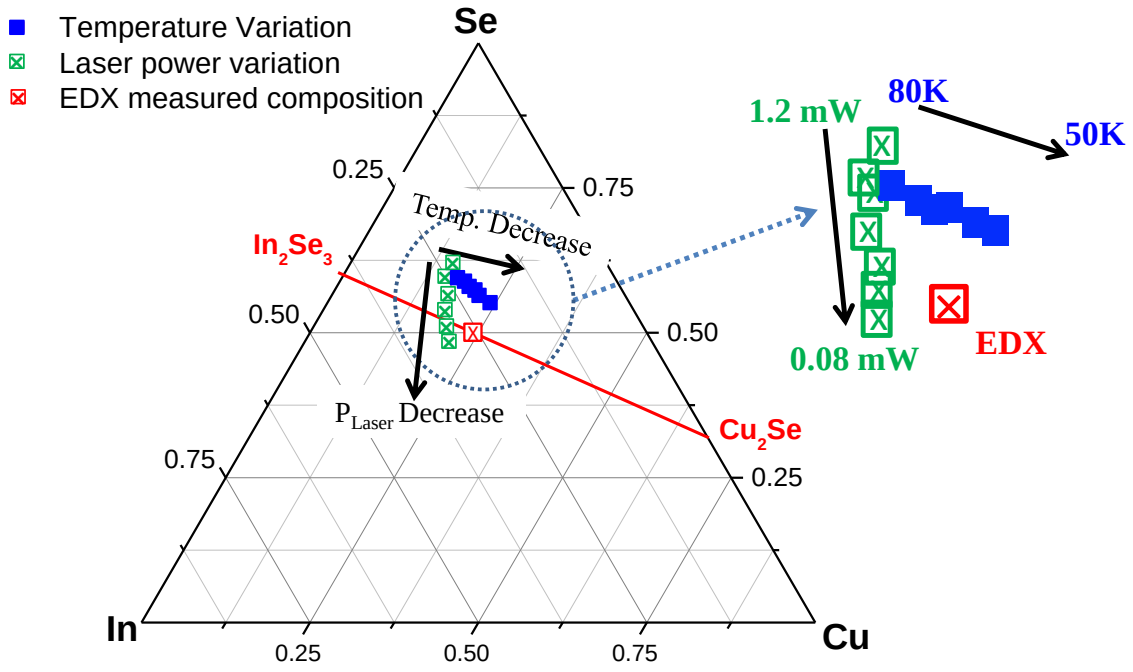

Figure 3.23: Ternary diagram of Cu, In, Se concentration. Composition measured by EDX is shown in red box and composition measured using APT at different specimen temperatures and different laser powers are shown in blue box and green box respectively.

High laser power was found to detect more Se atoms than other elements. This may be due to more evaporation of Se atoms due to high temperature rise at high laser power; hence lower laser power is recommended in this case. In this work LAWATAP (laser assisted tomographic atom probe) is used for APT studies. LAWATAP contained an inbuilt option to decrease laser power of green mode by a factor of 10 using optical density (OD) in front of laser. Hence due to low power capability and high signal to background ratio, green laser has been used in current work for all the APT analysis.

Figure 3.24 shows field-temperature (F-T) diagram for CIGSe. Starting point (points on left) represent the electric field at the tip apex and at respective temperature. In order to evaporate atoms from tip, laser pulses in form of thermal impulsions trigger field evaporation. Traversing from left to right side of the F-T diagram represent successful field evaporation.

Considering CIGSe system as containing two types of elements 1) High evaporation field elements (Cu) and 2) Low evaporation field elements (In, Ga, Se). As we utilize laser pulses for field evaporation, triggering pulses in figure are in horizontal direction considering pure thermal nature of field evaporation.

Figure 3.24 shows field evaporation behavior of different elements in CIGSe containing three possibilities:

1) High temperature: At high temperature (T1) thermal pulses are not efficient enough to uniformly evaporate all elements and preferential retention of Cu is apparent, as also observed in Figure 3.23.
2) Moderate temperature: Keeping thermal pulses similar to previous case, at temperature T2 (<T1) still there is fair possibility to preferentially retain Cu. As figure illustrate, field must be increased further to field evaporate Cu but may result in evaporation of other elements at point 2 without use of triggering pulses.
3) At low temperature T3 (< T2) the two F-T curves are closer and with the same thermal pulse we can homogeneously evaporate all species. However at low temperature, high electric field is required for field evaporation and it increases the chances of tip rupture during analysis. Also, referring to equation (2.2), low temperature results in lower evaporation rate and hence voltage must be increased to maintain optimum flux. The best possible regime is hence between point 2 and point 3.

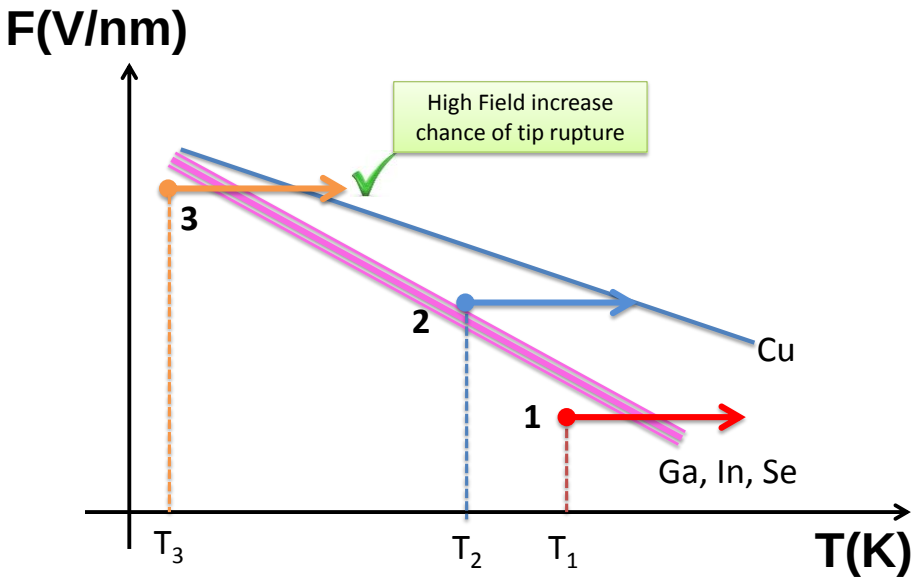

Figure 3.24: Schematic Field-Temperature (F-T) diagram for CIGSe.

Our schematic F-T model thus explains results observed in Figure 3.23. Hence the best condition here is to use low laser power and low temperature to ensure uniform field evaporation. Parameters thus optimized for CIGSe are temperature=50K and laser power=0.1mW with a maximum flux of 0.0050 atoms per pulse.

b) Mass Spectrum optimization

First step of post analysis starts with optimization of mass spectrum. As discussed in 2.5.4a) mass spectrum obtained depends on two major parameters: Mass of the ion and voltage at which it is evaporated, as length of flight is kept constant during the whole analysis and is about 10 cm in LAWATAP. Voltage corrections and average mass correction of a known mass peak (in this case Cu-63) is performed to obtain better resolved mass peaks. As radius of the tip is increased with amount of evaporated atoms, applied voltage is also increased to maintain proper detection flux which spreads mass spectrum following equation 2.8. Similarly according to figure 2.19 trajectory of ions towards detector may follow shortest or longest or in between path to detector depending on tip curvature. Due to difference in length of these trajectories, spread in mass spectrum is obvious following equation 2.8 and is corrected via Pythagoras correction. Voltage and mass corrections are important to resolve peaks better and improve accuracy of results. Two atomic species may also travel together resulting in additional peaks in the mass spectrum and can be identified by calculating total isotopic mass. A typical mass spectrum for CIGSe (x=0.36) after optimization is shown in

Figure 3.25a. Mass spectrum of CIGSe as shown is complex due to presence of four different elements. The presence of Na is mainly observed at GBs and also found in some cases uniformly distributed in grains in very low concentration. As certain elements naturally exist with different isotopic masses, they are respectively detected in proportion to their isotopic abundance. For example, Cu naturally exists with two isotopes (63 a.m.u. and 65 a.m.u.), so that two different peaks at 63 and 65 mass to charge ratio appear. Figure 3.25b shows isotopic abundance of Cu, Ga and In which match considerably well with APT results. To explore isotopic abundance of Se, mass ranges from 73 a.m.u. to 83 a.m.u. are selected.

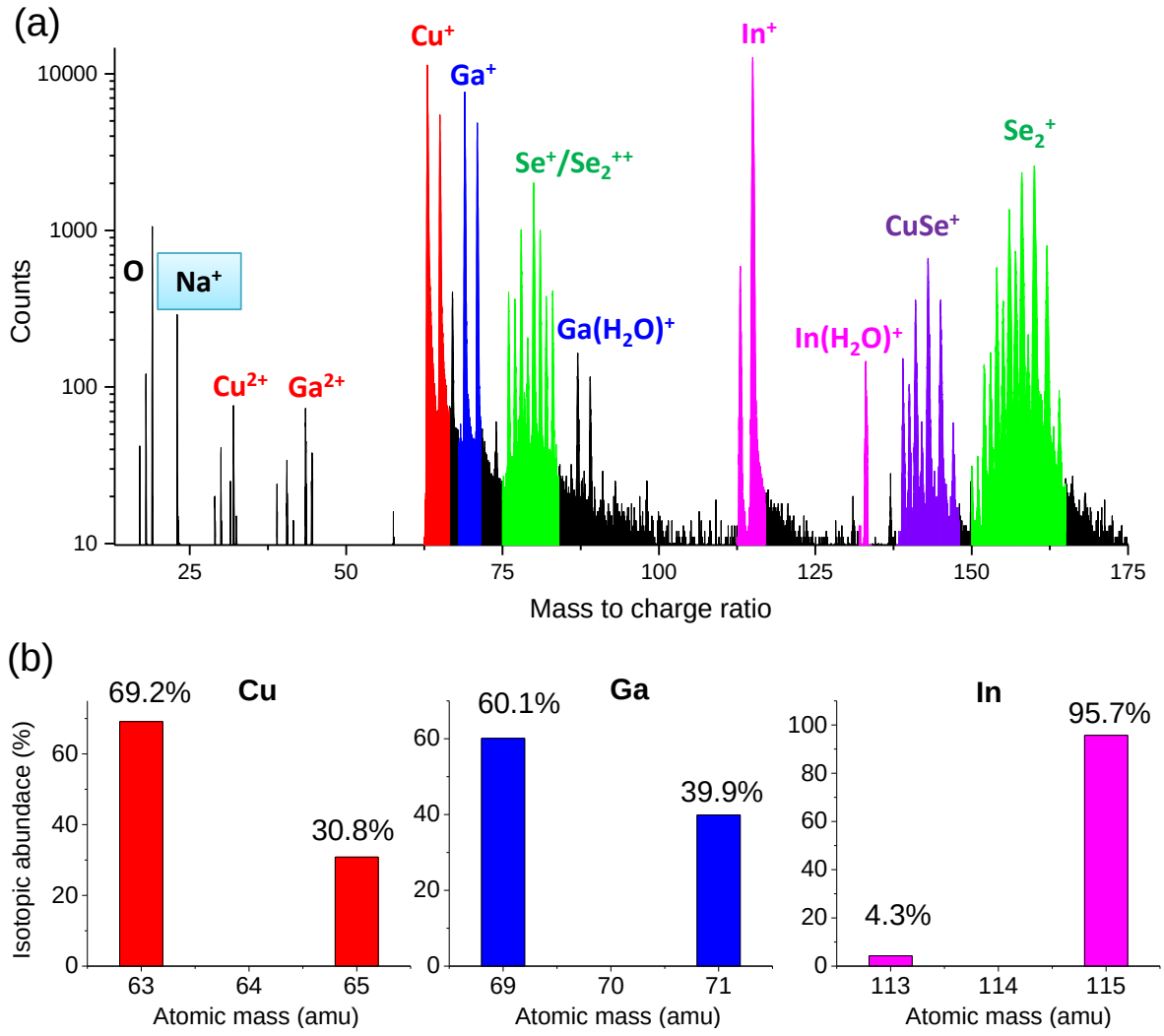

Figure 3.25: (a) Mass spectrum of CIGSe (x=0.36), different peaks corresponding to elements and molecular ions are shown. (b) Natural isotopic abundance (in %) of Cu, Ga and In.

Peaks from 73 a.m.u. to 83 a.m.u. are plotted with additional details in Figure 3.26a. Peaks here correspond to Se^{+} and Se_2^{++} which is confirmed by correlating the calculated isotopic distribution of Se in Figure 3.26b. Using known isotopic mass and their respective

abundance, total counts of Se atoms are calculated by addition of both respective ionic species. Se isotopes do not contain 79 a.m.u. peak and is present due to combination of 78 & 80 and 76 & 82 a.m.u. peaks. Similarly 83 a.m.u. peak is due to presence of molecular ions of Cu and H_2O and is written as $Cu(H_2O)^+$ and 81 a.m.u. peak is due to overlap of Se^+ and $Cu(H_2O)^+$.

Figure 3.26b shows natural abundance of Se_2^{++} and Se^+ ions considering equal amount of Se^+ and Se_2^{++}. However ionic species detected in atom probe do not contain both ions in 1:1 ratio and appropriate calculations are performed to obtain the total number of ions.

In Figure 3.26b, peak corresponding to 79 a.m.u. include only isotopes of Se_2^{++} and contain 25.23 % of total Se_2^{++} ions using isotopic abundance calculations. Hence total number of Se_2^{++} ions can be calculated using 79 a.m.u. peak.

Similarly total number of $Cu(H_2O)^+$ ions can be calculated using isotopic abundance calculation considering 83 a.m.u. peak which contain 30.85 % of $Cu(H_2O)^+$ ions. Hence Se^+ ions can be calculated by subtracting amount of Se_2^{++} and $Cu(H_2O)^+$ ions from observed spectra in Figure 3.26a. Thanks to isotopic abundance calculations, total number of Cu atoms can be calculated by accounting peaks corresponding to Cu^+, $CuSe^+$, Cu_2Se^+ and $Cu(H_2O)^+$ similarly all Se atoms can be measured by accounting Se^+, $CuSe^+$, Cu_2Se^+ and Se_2^{++} ions.

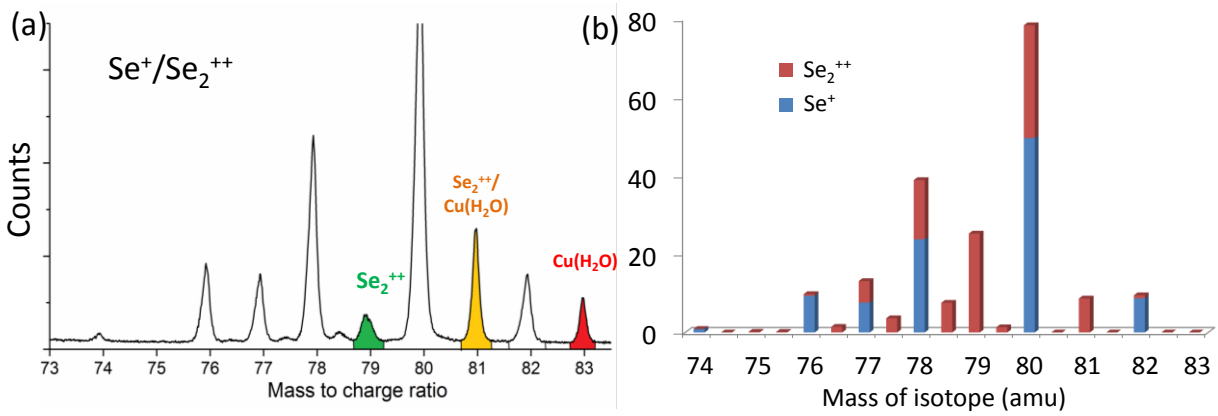

Figure 3.26: (a) Mass spectrum of CIGSe from 73 a.m.u. to 83 a.m.u., (b) Isotopic abundance of Se^+ and Se_2^{++}.

In some cases, peaks corresponding to $CuSe_2^+$ are also observed and are also accounted in calculations, however these peaks are not always present in mass spectrum and reasons for appearance or disappearance of these peaks is not known. Due to background noise in mass spectrum, each element would have its own detection limit i.e. below this concentration the element cannot be detected. Detection limit of elements in the mass spectrum can be

calculated as ratio of background noise around the element to the total number of detected ions. For elements in CIGSe, detection limits calculated are provided in Table 3-2.

Table 3-2: Detection limits of elements present in CIGSe.

Element	Detection limit (in ppm)
Cu	80 to 150
In	80 to 100
Ga	100 to 120
Se	50 to 80
Na	8 to 20

Due to lower atomic mass of Na (23 a.m.u.) as compared to majority of atoms, detectability of Na atom is very high when compared to other elements and is very beneficial for studies here.

3.5.2 Atom Probe Tomography of CIGSe Grains

As APT is a destructive technique, atomic distributions are obtained after 3D reconstruction procedures providing typical analyzed volume of 50×50×200 nm^3. 3D atomic scale distribution obtained from an analyzed atom probe tip of CIGSe (x=0.84) is reconstructed and is shown in Figure 3.27. This particular analyzed volume did not contain any GB (and thus no sodium) and shows distribution of Cu, In, Ga, Se atoms inside the grain. As illustrated, APT is capable of analyzing atomic distribution in three dimensions which enables this technique to obtain useful statistics at sub nanometer resolution. Statistics such as clustering, composition depth profile, GB composition profile, nearest neighboring distribution etc. can be obtained from statistical analysis in atom probe. Previous works have already shown tremendous capability of this instrument to understand photovoltaic cells at atomic scale [24–26]. Depth concentration profile of CIGSe (x=0.84) along tip is shown in Figure 3.27, as thin films were processed by CuPRO process, we observe no gradient in Ga/In concentration with depth and demonstrates capability of APT to quantify accurate composition profile at nanometer level with atomic level fluctuations. From Figure 3.27, it can be noted that atomic composition of all elements is uniform with small statistical fluctuations. Statistical analysis also showed that distribution of atoms in APT atomic volume

is homogenous without indication of any atomic clusters or biased composition. This is explained using pair correlation function in appendix A for case of CIGSe.

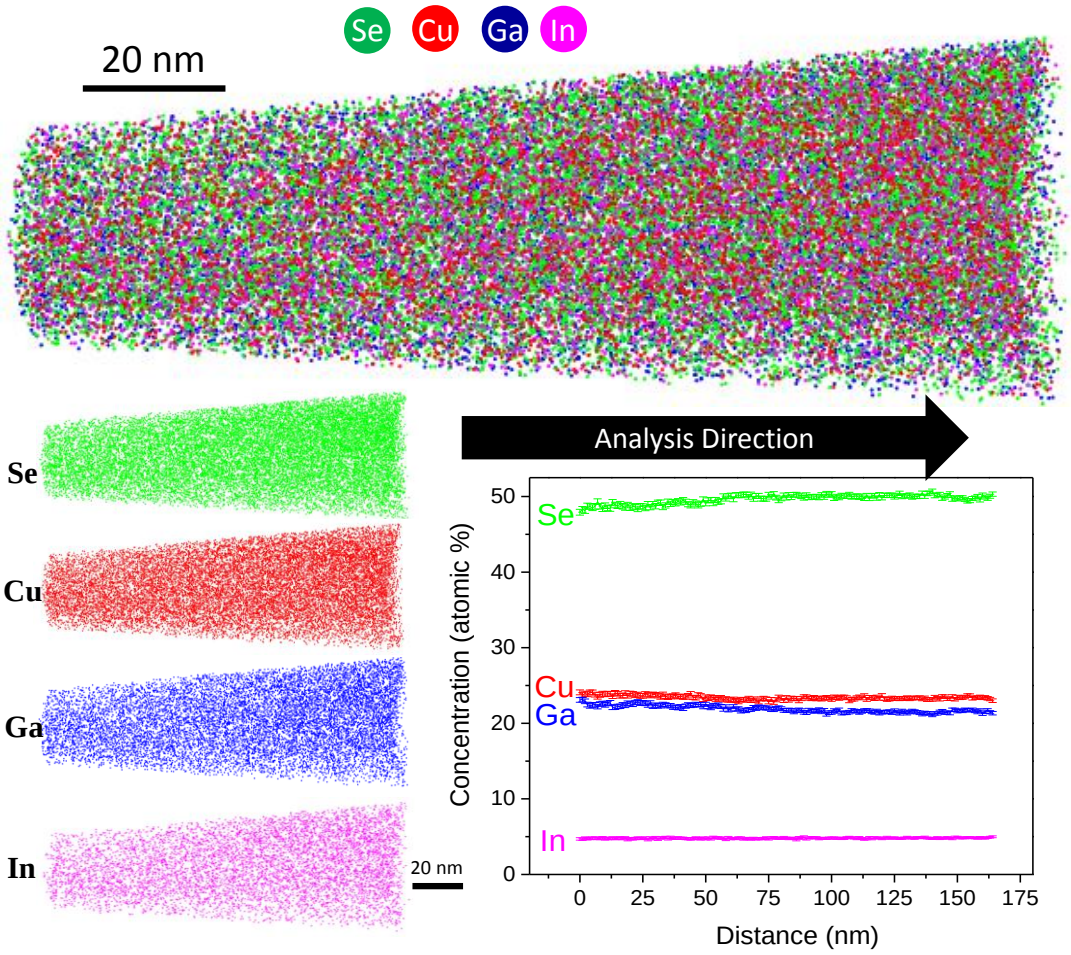

Figure 3.27: Reconstructed 3D APT image of CIGSe with x=0.84. Colors of respective elements are shown. Composition depth profile is shown in atomic % for respective elements.

Calculating Ga ratio (x) from Figure 3.27 measures x = 0.84 ± 0.02 which is in very well agreement with composition observed by EDX. Composition of all samples measured using APT is compared with EDX value in Table 3-3. Compositions of Cu, In, Ga and Se inside grains of CIGSe measured using APT for different CIGSe samples are shown. Comparison with EDX values shows well applicability of APT to measure compositions in sample regardless of their difference in Ga/In compositions. Also 'x' calculated using APT is compared with EDX values and the two results shows good consistency. This indicates well applicability of APT in analyzing CIGSe, provided optimized parameters.

Table 3-3: Atomic compositions measured using APT inside grains of CIGSe for respective different samples. Compositions measured using EDX are also shown to compare with APT.

Compositions measured by APT					
Sample	Cu (at %) ±0.1	In (at %) ±0.1	Ga (at %) ±0.1	Se (at %) ±0.2	Ga ratio (x)
1	23.7	26.1	0.0	48.9	0.00
2	24.5	21.0	4.8	49.6	0.18
3	24.8	18.1	10.9	46.0	0.37
4	25.0	14.3	13.1	46.5	0.48
5	24.9	10.6	16.9	47.2	0.61
6	24.8	10.1	19.4	45.0	0.66
7	22.9	5.2	23.8	47.2	0.82
8	23.0	0.0	27.2	48.8	1.00

Compositions measured by EDX					
Sample	Cu (at %)	In (at %)	Ga (at %)	Se (at %)	Ga ratio (x)
1	24.8±0.9	26.5±1.3	0.0	48.3±1.4	0.00
2	24.6±0.9	22.2±1.3	3.9±0.8	48.5±1.4	0.17
3	24.8±0.8	17.5±1.0	9.9±0.8	47.8±1.4	0.39
4	23.2±0.9	15.7±1.3	9.7±0.8	51.4±1.4	0.47
5	23.4±0.9	14.6±1.3	11.1±0.8	51.0±1.4	0.56
6	23.6±0.9	12.4±1.3	13.0±0.8	51.1±1.4	0.67
7	24.5±0.9	4.5±1.0	20.7±1.0	50.3±1.4	0.84
8	24.3±0.8	0.0	26.9±1.0	48.4±1.3	1.00

Applicability of APT for Ga poor CIGSe was already shown by Cadel et.al [24], hence the above example is illustrated for Ga rich CIGSe with similar experiment parameters. Well applicability of results in Figure 3.27 and Table 3-3 shows the technique is suitable for CIGSe with different Ga contents while using optimized pre analysis and post analysis parameters.

3.5.3 Presence of Defects

In present study, various CIGSe samples were analyzed in atom probe and repetitive measurements were performed on each sample to have better statistics. A large number of experiments were performed and Na distribution in CIGSe can be classified in four categories:

1. No Na in grains: Na was found absent in CIGSe grains, as discussed in Figure 3.27.
2. Na uniformly distributed in grains: In few cases (≈ 5% cases) Na was found homogenously distributed in CIGSe grains.
3. Na segregated along defects: Na was also found present in form of clusters, and also along linear and planar dislocations. As shown in Figure 3.28, Na is found to be present in form of clusters which can be due to point defects present in CIGSe grains and also in few cases Na was found linearly segregated which can be attributed to linear dislocations in CIGSe. Figure 3.29 shows a rare case (only 1 observed in this work) of decoration of Na along planar dislocation. It is interesting to note that composition of various elements vary in vicinity of dislocation as shown in Figure 3.29b for x=0.36. Similar results were obtained for GB composition profile (detailed in next chapter) for x=0.36. Recently Couzinie-Devy et.al [28] explored Na distribution in CIGSe and concluded that composition profile along these defects is similar to their GB composition profile, which is also observed independently in this work.

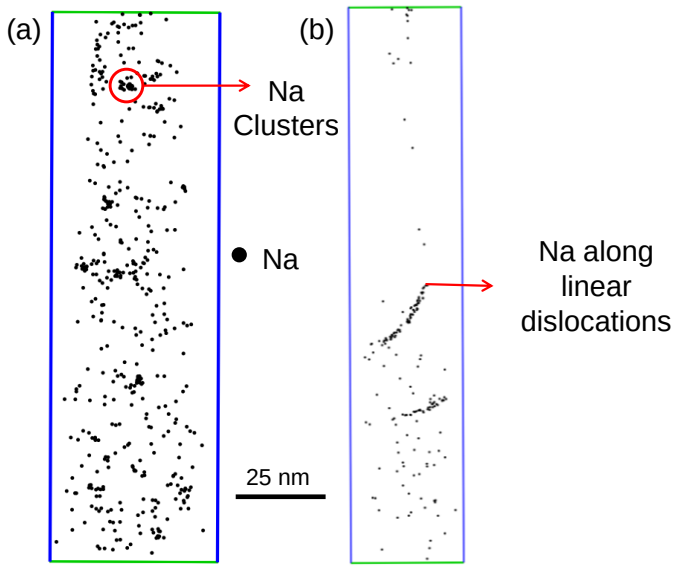

Figure 3.28: Distribution of Na atoms (shown in dots) present in CIGSe in form of (a) clusters, and decorated along (b) linear dislocations.

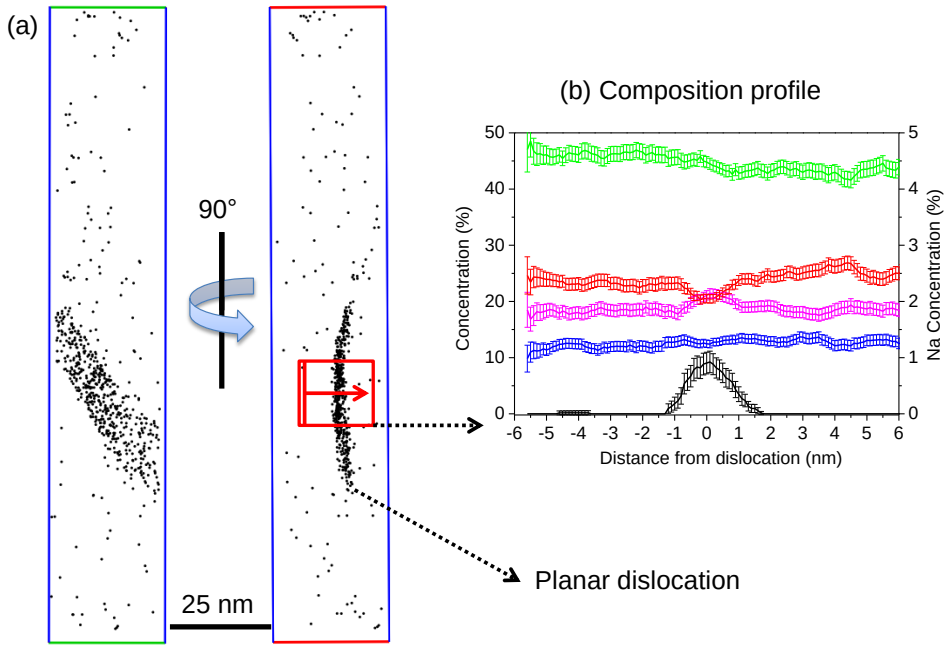

Figure 3.29: (a) 3D reconstructed APT volume depicting distribution of Na atoms along a planar dislocation present in CIGSe (x=0.36), volume is rotated to visualize dislocation. (b) Composition profile across dislocation, Na enrichment indicates position of dislocation.

4. Na segregated along GBs: In most of the results obtained here (80 % results), Na was found segregated along GBs which is thoroughly discussed in next chapter.

Conclusions

This chapter discussed characterization of CIGSe photovoltaic cells prepared with different Ga concentration fabricated using CuPRO process. Device performance test namely J-V and EQE measurements were performed to check device quality of CIGSe cell performance. Microstructural characterization techniques were performed by means of XRD, SEM, EBSD to ensure appropriate grain size distribution and orientation of the grains. These techniques demonstrated that cells processed here were genuine CIGSe cells with proper phase and composition. Electrical measurements and microstructural characterizations were important first, to ensure proper electrical nature of CIGSe absorber layer before analyzing in time consuming high resolution techniques like APT. It is also further demonstrated here that APT is well applicable for CIGSe with different Ga content subject to standardized experiment parameters and is appropriate for GB characterization.

In this study, we make an attempt to explore the microstructure and atomic distribution of CIGSe films for various Ga contents to explain deviation in device properties of CIGSe with a strong emphasis on grain boundaries as discussed in next chapter.

References

1. Meillaud F, Shah A, Droz C, Vallat-Sauvain E, Miazza C. Efficiency limits for single-junction and tandem solar cells. *Solar Energy Materials and Solar Cells* 2006; **90**: 2952–2959. DOI: 10.1016/j.solmat.2006.06.002

2. Singh P, Ravindra NM. Temperature dependence of solar cell performance—an analysis. *Solar Energy Materials and Solar Cells* 2012; **101**: 36–45. DOI: 10.1016/j.solmat.2012.02.019

3. Green MA. *Solar cells: operating principles, technology, and system applications*. Englewood Cliffs, NJ: Prentice-Hall 1982;

4. Kiess H, Rehwald W. On the ultimate efficiency of solar cells. *Solar Energy Materials and Solar Cells* 1995; **38**: 45–55. DOI: 10.1016/0927-0248(94)00214-2

5. Contreras MA, Mansfield LM, Egaas B, Li J, Romero M, Noufi R, Rudiger-Voigt E, Mannstadt W. Wide bandgap Cu(In,Ga)Se2 solar cells with improved energy conversion efficiency. *Prog Photovolt: Res Appl* 2012; **20**: 843–850. DOI: 10.1002/pip.2244

6. Contreras MA, Ramanathan K, AbuShama J, Hasoon F, Young DL, Egaas B, Noufi R. SHORT COMMUNICATION: ACCELERATED PUBLICATION: Diode characteristics in state-of-the-art ZnO/CdS/Cu(In1−xGax)Se2 solar cells. *Prog Photovolt: Res Appl* 2005; **13**: 209–216. DOI: 10.1002/pip.626

7. Shafarman WN, Klenk R, McCandless BE. Characterization of Cu(InGa)Se2 solar cells with high Ga content. in , *Conference Record of the Twenty Fifth IEEE Photovoltaic Specialists Conference, 1996*, 763–768. DOI: 10.1109/PVSC.1996.564240

8. Merdes S, Mainz R, Klaer J, Meeder A, Rodriguez-Alvarez H, Schock HW, Lux-Steiner MC, Klenk R. 12.6% efficient CdS/Cu(In,Ga)S2-based solar cell with an open circuit voltage of 879 mV prepared by a rapid thermal process. *Solar Energy Materials and Solar Cells* 2011; **95**: 864–869. DOI: 10.1016/j.solmat.2010.11.003

9. Hanket GM, Boyle JH, Shafarman WN. Characterization and device performance of (AgCu)(InGa)Se2 absorber layers. in *2009 34th IEEE Photovoltaic Specialists Conference (PVSC)*, 001240–001245. DOI: 10.1109/PVSC.2009.5411241

10. Jackson P, Hariskos D, Lotter E, Paetel S, Wuerz R, Menner R, Wischmann W, Powalla M. New world record efficiency for Cu(In,Ga)Se2 thin-film solar cells beyond 20%. *Progress in Photovoltaics: Research and Applications* 2011; **19**: 894–897. DOI: 10.1002/pip.1078

11. Eisenbarth T, Unold T, Caballero R, Kaufmann CA, Abou-Ras D, Schock H-W. Origin of defects in CuIn1 − xGaxSe2 solar cells with varied Ga content. *Thin Solid Films* 2009; **517**: 2244–2247. DOI: 10.1016/j.tsf.2008.10.142

12. Kodigala SR. *$Cu(In_{1-x}Ga_x)Se_2$ based thin film solar cells*. Amsterdam: Elsevier/Academic Press 2010;

13. Bakhori SKM, Raof NHA, Ng SS, Hassan HA, Hassan Z. Photoluminescence and XRD Crystalline Studies of InxAlyGa1-X-Yn Quaternary Alloys. *IOP Conf Ser: Mater Sci Eng* 2011; **17**: 012006. DOI: 10.1088/1757-899X/17/1/012006

14. Abou-Ras D, Caballero R, Kaufmann CA, Nichterwitz M, Sakurai K, Schorr S, Unold T, Schock HW. Impact of the Ga concentration on the microstructure of CuIn1–xGaxSe2. *phys stat sol (RRL)* 2008; **2**: 135–137. DOI: 10.1002/pssr.200802059

15. Abou-Ras D, Schorr S, Schock HW. Grain-size distributions and grain boundaries of chalcopyrite-type thin films. *Journal of Applied Crystallography* 2007; **40**: 841–848. DOI: 10.1107/S0021889807032220

16. Abou-Ras D, Gibmeier J, Nolze G, Gholinia A, Konijnenberg P. On the capability of revealing the pseudosymmetry of the chalcopyrite-type crystal structure. *Crystal Research and Technology* 2008; **43**: 234–239. DOI: 10.1002/crat.200711082

17. Humphreys FJ. Review Grain and subgrain characterisation by electron backscatter diffraction. *Journal of Materials Science* 2001; **36**: 3833–3854. DOI: 10.1023/A:1017973432592

18. Philip Jackson, Dimitrios Hariskos, Roland Wuerz, Oliver Kiowski, Andreas Bauer, Michael Powalla. Properties of High Efficiency Cu(In,Ga)Se2 Solar Cells. 2015; Available at: https://mrsspring.zerista.com/event/member/164716

19. Priester L. "Atomic Order of Grain Boundaries," in Grain Boundaries Springer Series in Materials Science. (Springer Netherlands), 49–92. Available at: http://link.springer.com/chapter/10.1007/978-94-007-4969-6_3 [Accessed July 23, 2015]

20. http://www.engineeringarchives.com/img/les_matsci_surfacedefects_1.png.

21. Illustration of tilt and twist grain boundaries. Remade in 3D to clarify details and rotation planes/axis (original: TiltAndTwistBoundaries.png). Copyright: Slinky puppet

22. Miller MK. *Atom probe field ion microscopy*. Oxford; New York: Clarendon Press ; Oxford University Press 1996;

23. Arnoldi L. PhD thesis: INTERACTION LASER-NANOPOINTE SOUS CHAMP ELECTRIQUE INTENSE : APPLICATION A LA SONDE ATOMIQUE. 2014; Available at: https://tel.archives-ouvertes.fr/tel-01095529/document [Accessed June 8, 2015]

24. Cadel E, Barreau N, Kessler J, Pareige P. Atom probe study of sodium distribution in polycrystalline Cu(In,Ga)Se2 thin film. *Acta Materialia* 2010; **58**: 2634–2637. DOI: 10.1016/j.actamat.2009.12.049

25. Choi P-P, Cojocaru-Mirédin O, Abou-Ras D, Caballero R, Raabe D, Smentkowski VS, Park CG, Gu GH, Mazumder B, Wong MH, et al. Atom Probe Tomography of Compound Semiconductors for Photovoltaic and Light-Emitting Device Applications. *Microscopy Today* 2012; **20**: 18–24. DOI: 10.1017/S1551929512000235

26. Raghuwanshi M, Lanterne A, Le Perchec J, Pareige P, Cadel E, Gall S, Duguay S. Influence of boron clustering on the emitter quality of implanted silicon solar cells: an atom probe tomography study. *Prog Photovolt: Res Appl* 2015;n/a–n/a. DOI: 10.1002/pip.2607

27. Cojocaru-Mirédin O, Choi P, Wuerz R, Raabe D. Atomic-scale distribution of impurities in CuInSe2-based thin-film solar cells. Ultramicroscopy 2011; 111: 552–556. DOI: 10.1016/j.ultramic.2010.12.034

28. Couzinie-Devy F, Cadel E, Barreau N, Arzel L, Pareige P. Na distribution in Cu(In,Ga)Se2 thin films: Investigation by atom probe tomography. Scripta Materialia 2015; 104: 83–86. DOI: 10.1016/j.scriptamat.2015.03.028

4 Chapter Four: Influence of Grain Boundary Chemistry on Device Performance of $Cu(In,Ga)Se_2$

In this chapter we investigate grain boundaries (GBs) in APT for different samples of CIGSe with varying Ga concentration. APT is a promising technique to analyze GB at atomic level resolution and to measure GB composition profile. GB chemistry of CIGSe is presented in this chapter illustrating atomic level variations across GB for various grain concentration of CIGSe.

4.1 Atomic scale characterization of grain boundaries in APT

As discussed previously, correlative EBSD-APT or TEM-APT on tip is not the best technique due to embrittlement of tip at high voltages. Hence we require a reference to identify location of GB after successful APT analysis. It is well known that Sodium (Na) atoms accumulate at GB which can be used to visualize GB interface in 3D atom probe volume. Being beneficial for device performance of CIGSe, Na is also helpful in our case in identifying the exact GB position and interface. Additionally, atomic mass of Na (23 a.m.u.) is far lighter than other elements (Cu, In, Ga, Se) keeping it far from background noise and providing high resolved signal of Na.

Grain boundary is hence identified here as planar accumulation of Na atoms. Atomic mass peak at 23 a.m.u. in mass spectrum is explicit to Na element and sometimes atomic mass peaks at 39 is also evident in mass spectrum which may correspond to Na + O or K (Potassium). Presence of other isotope of K (41 a.m.u.) confirms the presence of K, otherwise 39 a.m.u. peak is only due to NaO molecular specie. When atomic mass peak is observed at 41 a.m.u. (6 % K isotopic abundance) the total amount of K and Na atoms that are present can be calculated. Absence of 41 a.m.u. peak indicates absence of K and hence all atoms present are Na atoms.

A typical reconstructed APT volume of CIGSe is shown in Figure 4.1, SEM image of tip before analysis is shown on left side. Each dot in the 3D volume represents an atom of the element corresponding to color reference. Relative percentage of atoms of Cu, In, Ga, Se shown is in fewer amounts (2%) than Na (100%) to better visualize the GB. As shown in Figure 4.1, planar segregation of Na atoms is visible and signifies presence of GB interface in that position. To indicate GB interface clearly, 3D volume is rotated showing planar accumulation of Na atoms along GB interface which separates two different grains.

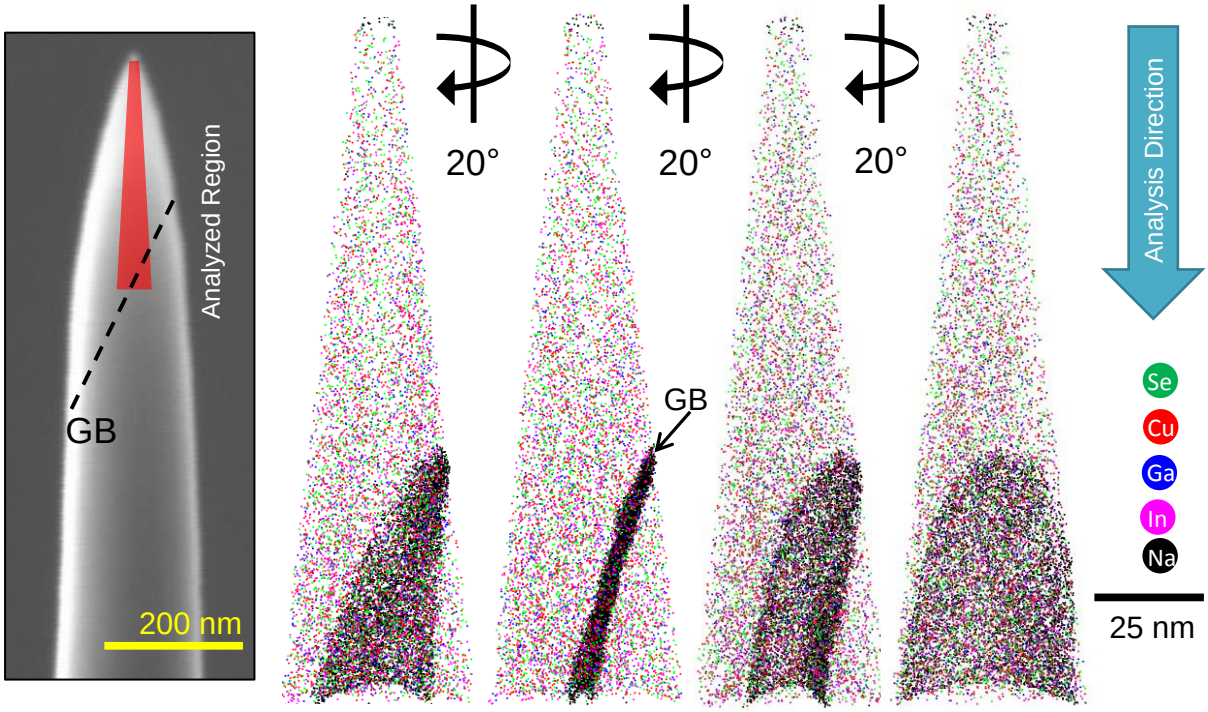

Figure 4.1: SEM image of CIGSe APT tip (left) before analysis and respective reconstructed volume after APT analysis containing one GB. APT volume is rotated along analysis direction to better visualize GB interface.

Optimized experimental parameters ensured uniform field evaporation of Cu, In, Ga, Se atoms, but at GB additional elements like Na are present which may perturb trajectory of atoms due to what is called Local Magnification (LM) effect [1,2]. LM effects arise due to the fact that elements/phase at GB might have field evaporation higher or lower than constituent phase/compound. Two cases of LM are shown in Figure 4.2:

a) Low-field GB: In this case, when field evaporation of GB is lower than the matrix, the GB is field evaporated preferentially than neighboring phase/compound, forming an inside curvature. Trajectory of ions in GB hence converges due to inside curvature resulting in higher density of ions at the GB.
b) High-field GB: In this case, when field evaporation of GB is higher than corresponding matrix, phase/compound at matrix is field evaporated preferentially than GB. This leads to formation of an outside curvature, hence trajectory of ions at GB diverges outside resulting in low density of ions at the GB.

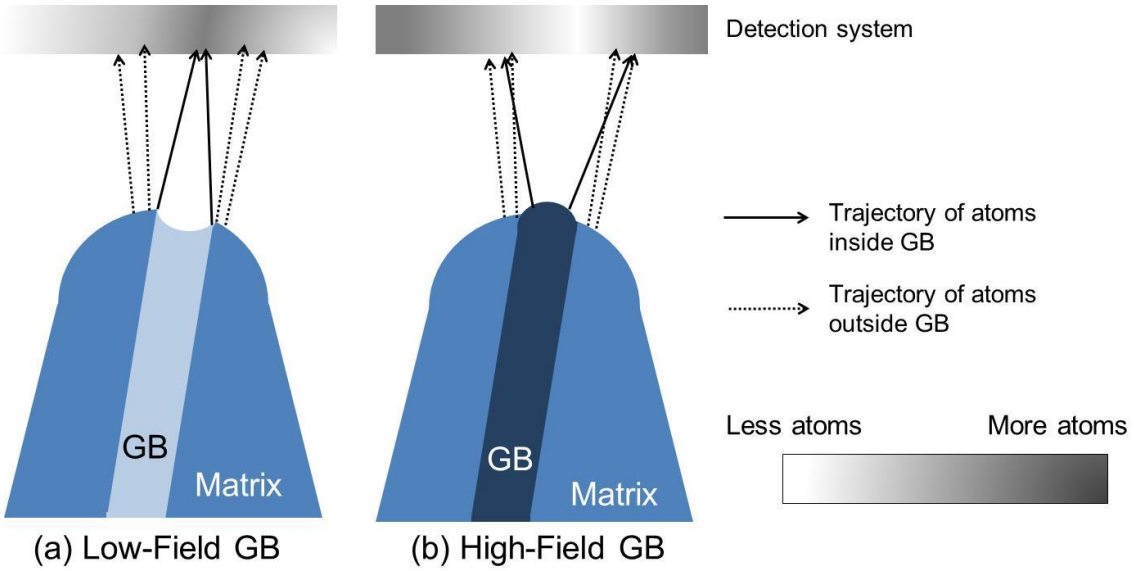

Figure 4.2: Schematic representation of trajectory of ions in a low field GB and high field GB. Trajectory of atoms in low field GB is converging and atomic density detected in APT is more at GB. For high field GB, trajectory of atoms is of diverging nature which results in fewer atoms at GB.

Here Na is found to segregate at GB. This element has a field of evaporation lower than other constituent elements as presented in Table 4-1 leading thus to a low field GB. Apart from Na, enrichment/depletion of other elements or formation of different phases at GB may also decide the type of GB (high field or low field which is discussed in next sections).

In order to minimize the possible LM effects during APT experiments, it is recommended to localize GB plane normal to analysis direction. However, alignment of GB exactly normal to APT analysis direction is statistically improbable and in most cases GB is located with a given angle with the analysis direction.

Table 4-1: Field evaporation of different elements in CIGSe as measured for singly charged ion. Data source: Gault et.al [3]

Elements	Field evaporation
Copper	30 V/nm
Indium	12 V/nm
Gallium	15 V/nm
Selenium	-
Sodium	11 V/nm

As typical analyzed volume in APT is of the order of 50×50×200 nm^3, most of the volumes can contain only one GB. However in fortunate cases more than one GB is observed. An example is shown in Figure 4.3 where three grains separated by a triple junction are observed. This is a very rare observation involving three grain boundaries localized on top of a tip. As the triple junction is not in the center, GB between grain 1 and grain 2 is very close to the surface of the analyzed region, hence due to high statistical fluctuations and also due to Ga contamination at tip surface, $GB_{1/2}$ and $GB_{1/3}$ are not taken into consideration in the data set in the following results. Therefore only $GB_{2/3}$ is considered here for statistical analysis.

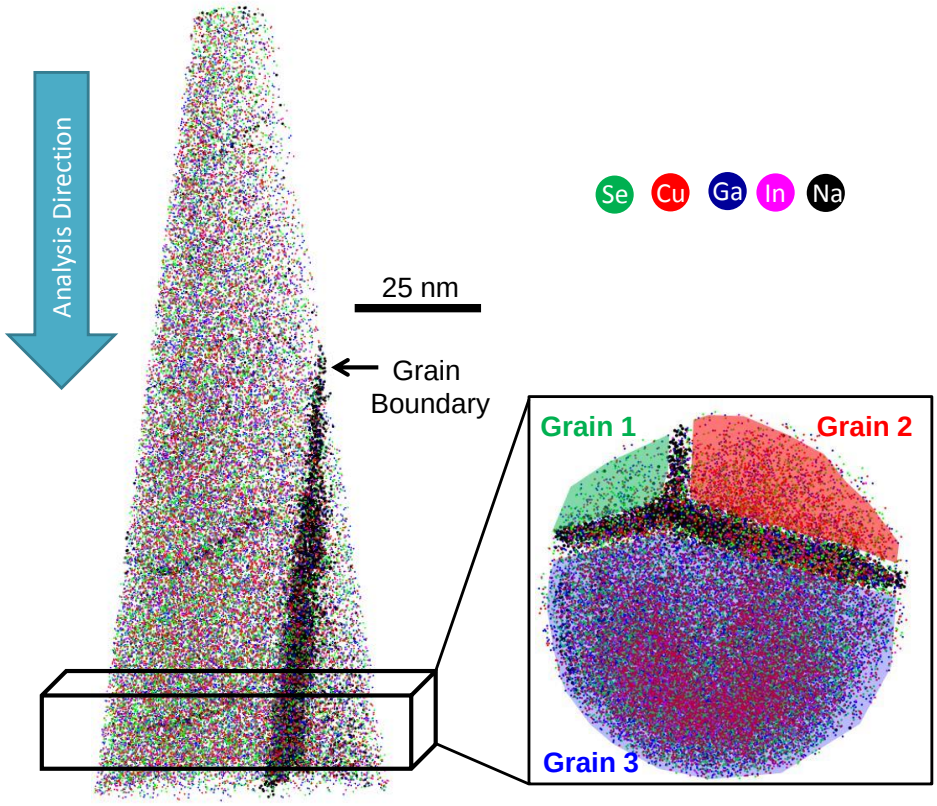

Figure 4.3: Reconstructed volume of an analyzed CIGSe APT tip containing a triple junction (crossing of three GBs). (Right) atomic distribution near bottom of analyzed volume demonstrating three grains separated by three GBs.

As APT involves experiments at high electric field, materials with a low resistance under the stress generated by the electric field may not sustain at high voltages due to increase in field at tip apex. Moreover polycrystalline samples are expected to be more prone to tip failure due to increase in stress at GB. Nevertheless, it is impressive to note that analyzed tip in Figure 4.3 was still active (not ruptured) even at high voltage (~10 kV) and containing three GBs. This shows CIGSe is able to withstand high electric fields, which is crucial to perform APT experiment.

4.2 Measurement of grain boundary composition profile

An example of analyzed 3D atomic volume of Ga poor CIGSe (x=0.39) containing a GB is shown in Figure 4.4a. As concentration of Na is particularly low (0.5 to 3 %) it is shown in a higher amount (100%) and larger size as compared to other atoms (5% shown in figure) for a better visualization of GB interface. A representative 3D volume box is extracted, containing GB for further analyses and composition calculations. Figure 4.4b shows the distribution of various elements in vicinity of the GB. All atoms accumulate at GB which can be quantified by measuring the atomic density profile across GB.

Figure 4.4c represents the number of atoms of respective elements distributed in vicinity of GB. It can be noticed that number of atoms of all species increase at GB which is basically due to local magnification effect as described in case of low field GB in Figure 4.2a. The low field characteristic in this case may be due to the lower evaporation field of Na or also due to formation of a low evaporation field phase at GB. The GB chemistry in this case is shown in Figure 4.4d illustrating Cu depletion at GB. From Table 4-1, Cu has a relatively higher evaporation field than other elements, hence in this case of Cu depletion at GB (Figure 4.4d) we expect a 'low evaporation field' phase at GB. Therefore increase in atomic density at GB can be due to the effect of Na or to a Cu poor phase at GB or both.

However the profile, Figure 4.4c could not reveal change in atomic composition. Composition profile (in atomic %) across GB is calculated to quantify concentration of various elements at grains and GBs. Sampling box with size of 1 nm width is moved by 0.1 nm along perpendicular to GB interface to measure GB chemistry has shown in Figure 4.4d for x=0.39. GB chemistry shows concentration profile of various elements in vicinity of GB. As in Figure 4.4d GB is identified by Na increment which is accompanied by Cu depletion and In enrichment, whereas no appreciable change is observed in Ga and Se concentration. Error bars in Figure 4.4d are due to statistical sampling error calculated during APT analysis with standard deviation 2σ where σ is given by:

$$\sigma\ (in\ \%) = 100 \times \sqrt{\frac{C(1-C)}{N}} \qquad \textbf{(4.1)}$$

Where C is the concentration of solute and N is the number of detected ions in the sampling box. To illustrate, the error in Cu composition in Figure 4.4d is obtained as follows: sampling width is chosen to be 1nm wide (with a surface area of 600 nm^2), thus containing N=20,000 atoms in the sampling box, C for Cu is here 0.24 (24%). Solving equation (4.1) for Cu yields

σ = 0.3 at. %. Hence Cu concentration is measured as = 24 % ± 0.6 % (at.). Similar calculations are performed for other elements and represented in Figure 4.4d. Figure 4.4d shows an apparent difference between Na enrichment maximum and Cu depletion minimum which mainly arise from local magnification effects. However an evident trend of increase or decrease in composition can be extracted using APT.

As there is no appreciable change in concentrations of Se and concentration of In, as Ga will vary from one sample to another and as Na is always present on crystalline defects, we characterize the GB by its Cu variations. Hence variation in Cu concentration (ΔCu) will be calculated by subtracting Cu concentration at GB by Cu concentration in grain, or mathematically:

$$\Delta Cu\ (\%) = \frac{[Cu]_{GB} - [Cu]_{Grain}}{[Cu]_{Grain}} \quad \textbf{(4.2)}$$

Hence ΔCu is negative for Cu depletion and positive for Cu enrichment at GB. GB chemistry is thus characterized for all the samples providing atomic scale information in vicinity of GB. For Figure 4.4, ΔCu is calculated and is equal to -16.7 % which represents 16.7% decrease in Cu concentration at GB.

It is better to use equation (4.2) for change in Cu concentration at GB instead of using Gibbsian Interfacial excess (discussed in next section) as the latter is a better statistical method for solutes having low concentration.

Figure 4.4 illustrates GB chemistry for Ga poor CIGSe; similar measurements are performed on Ga rich CIGSe and are shown in Figure 4.5.

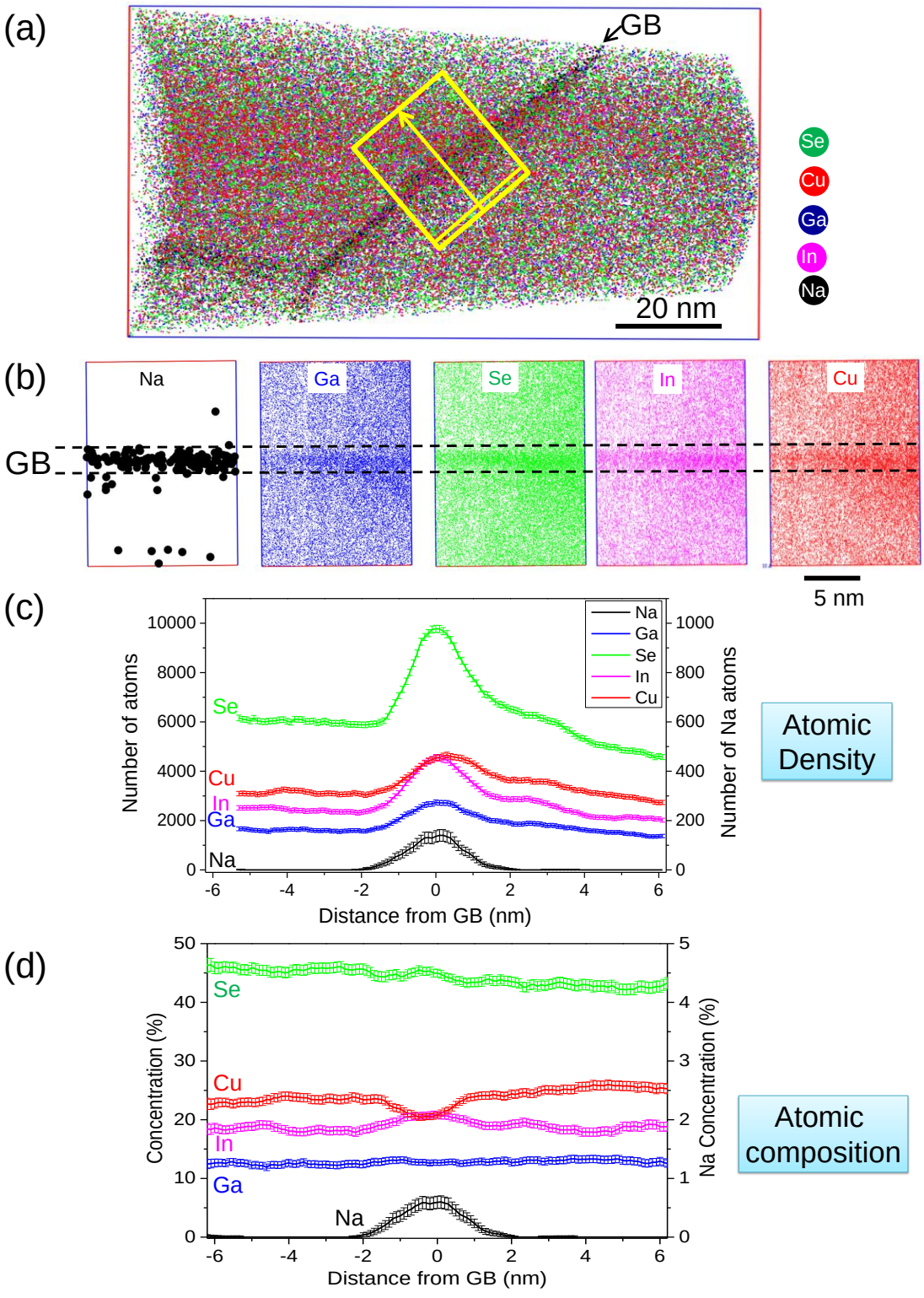

Figure 4.4: (a) Reconstructed 3D volume after APT analysis of CIGSe (x=0.39), Na atoms shown is in higher amount than other elements (5%). GB position is shown (b) Individual atoms mapped from extracted volume in box in (a). (c) GB chemistry of CIGSe for x=0.39, right axis represent concentration of Na and left axis shows concentration of other elements. (d) Number of atoms of respective elements versus distance. Right axis represents Na atomic density. An increase in atomic density at GB is apparent.

Figure 4.5a represents a reconstructed 3D APT volume of CIGSe (x=0.84), each dot representing an atom. For better visualization, Na atoms are shown in higher amount (100% Na) than other elements (2% Cu, In, Ga, Se). In contrary to the previous case of Ga poor CIGSe, a decrease in atomic density at GB is evident in Figure 4.5b. Figure 4.5c shows an overall decrease in number of atoms at GB indicating higher evaporation field at GB. Formation of high field GB can be due to the formation of a higher field phase at GB. GB chemistry as shown in Figure 4.5c shows Cu enrichment at GB indicating Cu rich phase at GB. As Cu possesses high evaporation field, Cu enriched GB turns into high field phase resulting in formation of outside curvature and diverging trajectory, following Figure 4.2b. Hence due to enrichment of Cu at GB, atomic density is reduced at GB. As similar to the previous case, Na is enriched at GB. The low field GB in Ga poor CIGSe and high field GB in Ga rich CIGSe is clearly explained by the difference in Cu content at GB in the two different cases.

Figure 4.5d represents GB chemistry measured for x=0.84. Significant changes in atomic distribution are observed for Ga poor and Ga rich cell when comparing Figure 4.4 and Figure 4.5. Ga depletion accompanied by Cu enrichment is observed in this case. However no significant change in Se and In concentration is observed. This shows that Cu amount at GBs shifts from depletion to enrichment while switching from Ga poor CIGSe to Ga rich CIGSe.

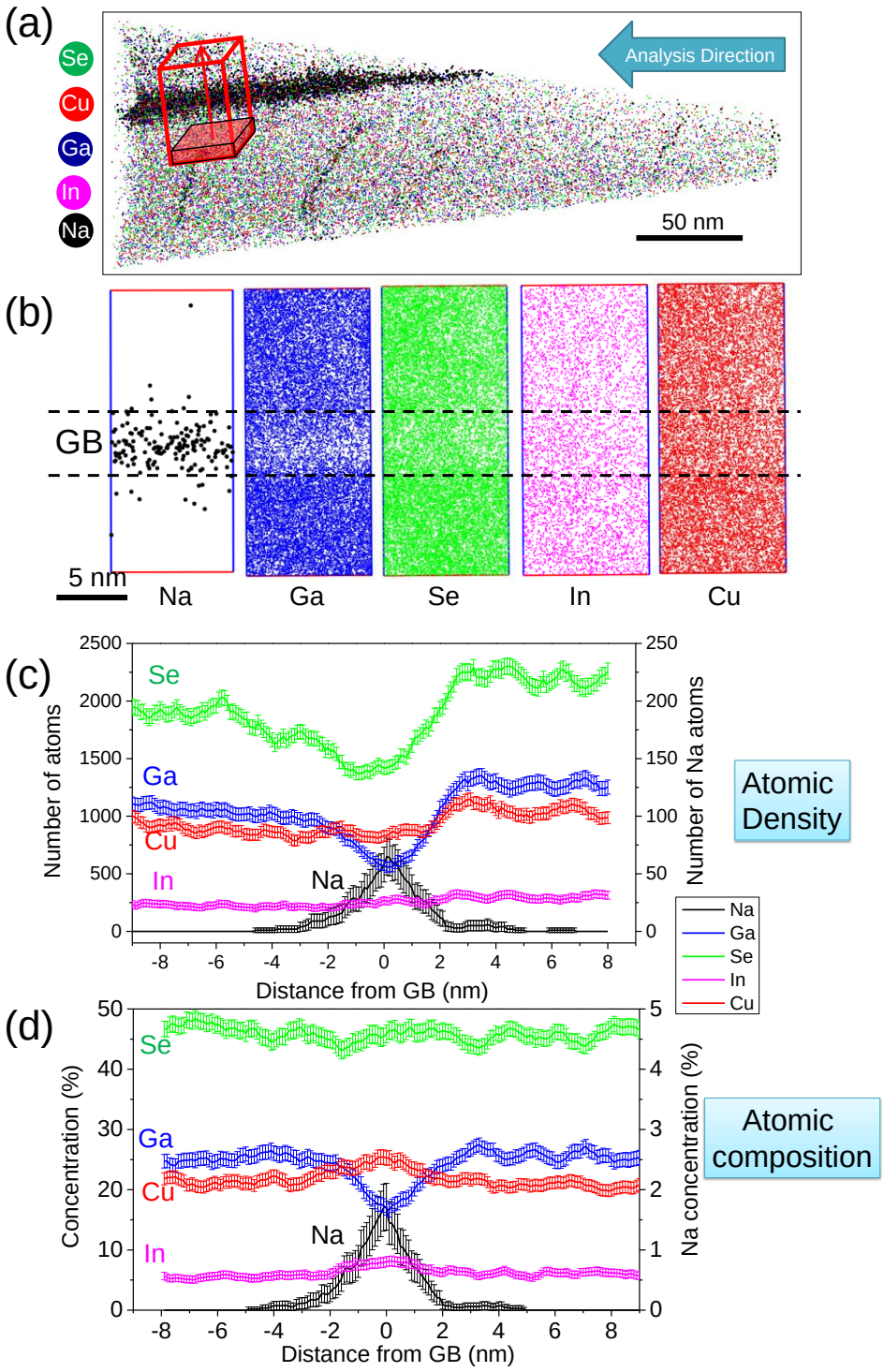

Figure 4.5: (a) Reconstructed 3D volume after APT analysis of CIGSe (x=0.84), Na atoms shown is in higher amount and size. (b) Individual atoms mapped from extracted volume in box in figure (a). (c) GB chemistry of CIGSe for x=0.84, right axis represent Na concentration and left axis shows concentration of other elements. (d) Atomic density in vicinity of GB, right axis represents Na atomic density. A decrease in atomic density at GB is apparent.

In all the analyses performed in this study, Cu poor GBs are always associated to increased atomic density and Cu rich GBs always resulted in decreased atomic density at GB. This is due to the high evaporation field of Cu and to its large variations at GB.

Increase or decrease in atomic density as measured by APT is mainly due to local magnification artifact in APT. Hence compositions at GB are mainly quantified by measuring composition profile across GB (or GB chemistry).

These results show that GB chemistry in CIGSe depends on its grain concentration and significant changes are observed for different 'x'. Two examples were shown for Ga poor and Ga rich compounds. Cu depletion is observed for Ga poor samples whereas Cu enrichment is observed for Ga rich samples. In order to inspect the point of transition where nature of GBs is converted from Cu poor to Cu rich type we investigate various CIGSe samples with different Ga contents.

4.3 Grain boundary investigation of CIGSe at various Ga/In concentration

4.3.1 Quantification of Na segregation at grain boundary

Beneficial effects of Na at GBs of CIGSe are known for years and thoroughly discussed in chapter 1. Soda lime glass substrates are known to produce high efficient CIGSe cell, due to segregation of Na atoms along GB. However one may argue that difference in Na concentration at GB for different samples may also be a potential reason for degraded performance of Ga rich CIGSe. Figure 4.6 shows variation of Na concentration at GB for different 'x'. From Figure 4.6 it can be noticed that Na concentration at GB is restricted within 0.4 to 3 atomic percent. Significant variations in Na concentration are observed even with same 'x'. However as a function of Ga content there is no specific pattern observed. Na concentration is found to be quite randomly distributed irrespective of Ga content as depicted from Figure 4.6.

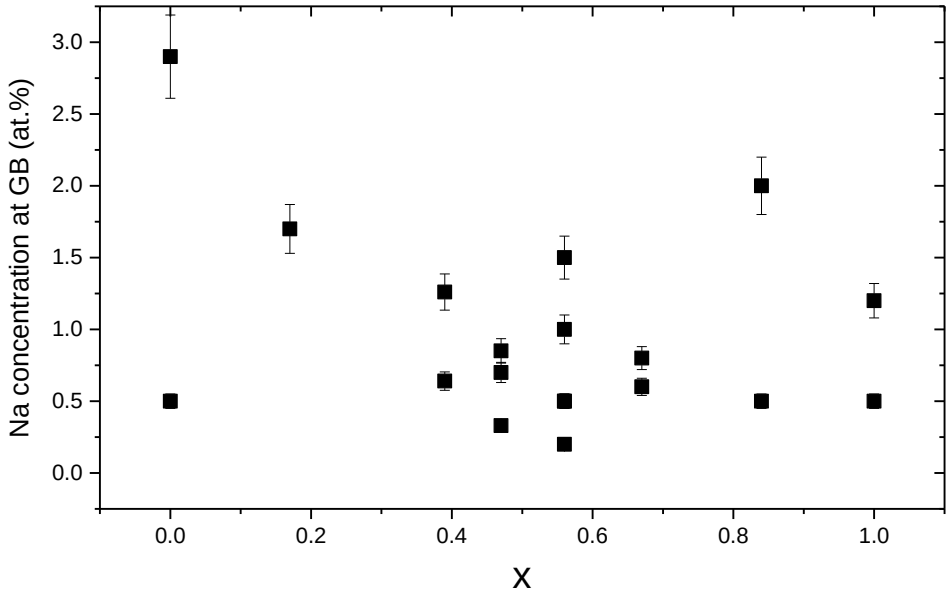

Figure 4.6: Na concentration at GB (at. %) as a function of x in $CuIn_{1-x}Ga_xSe_2$ measured in this work.

No significant effect of Ga/In concentration is observed on GB concentration of Na. However instead of measuring in atomic %, it is suggested to quantify segregation of solute species at GB using Gibbsian Interfacial Excess (Γ), a thermodynamic quantity [4] defined as number of segregated solute atoms per unit interfacial area. Calculation of Gibbsian Interfacial excess is thoroughly discussed in appendix B. Previous works have demonstrated Γ_{Na} (Gibbsian interfacial excess of Na) at different stages of thin film deposition in ref. [5], here we explore Γ_{Na} of CIGSe at GB as a function of 'x'.

Figure 4.7 represents Γ_{Na} measured in present work for CIGSe samples with various 'x' processed using CuPRO process. Results are compared with measurements on 3-stage processed samples in previous studies by Couzinie-Devy et.al [5] and Cojocaru et.al [6]. Figure 4.7 illustrates that Γ_{Na} varies from 0.5 atoms/nm^2 to 6.5 atoms/nm^2. No significant variation or pattern in Na segregation is observed in this study for different Ga contents and an average value of Gibbsian interfacial excess of Na (Γ_{Na}) is measured as ≈2.2 atoms/nm^2.

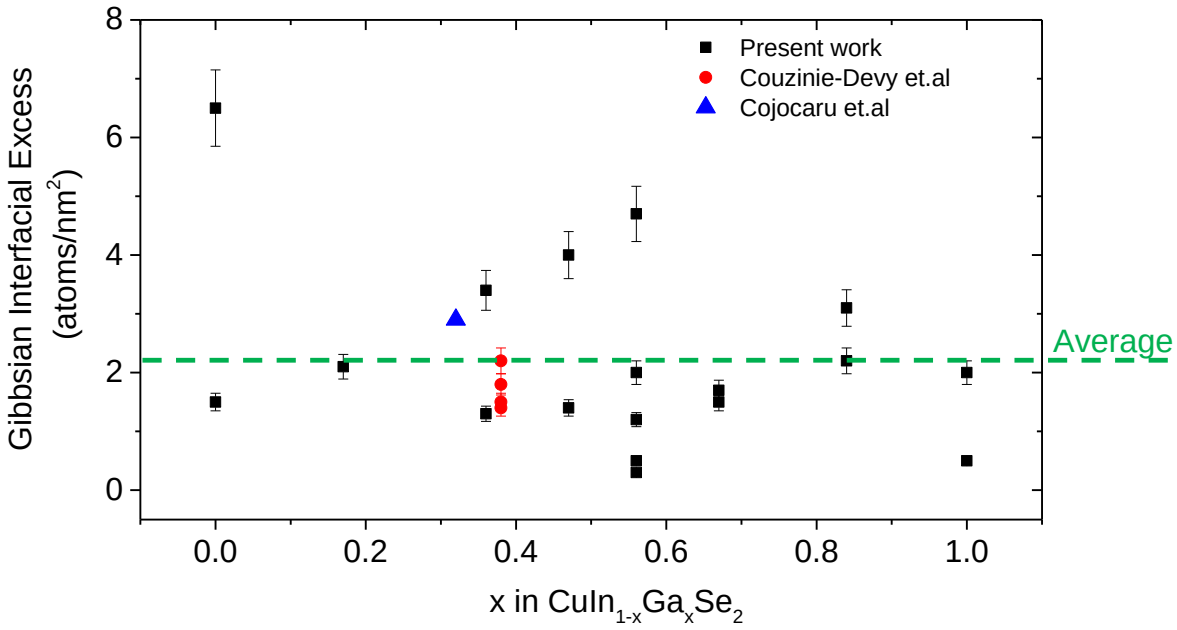

Figure 4.7: Γ_{Na} for various Ga content in CIGSe compared with results obtained by Couzinie-Devy et.al [5] and Cojocaru et.al [6] on 3-stage processed samples.

Amount of Na atoms at GB are thus found almost similar for all the samples (the difference is not very high). Therefore, the limited performance of Ga rich CIGSe cells is certainly not due to difference in Na levels at GB. In addition, it must be noted that GB misorientation is not taken into account in present study and hence not related with amounts of Na at GB segregation, which may be an important factor to decide amount of Na at grain boundaries.

Figure 4.8 represents number of GBs (per sq. μm) as a function of x calculated using EBSD results in chapter 3. Correlating Figure 4.7 (Na coverage at GBs is almost same for all samples) with Figure 4.8 (number of GBs increase as a function of x), it can be concluded that amount of Na at GBs is not dependent on total number of GBs and amount of Na at GB does not explain limited performance of wide band CIGSe.

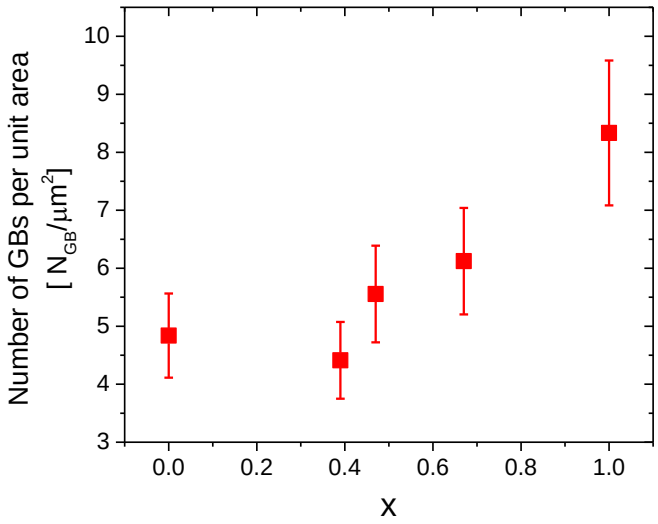

Figure 4.8: Number of GBs per unit area ($N_{GB}/\mu m^2$) as a function of x, calculated using EBSD measurements as described in chapter 3.

Hence in the following section, composition profiles of various elements are presented and discussed.

4.3.2 Composition profiles of Cu, In, Ga, Se and Na at GB

A systematic study of GB chemistry for different CIGSe grain concentration is presented here to determine transitions between two natures of GB: Cu poor and Cu rich and also variation in concentration of other elements at GB for different 'x'. All results presented in this work are based on measurement of random GBs. That is, we do not have any information on the misorientation angle of the GB before APT analysis and hence it is unknown that whether the GB is a twin boundary or a non-twin boundary. As GBs are identified by Na enrichment, composition profile of Na is shown to represent GB interface and is marked by distance from GB=0 nm in the composition profile.

Eight different prepared samples were divided into three regimes according to their Ga ratio (x), namely: Ga poor (x<0.4), Ga intermediate (0.4< x <0.7) and Ga rich (x>0.7).

Compositions of different elements at GB for three regimes are presented in this section:

1) Ga Poor (x < 0.4): GB chemistries for Ga poor cells are presented in Figure 4.9 for x = 0.0, 0.17 and 0.39.

Figure 4.9 represent GB chemistry for CIGSe cells having Ga concentration less than 12%. As it can be noticed from Figure 4.9, Na concentration at GB (right axis) is between 0.4 and 3 at% and is not specific to Ga ratio as discussed earlier.

Cu depleted GBs are observed for all samples in this regime which is accompanied by In and Se enrichments. Hence ΔCu is always negative in this case for all the GB chemistry. This point will be discussed in the next section.

Ga concentration is found unaffected at GBs for all Ga poor samples. It can be noticed from Figure 4.9 that full width at half maximum (FWHM) of the segregation peak for Na and Cu is similar for all samples. This is due to the fact that GB's planes are always observed to be tilted at 9 degrees up to 20 degrees with respect to the tip axis. With variations in tilt angles of GB, FWHM of Na may vary significantly according to the relation given in the work of Blavette et.al [2] where it is shown that FWHM for GBs normal to analysis direction is minimum and maximum for GBs along analysis direction.

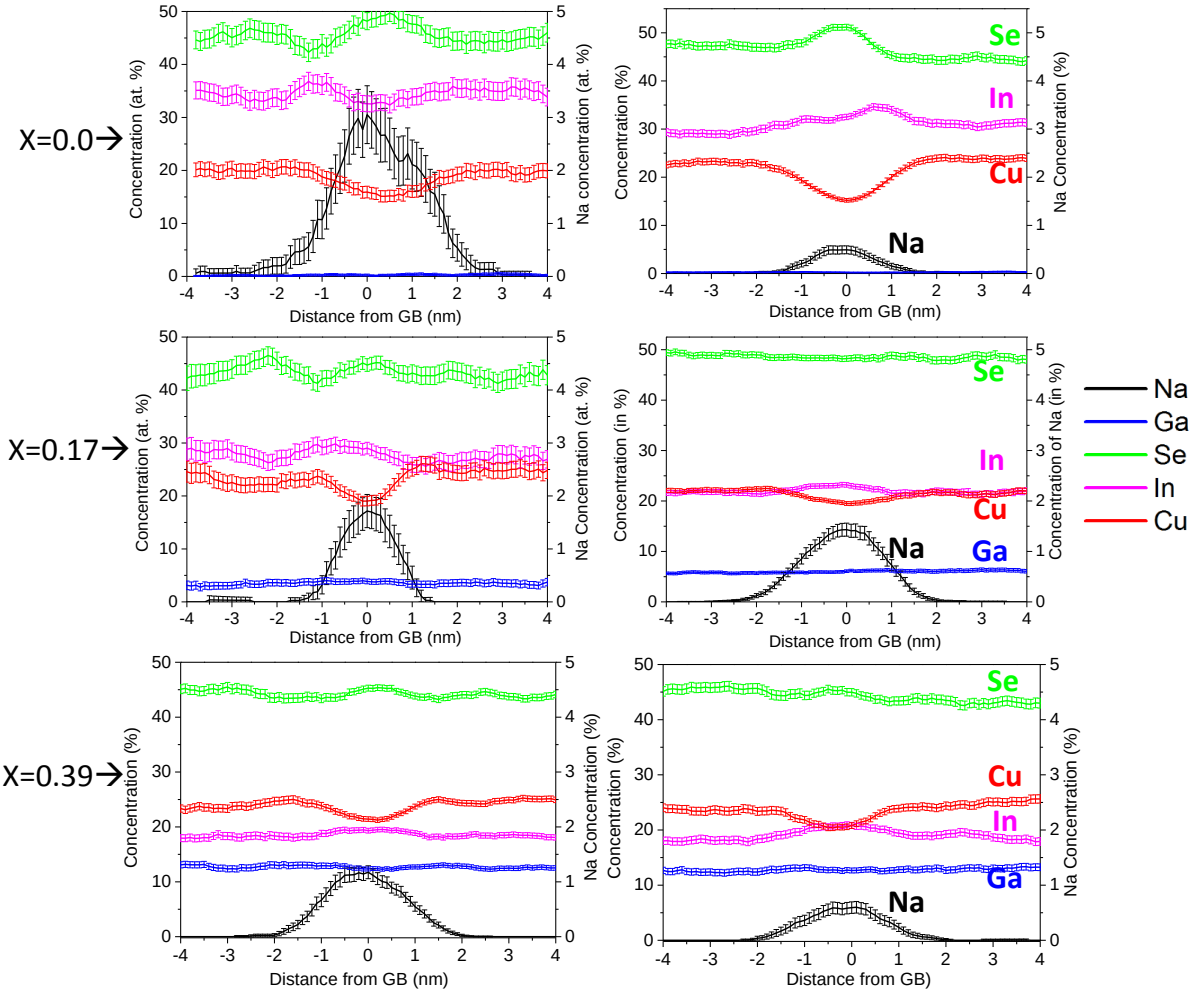

Figure 4.9: GB chemistry for Ga poor CIGSe cells. Composition profile in vicinity of GB is shown for various elements in CIGSe for x=0, 0.17, 0.39. Position of maximum Na concentration indicates GB interface. Right axis and Left axis are concentrations in at. % for Na and other elements respectively.

2) Ga intermediate (0.4 < x < 0.7): GB chemistry for intermediate regime is presented in Figure 4.10 for x=0.47, 0.56 and 0.67.

Samples with intermediate values of Ga ratio i.e. x between 0.4 and 0.7, exhibit two families of Cu GBs. Each of the Ga content (x=0.47, 0.56 & 0.67) demonstrates existence of both Cu depleted GBs and Cu enriched GBs. It is also interesting to note that Cu depletion is always accompanied with In and Se enrichment at GB. Again here, no appreciable change in Ga is observed when GBs are Cu depleted.

However in case of Cu enriched GBs, Cu enrichment at GB is always accompanied by Ga depletion and no change in Se and In content is observed at GB. These results are particularly new and have never been observed by any other groups. This strongly suggests the formation of Cu_{Ga} defect at GBs, which is not yet addressed previously in CIGSe using theoretical calculations.

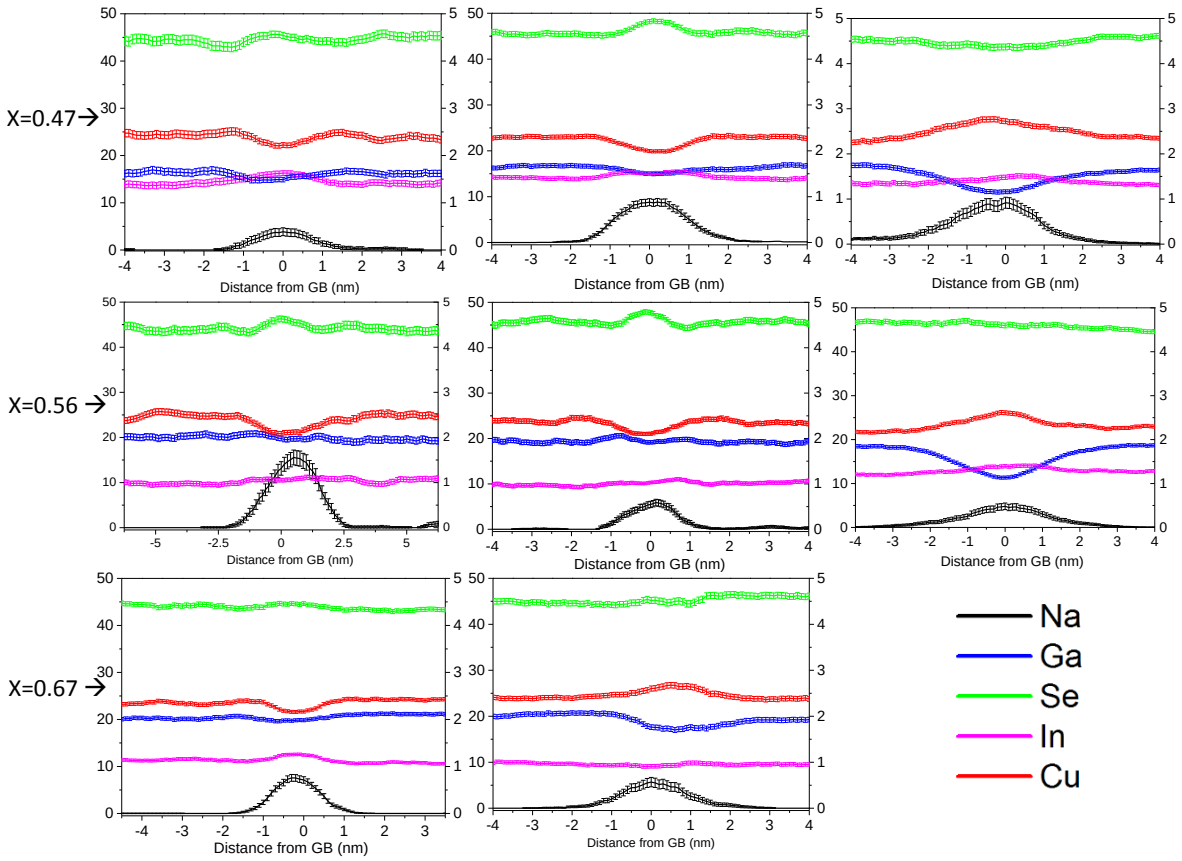

Figure 4.10: GB chemistry for intermediate values of 'x' = 0.47, 0.56, 0.67. Right axis and Left axis is concentration in at. % for Na and other elements respectively. Position of maximum Na concentration indicates GB interface.

3) Ga rich (x>0.7): GB chemistry for Ga rich regime is presented in Figure 4.11 for x=0.84 and x=1.0.

All GBs in Ga rich CIGSe were found to be Cu enriched and accompanied by Ga depletion. However no appreciable change/pattern in Se and In concentration at GB is observed for Ga rich samples. As suggested above, the presence of Cu enriched and Ga depleted GBs indicate occupancy of Cu over Ga sites.

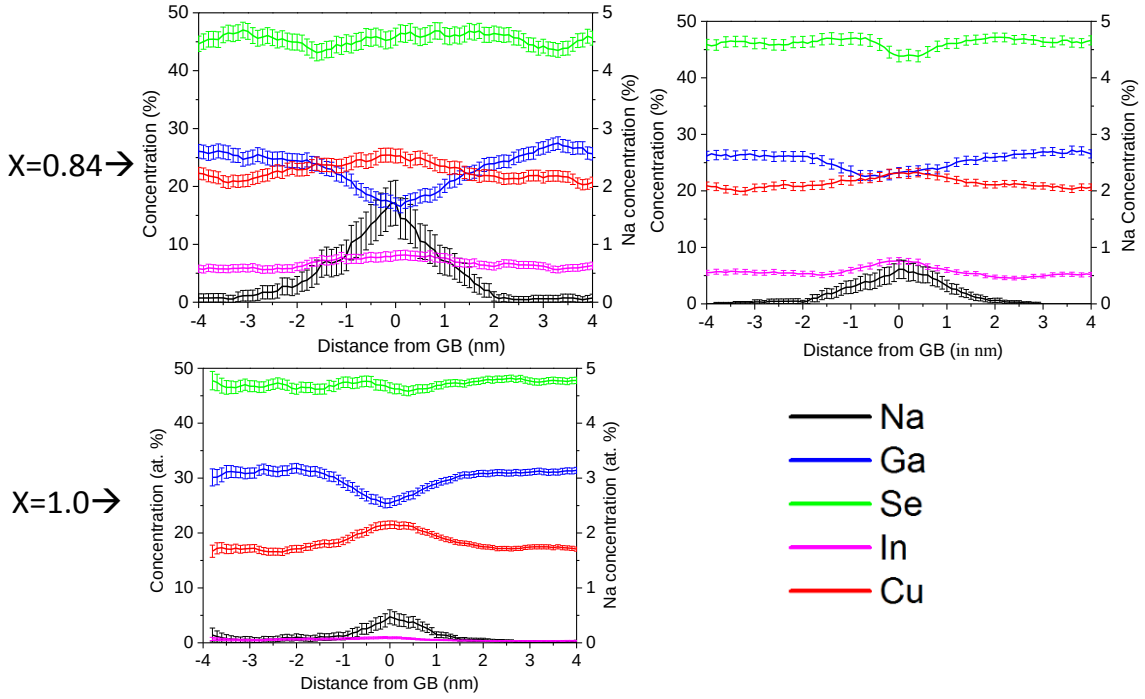

Figure 4.11: GB chemistry for Ga rich CIGSe cells, x=0.84, 1.0. Right axis and Left axis is concentration in at. % for Na and other elements respectively. Position of maximum Na concentration indicates GB interface.

Based on these results, the following conclusions are apparent:

1) From the three regimes, it is evident that Na concentration at GB does not follow any pattern and its segregation level range between 0.4 to 3 at. % whatever is the value of x (Ga level). The average Na coverage is 2.2 at/nm^2.
2) GBs are always observed to be In enriched or Ga depleted. In depleted and/or Ga enriched GB are never observed and perhaps do not exist in CIGSe.
3) Cu segregation or depletion at GBs is found to be lower than -10% or higher than +10% with no intermediate values. This suggests the absence of chemically neutral GBs (no change in Cu and/or other elements at GB).

4) Cu behavior at GB is found to be modified according to the grain concentration. Indeed, Cu is always depleted at GBs for Ga poor cells and always enriched for Ga rich ones. However intermediate values of grain concentration demonstrated the presence of both Cu rich and Cu depleted GBs.
5) From the three regimes it is also evident that tendency of elements segregating at GB follows as: In > Cu > Ga. In other words In is preferred over Cu and Cu over Ga to accumulate at GB.

For Ga poor samples, Cu depletion accompanied by In enrichment at GB is also found in refs. [5,7–9] shown in Figure 4.12 which is well supported theoretically by Zhang et.al [10] who also predicted In_{Cu} defect for Ga poor p-type CIGSe cells (more discussed in section 4.7). Cu depletion is observed irrespective of substrate used and is also observed for mild steel substrates by Choi et.al [8] for Ga poor cells. Results in Figure 4.12 were obtained on 3-stage processed samples which are in good correlation with present work on CuPRO processed samples.

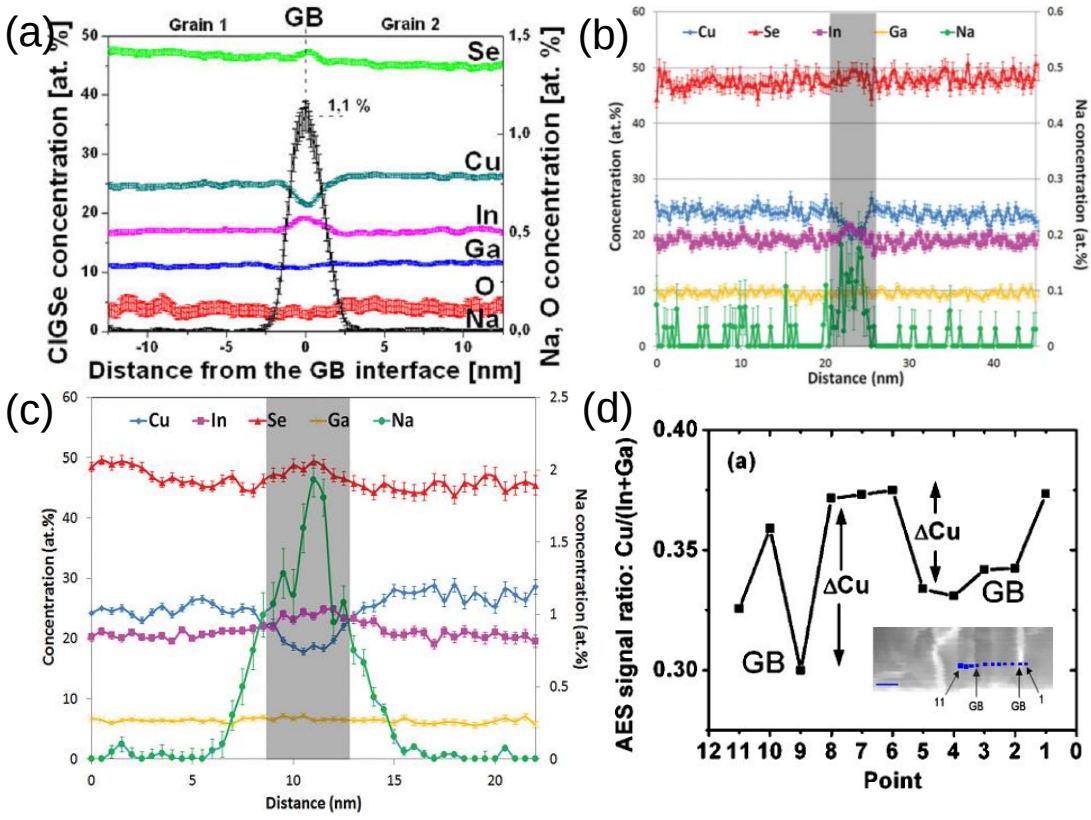

Figure 4.12: GB chemistry observed in refs. (a) Couzinie-Devy et.al [7], (b & c) Choi et.al [8] for glass substrate and steel substrate respectively, (d) Auger electron spectroscopy (AES) across GB performed by Hetzer et.al. [9].

Comparing results obtained in the present work with research performed by different groups on random GBs shows strong consistency. However TEM results obtained by Abou-Ras et.al [11] on grain boundaries with different symmetries showed the presence of Cu enriched GB for a random non-twin GB.

Reasons for the presence of both Cu enriched and Cu depleted GBs at same values of Ga content for intermediate cells is not clearly known and may also be due to different misorientation angle between grains. In later parts of this chapter an attempt is made to find reasons behind these elemental changes at GB for different CIGSe samples.

As misorientation angle and crystalline indexation of planes cannot be easily measured and identified using APT, chemical properties of GB could not be correlated with GB misorientation angle in this study. This requires correlated TEM or EBSD analysis on tip before APT analysis. Correlative TEM-APT or EBSD-APT is extremely time consuming and also involves projection of high energetic electrons which embrittle APT tip leading to their rupture in APT. Correlative analyses were thus not performed in this study.

4.4 Evolution of Cu composition at Grain Boundaries

In this section we quantify the Cu behavior at GB for the three regimes. The results representing ΔCu at GB are shown graphically in Figure 4.13. A pattern is evident from Figure 4.13 depicting ΔCu at GB for all samples (different x values). Line ΔCu=0 represent no change in Cu concentration at GB, positive ΔCu represents Cu rich GB and vice versa. For Ga poor and Ga rich domains one specific nature of GB is observed, leading to the presence of an empty region (white color) meaning the absence of GBs with such characteristics. As also illustrated earlier, intermediate grain concentration (0.4 to 0.7) shows presence of both types of GBs. The Figure 4.13 suggests that the transition between Cu rich and Cu poor GB domains is not an abrupt transition but a gradual transition. Emergence of first Cu enriched GB is observed just after x=0.4 and both types of GBs exists till x=0.67.

On increasing Ga concentration further, almost all GBs become Cu rich. Considering following statistics, domain of Ga ratio (x) in regime 1 is almost two times more than in regime 3 depicting biased variation of ΔCu towards Cu poor GB. It is also notable from Figure 4.13 that intermediate region contain more Cu depleted GBs than Cu enriched GBs hence the variation is not symmetric rather it is biased towards Cu poor GB. Figure 4.13 shows that 63% of total number of GBs is Cu depleted which indicates that polycrystalline CIGSe favors more Cu poor GB than Cu rich.

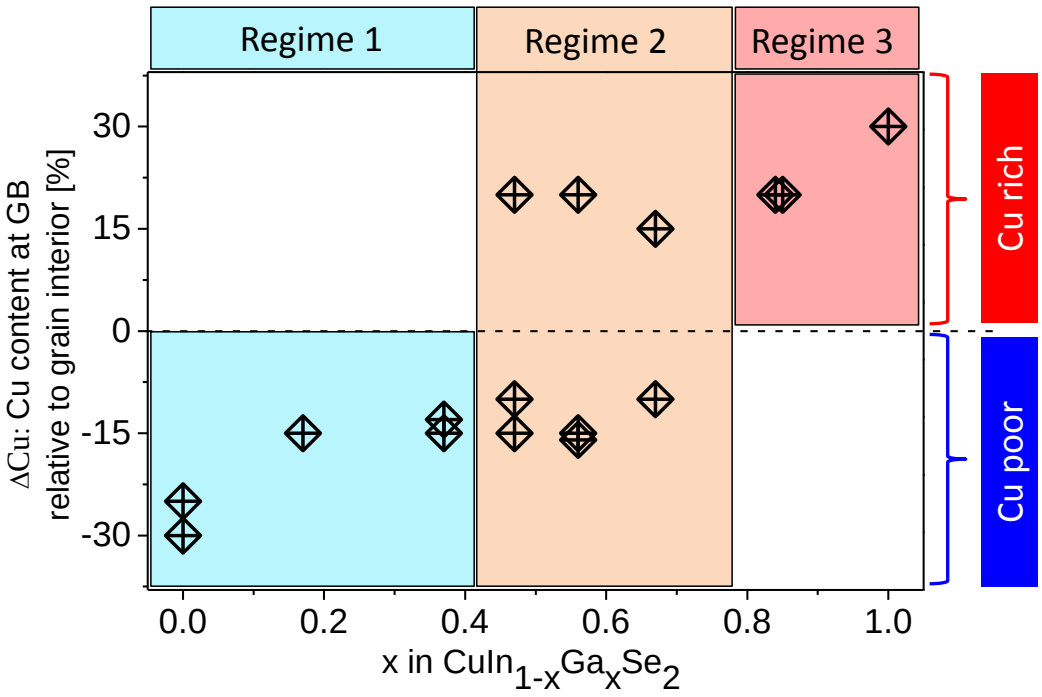

Figure 4.13: ΔCu as a function of Ga ratio (x). ΔCu below zero represents Cu poor GB and vice versa. Three regimes are highlighted containing specific type of GBs.

GB characterization of Ga poor cells have also been obtained in previous studies [5,8,12] on 3-stage processed CIGSe and are compared with results obtained in this work in Figure 4.14. As shown in this figure, results obtained in previous works also show presence of Cu poor GB for Ga poor cells which is consistent with our results. It is interesting to note that regardless of preparation process (CuPRO or 3-stage) Ga poor cells always exhibit Cu poor GBs. However, GB characterization of Ga rich CIGSe has not yet been performed by any other group using APT and is presented in this research for the first time.

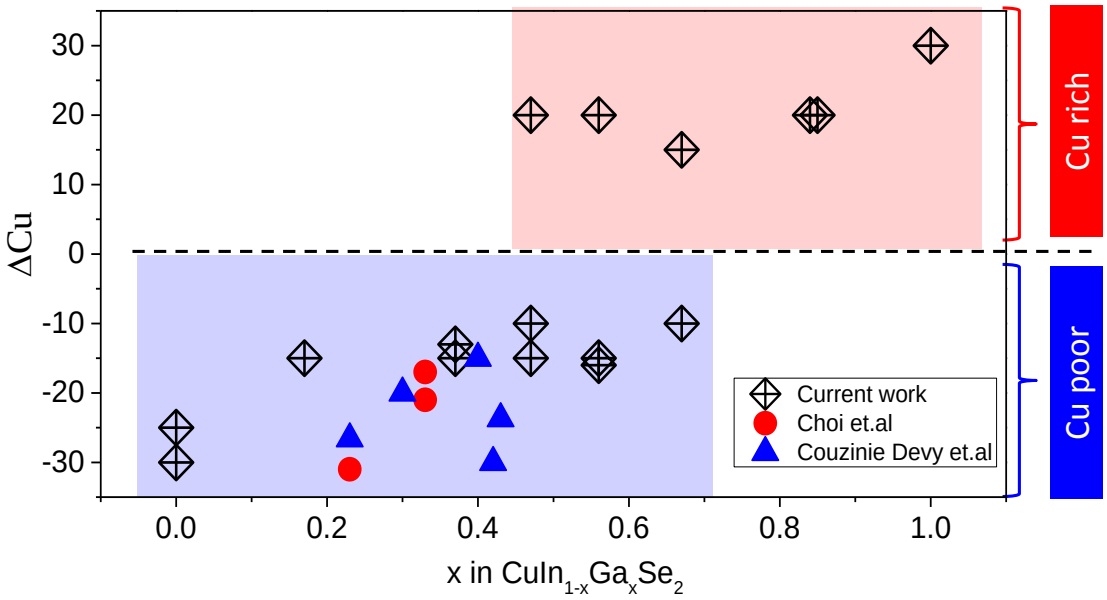

Figure 4.14: ΔCu as a function of x, comparing results obtained in current works (CuPRO CIGSe) with results obtained by Choi et.al [8] and Couzinie-Devy et.al [5,12] on 3-stage processed CIGSe samples.

Current statistics presented for Ga rich CIGSe show Cu rich GB, however due to less statistics it is unsure that all GBs are Cu rich for high Ga CIGSe. But sufficient statistics are available for Ga poor CIGSe demonstrating maximum amount of Cu depleted GBs.

It must also be noted that CIGSe cells prepared here are Cu poor cells i.e. overall Cu grain concentration is slightly less from Cu stoichiometry in $Cu(In_{1-x}Ga_xSe_2)$. Change in GB chemistry is well evidenced by Couzinie-Devy et.al [5] for 3-stage process when the grain concentration shifts from Cu-poor to Cu-rich. And even Ga poor cells may exhibit Cu rich GBs if overall grain concentration is Cu rich. May be this is one of the possible reason for lower performance of Cu rich CIGSe and hence CIGSe are always made Cu poor in overall composition.

A conclusion of Cu behavior for different regimes of Ga ratio (x) is presented in Figure 4.15 depicting schematically nature of GBs at different x. GBs in blue and red color represent Cu poor and Cu rich GB respectively.

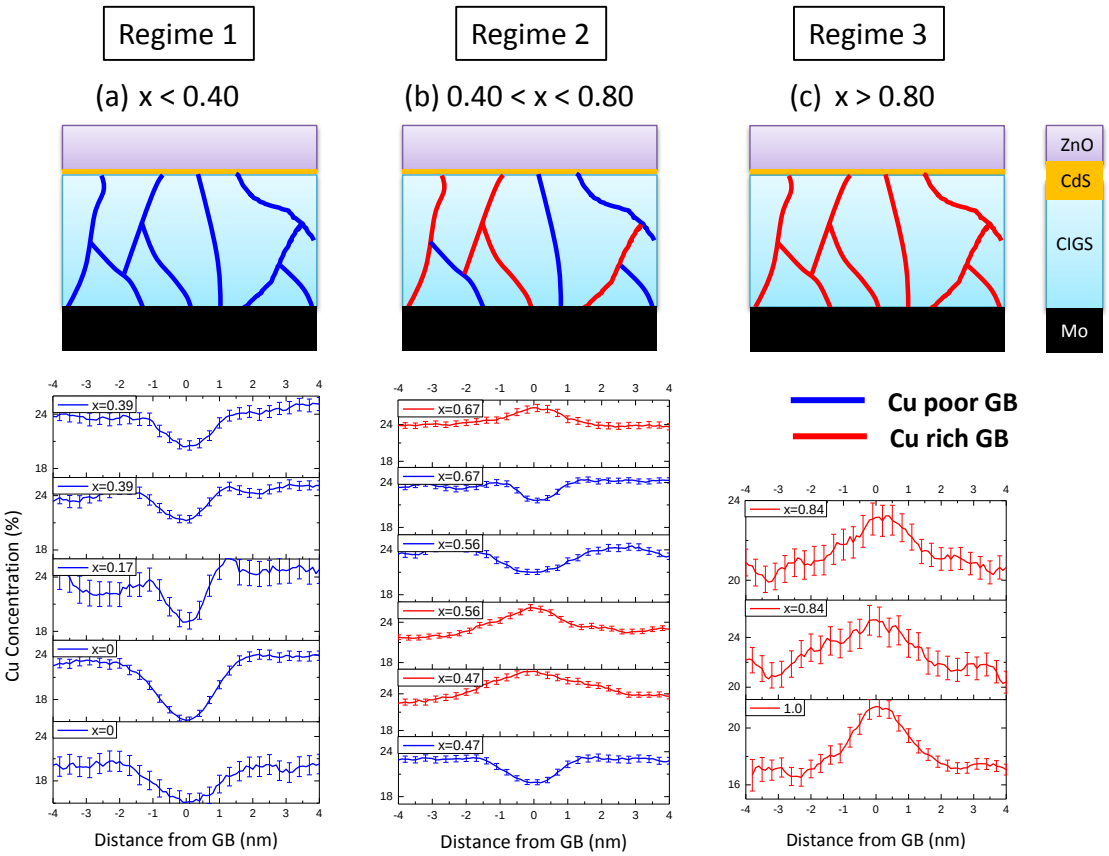

Figure 4.15: Schematic representation of modifications in Cu concentration at GB in CIGSe. GB model for (a) Ga poor CIGSe, (b) Ga intermediate CIGSe and (c) Ga rich CIGSe.

Figure 4.15 is further used in next section to explain photovoltaic properties of CIGSe.

4.5 Comparison of APT results with solar cell performance

Atom probe results presented in the previous section demonstrated significant modifications at GB with Ga content. Device performance of CIGSe solar cells are compared here with atom probe results by correlating their respective variations. Photovoltaic results in Figure 3.4 and APT results in Figure 4.13 are combined and illustrated in Figure 4.16.

Figure 4.16 represents variation of the cell efficiency and measured ΔCu as a function of x. Theoretical maximum efficiency correspond to a band gap energy close to 1.4 eV (x=0.7) as shown in the blue region in Figure 4.16. However observed efficiency is increased till x=0.39 and then decreased monotonically till x=1.0. Point of deviation of efficiency (red region) coincides with emergence of first Cu enriched GBs and further increase in amount of Cu rich GBs seems to further decrease the efficiency. Here we find that amount of Cu rich GBs is

consistent with degradation of device performance. Hence for Ga rich cells, efficiency could be minimum due to the presence of a maximum of Cu enriched GBs.

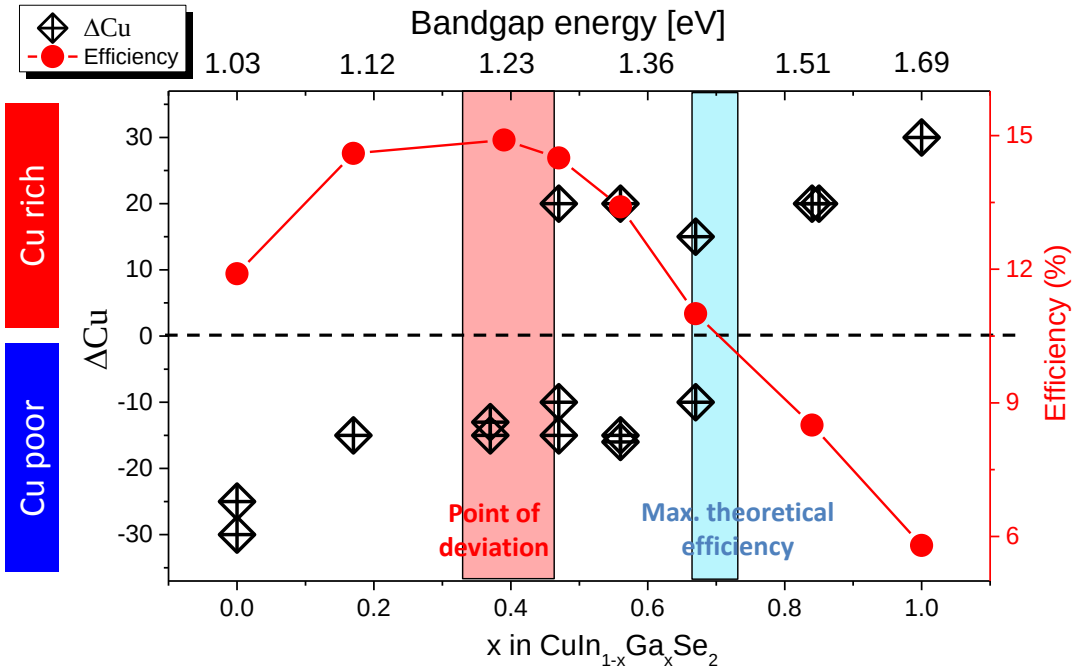

Figure 4.16: Efficiency (%) and ΔCu as a function of 'x'. Blue and red highlighted region correspond to theoretical maximum and experimental maximum efficiency of CIGSe respectively.

As discussed previously, J_{sc} varies according to expectations for CIGSe cells and hence the decline in efficiency is due to limitations in V_{oc}.

Figure 4.17 represents variation of V_{oc} (experimental and theoretical) and ΔCu as a function of 'x'. Figure 4.17 depicts that the variation of the experimental V_{oc} is consistent with theoretical expectations till x=0.4. However deviation of experimental V_{oc} from theoretical expectations is observed after Ga ratio x=0.40 where V_{oc} starts saturating. It is interesting to note that the emergence of the first Cu enriched GB is observed at x=0.47 i.e. just after x=0.4 coinciding with the emergence of V_{oc} deviation. The amount of Cu rich GBs increases with Ga content and illustrates more deviation of V_{oc} from expectations for higher 'x'. It is apparent from Figure 4.17 that presence of Cu poor GB is beneficial whereas Cu rich GBs have a negative influence on output voltage.

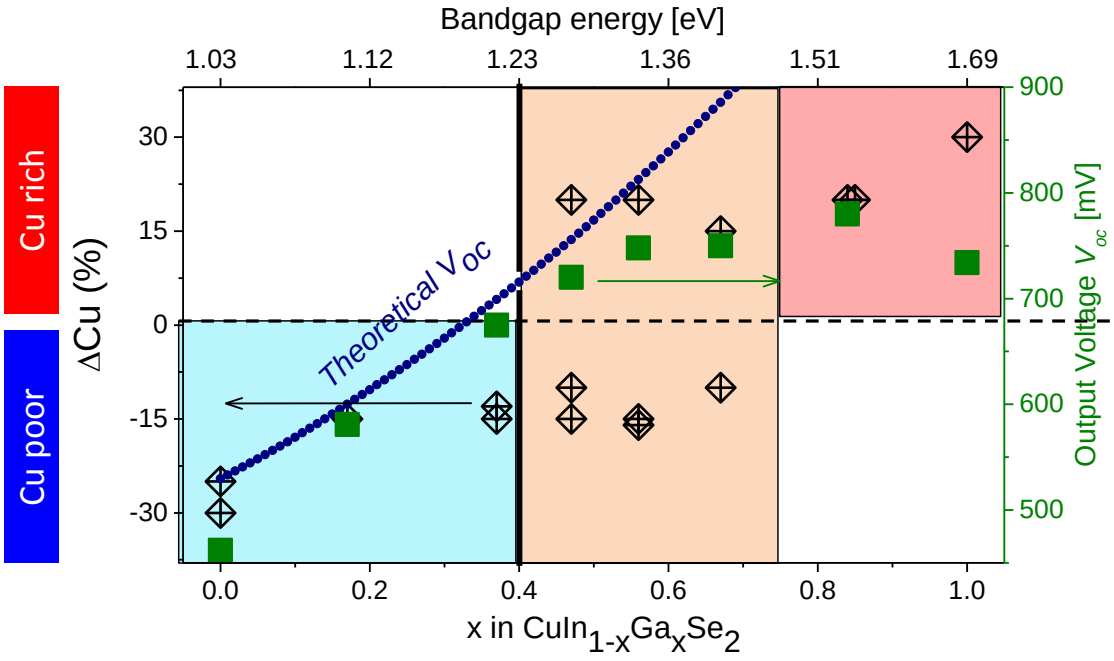

Figure 4.17: ΔCu (Relative change in Cu concentration at GB compared to Grain interior) and V_{OC} Vs Ga ratio (x). Experimental V_{OC} is shown in filled squares and compared with theoretical Voc (filled circles).

The comparison of GB quantification results from APT and device performance results has presented strong correlation. Results from APT and device performance show that GB chemistry notably affects device properties.

4.6 Reasons for limited performance of wide band gap CIGSe

APT results show that modifications at GB apparently tune the electrical properties of photovoltaic cells. We will try to give here and discuss some explanations:

4.6.1 Hole Barrier theory:

Figure 4.18 explains schematically hole barrier theory in (a) Cu poor GBs acting as hole barriers and repels hole from GB thereby making GB carrier specific and overall less recombination. (b) Cu rich GBs does not act as hole barriers hence not carrier specific and act as active recombination center for all carriers.

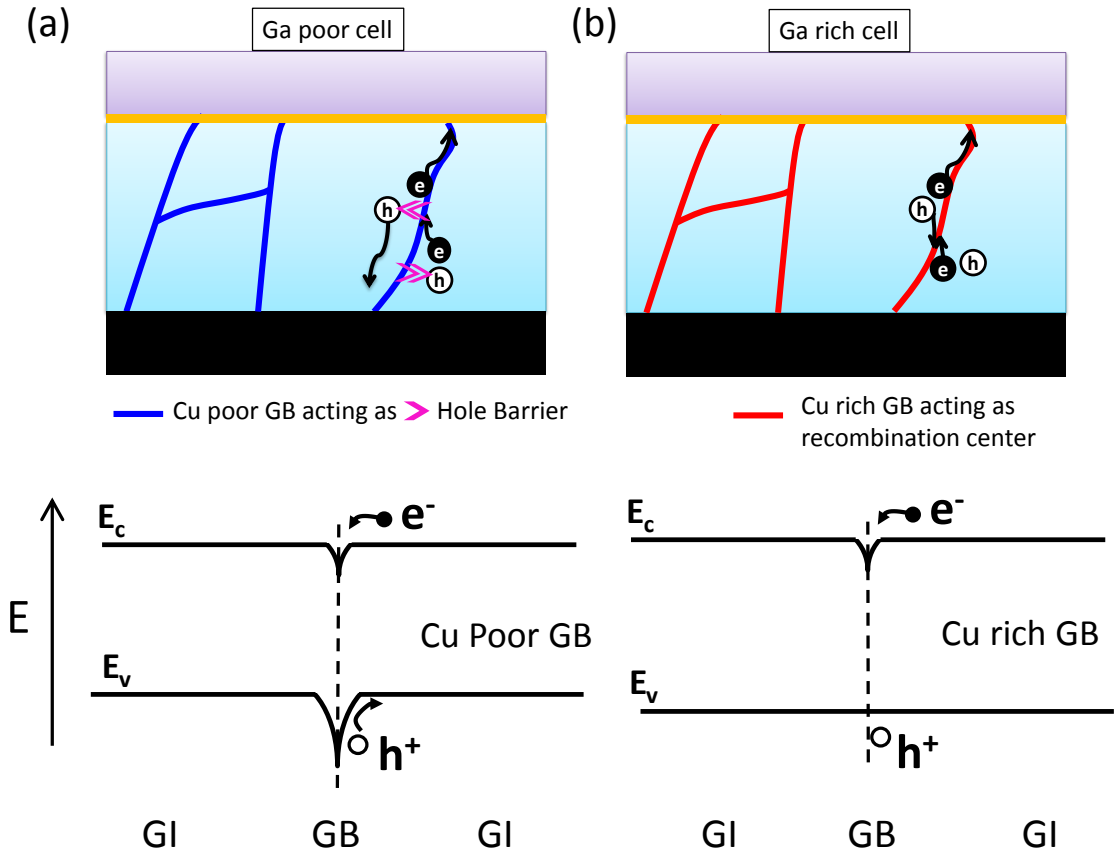

Figure 4.18: Schematic explanation of hole barrier theory for (a) Ga poor and (b) Ga rich cell, with their respective band gap energy diagrams below. Cu poor GBs (blue) act as hole barrier thus repulsing holes and prevents recombination. This property is absent in Cu rich GBs which makes GBs as active recombination centers.

As already predicted by Persson and Zunger [13] using theoretical calculation, all GBs in $CuInSe_2$ are Cu depleted, this removal of Cu atoms from GB reduces *p-d* repulsion (Se 'p' orbitals and Cu 'd' orbitals). This leads to lowering of valence band maxima (VBM) at GB as compared to GI and thus repels hole as shown in Figure 4.18. Thus Cu depleted GBs can act as hole barrier and thus improves carrier collection by preventing recombination. Our results are hence consistent with this theory for Ga poor cells where all GBs are Cu poor. GBs acting as hole barrier thus minimize carrier recombination and hence improve collection and output voltage. However Cu rich GBs cannot act as hole barrier leading to increased recombination at GB as shown in Figure 4.18b and detrimental photovoltaic properties. When all (or maximum) GBs are Cu rich, there is maximum carrier recombination and worst photovoltaic performance. Ga intermediate cells exhibit presence of both types of GBs and possess both beneficial properties of Cu depleted GBs and detrimental properties of Cu enriched GBs. Contrarily to this explanation, Hafemeister et.al. [35] shows benign behavior of GBs for Ga

rich CIGSe. Hence there is no strong evidence explaining this phenomenon and other possibilities must be checked.

4.6.2 Formation of dead grains

EBIC analysis on CIGSe cells with various Ga contents was performed by Contreras et.al in ref. [14]. Some random grains were found in CIGSe to be electrically inactive, which could not contribute towards carrier collection. These electrically inactive grains do not produce current and are referred in ref. [14] as "dead grains" as shown in Figure 4.19. Formation of these dead grains increases in depth for a cell and also increase with Ga content as observed in [14]. Reasons behind formation of these dead grains are however not properly understood and following our work is may be due to an increase in the Cu enriched GBs. If all GBs surrounding a grain are Cu rich, then maximum carriers generated in that grain recombines at GBs resulting in poor collection thus making the grain electrically dead. Reasons for active grains in upper half can be due to type inversion of grain surface at CIGSe-CdS heterojunction. As also grain size is much smaller for higher Ga samples, formation of maximum number of dead grains is expected.

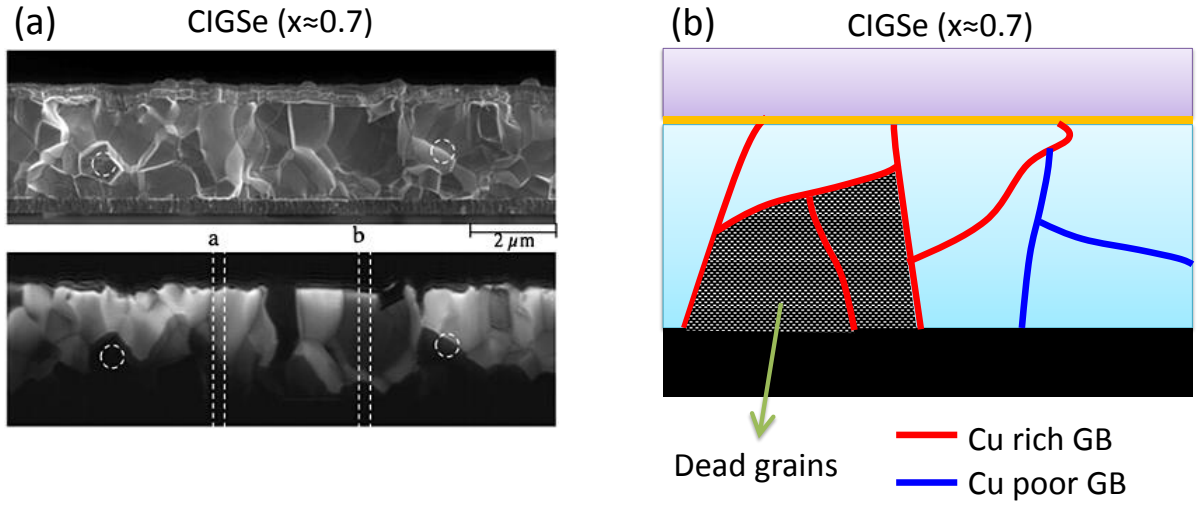

Figure 4.19: (a) Cross section SEM image (top), EBIC map (bottom) reprinted from [14] for E_g=1.4eV. (b) Schematic CIGSe solar cell model depicting formation of dead grains due to presence of Cu rich GBs.

EBIC measurements presented above were performed on different CIGSe samples, but our results might explain the origin of dead grains in CIGSe. To have better correlative studies it is thus suggested to perform correlative APT-EBSD-EBIC study on CIGSe samples with different Ga contents to verify above hypothesis.

4.6.3 GBs acting as shunt paths

Figure 4.20 represents a schematic solar cell circuit model for CIGSe and the role of shunt resistance in modifying its electrical properties. Due to difference in GB composition and properties with respect to grain, shunt resistance of grain and GB might not be the same. GBs with excess in Cu (metal) concentration may have higher conductivity than grain interior. If conductive enough, GBs may act as shunt paths in the device by delivering an alternate path for current as shown in Figure 4.20. Cu excess at GB may form Cu_2Se phase or may co-exist as individual atoms with other phase like chalcopyrite CIGSe. In both cases there is a chance of formation of conductive GB. Grains in this case are mostly columnar. Hence conductive GB will shunt the device and J-V equation in [equation 1.2] will modify as follows:

$$J(V) = J_0.\left[\exp\left(\frac{qV}{nkT}\right) - 1\right] - J_{photon} + \frac{V}{R_{Sh}} \qquad \textbf{(4.3)}$$

Where R_{Sh} is the shunt resistance.

Fill factor (FF) changes accordingly as:

$$FF_{Sh} = FF_0\left(1 - \frac{1}{R_{Sh}}\right) \qquad \textbf{(4.4)}$$

Above equation is plotted in Figure 4.20c showing significant effect of shunt resistance on FF and hence efficiency can be largely affected even due to small changes in shunt resistance.

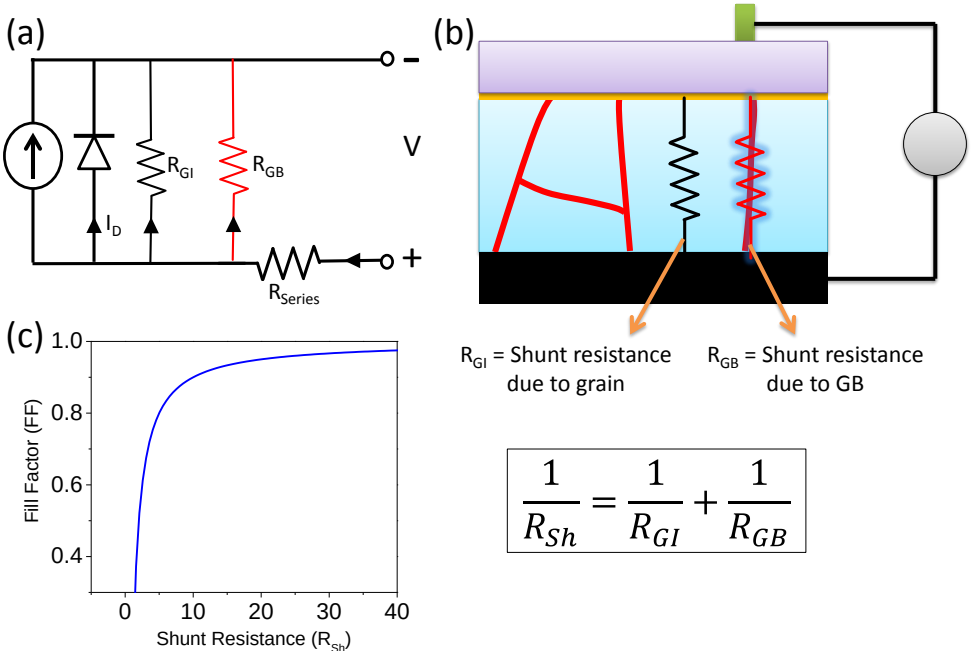

Figure 4.20: (a) Solar circuit model for CIGSe, (b) schematic electric structure of cell, (c) Fill factor versus shunt resistance for an ideal solar cell. Resultant shunt resistance is given by equation.

Shunt resistance in polycrystalline CIGSe can be considered to be composed of individual contributions from grain interior (GI) and from GB. If resistors are in parallel, resultant is given by reciprocal law as shown in figure. However this may not be correct as grain boundaries are adjacent to grains but this gives an idea of formation of shunt due to GB. Due to conductive nature of Cu, its excess at GB reduces R_{GB}, following above relation for low R_{GB}, $R_{Sh}=R_{GB}$. Hence shunt paths created by GBs may significantly degrade efficiency.

4.6.4 Type inversion at grain boundary

From Figure 4.9, Figure 4.10, Figure 4.11, concentration of Cu, In and Ga at grains and at GBs can be measured for all samples. Calculating ratio of [Cu]/[In]+[Ga] in grain interior provides the chalcopyrite desired phase along the region (yellow) as shown in Figure 4.21. This method can give an idea of possible phases at GB too, but is not very reliable due to absence of evidence. Since this phase diagram is established for bulk CIGSe it may not be relevant to consider the same for GBs which are few atomic planes thick. Nevertheless it must be noted that these attempts of identifying phases are unusual and hazardous and it is shown here just to demonstrate another possibility.

Due to compositional changes at GB, phase at GB might not be the same as phase in grain interior and can be estimated from APT composition profiles. Figure 4.21 shows the quaternary phase diagram adapted from ref. [15] for CIGSe with chalcopyrite (α) phase region in yellow. Experimental data from APT provide GB composition and corresponding phase can be estimated using this information. Approximate phases forming at GB are represented in Figure 4.21, dotted lines represent constant Ga ratio and stars represent Cu ratio (CGI) = [Cu]/[In]+[Ga] at GB for respective x. Blue and Red stars represent Cu poor and Cu rich GB respectively.

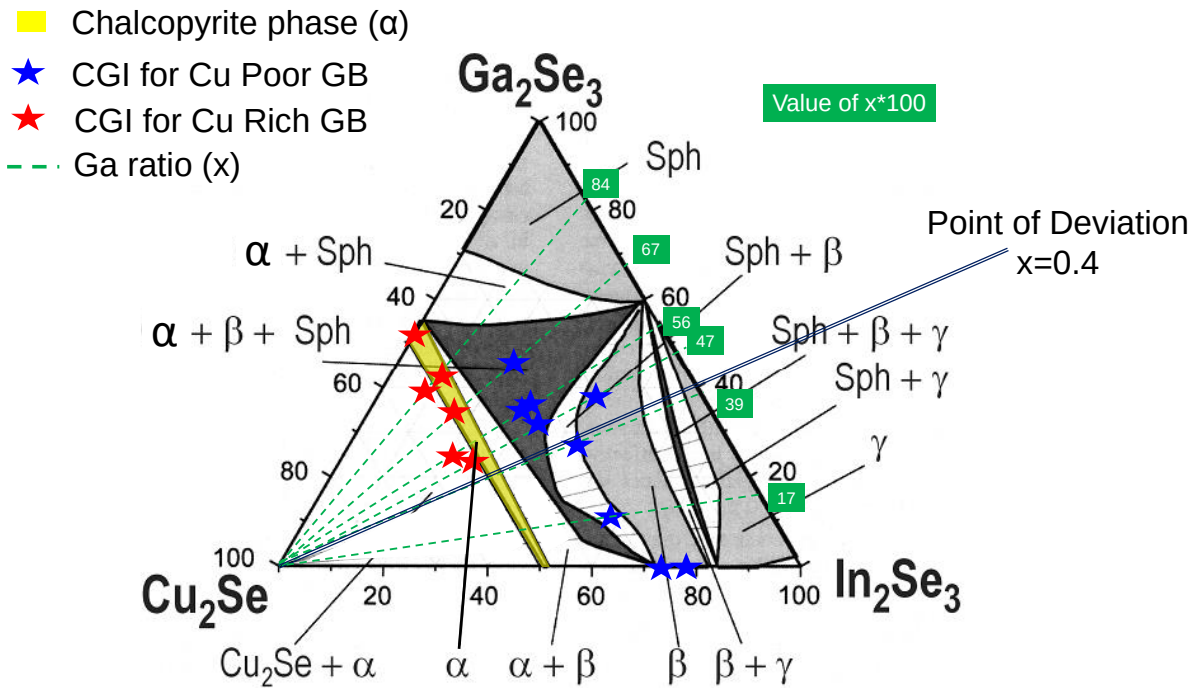

Figure 4.21: Quaternary phase diagram of CIGSe adapted from Ref. [15]. Stars represent phase at GB obtained from APT calculations performed here. Yellow highlighted region represents pure chalcopyrite phase of CIGSe. Sph represent sphalerite phase of CIGSe. Lines originating from Cu_2Se vertex represent constant Ga ratio along respective lines.

As Cu depletion is accompanied with In enrichment, CGI for Ga poor cells at GB is much lower than for α phase at grains. Hence GBs for x<0.4 are of β($CuIn_3Se_5$), γ or sphalerite phase containing the four elements.

It is proposed in previous studies that $CuIn_3Se_5$ is an n-type ordered defect compound forming at surface of CIGSe grain leading to buried pn junction at heterojunction. Considering similar properties of grain surface and GBs, β phase may form at GB leading to type inversion at GB [16–18]. Type inversion at GB would here mean n-type GBs in p-type CIGSe. As electrons are minority carriers, efficient transport of electrons along GB (n-type) would result in greatly reduced recombination and better photovoltaic properties. Referring to above figure, formation of β phase at GB is very probable in case of Ga poor CIGSe and is difficult to form in Ga rich CIGSe. Hence type inversion at GB may also be a reason for better performance of Ga poor CIGSe. If this theory is correct, then formation of pure β phase GBs in pure α phase CIGSe would present better efficiency, regimes of the two pure phase are shown clearly in Figure 4.22. Theoretically one must obtain maximum efficiency of CIGSe at x=0.7. However according to phase diagram in Figure 4.22, x=0.7 line does not

pass through β phase. Hence it would be impossible to have pure β phase GB in α phase CIGSe.

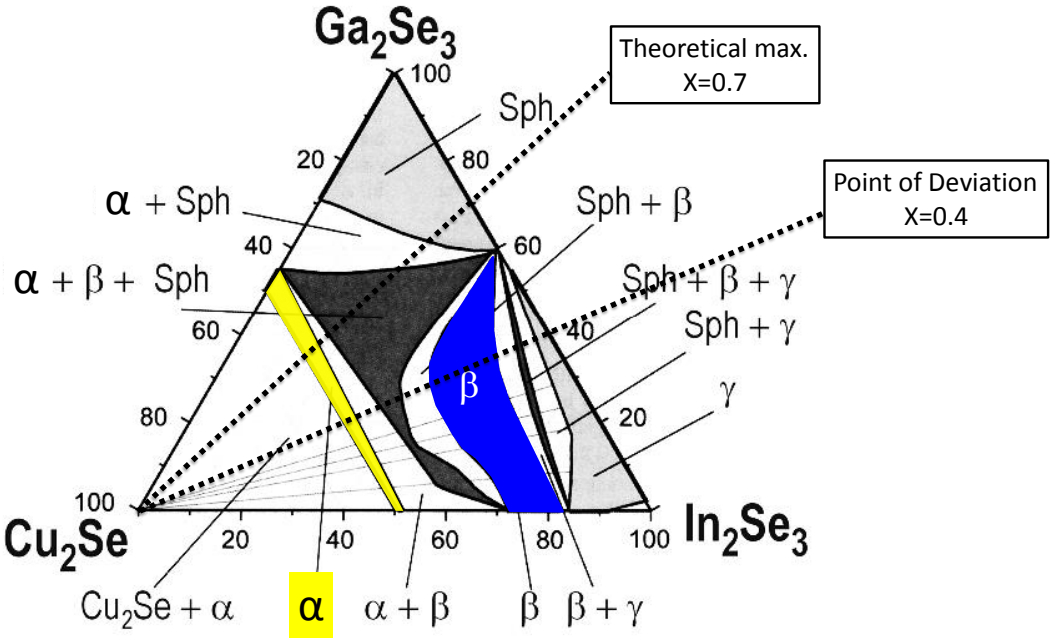

Figure 4.22: Quaternary Phase diagram of CIGSe adapted from ref. [15]. Highlighted region in yellow represent pure α (chalcopyrite) CIGSe phase and in blue represent pure β (ordered defect compound) $CuIn_3Se_5$ phase. Position of point of deviation (x=0.4) and theoretical maximum (x=0.7) is shown.

Therefore if this theory is correct then one would never obtain maximum CIGSe efficiency for x=0.7 including only four elements namely Cu, In, Ga, Se. This is one of the hypotheses supporting superiority of Ga poor CIGSe, instead some works have shown the absence of type inversion at GB [19,20] due to some potential differences at GB.

4.6.5 Further possible reasons

Apart from CIGSe absorber layer properties some issues are not discussed here such as modification in interfaces for CIGSe cells prepared with different Ga content [14]. Difference in CIGSe-CdS heterojunction may result in altered pn junction and SCR. Difference may also arise on Mo-CIGSe interface modifying properties of $MoSe_2$ formed in between the two layers. $MoSe_2$ is known to have a beneficial effect on CIGSe cell performance and may degrade with alterations in its properties.

4.7 Reasons for modifications in grain boundary segregation with Ga content

Experimental results performed previously indicate that grain boundary segregation depends principally on composition of CIGSe. As grain boundaries (GB) acts as defects in the material we expect change in defect physics of CIGSe with varying Ga content. To understand defect physics in CIGSe for various Ga concentrations, it is important to develop a model which can explain major factors leading to changes in GB composition. Development of a model will thus help to understand and enhance CIGSe thin film solar cell. As CIGSe is a quaternary compound involving interplay of four main elements (Cu, In, Ga, Se), developing a well suited model is time consuming. Hence an attempt is proposed to explain our results by the help of existing calculations performed in previous studies on CIGSe. There are different approaches to computationally model CIGSe, some results obtained in previous studies are compared with our observations and are presented in this section.

1) Phase stability after mixing of CIS-CGS ($CuInSe_2$-$CuGaSe_2$) binary alloy:

CIGSe can be considered as a pseudobinary alloy ($A_{1-x}B_x$) and $CuIn_{1-x}Ga_xSe_2$ can also be written as $(CuInSe_2)_{1-x}(CuGaSe_2)_x$. An interesting work has been performed by Xue et.al [22] combining several methods to study the phase diagram of CIS-CGS pseudobinary system. Methods used by Xue et.al [22] are namely: special quasirandom structures (SQS) [21], ab-initio DFT and thermodynamic calculations. They studied the phase stability of CIS-CGS which is described here. In their calculations it was accepted that physical properties of a binary alloy are mainly governed by the interactions of their neighboring atoms, which could be accurately calculated by arranging atoms in small supercells, which are termed as SQS [21,23]. Thus CIGSe can be considered as a random mixture of two ternary compounds CIS and CGS and Gibb's free energy (at constant temperature) for mixing of CIGSe can given as [22]:

$$\Delta G_{mix} = \Delta H_{mix} - T\Delta S_{mix} \quad \textbf{(4.5)}$$

Where, ΔH_{mix} (mixing enthalpy) and ΔS_{mix} (mixing entropy) according to Bragg-Williams approximation can be written as:

$$\Delta H_{mix} = x(1-x)\Omega(x) \quad \textbf{(4.6)}$$

$$\Delta S_{mix} = -k_B[x\, lnx + (1-x)\ln(1-x)] \quad \textbf{(4.7)}$$

Where k_B is the Boltzmann constant and Ω(x) is the interaction parameter [22] which mainly depends on x. At 0 K, Ω(x) can be written as using Redlich-Kister formalism [24]:

$$\Omega(x) = \sum_{i=0}^{n} C_i(1-2x)^i \quad \textbf{(4.8)}$$

Where C_i is the model (best fit) parameter and calculations were performed by using n=2 as given in Xue et.al [22].

Mixing enthalpy can be calculated by using equation 4.2 and 4.4 for different Ga ratio (x) and are illustrated in Figure 4.23.

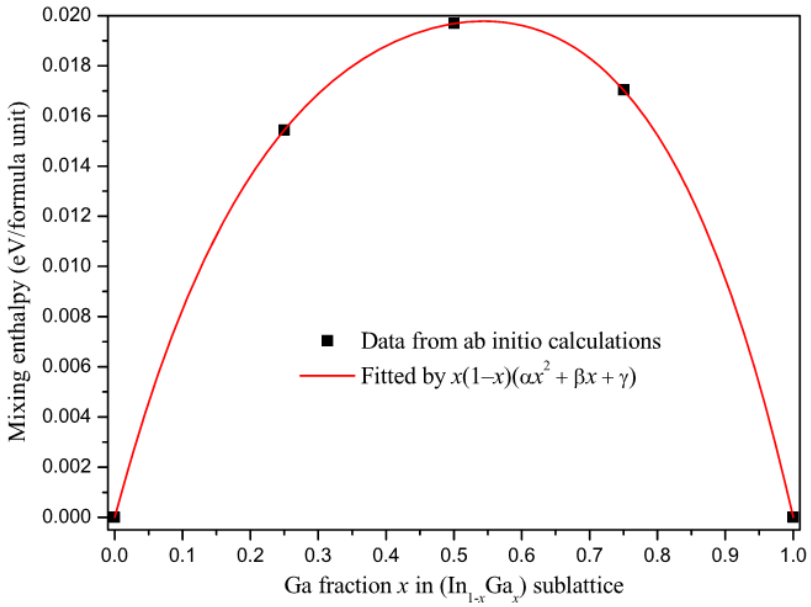

Figure 4.23: Mixing enthalpy as a function of Ga content (x) calculated using ab initio calculations (square dots) and fitted by Redlich-Kister formalism. Image courtesy: Xue et.al [22].

As noticed from Figure 4.23, except for the extreme compositions (x=0, x=1) mixing enthalpy of CIGSe is always positive which means that solid solution becomes unstable for intermediate values of x and stabilizes towards extreme compositions. Also, mixing enthalpy is apparently biased towards higher 'x' leading to skewness in curve. Two compositions x=0.25 (near to most efficient CIGSe observed) and x=0.75 (corresponding to most efficient

CIGSe expected) can be compared which shows better stability of Ga poor samples as compared to Ga rich samples.

2) Intrinsic Defects

CIGSe prepared and discussed in this work is of p-type conductive nature with typical free hole densities of 10^{16} – 10^{18} cm^{-3} [25,26] at 25°C. As discussed in chapter 1, emergence of doping densities arises from 12 intrinsic defects in CIGSe. Grain boundaries can be thought as defects present in the material. Hence defect physics at intrinsic defects can be used to understand GB physics. An overview of formation energy of different intrinsic neutral defects for two extreme values of 'x' i.e. $CuInSe_2$ and $CuGaSe_2$ is presented in Table 4-2. It can be noticed that the formation enthalpy of $V_{In} > V_{Ga}$, $Cu_{In} > Cu_{Ga}$, $In_{Cu} > Ga_{Cu}$ which indicates formation of In poor GB and/or formation of Ga rich GB is not energetically favorable and hence less probable. This explains our APT findings which demonstrated absence of In poor and/or Ga rich GB in any of the sample. Moreover the formation enthalpy of $Cu_{In} > Cu_{Ga}$ which explains the presence of Cu rich GBs accompanied by Ga depletion for CGS as observed using APT.

Table 4-2: Formation enthalpy of 12 possible intrinsic neutral defects in $CuInSe_2$ (CIS) and $CuGaSe_2$ (CGS). Adapted from ref. [20] with values from refs. [27–30]. Type A and D represent acceptor and donor types respectively. III indicate In or Ga.

	Point defect	Type	ΔH_{CIS} [eV]	ΔH_{CGS} [eV]
Vacancy	V_{Cu}	A	0.60	0.66
	V_{III}	A	3.04	2.83
	V_{Se}	D	3.00	-
Interstitial	Cu_i	D	2.88	3.38
	III_i	D	9.1	-
	Se_i	A	22.4	-
Antisite	Cu_{III}	A	1.54	1.41
	III_{Cu}	D	3.34	4.22
	Cu_{Se}	A	5.4	-
	Se_{Cu}	D	6.0	-
	III_{Se}	A	5.0	-
	Se_{III}	D	5.2	-

Table 4-2 also shows very less formation enthalpy of copper vacancy which explains overall high number of Cu depleted GBs (as discussed in previous sections). However above table fails to explain absence of In depleted Cu enriched GB.

3) Segregation tendency

APT results on CIGSe on various Ga compositions demonstrate Cu poor GB for Ga poor cells accompanied with In and Se enrichment and Cu enrich GB for Ga rich cells accompanied with Ga depletion. No experimental evidences in this study were found to contain In depleted and / or Ga enriched GB for any CIGSe sample. Hence our results show that tendency of various elements to segregate at GB in CIGSe follow as In > Cu > Ga. As involvements of four elements are complicated, we consider the extreme concentrations (CIS and CGS) to explain respective differences in their GB chemistry. There may be a variety of different driving forces leading to selective segregation of elements which are discussed here:

a) Site effect:

In this case of multi element alloys, mutual interactions between neighborhood atoms are complex and hence site competition presents an important role. Cohesive (or Binding) energy plays an important role in deciding segregation of a certain element in a solid solution. Elements with low cohesive energy are expected to segregate more at GB due to their relatively less binding nature. Hence in a quaternary compound like CIGSe, there is a competition among respective four elements (Cu, In, Ga, Se). Table 4-3 provides cohesive energies of Cu, In, Ga and Se in eV/atom and follow the trend Se < In < Ga < Cu. This suggests that, due to the more cohesive nature of Cu, it may not preferentially segregate and hence Cu poor GBs are observed for Ga poor cells (CIS) accompanied by In and Se enrichment at GB. Higher formation enthalpy of Ga_{Cu} in CGS as compared to In_{Cu} in CIS is mainly due to larger cohesive energy of Ga than In [27] and explains formation of Cu poor In rich GB is more energetically favorable.

Table 4-3: Cohesive energy of Cu, In, Ga, Se. Data source: Kittel C. [31]

Element	Cohesive energy (eV/atom)
Cu	3.5
In	2.52
Ga	2.81
Se	2.46

However cohesive energy trend fails to explain Cu segregation and Ga depletion at GB for higher Ga samples, indicating dominance of other effects.

b) Size effect:

Energy of segregation (E_S) [32] plays an important role in GB segregation phenomenon and atoms with low energy of segregation are expected to segregate at GB. It was found in Sutton et.al [32] that in the case of bismuth (Bi) and silver (Ag) solute atoms in a Cu matrix, E_S is principally governed by the size of the solute species and elements with higher ionic radii are found to segregate more. Hence Ag due to its higher ionic radii was found to be energetically more favorable to segregate. Comparing ionic radius of various elements as shown in Table 4-4 for CIGSe, the following sequence appears: $E_{Se} > E_{In} > E_{Cu} > E_{Ga}$. GB sites are known to better accommodate bigger atoms as in case of Bi and Ag in Cu [33]. In our case, ionic radius of Ga is the smallest; it is thus not expected to segregate at GB as compared to other elements. Hence size effect may explain why Ga is never found to be enriched at GB. Size effect predicts maximum segregation of Se for all samples; however Se concentration is almost constant at grains and GBs for Ga rich samples. Hence size effect may explain why In is preferred over Cu over Ga but could not correctly determine Se.

Table 4-4: Ionic radius of Cu, In, Ga, Se. Data source: Ref [34]

Elements	Ionic radius (pm)
Cu	73
In	80
Ga	62
Se	198

Both site effect and size effect explain the segregation of In and Se accompanied by Cu depletion at GB for CIS. For CGS, size effect suggests preference of Cu over Ga and hence to some order explains results obtained in this work. CIGSe is most efficient for quaternary compound $CuIn_{0.7}Ga_{0.3}Se_2$ however due to band gap effects it was expected that $CuIn_{0.3}Ga_{0.7}Se_2$ must present highest efficiency. Hence to understand GB segregation in more details and to explain findings obtained in this work, advanced theoretical computation is required.

Conclusions

In this chapter, grain boundary chemistry of CIGSe cells for various ‘x’ was investigated. Amount of Na at GB is found to be independent of ‘x’ despite of the fact that number of grain boundaries increase with ‘x’. Hence, Na is not expected to degrade efficiency with ‘x’. Cu is always found depleted at GB for Ga poor samples and enriched at GB for Ga rich samples. Samples with intermediate Ga content contained both Cu poor and Cu rich GBs. Cu depletion is always accompanied with In and Se enrichment with no change in Ga and Cu enrichment is always accompanied with Ga depletion with no change in In and Se. It was interesting to find that all GBs were either Cu rich or Cu poor. Efficiency and Voc was compared with change in Cu concentration at GB and good correlation was found. Cu rich GBs is shown to degrade device performance. Higher Ga samples (x>0.7) contained maximum amount of Cu rich GBs and demonstrated worst efficiency. Possible phenomenons were discussed in this chapter which may affect CIGSe performance due to presence of Cu rich GBs. An attempt to explain observed changes in GB composition at different ‘x’ is made in the end of this chapter. However due to complexity of the system, accurate explanations could not be given and is kept as future perspectives. Hence we explained that limited performance of wide band gap CIGSe arises due to increased amount of Cu rich GBs. Next chapter discusses on possible strategies and some attempts made in this work to rectify this issue.

References

1. Vurpillot F, Bostel A, Blavette D. Trajectory overlaps and local magnification in three-dimensional atom probe. *Applied Physics Letters* 2000; **76**: 3127–3129. DOI: doi:10.1063/1.126545

2. Blavette D, Duval P, Letellier L, Guttmann M. Atomic-scale APFIM and TEM investigation of grain boundary microchemistry in Astroloy nickel base superalloys. *Acta Materialia* 1996; **44**: 4995–5005. DOI: 10.1016/S1359-6454(96)00087-0

3. Gault B. *Atom probe microscopy*. New York: Springer 2012; Available at: http://dx.doi.org/10.1007/978-1-4614-3436-8 [Accessed August 20, 2013]

4. Cahn JW. Johnson WC, Blakely JM. Interfacial Segregation. Metals Park, OH: American Society of Metals; 1979. pp. 3–23.

5. Couzinie-Devy F, Cadel E, Barreau N, Arzel L, Pareige P. Atom probe study of Cu-poor to Cu-rich transition during Cu(In,Ga)Se2 growth. *Applied Physics Letters* 2011; **99**: 232108–232108–3. DOI: doi:10.1063/1.3665948

6. Cojocaru-Mirédin O, Schwarz T, Choi P-P, Herbig M, Wuerz R, Raabe D. Atom Probe Tomography Studies on the Cu(In,Ga)Se2 Grain Boundaries. *J Vis Exp* 2013; DOI: 10.3791/50376

7. Couzinie-Devy F, Cadel E, Barreau N, Pareige P, Kessler J. Atom probe contribution to the caracterisation of CIGSe grain boundaries. in, 001966 –001971. DOI: 10.1109/PVSC.2011.6186339

8. Choi P-P, Cojocaru-Mirédin O, Wuerz R, Raabe D. Comparative atom probe study of Cu(In,Ga)Se2 thin-film solar cells deposited on soda-lime glass and mild steel substrates. *Journal of Applied Physics* 2011; **110**: 124513–124513–7. DOI: doi:10.1063/1.3665723

9. Hetzer MJ, Strzhemechny YM, Gao M, Contreras MA, Zunger A, Brillson LJ. Direct observation of copper depletion and potential changes at copper indium gallium diselenide grain boundaries. *Applied Physics Letters* 2005; **86**: 162105. DOI: 10.1063/1.1906331

10. Zhang SB, Wei S-H, Zunger A, Katayama-Yoshida H. Defect physics of the CuInSe_{2} chalcopyrite semiconductor. *Phys Rev B* 1998; **57**: 9642–9656. DOI: 10.1103/PhysRevB.57.9642

11. Abou-Ras D, Schaffer B, Schaffer M, Schmidt SS, Caballero R, Unold T. Direct Insight into Grain Boundary Reconstruction in Polycrystalline Cu(In,Ga)Se_{2} with Atomic Resolution. *Phys Rev Lett* 2012; **108**: 075502. DOI: 10.1103/PhysRevLett.108.075502

12. Couzinie-Devy et.al. Unpublished Works.

13. Persson C, Zunger A. Anomalous Grain Boundary Physics in Polycrystalline CuInSe2: The Existence of a Hole Barrier. *Phys Rev Lett* 2003; **91**: 266401. DOI: 10.1103/PhysRevLett.91.266401

14. Contreras MA, Mansfield LM, Egaas B, Li J, Romero M, Noufi R, Rudiger-Voigt E, Mannstadt W. Wide bandgap Cu(In,Ga)Se2 solar cells with improved energy conversion efficiency. *Prog Photovolt: Res Appl* 2012; **20**: 843–850. DOI: 10.1002/pip.2244

15. Cornelia Beilharz. *Charakterisierung von aus der Schmelze gezüchteten Kristallen in den Systemen Kupfer-Indium-Selen und Kupfer-Indium-Gallium-Selen für photovoltaische Anwendungen*. 1999;

16. Probst V, Karg F, Rimmasch J, Riedl W, Stetter W, Harms H, Eibl O. Advanced Stacked Elemental Layer Process for Cu(InGa)Se2 Thin Film Photovoltaic Devices. in *Symposium J – Thin Films for Photovoltaic and Related Device* MRS Online Proceedings Library. DOI: 10.1557/PROC-426-165

17. Probst V, Rimmasch J, Riedl W, Stetter W, Holz J, Harms H, Karg F, Schock H-W. The impact of controlled sodium incorporation on rapid thermal processed Cu(InGa)Se2-thin films and devices. in *IEEE Photovoltaic Specialists Conference - 1994, 1994 IEEE First World Conference on Photovoltaic Energy Conversion, 1994., Conference Record of the Twenty Fourth*, 144–147 vol.1. DOI: 10.1109/WCPEC.1994.519828

18. Sadewasser S, Abou-Ras D, Azulay D, Baier R, Balberg I, Cahen D, Cohen S, Gartsman K, Ganesan K, Kavalakkatt J, et al. Nanometer-scale electronic and microstructural properties of grain boundaries in Cu(In,Ga)Se2. *Thin Solid Films* 2011; **519**: 7341–7346. DOI: 10.1016/j.tsf.2010.12.227

19. Baier R, Lehmann J, Lehmann S, Rissom T, Alexander Kaufmann C, Schwarzmann A, Rosenwaks Y, Lux-Steiner MC, Sadewasser S. Electronic properties of grain boundaries in Cu(In,Ga)Se2 thin films with various Ga-contents. *Solar Energy Materials and Solar Cells* 2012; **103**: 86–92. DOI: 10.1016/j.solmat.2012.04.002

20. Robert Baier. Electronic grain boundary properties in polycrystalline Cu(In,Ga)Se2 semiconductors for thin film solar cells. 2012;

21. Zunger A, Wei S-H, Ferreira LG, Bernard JE. Special quasirandom structures. *Phys Rev Lett* 1990; **65**: 353–356. DOI: 10.1103/PhysRevLett.65.353

22. Xue HT, Lu WJ, Tang FL, Li XK, Zhang Y, Feng YD. Phase diagram of the CulnSe2-CuGaSe2 pseudobinary system studied by combined ab initio density functional theory and thermodynamic calculation. *Journal of Applied Physics* 2014; **116**: 053512. DOI: 10.1063/1.4891829

23. Wei S-H, Ferreira LG, Bernard JE, Zunger A. Electronic properties of random alloys: Special quasirandom structures. *Phys Rev B* 1990; **42**: 9622–9649. DOI: 10.1103/PhysRevB.42.9622

24. Redlich O, Kister AT. Algebraic Representation of Thermodynamic Properties and the Classification of Solutions. *Ind Eng Chem* 1948; **40**: 345–348. DOI: 10.1021/ie50458a036

25. Siebentritt S, Rau U eds. *Wide-Gap Chalcopyrites*. Berlin/Heidelberg: Springer-Verlag 2006; Available at: http://link.springer.com/10.1007/b105644 [Accessed July 10, 2015]

26. Shay JL, Wernick JH. *Ternary chalcopyrite semiconductors: growth, electronic properties, and applications*. Oxford; New York: Pergamon Press 1975;

27. Wei S-H, Zhang SB, Zunger A. Effects of Ga addition to CuInSe2 on its electronic, structural, and defect properties. *Applied Physics Letters* 1998; **72**: 3199–3201. DOI: doi:10.1063/1.121548

28. Wei S-H, Zhang SB, Zunger A. Effects of Na on the electrical and structural properties of CuInSe2. *Journal of Applied Physics* 1999; **85**: 7214–7218. DOI: doi:10.1063/1.370534

29. Möller HJ. Structure and defect chemistry of grain boundaries in CuInSe2. *Solar Cells* 1991; **31**: 77–100. DOI: 10.1016/0379-6787(91)90008-D

30. Rincón C, Bellabarba C, González J, Sánchez Pérez G. Optical properties and characterization of CuInSe2. *Solar Cells* 1986; **16**: 335–349. DOI: 10.1016/0379-6787(86)90093-1

31. Kittel C. *Introduction to solid state physics*. New York: Wiley 1966;

32. Sutton AP, Vitek V. An atomistic study of tilt grain boundaries with substitutional impurities. *Acta Metallurgica* 1982; **30**: 2011–2033. DOI: 10.1016/0001-6160(82)90105-5

33. Schweinfest R, Paxton AT, Finnis MW. Bismuth embrittlement of copper is an atomic size effect. *Nature* 2004; **432**: 1008–1011. DOI: 10.1038/nature03198

34. http://www.webelements.com.

35. Hafemeister M, Siebentritt S, Albert J, Lux-Steiner MC, Sadewasser S. Large Neutral Barrier at Grain Boundaries in Chalcopyrite Thin Films. Phys Rev Lett 2010; 104: 196602. DOI: 10.1103/PhysRevLett.104.196602

5 Chapter Five: Towards the improvement of Ga rich CIGSe

The results presented in the previous chapter demonstrated clearly the importance of GB chemistry on CIGSe cell efficiency. It was shown that the presence of Cu enriched GBs is suspected to be the main reason for hindered performance of Ga rich CIGSe. In this chapter, we highlight possible strategies to improve Ga rich CIGSe cell performance and detail some approaches performed in this work. An approach towards improvement of wide band gap CIGSe solar cells is discussed in this chapter.

5.1 Strategies for improving Ga rich CIGSe:

As discussed previously, according to band gap modulation, x=0.7 (Ga rich) cell must present a maximum efficiency. Modifications in GBs as a function of Ga content are shown responsible for degraded performance of wide band gap solar cells. Thus, to improve device performance of wide band gap cells, two options are apparent:

1. Increase band gap of Ga poor CIGSe: this option seems rather impossible as band gap is a characteristic (or intrinsic) property of the material and is specific to Ga/In concentration in CIGSe.
2. Supply other element to favor Cu-poor GB : Cu enrichment at GB is the main reason for limited performance of Ga rich CIGSe. Indeed as already shown, chemical segregation tendency at GB is in the order: In > Cu > Ga. Thus for Ga rich CIGSe Cu tends to segregate more at GB replacing Ga. Hence if introduction of other elements modifies GB properties resulting in Cu poor boundaries then it is possible to achieve further higher efficiency of CIGSe most probably at x=0.7. This is only possible if GB properties of CIGSe can be manipulated! In order to form Cu poor GB one must look for an element whose tendency is to segregate more at GB and induce defect sites as compared to Cu. Recently Cojocaru-Mirédin et.al [1] demonstrated a Cu depleted and Cd enriched region at the surface of CIGSe and also at GBs connected to CdS near to surface of CIGSe [2]. Cd takes over Cu sites (Cd_{Cu}) at GB demonstrating higher tendency of Cd to segregate at GB. In order to test this hypothesis, doping CIGSe with Cd by adding a CdS layer early in the process has been carried out to study the evolution of GB chemistry especially for high Ga content.

5.2 Introduction of Cadmium Sulphide before growth process

Usually equipment used for CIGSe synthesis does not have a direct or indirect source to add Cd or CdS during thin film growth. Hence CdS is deposited here before thin film growth on top of Mo using standard CdS chemical bath deposition. Thickness of CdS deposited is few nanometers and is followed by a 3-stage deposition process (CIGSe). Preparation of CdS chemical bath is the same as the one used for buffer layers and the modified cell contains CdS on top of Mo/SLG before thin film growth. A reference cell contains only Mo/SLG. For accurate results, we inserted the two samples 1) Mo coated SLG (Reference sample) and 2) CdS chemical bath deposition on Mo coated SLG (modified sample) adjacently to deposit CIGSe thin films using co-evaporation. This avoids possibility of minor changes which might occur if prepared separately.

The 3-stage process is mostly known (see chapter 2) for producing high efficient CIGSe, hence here we use 3-stage deposition process to compare photovoltaic device properties and correlate it with modifications in grain and GB properties. Six samples were prepared with 3 reference samples and corresponding 3 modified with CdS. Summary of the composition of cells prepared are described in Table 5-1.

Table 5-1: Composition in at.% (measured using EDX) for reference and modified cells of CIGSe.

Samples	Cu	In	Ga	Se	x (EDX)
CIS Reference	25.2	25.7	0	49.0	0
CIS Cd Modified	23.7	27.2	0	49.1	0
CIGS, x=0.5 Reference	25	11.3	13.8	49.9	0.55
CIGS, x=0.5 Modified	25.2	11.1	13.1	49.6	0.55
CIGS, x=0.7 Reference	24.4	7.5	19.1	49	0.72
CIGS, x= 0.7 Modified	24.4	7.7	19	49	0.71

EDX results confirm that composition of CIGSe in reference and modified cells are almost the same for all the prepared samples with minor variations which show the accuracy of the method used.

5.3 Improvement in device performance of Ga rich CIGSe

CIGSe device performance was measured for cells modified with CdS and compared with reference samples (without CdS) in Figure 5.1. Figure 5.1a represents J-V curve for reference cells and CdS modified cells for x=0.5 and x=0.7. Figure 5.1b represents EQE for reference and modified cells which shows improvement in EQE for CdS modified cells. Figure 5.1 c and d represent Voc and FF (fill factor) respectively for reference and CdS modified cells for x=0.7. Significant improvement in Voc, Jsc and fill factor is observed for CdS modified cells while comparing to reference cells.

Introduction of CdS before thin film growth thus demonstrates significant improvement in photovoltaic properties of CIGSe. Results here are shown for Ga rich CIGSe, however similar experiments were performed also on pure In sample $CuInSe_2$ and no improvement in device performance was observed. Following conclusions can be drawn from Figure 5.1:

1. Modified cells show improved efficiency, FF, QE, Voc and Jsc as compared to reference cells.
2. Higher Ga cells (x=0.7) presented more improvement in photovoltaic properties as compared to lower Ga cell (x=0.5).

The addition of impurities in a semiconductor usually leads to degraded device performance however in this case we found that the addition of a substantial amount of CdS before the thin films growth improved the CIGSe performance.

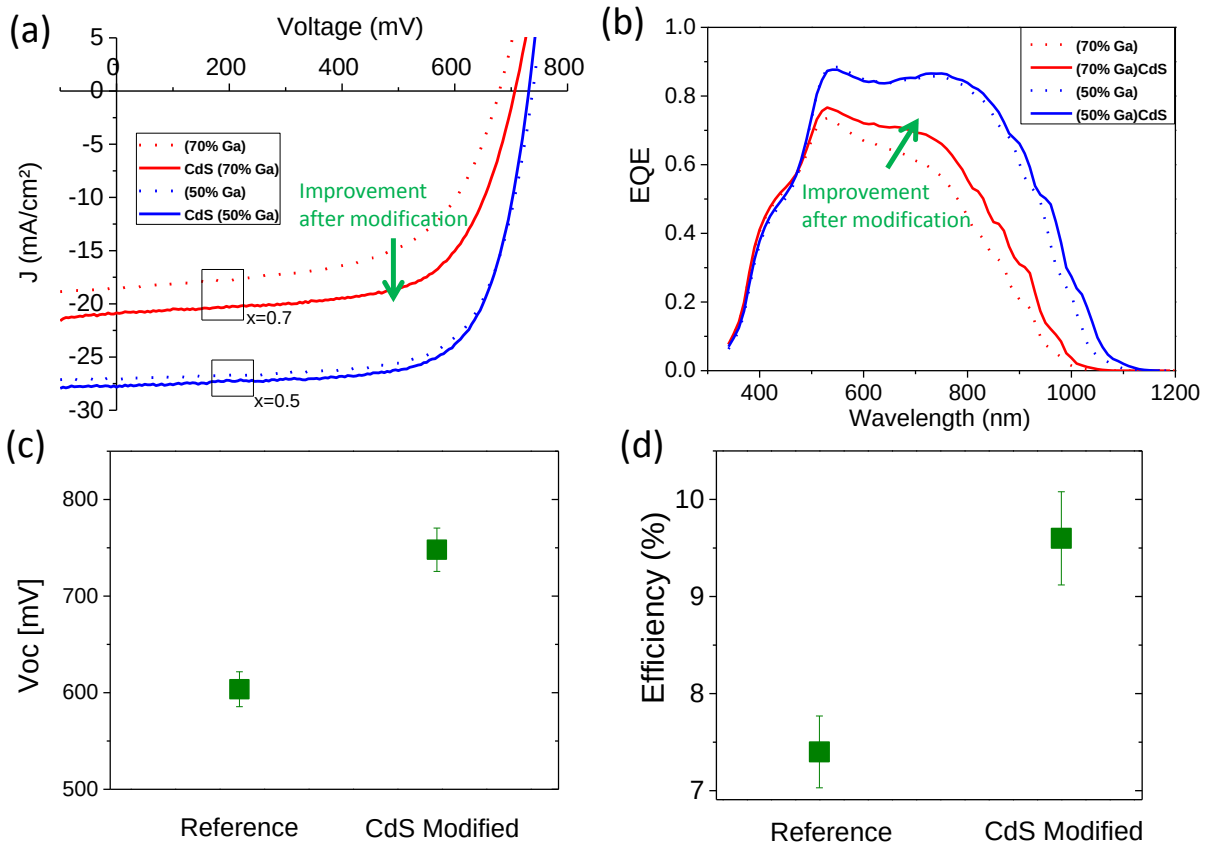

Figure 5.1: (a) JV curve, (b) EQE of CIGSe cells for x=0.5 and x=0.7 for reference cells and cells modified with CdS. (c) Voc and (d) Fill factor (FF) for modified and reference cells of x=0.7.

These results are impressive and need to be understood more deeply as they may open new perspective for improvements in wide band gap CIGSe solar cells.

5.4 Microstructural characterization using EBSD

To understand improvements due to CdS addition, modifications occurring due to CdS were studied both at microstructural level and at atomic scale by performing EBSD and APT on reference and modified cells. As the grain size plays an important role in tuning efficiency of a polycrystalline solar cell, it is crucial to explore grain distribution. Similar methods as used in chapter 3 are used here to explore grain distribution in modified and reference cells using EBSD. Figure 5.2 represents EBSD orientation distribution maps of reference and CdS modified CIGSe cells for x=0.0, 0.5 and 0.7. Individual grain orientations can be extracted from color legend shown in the figure.

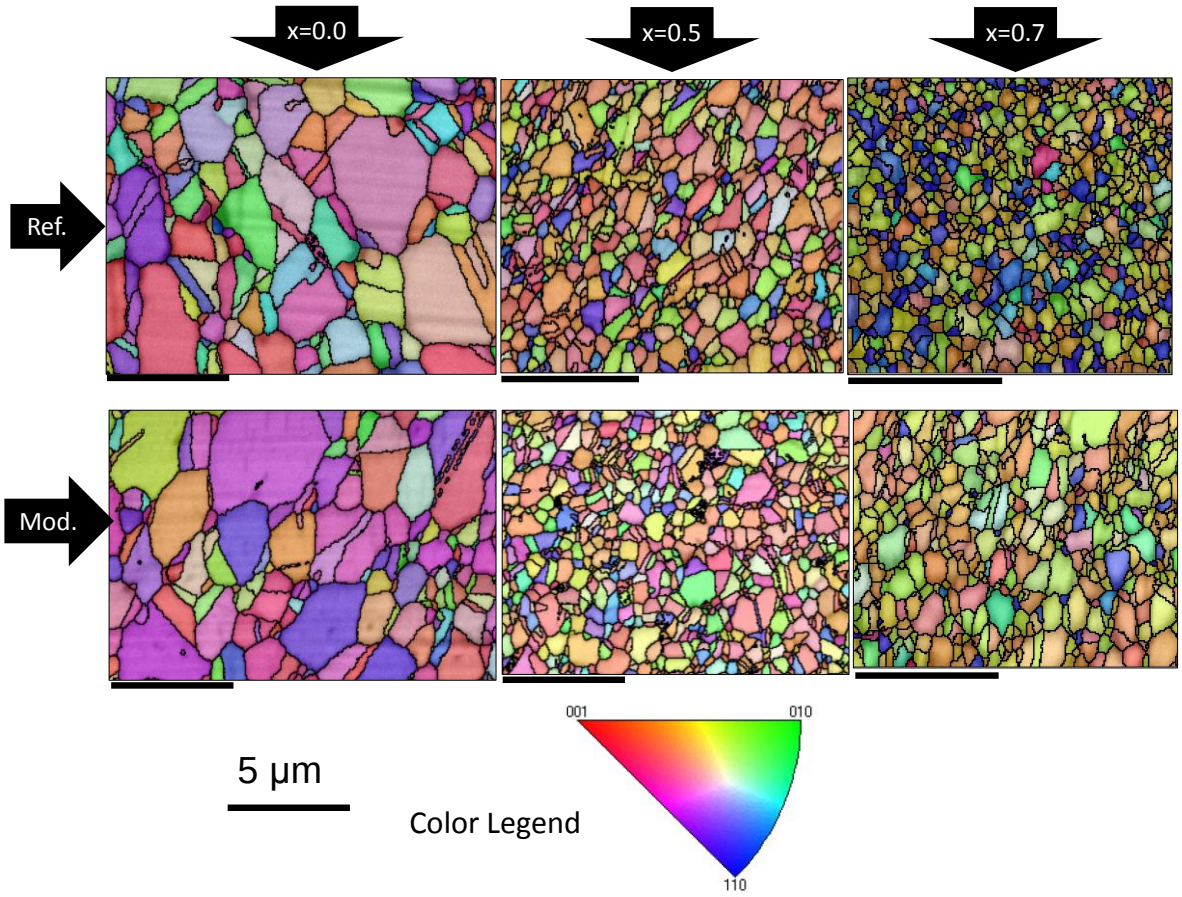

Figure 5.2: Orientation distribution maps (Inverse pole figure color maps) combined with back contrast image for reference and CdS modified cells with Ga ratios x=0.0, 0.50, 0.70. Scale bar (black) is 5µm in width.

Figure 5.2 demonstrates that the difference caused by CdS addition for CISe (x=0.0) is hardly noticeable. Also for x=0.5 there is no significant difference observed.

For higher Ga cells (x=0.7) it can be noted that the reference cells contain a higher number of grains oriented along (220) which is apparently not the case in the modified cells. Also a minor increment in grain size is observed for higher Ga cells (x=0.7) as also shown in grain size distribution in Figure 5.3, referring to Figure 5.2. This small increase is mainly due to errors in EBSD measurements resulting from elongation of grains along downward direction as can be seen in Figure 5.2.

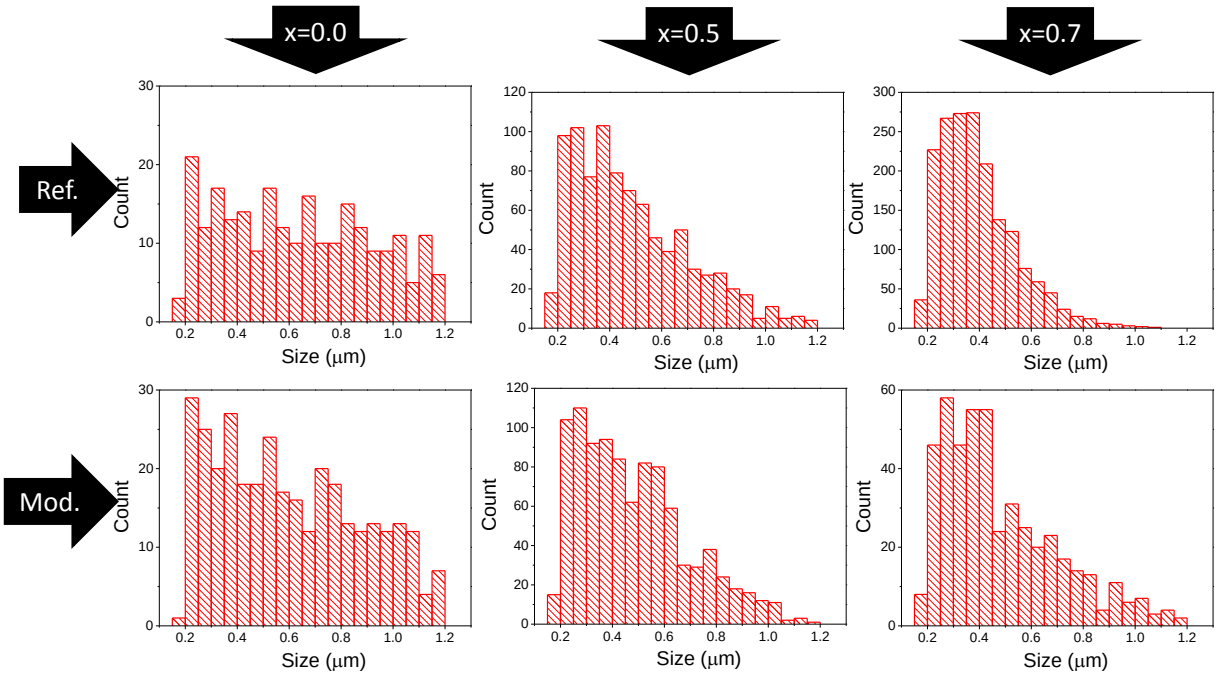

Figure 5.3: Size distribution for reference and CdS modified CIGSe cells with Ga ratios x=0.0, 0.50, 0.70.

From the two figures, it is observed that apparently there is no effect of CdS addition on grain size and distribution.

Misorientation angle distribution

Misorientation between grains can be measured using EBSD for scanned area and is presented for the six different cases in Figure 5.4. Following conclusions can be drawn from the determined misorientation distributions:

1. Comparing reference and CdS modified samples for x=0.0 and x=0.5: As observed in the case of the CuPRO samples, GBs at misorientation angles 60° and 70° are more prominent and are Σ3 twin boundaries. Also GB misorientation at 60° is higher than 70° misorientation, this was also observed for all CuPRO samples.
2. Comparing Figure 3.18 and Figure 5.4, it is impressive to note that the misorientation angle distribution is apparently similar for CuPRO samples and 3-stage samples. This shows the presence of similar microstructural properties of CIGSe regardless of thin film deposition process.
3. For x=0.7, apparently more misorientations are observed at 70° as compared to 60°.

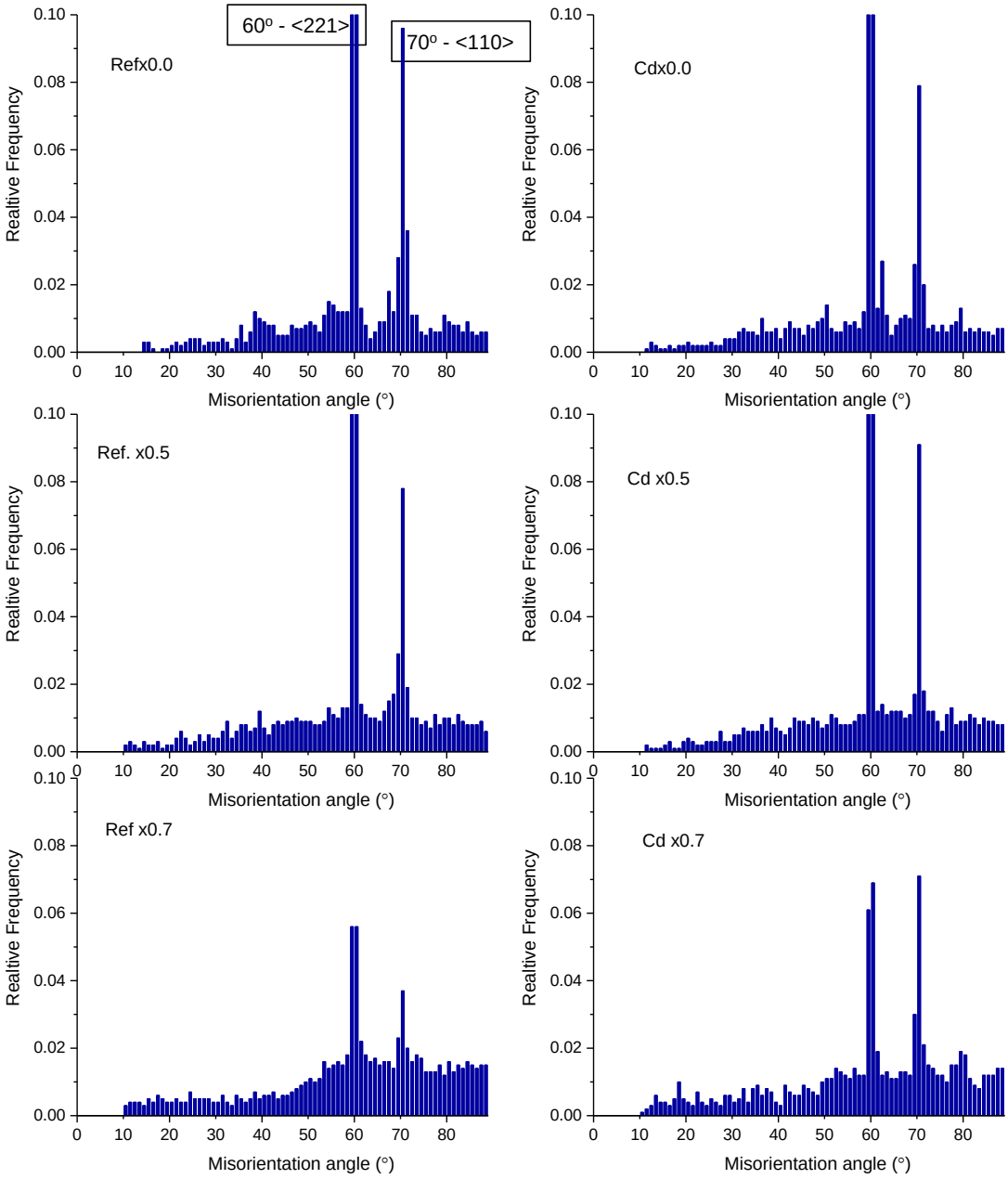

Figure 5.4: Misorientation angle distribution for reference and CdS modified CIGSe for different Ga ratios x=0, 0.5 and 0.7.

A significant increase in the amount of "70° misorientation" between grains may be attributed to microstructural changes occurring at atomic level. Main reasons behind these changes are beyond the scope of EBSD, hence APT is used in this study to detect atomic level changes at GB.

5.5 Atomic scale characterization using Atom Probe Tomography

In this part, the investigation of modifications in CIGSe grains or at GBs in modified cells is studied using APT in order to understand Cd role on cell improvement. This might be due to the addition of CdS before synthesis. APT is again realized as one of the best techniques to investigate atomic level modifications in CIGSe grains or GBs.

5.5.1 Specific sample preparation

APT is used here to explore the atomic distribution of CdS in CIGSe and to detect if there are any changes in GB chemistry for reference and modified cells. Sample preparation techniques for this study is slightly modified, as CdS is deposited on Mo before thin film preparation, more CdS is expected in the lower half of thin film. Hence APT tips prepared in transverse direction are made with apex towards lower half as shown in Figure 5.5. Final APT tip prepared in this study is more localized towards lower half of thin film, keeping apex of the tip in vicinity of yellow circle region as shown in the figure.

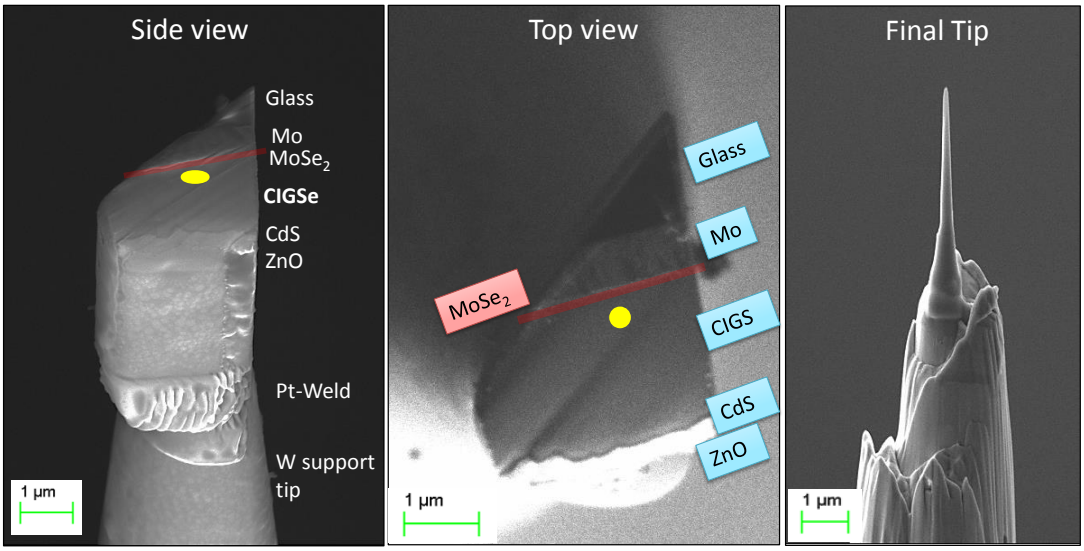

Figure 5.5: Chunk of CIGSe deposited on a W tip. Yellow circle shows approximate location of final prepared APT tip.

As thin films are prepared using 3-stage process, Ga grading is expected throughout the sample. In these samples Ga concentration is increased with thin film depth as shown in Figure 5.6. As EDX measurement is performed on top surface and APT measurements are

performed on lower half of thin films, concentrations of elements measured by the two techniques may not match. Similar tip location is used for all reference and modified samples.

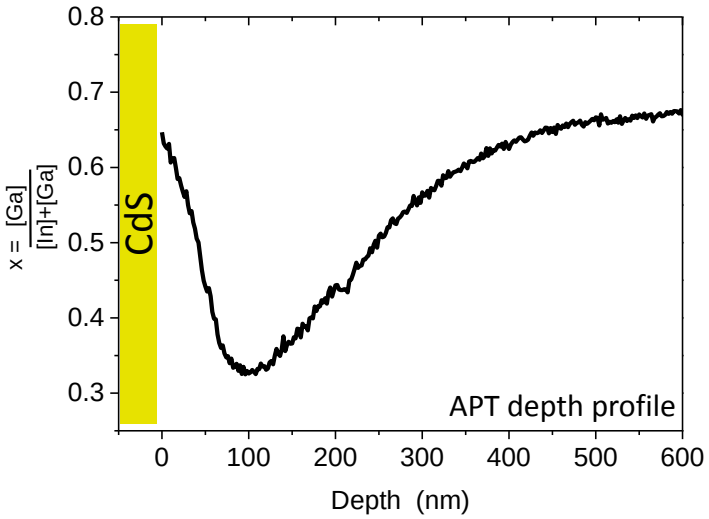

Figure 5.6: Ga ratio (x) as a function of thin film depth for CIGSe sample x=0.5 prepared using 3-stage process. This measurement is performed in APT by preparing tip parallel to thin film growth direction.

5.5.2 Atomic scale analysis of grains and grain boundaries

3D atomic distributions of all elements are explored for modified cells and reference cells. A small amount of Cd is observed in $CuInSe_2$, as illustrated in APT mass spectrum in Figure 5.7a. Different isotopic peaks of Cd are observed, namely 110, 111, 112, 114 a.m.u. and compared with natural isotopic abundance of Cd. Other peaks (113 and 116 a.m.u.) could not be resolved as they are obscured by In peaks at 113 and 115 a.m.u. respectively and hence are under detection limit of APT. Other isotopes of Cd namely 106 and 108 a.m.u. were under the detection limit of the atom probe. Isotopic ratio of resolved Cd peaks observed is consistent with natural abundance thus demonstrating these atomic peaks definitely correspond to Cd. The total amount of Cd can be calculated by using isotopic abundance calculations considering 112 a.m.u. peak of Cd.

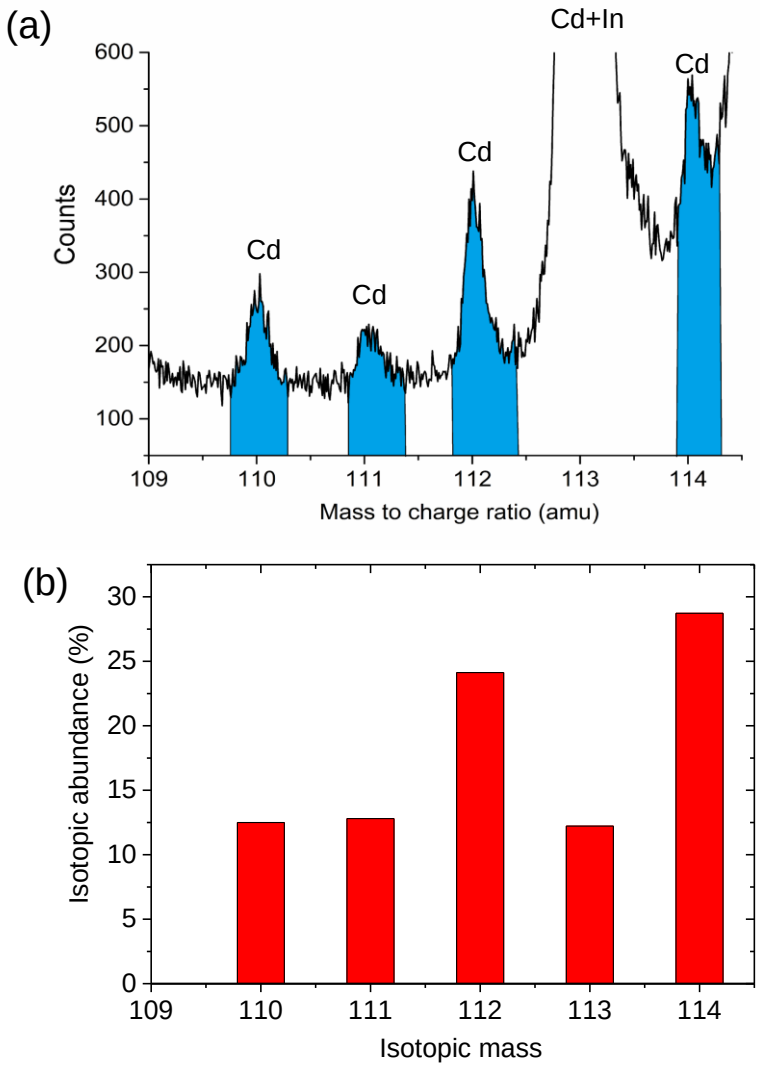

Figure 5.7: Mass spectrum of CdS modified $CuInSe_2$ illustrating atomic peaks from 109 a.m.u. to 114 a.m.u..

Atomic distributions corresponding to these peaks are displayed in Figure 5.8. 3D atomic distribution of Na and Cd atoms are shown in the figure with each dot corresponding to single atom. Cadmium is found to be uniformly distributed in grains of CIS with some local fluctuations around 0.08 at%. Cd in the grain has a maximum concentration of 0.1at.% and an average concentration of about 0.08 atomic %. Concentration profile of Cd along whole atomic volume shown is illustrated in Figure 5.8 demonstrating local fluctuations in Cd concentration; composition profile shows that Cd is not preferentially segregated in grains or GBs.

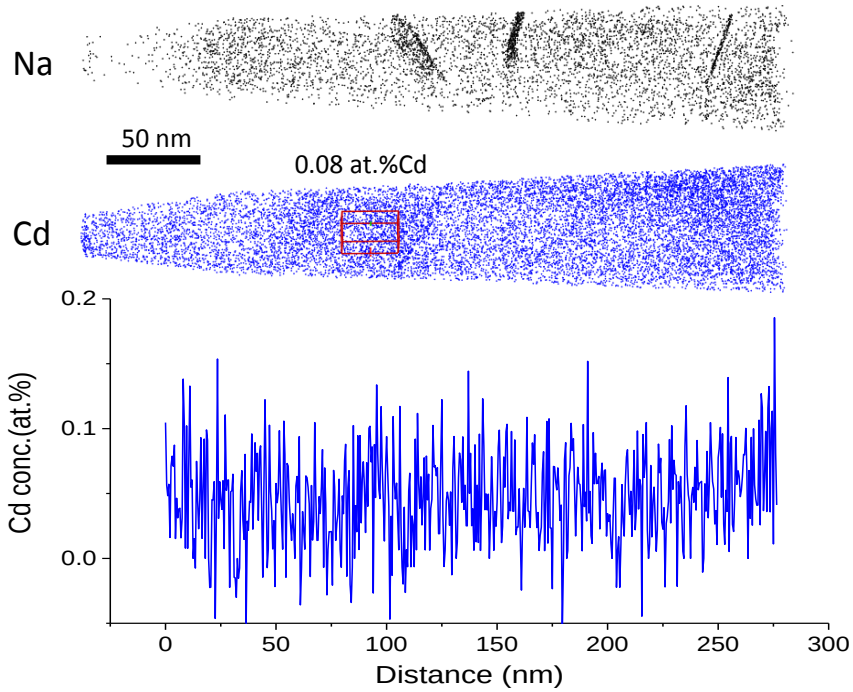

Figure 5.8: Atomic distribution of atoms of Na and Cd in Cd modified CIS. Below is concentration profile of Cd in atomic % along tip.

Cd is thus found to be distributed inside CIS grain and may act as an impurity degrading the device. Distribution of all atoms in vicinity of GB for modified CIS cell is shown in Figure 5.9. As usual Na and In enrichment accompanied with Cu depletion is observed for Ga poor CIGSe cell. Figure also illustrates that Cd distribution is unaffected in vicinity of GB and is uniformly distributed. If CdS is added before the thin film deposition, only Cd isotopes were found and Sulphur (S) is absent in grains and at GBs. This may be due to higher diffusion coefficient of S (3×10^{-10} cm^2/s) [8] at high temperatures (520°C), which accounts an average diffusion length of 850 μm for 40 minutes (deposition time).

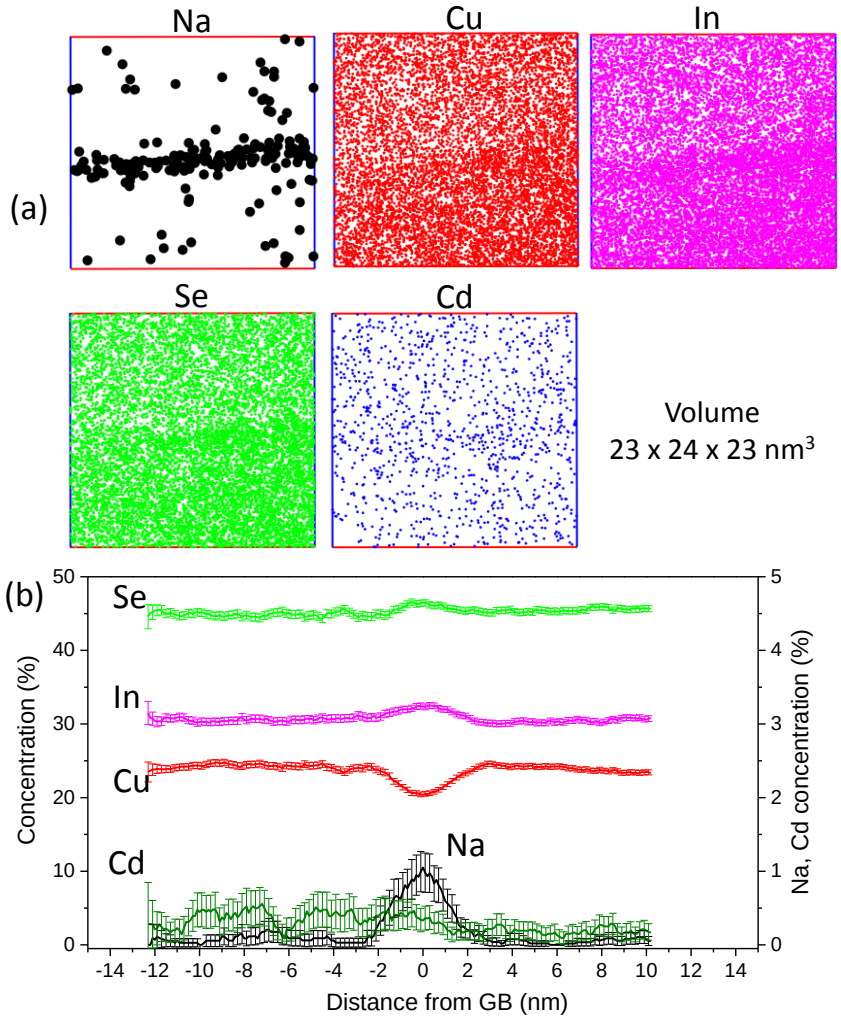

Figure 5.9: (a) Atomic distribution of elements in vicinity of GB for, (b) GB chemistry for corresponding volume.

The above results illustrate the pure In sample (no Ga x=0) and no appreciable changes were observed in GB chemistry comparing with previous results. Similar measurements were performed on Ga intermediate (x=0.5) and Ga rich (x=0.7) cells and Cd was found to be absent throughout the atomic volume including grains and grain boundaries and hence was under detection limit of APT. Figure 5.10 shows mass spectrum for Cd modified CIGSe x=0.7, unlike Figure 5.7 (for x=0) in this case (x=0.7) we found absence of Cd throughout the volume. None of the isotopes of Cd were identified or were under the detection limit of the atom probe. Figure 5.10 represent the mass spectrum for x=0.7, similarly to modified CIGSe x=0.5, no presence of Cd was observed.

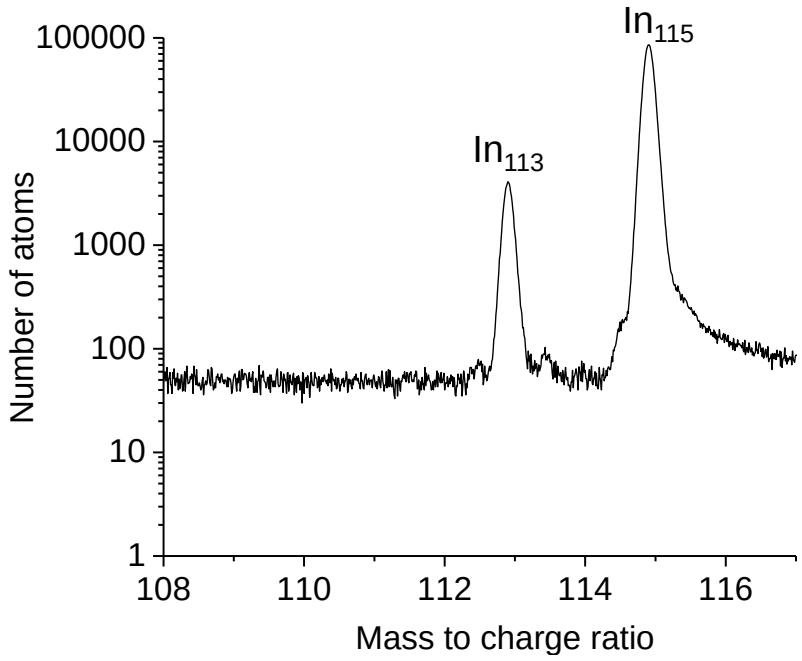

Figure 5.10: Mass spectrum of Cd modified cells for x=0.7 shown in mass range 108 to 117 a.m.u..

After performing repeated analysis on many atom probe tips, we conclude that Cd is not present in modified CIGSe for x=0.5 and x=0.7 or the concentration is very low and is under the APT detection limit.

The presence of Cd in grains in CIS sample and its absence in CIGSe sample can be due to the higher diffusion coefficient of Cd in CIGSe as compared to CIS as shown in Figure 5.11. Cadmium diffusion measurements are adapted from refs. [3,4] for CIS and CIGSe respectively and represent significantly the high diffusion capability of Cd in CIGSe as compared to CIS. Hence Cd is out diffused to grain surface for CIGSe due to high diffusion coefficient of Cd in CIGSe plus high temperature (≈900 K for 40 minutes) during thin film deposition (diffusion length ≈ 150 μm). In case of CIS, a small amount of Cd is retained in CIS and is suspected to be due to a lower diffusion coefficient of Cd in CIS (diffusion length ≈ 1.5 μm).

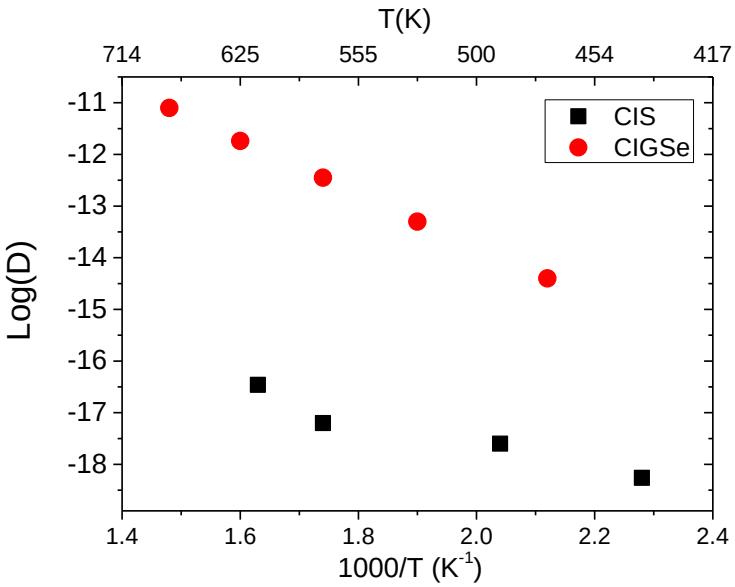

Figure 5.11: Cadmium diffusion (D measured in cm^2s^{-1}) for CIS thin films provided by Kumar et.al [3] and in CIGSe provided by Hiepko et.al [4] as a function of temperature.

Notable changes in GB chemistry is observed comparing modified and reference samples for x=0.5 and x=0.7. As we observed difference in Cu behavior at GB for different Ga samples, we focus here essentially on the composition profile of Cu across GB.

5.5.3 Influence of modification on grain boundary and correlation with device performance

GB chemistry of CIGSe cells with various 'x' present an increased amount of Cu rich GBs as a function of Ga content as discussed in chapter 4. No effect on GB chemistry for Cd-modified Ga poor CIGSe cells was observed and always a Cu depletion is observed at GB. An example is already shown in Figure 5.9.

However a significant effect on GB for Cd-modified Ga rich cell is observed and presented in Figure 5.12 (high Ga samples, x=0.7). Atom probe analyses were carried out at about 100 nm from Mo back contact as shown in Figure 5.5. Because these cells were prepared using 3-stage process, Ga grading is present in the sample and is increased towards back contact. Hence Ga concentration is higher than the average in the APT analyzed region as observed in Figure 5.12. As seen in previous cases, here also we observed the presence of Cu rich GB for Ga rich reference cell, but it is interesting to note that for cells modified with CdS before thin film deposition, GBs are observed Cu depleted which is apparently accompanied by In

enrichment as shown in Figure 5.12. This case is described for two different GBs, to have large statistics more experiments were performed.

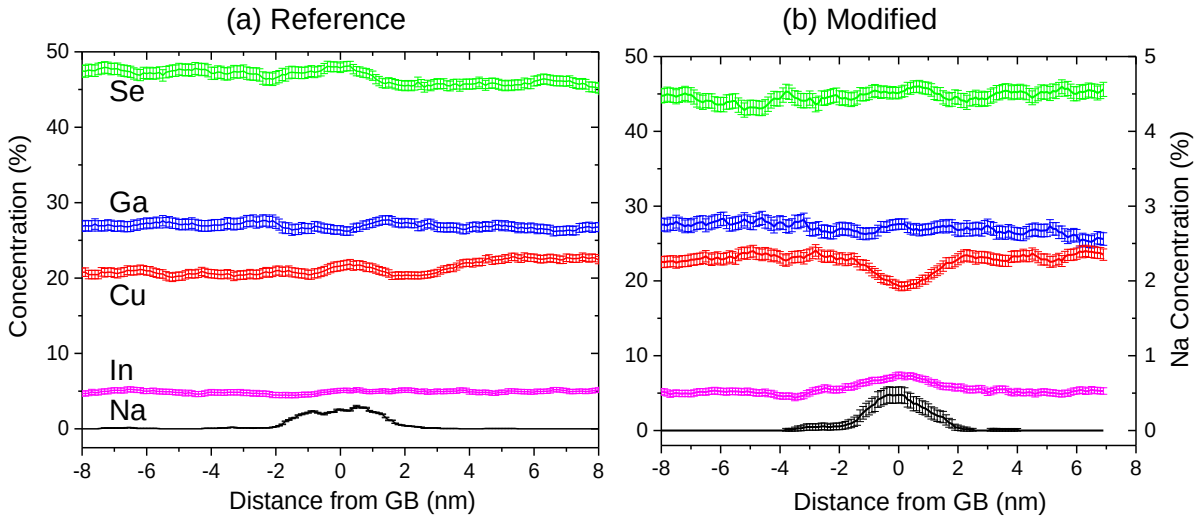

Figure 5.12: GB chemistry for x=0.7 CIGSe for (a) Reference and (b) CdS modified cells.

Many experiments were further performed to increase statistics and behavior of Cu at GB is summarized in Figure 5.13.

Figure 5.13 illustrates the change in Cu concentration at GB for reference and modified cells for x=0.5 and x=0.7. From this, the following conclusions can be made:

1. Presence of Cu rich GBs is observed for reference cells, which was also present in CuPRO samples for this level of Ga content.
2. Hence GB chemistry is found similar for 3-stage samples and CuPRO samples, whit a significant number of Cu rich GBs.
3. For cells modified with CdS before thin film preparation, all GB chemistries observed were Cu depleted and after repeated APT experiments we conclude that some/most of Cu enriched GBs are converted to Cu deprived.

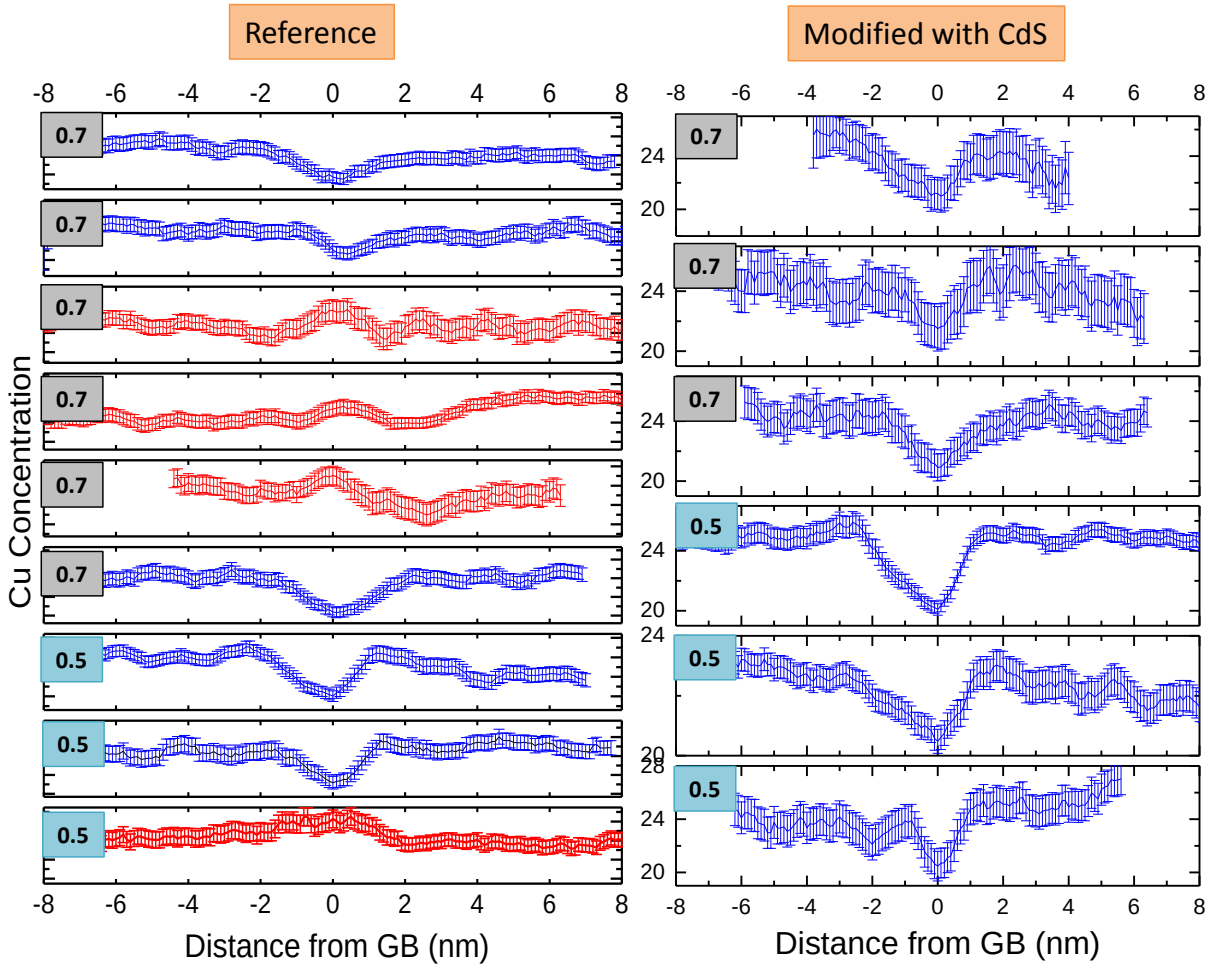

Figure 5.13: Grain boundary chemistry of Cu for x=0.5 and x=0.7 for reference and CdS modified cells. Red & Blue represent Cu rich and Cu poor GB respectively.

This conversion of GBs from Cu rich to Cu poor is apparently due to the occupation of Cu sites by Cd atoms (Cd_{Cu}) during thin film preparation and discussed in later parts of this chapter.

Cu behavior from Figure 5.13 is summarized in Figure 5.14 explaining significant amount of GBs are converted from Cu rich to Cu poor after modification of CIGSe cells. From presented analyzed dataset, only one GB was observed to be Cu enriched for reference CIGSe x=0.5, however almost half of the GBs were Cu enriched for reference CIGSe x=0.7. It is impressive to note that after modifications with Cd, all GBs are observed Cu deprived and is possibly due to modifications in GBs during thin film preparation.

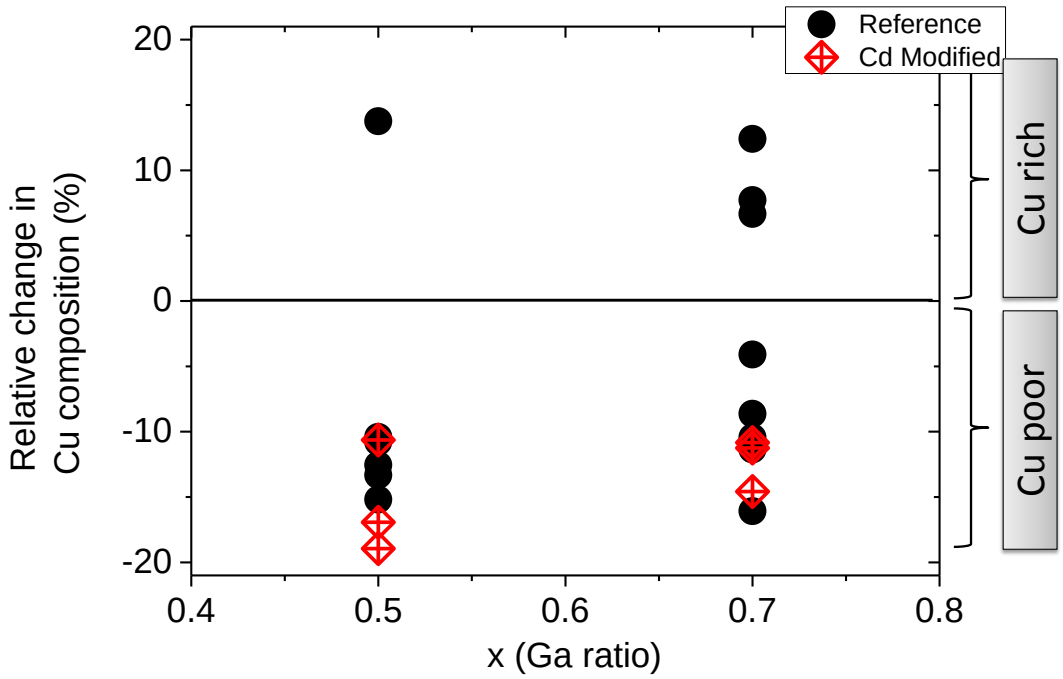

Figure 5.14: ΔCu (relative change in Cu composition in %) as a function of Ga ratio (x) for reference and modified cells.

Comparing Figure 5.1 and Figure 5.14, the improvement in performance of CIGSe can be directly correlated to the increased amount of Cu depleted GBs in Ga rich cells and is explained as follows:

1. Figure 5.1 illustrates that Cd modification impacts more on Ga rich samples as compared to ones with less Ga.
2. Hence, as Ga concentration is increased improvement from its reference is much important, i.e. x=0.7 modified cells presented more improvement than x=0.5.
3. Figure 5.14 shows that higher amount of Cu rich GBs are converted to Cu poor for x=0.7, whereas there were only few Cu rich GBs in reference samples which are now converted to Cu poor.

As Cu poor GBs are shown to have much better influence on CIGSe device performance, higher Ga samples showed much improvement due to more conversion of Cu poor GBs from Cu rich GBs. These improvements observed due to CdS modification are observed for first time and opens up new perspectives for future developments of CIGSe cells.

5.5.4 Cadmium diffusion in CIGSe

Results discussed in the previous section predicted the occupation of Cu sites by Cd atoms at GB. To verify this hypothesis, we performed the analysis of a p-n junction between CIGSe and CdS by exploring the heterojunction. This may not explain actual phenomenon occurring during thin film deposition but can give an idea of CdS-CIGSe interaction at room temperature.

This junction is shown in Figure 5.15 for a standard CIGSe sample (x=0.15). This concentration has not been explored in previous section; however it can provide useful information in vicinity of CdS-CIGSe interface. Figure 5.15a shows the 3D atomic distribution in vicinity of CdS-CIGSe heterojunction. For a better visualization, only Cd and Se atoms are shown. Higher amount of S than Cd in Figure 5.15 is apparently due to the overlapping of O_2^+ (32 a.m.u.) peaks with S^+ (32 a.m.u.).

A 3D volume is selected normal to the heterojunction and the associated concentration profile is plotted in Figure 5.15b. As compared to other elements, Cu is depleted few nanometers earlier while scanning towards CdS. Moreover Cd atoms are observed to enrich few nanometers ahead suggesting replacement of Cu atoms by Cd. Cu depletion near heterojunction (highlighted in grey) is observed and marked in the profile which is occupied by Cd atoms marked in the profile. This confirms the presence of a Cu poor CIGSe grain surface and is accompanied by diffusion of Cd in the first few atomic layers of CIGSe. This can be explained by occupation of Cd atoms over Cu atoms which is also evidenced in ref. [1,4,5]. Research in previous works proposed formation of Cd_{Cu} i.e. accommodation of Cd on Cu-sublattice is possible due to similar ionic radii of Cd^{2+} (0.097 nm) and Cu^+ (0.096 nm) [1]. Nakada et.al [5] have shown that Cd is diffused in the first few nanometers (using TEM imaging) occupying Cu sites. Similar results were obtained by Hiepko et.al [4] for x=0.30. Considering these results we can expect the same behavior for higher Ga samples.

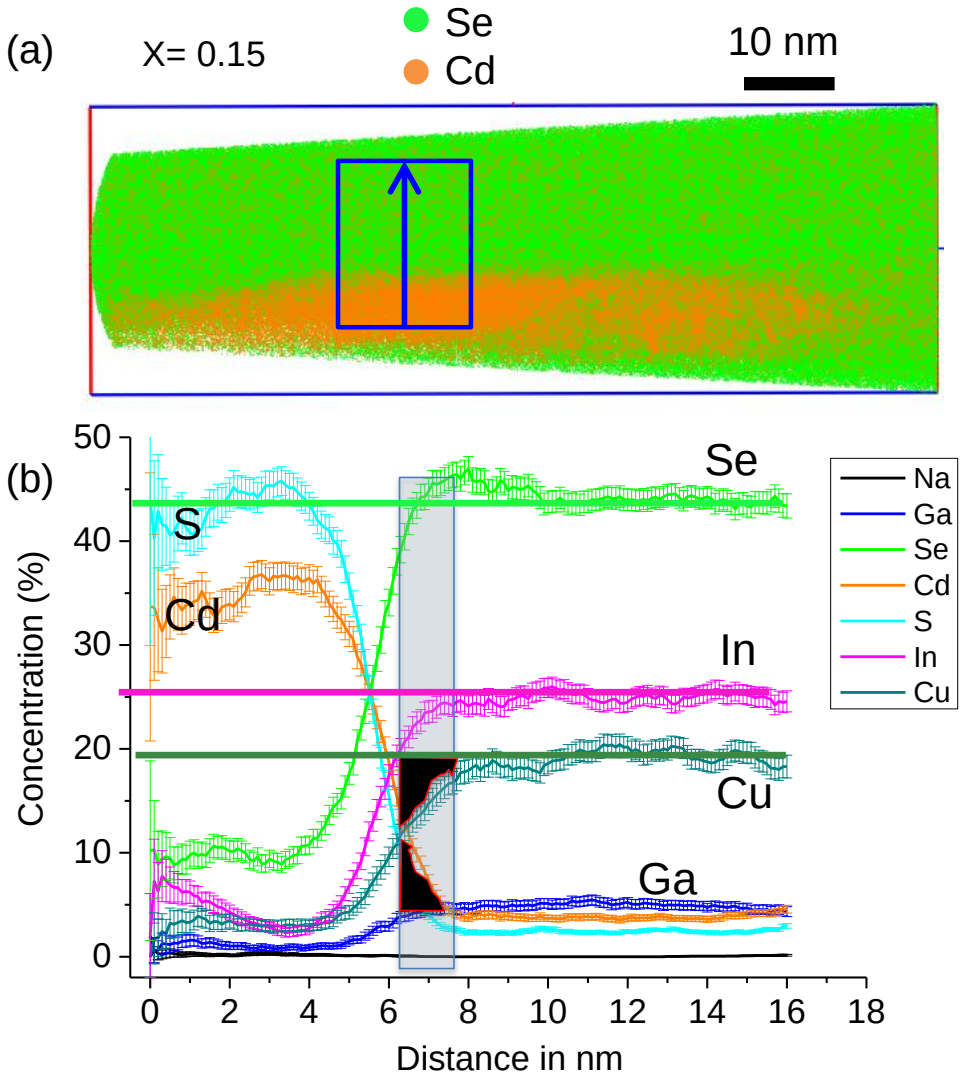

Figure 5.15: (a) 3D atomic distribution in vicinity of CdS-CIGSe heterojunction for x=0.15 depicting distribution of Cd and Se for better visualization. (b) Composition profile of various elements along direction shown in sampling box.

As GBs are also grain surface, the formation of Cd_{Cu} at GBs during thin film growth is expected.

5.5.5 Previous works on different stages of thin film deposition

Above results indicate formation of Cu poor grain surface at the end of thin film preparation. Cu poor GB is shown to be beneficial for solar cell performance; hence it is necessary to understand the origin of Cu rich GBs. Formation of Cu rich GBs is well explained in studies performed by Couzinie-Devy et.al [6] which is detailed here to answer some questions. Couzinie-Devy et.al [6] studied GB chemistry of CIGSe for different stages of 3-stage process and presented change in GB chemistry for different stages as illustrated in Figure

5.16. Elemental flow during 3-stage process is shown in Figure 5.16 representing change in composition of Cu as a function of process time when overall composition switches from Cu poor (point A) to Cu rich (point B) to Cu poor (point C). Three points A, B and C are chosen as shown in the figure to explore their respective GB chemistry. Results show that GB chemistry is tuned from Cu poor to Cu rich to Cu poor for CIGSe composition at A (Cu poor), B (Cu rich) and C (Cu poor) respectively. It is apparent that Cu rich stage leads to formation of Cu rich GBs.

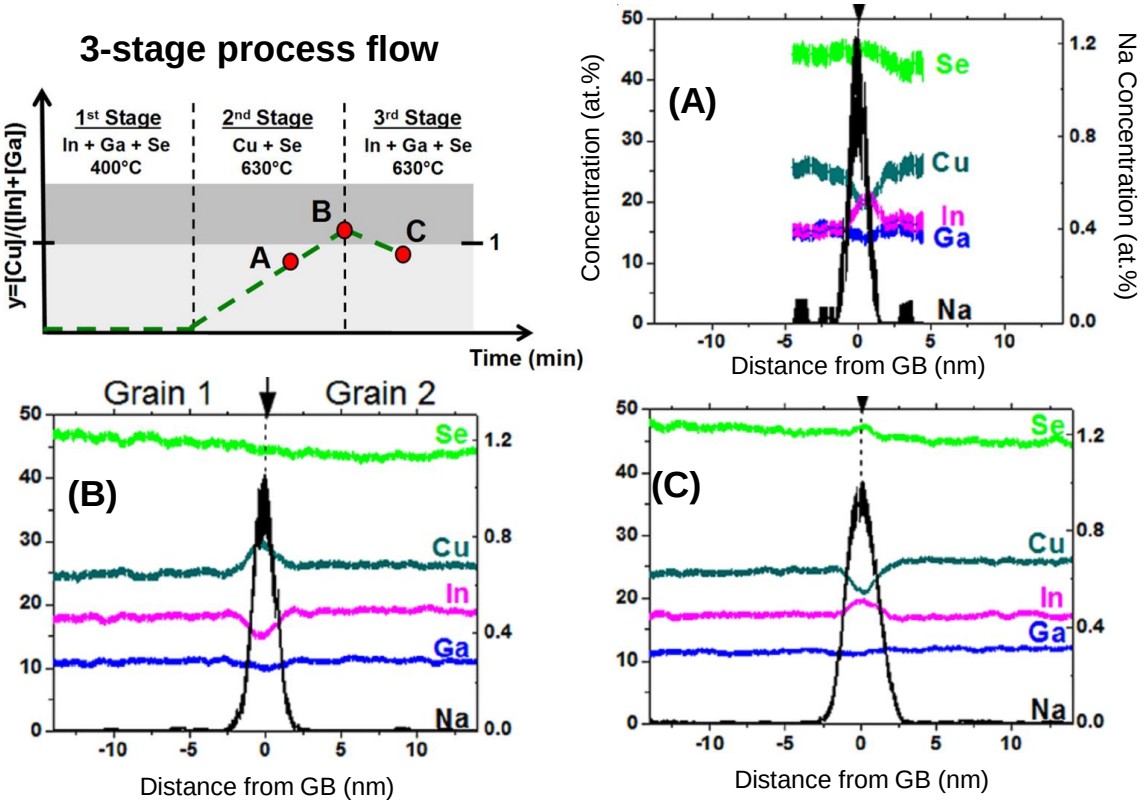

Figure 5.16: (top left) deposition process flow for 3-stage process and GB chemistry measured using APT during different stages (A, B, C) as marked in diagram. Image courtesy: Couzinie-Devy et.al [6].

Hence, at the end of the thin film deposition, overall CIGSe composition is maintained Cu poor.

However considering our case, for Ga rich cell we observed presence of Cu rich GBs even for overall Cu poor CIGSe composition. Hence we expect that for Ga rich CIGSe, while traversing from point A to B, GBs are converted Cu rich, but while traversing from B to C maximum GBs are retained Cu rich and DO NOT convert back to Cu poor. This phenomenon is expected for Ga rich cells as there is very few In concentration to occupy all the defect sites and maintain chalcopyrite phase. To confirm this hypothesis, atom probe investigations are

required for reference and modified cells between different stages of thin film deposition. This part is not performed in the framework of this PhD work and is reserved for future perspectives.

Therefore when CdS is added before thin film deposition, it prevents Cu enrichment at GBs (or grain surfaces) and maintains Cu depleted GBs till the end of the process. A part may also diffuse out to/from grain surface at high temperatures. Regarding Sulphur (S), no S atoms either in grains or at GBs of any of the modified samples were observed and must be due to high diffusion coefficient of S.

There is no proof of this hypothesis and much more physics is involved which requires further detailed study to confirm or to develop another theory to explain conversion of Cu rich to Cu poor GBs due to addition of CdS before thin film preparation. As the theoretical calculations of quaternary system (CIGSe) is itself complicated, inclusion of two more elements Cd, S leads to interplay of overall six main elements (without counting Na) making the system even more complex to study.

Conclusions

In this chapter, possible strategies to improve Ga rich CIGSe cells are discussed. It is proposed that Ga rich CIGSe cells can be improved by addition of CdS before thin film preparation and improvement is observed more for higher Ga concentrations. It is illustrated that due to CdS addition before CIGSe deposition, a large amount of GBs are Cu deprived which was previously demonstrated to be beneficial for GBs properties and cell efficiency. As higher Ga samples contained higher amount of Cu rich GBs, more improvement in Ga rich cells is observed. Studies presented here show the formation of Cu poor GB at Cu rich step for modified samples which was however absent in reference samples and proved to be beneficial for cell performance. Although CdS is used in this work before thin film preparation, it is recommended that other elements or compounds with occupancy over Cu sites must be tested, for example ZnS. This is also better as Cd is not a recommended chemical element.

Hence it is still an open question to explain the conversion of nature of GBs due to addition of different elements. However, it opens new perspectives towards the improvement of wide band gap CIGSe as shown in this work.

References

1. Cojocaru-Mirédin O, Choi P, Wuerz R, Raabe D. Atomic-scale characterization of the CdS/CuInSe2 interface in thin-film solar cells. *Applied Physics Letters* 2011; **98**: 103504–103504–3. DOI: doi:10.1063/1.3560308

2. Cojocaru-Mirédin O, Choi P, Wuerz R, Raabe D. Exploring the p-n junction region in Cu(In,Ga)Se2 thin-film solar cells at the nanometer-scale. *Applied Physics Letters* 2012; **101**: 181603–181603–5. DOI: doi:10.1063/1.4764527

3. Kumar AP, Reddy KV. Cadmium diffusion in thin films. *Semicond Sci Technol* 1997; **12**: 966. DOI: 10.1088/0268-1242/12/8/006

4. Hiepko K, Bastek J, Schlesiger R, Schmitz G, Wuerz R, Stolwijk NA. Diffusion and incorporation of Cd in solar-grade Cu(In,Ga)Se2 layers. *Applied Physics Letters* 2011; **99**: 234101. DOI: 10.1063/1.3665036

5. Nakada T, Kunioka A. Direct evidence of Cd diffusion into Cu(In, Ga)Se2 thin films during chemical-bath deposition process of CdS films. *Applied Physics Letters* 1999; **74**: 2444–2446. DOI: 10.1063/1.123875

6. Couzinie-Devy F, Cadel E, Barreau N, Arzel L, Pareige P. Atom probe study of Cu-poor to Cu-rich transition during Cu(In,Ga)Se2 growth. *Applied Physics Letters* 2011; **99**: 232108–232108–3. DOI: doi:10.1063/1.3665948

7. Liu C-P. A Study of Sulfide Conversion Process of CuInSe2. 2006; Available at: http://oatd.org/oatd/record?record=oai%5C%3ANSYSU%5C%3Aetd-0825106-154239 [Accessed August 19, 2015]

8. Engelmann M, Mccandless BE, Birkmire RW. Formation and analysis of graded CuIn(Se1-ySy)2 films. in Thin solid films (Elsevier), 14–17. Available at: http://cat.inist.fr/?aModele=afficheN&cpsidt=944335 [Accessed August 25, 2015]

6 Conclusion and General Perspectives

This thesis is dedicated to understand the limited performance of wide band gap Cu(In,Ga)Se_2 (CIGSe) solar cells. Polycrystalline CIGSe is known to have a better efficiency than its monocrystalline counterpart, mostly supposed to be attributed to the beneficial effects of grain boundaries (GBs). In this work, the study of these GBs has been undertaken at the atomic scale in order to investigate the atomic distribution of solute atoms and impurities in vicinity of these important defects, namely the grain boundary (GB) of CIGSe photovoltaic cells. In order to achieve this goal, these intrinsic defects were explored by means of high resolution microscopic techniques of the GPM group. In addition to XRD, SEM and TEM, the 3D atom probe tomography (APT) is utilized as the main tool for the atomic scale characterization. APT is the only technique able to detect atomic fluctuations in close vicinity of GB which as it will be seen explains CIGSe device performance.

The band gap of CIGSe can vary co-linearly from 1.04 eV ($CuInSe_2$) to 1.67 eV ($CuGaSe_2$) by tuning the Ga/In concentrations. The possibility to play with the band gap of CIGSe gives this compound a better adaptability towards the solar spectrum. The record efficiency cells, till today, contain 8 at.% of overall Ga concentration. However due to its optimum band gap regarding solar conditions (1.4 eV), Ga rich CIGSe with 18% Ga was expected to have a better efficiency than the Ga poor CIGSe. But, results obtained in this work and in previous works found a poor efficiency for higher Ga cells. This disagreement has led to debate over the years suggesting some important changes in GBs being the main reason. Thus, the aim of the current work was to find any particular changes in GB for Ga rich CIGSe which might hinder their performance. As GBs are few atomic layers thick, we used the atomic probing technique "APT" to investigate their chemistry. Due to its limited analyzing capability (50 × 50 × 100 nm^3), thin films are first characterized at microscopic scale. Microscopic scale characterization is important to confirm that changes in device performance are not due to modifications in their microstructures.

After generalities on CIGSe cells given in chapter one, Chapter 2 focusses on physical principles of all the microscopic analytical techniques namely: SEM, EBSD, EDX and XRD. Details of CIGSe synthesis process used in this work and completion of solar cell circuit are also well explained. Eight CIGSe samples were prepared using the CuPRO (Cu poor-rich-off) process for various "x" or Ga ratio (**x** = [Ga]/[In]+[Ga]). This process was intentionally used in order to prepare CIGSe layer with homogenous composition. A homogenous chemistry in grains is necessary to compare the APT results and to avoid a possible overall composition

effect. Sample preparation techniques, physical principles and reconstruction procedures involved in APT are critical for any analysis, thus their optimizations were first performed to obtain accurate results.

The chapter 3 discusses changes in various properties and characteristics of CIGSe for the different compositions studied in this work. Significant differences in J-V curves, efficiency and quantum efficiency were observed for different samples. Efficiency of the device was found to be maximum for **x**=0.39 and was significantly lower for x=0.7, which was expected to be most efficient, according to band gap modulations. Increase in band gap with Ga content explained linear decrease in short circuit current with Ga content in CIGSe, but could not explain saturation of open circuit voltage (Voc) for Ga rich samples. Hence to understand unexpected decline in device performance for higher **x**, structural and chemical investigation were undertaken. EDX allows to accurately determine CIGSe composition and hence used to calibrate experimental parameters involved in APT instrument. XRD results confirmed the formation of a single chalcopyrite phase in all samples. This simple result approves that the difference in the device performance is not due to the formation of undesired phases. EBSD was used to investigate grain size distribution and the statistical distribution of GB misorientation angles for various x values. . These characteristics (grain size, GB misorientation) were again here unable to explain the reasons for the poor performance of the Ga rich CIGSe cell. This showed that modifications at atomic level are the main reason behind the degraded performance of CIGSe cell. To that point APT was realized. Optimizations of various parameters (laser characteristics, specimen temperature) necessary for APT experiments were calibrated to ensure obtaining accurate results.

In the chapter 4 APT investigations on $CuIn_{1-x}Ga_xSe_2$ with various Ga ratio (**x**) are discussed. This work showed that GB chemistry is largely dependent on respective compositions of CIGSe and three ranges of Ga concentration were identified giving similar GBs composition profiles. In the first regime, $\mathbf{x} < 0.4$, all GBs were found Cu depleted and In enriched which is also consistent with previous studies and theoretical calculations reported in the literature. In the second regime, where $0.4 < \mathbf{x} < 0.7$, two different types of GBs are observed in the film: i) Cu depleted and In enriched and ii) Cu enriched and Ga depleted. In the third regime, $x > 0.7$, Ga rich cells contained only Cu rich GBs and were found to be the less efficient cells. The highest efficiency of CIGSe film in this work was found for x=0.39. It is remarkable to note that after this value of x, the efficiency decreases, which is consistent with the presence of Cu rich GBs. Further decrease in efficiency was consistent with the increasing number of

Cu rich GBs and a correlation between both was evident. Hence, the defect's physics at GBs for Ga poor cells would be different from that of Ga rich cells, which finally reflects their device performances. Some possible explanations were provided in order to explain the physical phenomenon behind the beneficial effect of Cu poor GB and detrimental effect of Cu rich GB. Some previous studies suggested that Cu poor GB act as hole barriers thus preventing carrier recombination. Cu rich GB may increase recombination leading to poor performance. Contreras et.al, on his side, explained that the formation of dead grains (grains which do not contribute in carrier collection) in Ga rich cells may degrade their performance. Results in this work may explain that these dead grains, probably surrounded by Cu rich GBs, are due to poor electronic activity in vicinity of Cu rich GBs. Some more possible phenomenons were proposed, such as formation of shunt paths due to Cu rich GB and/or formation of undesired phases at GB, which explain possible reasons for their limited performance. Hence it was concluded that Cu rich GB hinders CIGSe performance. However a particular physical phenomenon at the origin of this is not clearly detected and proved. In addition, it was interesting to note that GB chemistry is largely dependent on the overall grain concentration. Cu can either be enriched at GB (accompanied with Ga depletion) or depleted at GB (accompanied with In enrichment) depending on the overall grain concentration. The possible driving forces leading change in GB chemistry with Ga content, or in other words leading to thermodynamic solute segregations, were proposed such as: mixing segregation enthalpy, intrinsic defect physics and segregation tendency due to size effect or site effect. As the system involves the interplay of four elements (excluding impurities, Na…), calculation of interactions among them is very complicated. A clear explanation to these observations is an open question and should be a (numerical modeling) perspective. In addition, for intermediate Ga contents ($0.4 < \mathbf{x} < 0.7$) both Cu rich and Cu poor GBs are observed, which can be due to different misorientation angles between the GBs. An immediate explanation to this is not yet found. This could be achieved by performing correlative EBSD or TEM measurements on APT tip before analysis, this work is also reserved as future perspective.

In chapter 5, some efforts were made to improve GBs properties of CIGSe. As Cu poor GB is found beneficial, some strategies were attempted to convert Cu rich GB to Cu poor GB. It was found that incorporation of Cd which is found to occupy Cu sites is beneficial. In order to achieve this, a CdS layer was deposited before the CIGSe thin film deposition. This process shows an improvement of the device properties but only for high Ga content.

Microstructural investigations using SEM/EBSD did not revealed any significant changes due to CdS addition. However, investigation of GBs for reference and CdS modified cells demonstrated the conversion of Cu rich GBs to Cu poor GBs for higher Ga cells. Hence improve in efficiency was attributed to changes in GB chemistry. Cd atoms are thought to occupy Cu sites during thin film deposition thus preventing Cu to segregate at GBs. It was interesting to note that besides acting as an impurity, incorporation of CdS improves the device. Accurate explanation of this phenomenon is not yet clearly understood also because of the complex elaboration process (copper poor/copper rich). The perspective in this aspect is to understand the beneficial effects of CdS addition and to try elements other than Cd and S, Cd being not recommended.

In summary, due to their high efficiency and good stability, CIGSe thin films are promising candidates for future development of solar cells. Limited efficiency of Ga rich CIGSe is a major concern and the main reasons of this are thoroughly described in this work. As CIGSe is a quaternary compound, the development of accurate theoretical models to explain GBs solute segregation and properties will need time but will find in this work a large data base to be compare and / or reproduce tendencies.

7 Appendices

Appendix A:

Checking Homogeneity using pair correlation function.

Atom probe tomography (APT) provides 3D atomic distribution of all elements in CIGSe as discussed previously. In order to test whether the technique provides homogeneous atomic distribution and does not bias the results, we perform pair correlation statistical test. Figure 1 shows a typical reconstructed APT volume of CIGSe. Considering a volume V as shown in figure 1, if N_i is the number of an atomic specie "i" in a volume V, its atomic density can be written as $\rho_i=N_i/V$. Probability density to find an atom "j" from atom "i" at a given distance is given by the radial distribution function G_{ij} [1].

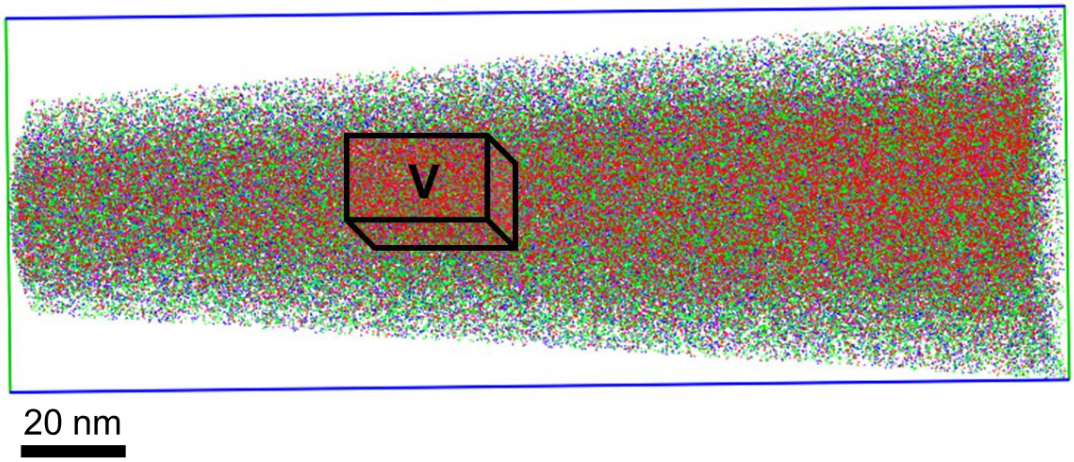

Figure 1: Reconstructed 3D atomic volume of a CIGSe grain with Ga ratio=0.84. Selected volume 'V' is used for further calculations.

G_{ij} at a distance 'r' from atom "i" can be calculated by taking into account the number of atoms between spherical shell r and r + dr. G_{ij} equals volume of the shell multiplied by the atomic density and multiplied by the correction factor g_{ij} which accounts the deviation from random distribution.

$$G(r)_{ij} = g(r)_{ij}\rho_j 4\pi r^2 dr \quad \textbf{(1)}$$

The correcting factor $g(r)_{ij}$ is the correlation function for the pairs i-j. This function can be deduced from above equation and can be written as:

$$g(r)_{ij} = \frac{G(r)_{ij}}{\rho_j 4\pi r^2 dr} \quad \textbf{(2)}$$

Three cases of pair correlation function $g(r)_{ij}$ is evident:

1) Greater than 1: Positive correlation, tendency to cluster
2) Less than 1: Anti-correlation, tendency to order
3) Equal to 1: Random distribution, homogenous.

Pair-correlation tests can be performed from inbuilt option in post processing software GPM3Dsoft, by selecting any element present in the volume. Pair-correlation tests have been performed in this case for a CIGSe grain which is shown in figure 2 for the volume 'V' obtained from figure 1. Figure 2 represents selected 3D volume of Ga atoms and Se atoms, on their respective right side is shown the pair correlation function of Ga-Ga atoms and for Se-Se atoms. It is clear from the figure that the pair correlation function for the two species is = 1±0.03. This shows that the obtained atomic distribution is very homogenous without presence of any clusters. Below results are shown for Ga and Se and similar results were obtained for Cu and In (not shown here). These results show that APT experiment does not bias the results obtained and gives an accurate representation of atomic distribution for CIGSe.

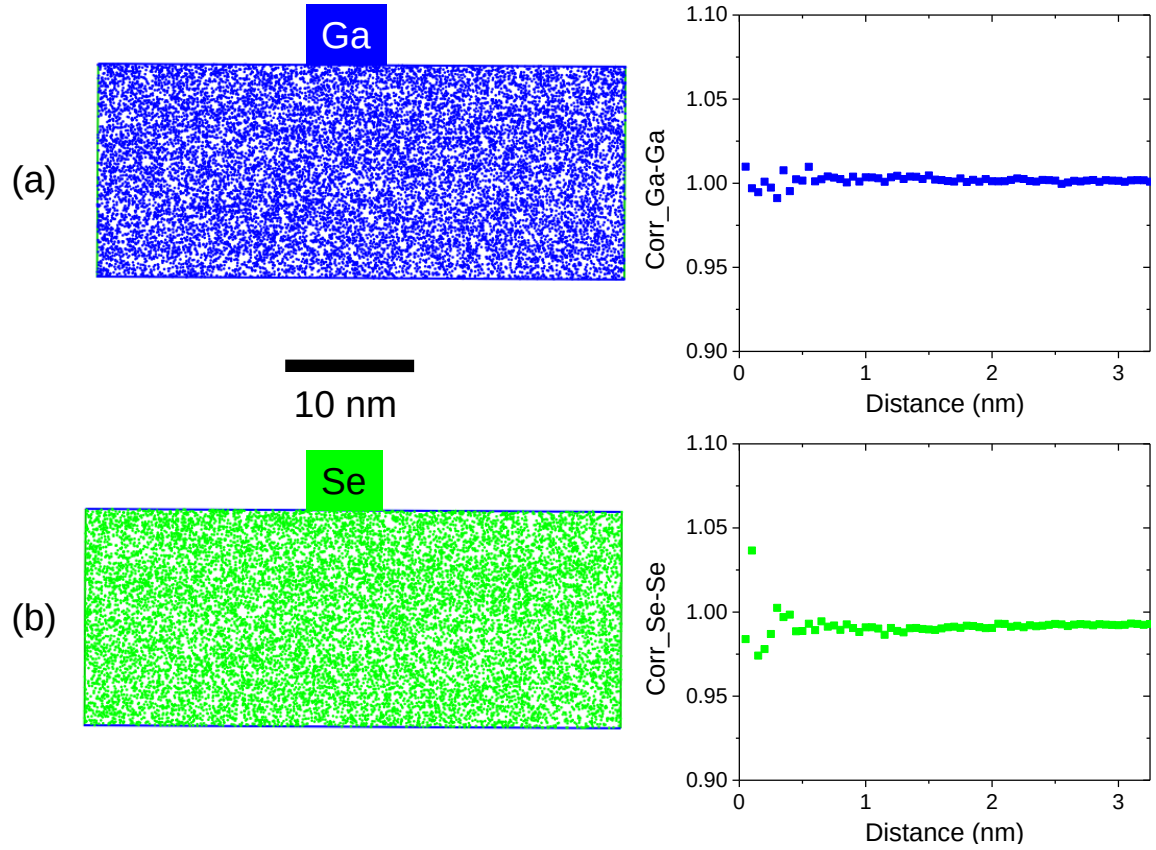

Figure 2: Selected 3D volume from figure 1 depicting atomic distribution for (a) Ga and pair correlation function for Ga atoms and (b) Se and pair correlation function for Se atoms.

References

1. Geuser FD. Interprétation et traitement des données de sonde atomique tomographique : application à la precipitation dans les Al-Mg-Si. 2005; Available at: https://tel.archives-ouvertes.fr/tel-00077980/document [Accessed September 1, 2015]

Appendix B: Calculation of Na Gibbsian Interfacial Excess in CIGSe grain boundaries (GBs).

Gibbsian Interfacial Excess of Na (Γ_{Na}) provides number of Na atoms segregated per unit of interfacial area [1]. Thanks to atom probe tomography (APT) which can provide 3D distribution of Na atoms along GB. Statistical information from APT data can be used to calculate Γ_{Na}. Figure3a shows decoration of Na atoms along GB of a typical CIGSe sample, extracted 3D volume in (b) can be used to plot cumulative distribution between Na atoms and total number of atoms as shown in (c). Cumulative distribution is then used to calculate Γ_{Na}.

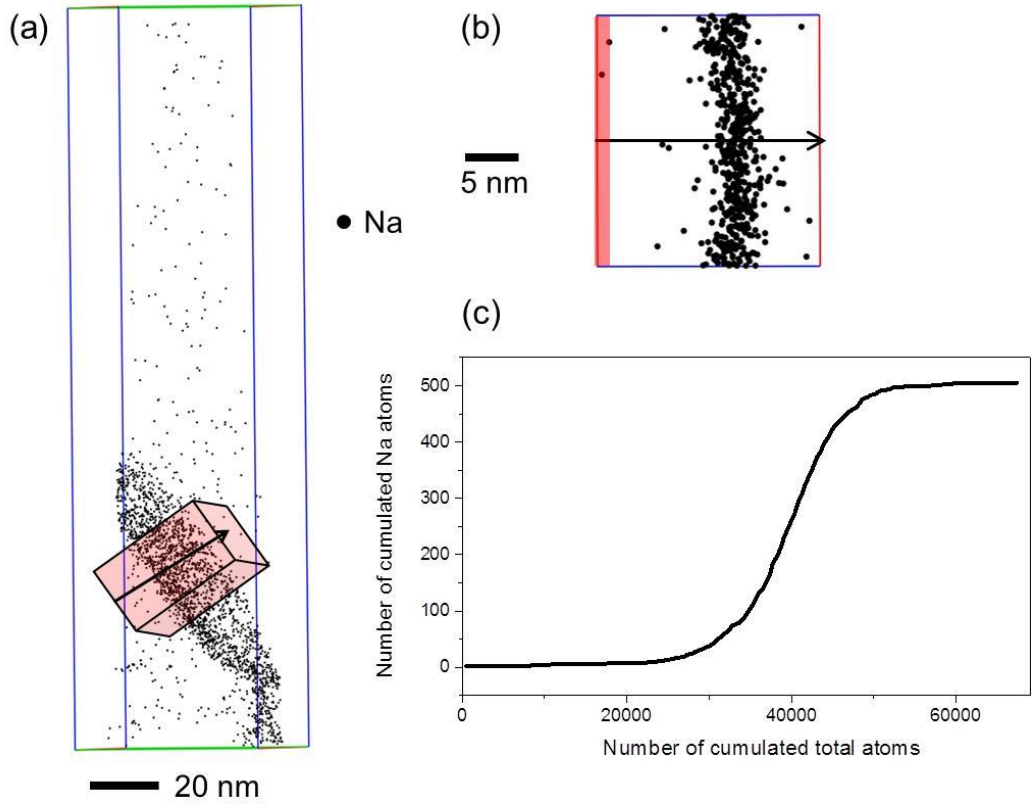

Figure 3: (a) 3D reconstructed APT volume of an analyzed CIGSe tip depicting distribution of only Na atoms. A 3D box is extracted in vicinity of GB to quantify Na distribution. (b) Extracted 3D volume, 1 Å wide sampling box is moved perpendicularly to GB in steps of 1 Å. (c) Integral profile measured for Na from selected 3D volume.

Figure 4 shows integral profile of Na decorated in between two grains G1 and G2. N_{Na}(G1) and N_{Na}(G2) represents number of Na atoms in G1 and G2 respectively. Number of Na atoms in excess can be measured then directly using the relation:

$$\Gamma_{Na} = \frac{N_{Na(total)} - N_{Na(G1)} - N_{Na(G2)}}{\eta A} = \frac{N_{Na(excess)}}{\eta A}$$

where, η is detection efficiency of atom probe (0.63 in this case), A is interfacial area used for integral profiling (25 nm in this case).

Γ_{Na} is then calculated from above equation and is equal to 2 atoms per nm^3.

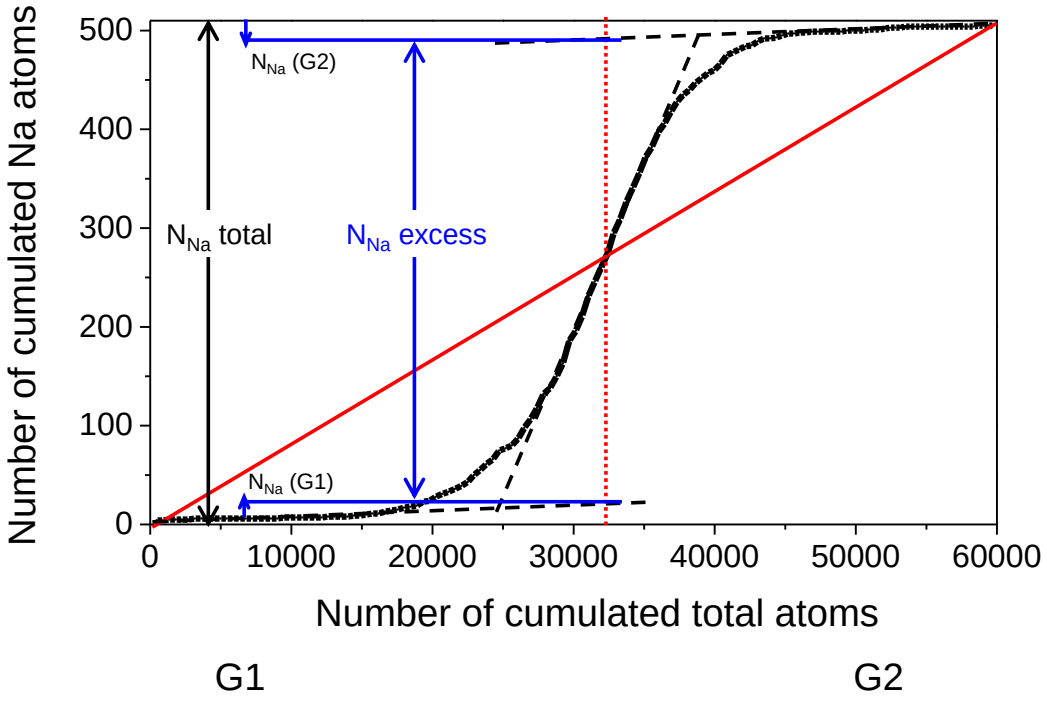

Figure 4: Integral profile of Na traced perpendicular to GB between grain 1 (G1) and grain 2 (G2).

References

1. Hellman OC, Seidman DN. Measurement of the Gibbsian interfacial excess of solute at an interface of arbitrary geometry using three-dimensional atom probe microscopy. *Materials Science and Engineering: A* 2002; **327**: 24–28. DOI: 10.1016/S0921-5093(01)01885-8

Abstract

With efficiency more than 21%, polycrystalline Cu(In,Ga)Se_2 (CIGSe) semiconductors present maximum efficiency among thin film solar cells, making them a promising material to develop solar cell modules. Most efficient CIGSe cells produced till date are Ga poor cells (≈7.5% Ga) having band gap (E_g) =1.2 eV, however cells with optimum band gap (according to solar spectrum) 1.4 eV (≈18% Ga) presented much lower efficiency. This degraded performance of wide band gap CIGSe lead to scientific debates for many years suggesting various theories behind its decline in performance. Beneficial properties of Grain boundaries (GBs) are one of the main reasons for high efficiency of CIGSe and modifications in GBs could be the reason for hindered performance of Ga rich cells. In order to detect changes in chemistry of GBs, a technique able to resolve materials at atomic scale is employed in this research, known as atom probe tomography (APT). Exploring GB chemistry, we found that Ga poor cells always exhibit Cu deprived GBs which are known beneficial for cells due to their hole barrier properties, however Cu enriched GBs emerges for Ga concentration higher than 7.5%. This composition surprisingly coincides with decline in CIGSe performance and further increase in Ga concentration results in increase in Cu enriched GBs followed by degraded CIGSe performance. This suggests modifications in GBs can alter device's performance, hence to retain GB properties some propositions and experiments are illustrated in the end.

Résumé

Avec une efficacité de plus de 21%, le matériau polycristallin semiconducteur Cu(In,Ga)Se_2 (CIGSe) présente le maximum d'efficacité pour les cellules solaires dites à couches minces. Les cellules CIGSe les plus efficaces produites jusqu'à ce jour sont des cellules pauvres en Ga (≈7.5% Ga) et ayant une largeur de bande interdite (Eg) de 1,2 eV. Cependant, les cellules avec une largeur de bande optimale d' 1,4 eV (≈18% Ga) présentent une efficacité beaucoup plus faible. Cette dégradation des performances des cellules à large bande interdite CIGSe conduit à des débats scientifiques depuis de nombreuses années ayant mené à diverses théories pour expliquer le déclin des performances de ces cellules avec l'augmentation de Ga. Les propriétés bénéfiques des joints de grains (GB) sont l'une des principales raisons de rendement élevé du CIGSe et les modifications de la chimie des GB pourraient être la raison de la performance limitée des cellules riches en Ga. Afin de détecter des changements dans la chimie des GB, une technique capable d'imager des matériaux à l'échelle atomique est employée dans ce travail : la sonde atomique tomographique (APT). L'exploration de la chimie des GB nous a permis de constater que les cellules pauvres en Ga présentent toujours une déplétion en Cu. Cette chimie semble bénéfique pour les cellules en raison de leurs car les GB agissent alors comme barrière pour trous, évitant ainsi les recombinaisons aux joints de grain. Cependant pour des concentrations de Ga supérieures à 7,5%, un enrichissement en Cu est observé. Cette composition coïncide étonnamment avec la baisse de la performance des cellules CIGSe. Cela suggère que des modifications dans les joints de grains peuvent altérer les performances de l'appareil. Donc, pour améliorer les propriétés des joints de grains, de nouvelles pistes sont envisagées à la fin du document.